



National Library  
of Canada

Bibliothèque nationale  
du Canada

Canadian Theses Service

Services des thèses canadiennes

Ottawa, Canada  
K1A 0N4

## CANADIAN THESES

## THÈSES CANADIENNES

### NOTICE

The quality of this microfiche is heavily dependent upon the quality of the original thesis submitted for microfilming. Every effort has been made to ensure the highest quality of reproduction possible.

If pages are missing, contact the university which granted the degree.

Some pages may have indistinct print especially if the original pages were typed with a poor typewriter ribbon or if the university sent us an inferior photocopy.

Previously copyrighted materials (journal articles, published tests, etc.) are not filmed.

Reproduction in full or in part of this film is governed by the Canadian Copyright Act, R.S.C. 1970, c. C-30.

**THIS DISSERTATION  
HAS BEEN MICROFILMED  
EXACTLY AS RECEIVED**

### AVIS

La qualité de cette microfiche dépend grandement de la qualité de la thèse soumise au microfilmage. Nous avons tout fait pour assurer une qualité supérieure de reproduction.

S'il manque des pages, veuillez communiquer avec l'université qui a conféré le grade.

La qualité d'impression de certaines pages peut laisser à désirer, surtout si les pages originales ont été dactylographiées à l'aide d'un ruban usé ou si l'université nous a fait parvenir une photocopie de qualité inférieure.

Les documents qui font déjà l'objet d'un droit d'auteur (articles de revue, examens publiés, etc.) ne sont pas microfilmés.

La reproduction, même partielle, de ce microfilm est soumise à la Loi canadienne sur le droit d'auteur, SRC 1970, c. C-30.

**LA THÈSE A ÉTÉ  
MICROFILMÉE TELLE QUE  
NOUS L'AVONS REÇUE**

THE UNIVERSITY OF ALBERTA

CHARACTERIZATION OF THE  
INDUCTIVELY COUPLED PLASMA - MASS SPECTROMETER

by

© SAMANTHA S. H. TAN

A THESIS

SUBMITTED TO THE FACULTY OF GRADUATE STUDIES AND  
RESEARCH IN PARTIAL FULFILMENT OF THE REQUIREMENT FOR  
THE DEGREE OF DOCTOR OF PHILOSOPHY

DEPARTMENT OF CHEMISTRY

EDMONTON, ALBERTA

SPRING 1987

Permission has been granted to the National Library of Canada to microfilm this thesis and to lend or sell copies of the film.

The author (copyright owner) has reserved other publication rights, and neither the thesis nor extensive extracts from it may be printed or otherwise reproduced without his/her written permission.

L'autorisation a été accordée à la Bibliothèque nationale du Canada de microfilmer cette thèse et de prêter ou de vendre des exemplaires du film.

L'auteur (titulaire du droit d'auteur) se réserve les autres droits de publication; ni la thèse ni de longs extraits de celle-ci ne doivent être imprimés ou autrement reproduits sans son autorisation écrite.

ISBN 0-315-37664-3

THE UNIVERSITY OF ALBERTA

RELEASE FORM

NAME OF AUTHOR: SAMANTHA S. H. TAN

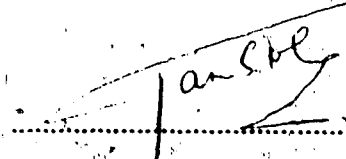
TITLE OF THESIS: CHARACTERIZATION OF THE INDUCTIVELY  
COUPLED PLASMA - MASS SPECTROMETER

DEGREE FOR WHICH THESIS WAS PRESENTED: Ph.D.

YEAR THIS DEGREE GRANTED: 1987

Permission is hereby granted to THE UNIVERSITY OF ALBERTA LIBRARY to reproduce single copies of this thesis and to lend or sell such copies for private, scholarly or scientific research purposes only.

The author reserves other publication rights, and neither the thesis nor extensive extracts from it may be printed or otherwise reproduced without the author's written permission.

  
-----  
(Student's signature)

Permanent address:

71, Labelle Crescent, St. Albert  
Alberta, Canada T8N 2G6

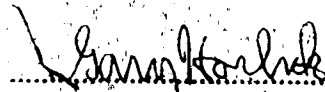
Date: 1987




THE UNIVERSITY OF ALBERTA

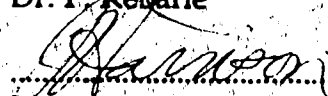
FACULTY OF GRADUATE STUDIES AND RESEARCH

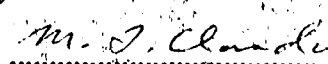
The undersigned certify that they have read, and recommend to the Faculty of Graduate Studies and Research for acceptance, a thesis entitled CHARACTERIZATION OF THE INDUCTIVELY COUPLED PLASMA - MASS SPECTROMETER submitted by Samantha S. H. Tan in partial fulfilment of the requirements for the degree of Doctorate of Philosophy.

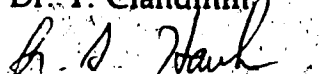
  
.....  
Dr. G. Horlick (supervisor)

  
.....  
Dr. B. Kratochvil

  
.....  
Dr. P. Kekarle

  
.....  
Dr. J. Harrison

  
.....  
Dr. T. Clandinin

  
.....  
Dr. S. Houk

Date: 13 April 1987

To my dad

## ABSTRACT

In this thesis, the technique of ICP-MS is studied and evaluated for trace elemental analysis. All experiments were carried out with the SCIEX Elan 250 ICP-MS. A systematic study of the effects of plasma operating parameters on analyte ion signals was carried out. Analyte signals were found to be most affected by two key parameters; nebulizer flowrate and plasma power. To a lesser degree, ion signals were also dependent on the auxiliary gas flowrate and sampling depth. The data are presented graphically as nebulizer flowrate-power parameter behavior plots. This study provides guidelines for sensible selection of optimum plasma operating conditions and clarifies confusing trends observed at single parameter setting.

Background spectral features of water, 5% nitric acid, 5% hydrochloric acid, 5% sulfuric acid and 5% phosphoric acid are reported. Mass spectra and tables are presented showing in detail the background species. The knowledge of these background species is important in order to avoid potential interferences that may occur in these matrices.

The basic quantitative performance of the ICP-MS was also investigated. The method has excellent detection limits (sub-ppb levels) and 4-5 orders of magnitude of linear dynamic concentration range. Calibration plots have negative deviation if concentration exceeds 10 ppm; this deviation can be corrected by using an internal standard.

Matrix effects in ICP-MS were studied for a range of plasma operating conditions. Analyte signals were found to be susceptible to matrix effects at relatively low concentrations (< 100 ppm) of all types of matrix elements. Matrix effects were strongly dependent on the nebulizer flowrate and were most serious at high nebulizer flowrates. Minimization of matrix effects in ICP-MS can be

brought about by dilution of the sample and by operating the plasma at a low nebulizer flowrate. However, both of these steps result in a loss of analyte sensitivity.

Several possible mechanisms for matrix effects in ICP-MS are discussed. Matrix effects are thought to be occurring in the plasma discharge as well as in the sampling interface and mass spectrometer.

## ACKNOWLEDGEMENT

First, I wish to thank my supervisor, Gary Horlick who has provided me with valuable assistance and supervision, and also because he is a nice guy.

I would like to thank all my colleagues and professors especially in the analytical division who have made my stay in the University of Alberta very enjoyable.

Finally, I wish to thank my husband, Frank whose love I can always depend on and whose patience I have taxed. Without his support and encouragement, I would not have embarked on the journey for graduate studies.

## TABLE OF CONTENTS

| CHAPTER  | PAGE |
|--|------|
| <b>1. INTRODUCTION</b>   |      |
| A. Inductively Coupled Plasma-Mass Spectrometry.....   | 1    |
| B. The Inductively Coupled Plasma as an Ion Source.....  | 2    |
| C. Ion Sampling of the ICP.....  | 8    |
| D. Quadrupole Mass Spectrometer.....   | 14   |
| E. ICP-MS Literature Review.....   | 18   |
| F. Thesis Objective.....   | 23   |
| <br><b>2. EFFECTS OF PLASMA OPERATING PARAMETERS ON ANALYTE ION SIGNALS IN ICP-MS</b>                  |      |
| A. ICP-MS Instrumentation.....   | 24   |
| B. Experimental.....   | 34   |
| C. Dependence of Analyte Ion Signals on Aerosol Carrier (Nebulizer) Gas Flowrate and Plasma Power..... | 37   |
| C1. First Row Transition Metals.....   | 37   |
| C2. Alkali Metals.....   | 41   |
| D. Dependence of Analyte Ion Signals on Sampling Depth...  | 45   |
| E. Dependence of Analyte Ion Signals on Intermediate (Auxiliary) Gas Flowrate.....                     | 48   |
| F. Parameter Behavior Plots at 5mm to 20mm using a MAK Torch.....                                      | 52   |
| G. Discussion.....   | 59   |
| H. Conclusion.....   | 64   |

|   |     |
|---|-----|
| <b>3. BACKGROUND SPECTRAL FEATURES IN ICP-MS</b>  |     |
| A. Introduction.....  | 65  |
| B. Experimental.....  | 65  |
| C. Distilled Water and 5% Nitric Acid.....  | 66  |
| D. 5% Hydrochloric Acid.....  | 75  |
| E. 5% Sulfuric Acid.....  | 80  |
| F. 5% Phosphoric Acid.....  | 88  |
| G. Conclusion.....  | 88  |
| <br>  |     |
| <b>4. QUANTITATIVE PERFORMANCE IN ICP-MS</b>  |     |
| A. Introduction.....  | 95  |
| B. Experimental.....  | 95  |
| C. Detection Limits.....  | 97  |
| D. Analytical Calibration Curves.....   | 103 |
| D 1. Linearity and Dynamic Range.....   | 103 |
| D 2. Analytical Curves with Internal Standard.....  | 103 |
| D 3. Analytical Curves of Elements forming Oxides<br>and Doubly Charged Ions.....             | 108 |
| E. Conclusion.....  | 118 |
| <br>  |     |
| <b>5. MATRIX EFFECTS IN ICP-MS (PART 1)</b>   |     |
| A. Introduction.....  | 119 |
| B. Experimental.....  | 123 |
| C. Effect of Sodium on Analyte Ion Signals at Different<br>Plasma Operating Conditions.....   | 124 |
| D. Effect of High Concentrations of a Range of Matrix<br>Elements on Analyte Ion Signals..... | 132 |

|   |     |
|---|-----|
| E. Effect of Photon Stop Voltage (Lens B) on the Matrix Effect.....                                       | 139 |
| F. Effect of Varying Concomitant Concentrations on Analyte Ion Signals.....                               | 144 |
| G. Matrix Effects for Solutions Containing Constant Molar Ratio of Analyte Element to Matrix Element..... | 152 |
| H. Summary and Conclusion.....  | 156 |
| <br>  |     |
| 6. MATRIX EFFECTS IN ICP-MS (PART 2)  |     |
| A. Introduction.....  | 158 |
| B. Experimental.....  | 158 |
| C. Precision and Reproducibility of Data.....   | 161 |
| D. Matrix Effects at a Nebulizer Flowrate of 0.9 l/min.....   | 163 |
| E. Matrix Effects at Nebulizer Flowrates of 0.8, 0.85, 0.9, 0.95, 1.0 and 1.05 l/min.....                 | 168 |
| F. Effect of a Matrix Element on Ion Signal-Nebulizer Flowrate Plot Profile for Co and Pb.....            | 173 |
| G. Matrix Effects in ICP-AES.....   | 179 |
| H. Summary on Matrix Effects in ICP-MS .....  | 181 |
| I. Discussion and Conclusions .....   | 182 |
| <br>  |     |
| 7. CONCLUSION .....   | 187 |
| REFERENCES .....  | 191 |



## LIST OF TABLES

| TABLE  | PAGE |
|--|------|
| 1. Elements with their corresponding degree of ionization in an argon ICP.....   | 6    |
| 2. A summary of the ICP-MS instrumental parameters.....  | 33   |
| 3. Ionization potentials, isotopic masses and natural abundances for alkali and first row transition elements.....                 | 35   |
| 4. Calibration of nebulizer pressure vs aerosol carrier gas flowrate.....  | 36   |
| 5. Background species for water and 5 % nitric acid with corresponding element masses.....   | 72   |
| 6. Background species for 5 % hydrochloric acid with corresponding element masses.....   | 79   |
| 7. Background species for 5 % sulfuric acid with corresponding element masses.....   | 86   |
| 8. Background species for 5 % phosphoric acid with corresponding element masses.....   | 91   |
| 9. Summary of major background species for water/5 % nitric, 5 % sulfuric acid, 5 % hydrochloric acid and 5 % phosphoric acid..... | 93   |
| 10. Detection limits for the first row elements and the alkali metals.....   | 101  |
| 11. Detection limits at compromise plasma operating conditions (power, 1.2 kW and nebulizer flowrate, 1.1 l/min).....              | 102  |

|     |   |     |
|-----|---|-----|
| 12. | Lanthanum and cerium oxide ratios and cerium doubly charged ratios at different analyte concentrations..... | 117 |
| 13. | Concentration of the analytes and matrix elements used in Section G.....                                    | 154 |
| 14. | Mass, ionization potential and degree of ionization of the matrix elements and analyte elements.....        | 160 |
| 15. | Matrix effects in ICP-AES.....  | 180 |

## LIST OF FIGURES

| FIGURE |   | PAGE |
|--------|---|------|
| 1.     | Schematic diagram of the ICP source.....  | 3    |
| 2.     | Ion sampling of the inductively coupled plasma.....   | 9    |
| 3.     | a) Skimmer cone sampling at Mach disk, b) Skimmer cone sampling after Mach disk, c) Skimmer cone sampling before Mach disk..... | 13   |
| 4.     | Schematic layout of the quadrupole mass filter and its power supply.....  | 15   |
| 5.     | Stability diagram showing x and y stability envelope and scan line.....   | 17   |
| 6.     | Block diagram of the ICP-MS.....  | 25   |
| 7.     | Schematic diagram of the Sciex Elan 250 ICP-MS.....   | 26   |
| 8.     | ICP torches.....  | 28   |
| 9.     | Original input ion optics of the mass spectrometer.....   | 29   |
| 10.    | New input ion optics of the mass spectrometer.....  | 31   |
| 11.    | Mass spectrum of the first row transition elements.....   | 38   |
| 12.    | Nebulizer pressure-power parameter behavior plot for Cr.....  | 39   |
| 13.    | Dependence of ion count on nebulizer pressure (power = 1.3 kW) for Mn, V, Cr, Ti, Fe, Co, Ni and Cu.....                        | 40   |
| 14.    | Averaged and normalized nebulizer pressure-power parameter behavior plot for Ti, V, Cr, Mn, Fe, Co, Ni and Cu.....              | 42   |
| 15.    | Nebulizer pressure-power parameter behavior plots for Li, Na, Rb and Cs.....  | 43   |
| 16.    | Normalized ion count vs nebulizer pressure plots for Li, Na, Rb and Cs at 1.2 kW.....   | 44   |

|      |  |    |
|------|--|----|
| 17.  | Dependence of ion count on nebulizer pressure for Li, Na, Rb and Cs at sampling depths of 17, 20, 23, 26 and 29 mm from the load coil..... | 46 |
| 18.  | Dependence of ion count on nebulizer pressure for V, Mn, Zn and Cd at sampling depths of 17, 19, 21, 23 and 25 mm from the load coil.....  | 47 |
| 19.  | Dependence of ion count on auxiliary flowrate for Ti, Mn and Cu at sampling depths of 17, 19, 21 and 23 mm from the load coil.....         | 49 |
| 20.  | Dependence of ion count on auxiliary flowrate for Li, Na, Rb and Cs at sampling depths of 17, 19, 21 and 23 mm from the load coil.....     | 51 |
| 21a. | Nebulizer flowrate-power parameter behavior plots at sampling depths of 5, 10, 15 and 20 mm for Li.....                                    | 53 |
| 21b. | Nebulizer flowrate-power parameter behavior plots at sampling depths of 5, 10, 15 and 20 mm for Na.....                                    | 54 |
| 21c. | Nebulizer flowrate-power parameter behavior plots at sampling depths of 5, 10, 15 and 20 mm for Rb.....                                    | 55 |
| 21d. | Nebulizer flowrate-power parameter behavior plots at sampling depths of 5, 10, 15 and 20 mm for Cs.....                                    | 56 |
| 22a. | Nebulizer flowrate-power parameter behavior plots at sampling depths of 5, 10, 15 and 20 mm for Sc.....                                    | 57 |
| 22b. | Nebulizer flowrate-power parameter behavior plots at sampling depths of 5, 10, 15 and 20 mm for Cu.....                                    | 58 |
| 23.  | Zones of the ICP discharge.....  | 61 |
| 24.  | Normalized ion count vs nebulizer pressure plots for Li, Na, Rb, Cs and Sc for a MAK torch.....  | 63 |

|     |  |    |
|-----|--|----|
| 25. | Background spectra for water for the mass range<br>1-43 amu.....   | 67 |
| 26. | Background spectra for water for the mass range<br>42-84 amu.....  | 68 |
| 27. | Background spectra for 5 % nitric acid for the mass range<br>1-43 amu.....   | 69 |
| 28. | Background spectra for 5 % nitric acid for the mass range<br>42-84 amu.....  | 70 |
| 29. | Background spectra for 5 % hydrochloric acid for the mass<br>range 1-43 amu. Source of stock acid: Pfaitz & Bauer.....   | 76 |
| 30. | Background spectra for 5 % hydrochloric acid for the mass<br>range 42-84 amu. Source of stock acid: Pfaitz & Bauer.....  | 77 |
| 31. | Background spectra for 5 % hydrochloric acid for the mass<br>range 1-43 amu. Source of stock acid: Baker & Adamson.....  | 81 |
| 32. | Background spectra for 5 % hydrochloric acid for the mass<br>range 42-84 amu. Source of stock acid: Baker & Adamson..... | 82 |
| 33. | Background spectra for 5 % sulfuric acid for the mass range<br>1-43 amu.....   | 83 |
| 34. | Background spectra for 5 % sulfuric acid for the mass range<br>42-84 amu.....  | 84 |
| 35. | Background spectra for 5 % phosphoric acid for the mass<br>range 1-42 amu.....   | 89 |
| 36. | Background spectra for 5 % phosphoric acid for the mass<br>range 42-82 amu.....  | 90 |
| 37. | Signal-to-noise ratio and standard deviation vs<br>measurement time for Cu.....  | 98 |
| 38. | Signal-to-noise ratio and standard deviation vs ion signal   |    |

|     |   |     |
|-----|---|-----|
|     | intensity for V.....  | 99  |
| 39. | Calibration plots for V51 and V50.....  | 104 |
| 40. | Calibration plots for Zn67 with and without an internal<br>standard. The internal standard was 0.4 ppm Co.....            | 106 |
| 41. | Calibration plots for Cd111 with and without an internal<br>standard. The internal standard was 0.5 ppm Rh.....           | 107 |
| 42. | Calibration plots for Li6, Li7, Cu65 and Rb85.....  | 109 |
| 43. | Calibration plots for La and LaO.....   | 111 |
| 44. | Calibration plot for Sc.....  | 112 |
| 45. | Calibration plots for Ce with and without an internal<br>standard. The internal standard was 0.5 ppm Cs.....              | 113 |
| 46. | Calibration plots for CeO with and without an internal<br>standard. The internal standard was 0.5 ppm Cs.....             | 114 |
| 47. | Calibration plot for Ce <sup>2+</sup> with and without an internal<br>standard. The internal standard was 0.5 ppm Cs..... | 115 |
| 48. | Types of interferences in ICP-AES.....  | 120 |
| 49. | Effect of 100 ppm Na on the Sc signal as a function of<br>nebulizer flowrate and power.....                               | 125 |
| 50. | Effect of 1000 ppm Na on the Sc signal as a function of<br>nebulizer flowrate and power.....                              | 126 |
| 51. | Effect of 100 ppm Na on the Sc signal as a function of<br>nebulizer flowrate and sampling depth.....                      | 128 |
| 52. | Effect of 1000 ppm Na on the Sc signal as a function of<br>nebulizer flowrate and sampling depth.....                     | 129 |
| 53. | Effect of 1000 ppm Na on the signals for Cr, Zn, Ga, and ScO<br>as a function of nebulizer flowrate.....                  | 130 |
| 54. | Effect of 1000 ppm Na on the Cu signal as a function of   |     |

|      |  |     |
|------|--|-----|
|      | nebulizer flowrate and power.....  | 131 |
| 55.  | Dependence of ArNa ion signal on nebulizer flowrate and Na matrix concentration.....   | 133 |
| 56.  | Effect of 1000 ppm Cd on the signals for Sc, Cr, Co, Cu, Zn and Ga as a function of nebulizer flowrate. Sampling depth was 18 mm from the load coil..... | 134 |
| 57.  | Effect of 1000 ppm Cs on 1 ppm Sc, Cr, Mn, Co, Cu and Zn as a function of nebulizer flowrate.....  | 136 |
| 58.  | Effect of 863 ppm In on 1 ppm Sc, Cr, Mn, Co, Cu and Zn as a function of nebulizer flowrate.....   | 137 |
| 59.  | Effect of 845 ppm Cd on 1 ppm Sc, Cr, Mn, Co, Cu and Zn as a function of nebulizer flowrate.....   | 138 |
| 60.  | Effect of 775 ppm Rh on 1 ppm Sc, Cr, Mn, Co, Cu and Zn as a function of nebulizer flowrate.....   | 140 |
| 61.  | Effect of 893 ppm Sn on 1 ppm Sc, Cr, Mn, Co, Cu and Zn as a function of nebulizer flowrate.....   | 141 |
| 62.  | Effect of 916 ppm Sb on 1 ppm Sc, Cr, Mn, Co, Cu and Zn as a function of nebulizer flowrate.....   | 142 |
| 63.  | Dependence of matrix effect on the photon stop (lens B) for Co and Cd signals at nebulizer flowrates of 1.1, 0.9 and 0.6 l/min.....                      | 143 |
| 64a. | The effect of Na on 0.1 ppm Li, Al, Co and Ba <sup>2+</sup> as a function of Na concentration and nebulizer flowrate.....                                | 145 |
| 64b. | The effect of Na on 0.1 ppm Rh, Ba, Pb and Th as a function of Na concentration and nebulizer flowrate.....  | 146 |
| 65.  | Matrix effect of Na on Al, Co, Ba and Pb as a function of Na concentration at nebulizer flowrates of 0.9, 1.0 and 1.1 l/min....                          | 147 |

|      |  |     |
|------|--|-----|
| 66a. | The effect of Cs on 0.1 ppm Li, Al, Sc and Co as a function of Cs concentration and nebulizer flowrate.....  | 149 |
| 66b. | The effect of Cs on 0.1 ppm Ba <sup>2+</sup> , Ba, Pb and Th as a function of Cs concentration and nebulizer flowrate.....   | 150 |
| 67.  | Matrix effect of Cs on Al, Co, Ba and Pb as a function of Cs concentration at nebulizer flowrates of 0.9, 1.0 and 1.1 l/min....  | 151 |
| 68.  | Effect of matrix element concentration (Zn and K) on analyte elements. Concentration listed for each column is that for the analyte element and the molar ratio of matrix element to analyte is 1000:1 in all cases..... | 155 |
| 69.  | Reproducibility of two nebulizer flowrate parameter plots for Sc and Ba taken one-half hour apart.....   | 162 |
| 70.  | Matrix effects on Sc for equi-molar amounts ( $4.2 \times 10^{-3}$ M) of the matrix elements B, Na, Zn, Rb, Cd, Cs, Au, Tl and U.....  | 164 |
| 71.  | Matrix effects on Li, Al, Sc, Co, Rh, Ba, Pb and Th for equi-molar amounts of matrix elements.....   | 166 |
| 72.  | Matrix effect on Al, Co, Rh, Ba and Th as a function of the mass of the matrix element for high ionization potential matrices (upper graph) and for low ionization potential matrices (lower graph).....                 | 167 |
| 73.  | Matrix effect as a function of the mass of the analyte for high ionization potential matrices (upper graph) and for low ionization potential matrices (lower graph).....   | 169 |
| 74.  | Mass dependency of the matrix effect for Ba <sup>2+</sup> (upper graph) and Ba <sup>+</sup> (lower graph).....   | 170 |
| 75.  | Effect of nebulizer flowrate on the mass dependency of the matrix effect.....  | 172 |



|     |  |     |
|-----|--|-----|
| 76. | Matrix effect as a function of nebulizer flowrate and mass of matrix element for the high ionization potential matrices (first column) and for low ionization potential matrices (second column).....  | 174 |
| 77. | Matrix effect as a function of nebulizer flowrate and mass of analyte element for the high ionization potential matrices (first column) and for low ionization potential matrices (second column)..... | 175 |
| 78. | Effects of B, Zn, Cd and Au matrices on the ion signal-nebulizer flowrate plots for Co and Pb .....  | 177 |
| 79. | Effects of Na, K, Rb, Cs and Tl matrices on the ion signal-nebulizer flowrate plots for Co and Pb .....  | 178 |

## CHAPTER 1

### INTRODUCTION

#### A. Inductively Coupled Plasma-Mass Spectrometry

The coupling of an inductively coupled plasma to a quadrupole mass spectrometer has given rise to a new technique known as inductively coupled plasma-mass spectrometry (ICP-MS). Traditionally, the ICP has been used as an atomization/ionization-excitation source for atomic emission, atomic absorption or atomic fluorescence spectroscopy. In atomic emission spectroscopy, the ICP has achieved great success and extensive analytical methodology has been developed for elemental analysis. The ICP is well-known to exhibit many advantages for elemental analysis such as low detection limits, wide linear dynamic range and comparatively little or no matrix and inter-element interferences [1].

In inductively coupled plasma-mass spectrometry, the ICP serves as an ion source in the production of singly charged monoatomic species which are extracted into a vacuum system. The ions are then separated and detected by a quadrupole mass spectrometer. Mass spectrometric detection provides additional advantages to the method which include sensitivity and specificity. Thus, with the combined advantages of both the inductively coupled plasma and the mass spectrometer, ICP-MS has great potential to be an extremely powerful method for elemental analysis.

The original claims to the advantages of the method were impressive [2-5]. For trace elemental analysis, the detection limits achievable are in the range of 10-100 pg/ml which are 1-2 orders of magnitude better than optical ICP detection limits. The linear dynamic concentration range ( $10^6$ ) obtained is comparable to that observed in inductively coupled plasma-atomic emission

spectroscopy (ICP-AES). Mass spectra are much simpler than optical emission spectra thus spectral overlaps are less problematic and easier to manage. As the mass spectrum of each element is simple and unique, qualitative determination of elements in an unknown sample can be readily performed. In addition, the method is applicable to almost all elements in the periodic table except helium, neon and fluorine.

Another feature of ICP-MS is its capability for rapid determination of isotope abundances [6-8]. This feature is significant because isotope ratio determinations by traditional methods such as thermal ionization mass spectrometry are slow and often tedious. Presently however, the precision and accuracy obtained for isotope ratio measurements by ICP-MS tend to be inferior to those obtained by thermal ionization mass spectrometry. With future developments and improvements, ICP-MS should emerge as a powerful tool for isotope ratio determinations. The ease with which isotope ratios can be measured should certainly encourage the use of stable isotope tracers in biological systems, expand the utilization of isotope data in mineral exploration and also expand the utilization of stable isotope dilution for accurate quantitative determinations.

The general principles involved in ICP-MS will be discussed in the following sections and a literature review of the technique is presented at the end of the chapter.

#### B. The ICP as an Ion Source

In contrast to ICP-AES, where the inductively coupled plasma is used both to generate and excite atoms and ions, the principal function of the ICP in ICP-MS is to simply convert analyte species efficiently to singly charged positive ions. A schematic diagram of an ICP source is shown in Figure 1.

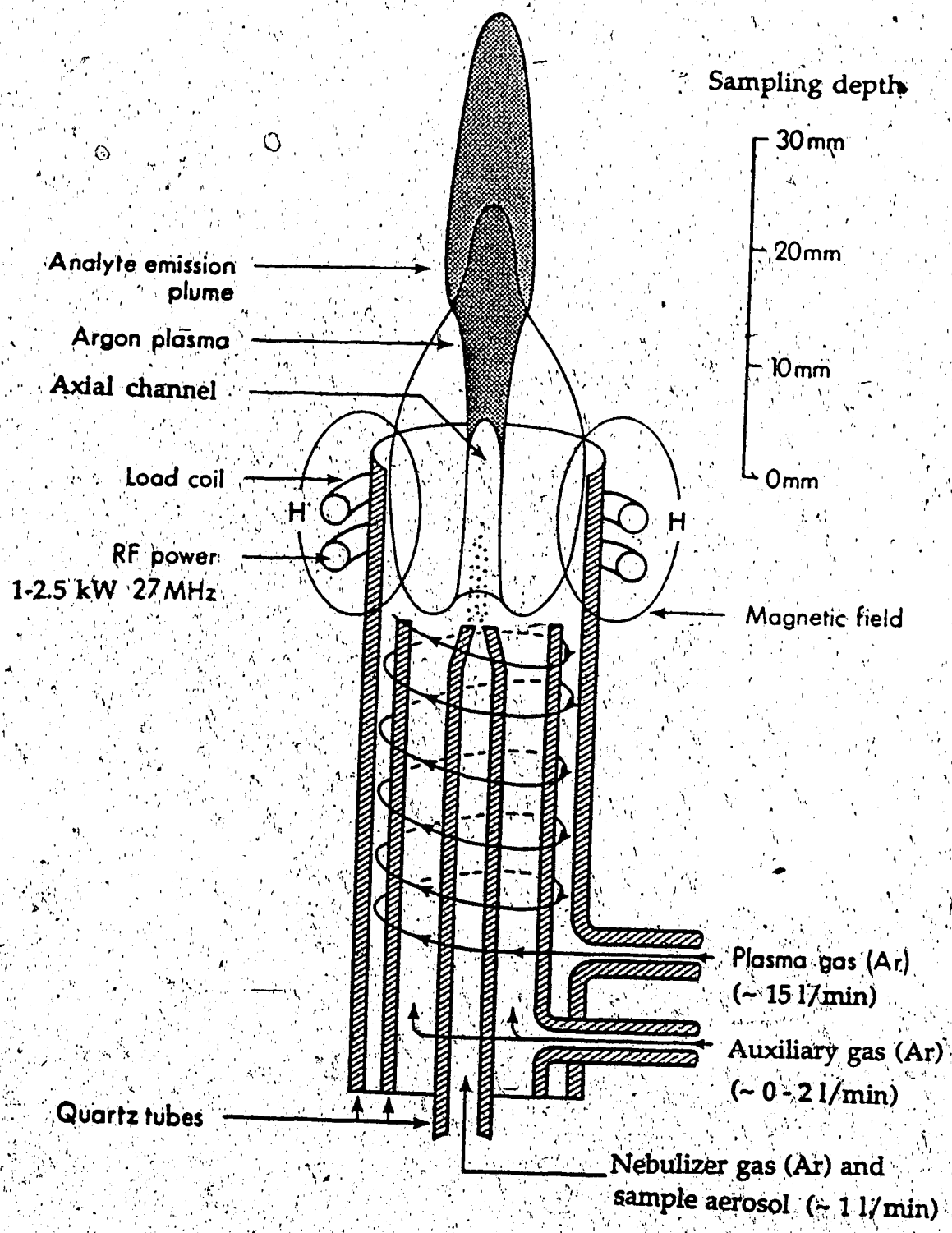


Figure 1. Schematic diagram of the ICP source

Only a brief description of the general characteristics of the ICP will be mentioned here, several excellent overview articles on the subject can be found in the literature [1, 9-11]. The plasma torch consists of three concentric quartz tubes and their argon gas flows are shown in Figure 1. The torch is surrounded by a 3-4 turn induction coil to which rf power is applied (27 MHz, 1-2.5 kW). The plasma is "lit" with a Tesla coil. The plasma is tear-drop in shape and when viewed from the top it has the appearance of a doughnut. The temperature of the plasma in the axial channel is about 6,000 K at the normal observation zone.

Sample solution is usually converted into aerosol droplets by a nebulizer-spray chamber system and injected into the plasma via the central aerosol tube. During passage through the axial channel of the plasma, the aerosol droplets are desolvated, vaporized, atomized, ionized and excited. In most instances, these processes are efficiently carried out because of the high temperatures of the plasma and the relatively long sample residence time (typically 2-3 ms). The number density of analyte species in the axial channel of the plasma may be estimated from the following equation [12]:

$$n_M = \frac{R_{Neb} \cdot \epsilon_{NEB} \cdot \epsilon_{ICP} \cdot N_0 \cdot T_{Rm} \cdot C_M}{F_{Aer} \cdot T_{ICP} \cdot m} \quad (1)$$

where  $R_{Neb}$  = solution uptake rate (ml/min)

$\epsilon_{NEB}$  = nebulization efficiency

$\epsilon_{ICP}$  = injection efficiency of aerosol into axial channel

$N_0$  = Avogadro's number (mole<sup>-1</sup>)

$T_{Rm}$  = room temperature (K)

- $C_M$  = solution concentration (g/ml)  
 $F_{Aer}$  = aerosol gas flowrate (ml/min)  
 $T_{ICP}$  = ICP temperature (K)  
 $m$  = mass of the analyte element (g/mole)

Under normal plasma operating conditions, a 1 ppm Cu solution yields  $n_M \sim 10^{10} \text{ cm}^{-3}$ . The total number density of argon species in the plasma is  $10^{17} \text{ cm}^{-3}$  and the degree of ionization of the argon gas is about 1 %. The fraction of analyte element that is ionized in the plasma may be calculated from the Saha equation, assuming that the plasma is in local thermodynamic equilibrium [13],

$$\frac{n_i n_e}{n_a} = S_n = \frac{(2\pi m k T)^{3/2}}{h^3} \cdot \frac{2 Z_i}{Z_a} \cdot \exp(-V_i/kT) \quad (2)$$

where  $n_i, n_a, n_e$  = number densities for the ions, atoms and electrons respectively ( $\text{cm}^{-3}$ )

$S_n$  = ionization constant

$m$  = mass of the electron

$k$  = Boltzman constant

$h$  = Planck constant

$Z_i, Z_a$  = partition functions of the ion and the atom

$T$  = temperature

$V_i$  = ionization potential of the element (eV)

Table 1. Elements with their corresponding degree of ionization in an argon ICP

| <u>Element</u> | <u>IP (eV)</u> | <u>Degree of Ionization*1</u> | <u>Degree of Ionization*2</u> |
|----------------|----------------|-------------------------------|-------------------------------|
| Cs             | 3.894          | 100                           | 100                           |
| Rb             | 4.177          | 100                           | 100                           |
| K              | 4.341          | 100                           | 100                           |
| Na             | 5.139          | 100                           | 100                           |
| Ba             | 5.212          | 100                           | 91                            |
| Ra             | 5.279          | 100                           | -                             |
| Li             | 5.392          | 100                           | 100                           |
| La             | 5.577          | 100                           | 90                            |
| Sr             | 5.695          | 100                           | 96                            |
| In             | 5.786          | 99                            | 99                            |
| Al             | 5.986          | 99                            | 98                            |
| Ga             | 5.99           | 99                            | 98                            |
| Tl             | 6.108          | 99                            | 100                           |
| Ca             | 6.113          | 100                           | 99                            |
| Y              | 6.38           | 99                            | 98                            |
| Sc             | 6.54           | 100                           | 100                           |
| V              | 6.74           | 99                            | 99                            |
| Cr             | 6.766          | 99                            | 98                            |
| Ti             | 6.82           | 99                            | 99                            |
| Zr             | 6.84           | 99                            | 99                            |
| Nb             | 6.88           | 99                            | 98                            |
| Hf             | 7.0            | 99                            | 98                            |
| Mo             | 7.099          | 99                            | 98                            |
| Tc             | 7.28           | 98                            | -                             |
| Bi             | 7.289          | 94                            | 92                            |
| Sn             | 7.344          | 97                            | 96                            |
| Ru             | 7.37           | 97                            | 96                            |
| Pb             | 7.416          | 98                            | 97                            |
| Mn             | 7.435          | 97                            | 95                            |
| Rh             | 7.46           | 96                            | 94                            |
| Ag             | 7.576          | 94                            | 93                            |
| Ni             | 7.635          | 93                            | 91                            |
| Mg             | 7.646          | 98                            | 98                            |
| Cu             | 7.726          | 92                            | 90                            |
| Co             | 7.86           | 95                            | 93                            |
| Fe             | 7.870          | 97                            | 96                            |
| Re             | 7.88           | 95                            | 93                            |
| Ta             | 7.89           | 96                            | 95                            |
| Ge             | 7.899          | 92                            | 90                            |
| W              | 7.98           | 95                            | 94                            |

|    |        |             |          |
|----|--------|-------------|----------|
| Si | 8.151  | 88          | 85       |
| Be | 8.298  | 62          | 58       |
| Pd | 8.34   | 94          | 93       |
| Sb | 8.461  | 81          | 78       |
| Os | 8.7    | 80          | 78       |
| ed | 8.993  | 85          | 85       |
| Pt | 9.0    | 62          | 62       |
| Te | 9.009  | 67          | 66       |
| Au | 9.225  | 49          | 51       |
| Be | 9.322  | 75          | 75       |
| Zn | 9.394  | 75          | 75       |
| Se | 9.752  | 31          | 33       |
| As | 9.81   | 49          | 52       |
| S  | 10.360 | 12          | 14       |
| Hg | 10.437 | 32          | 38       |
| I  | 10.451 | 25          | 29       |
| P  | 10.486 | 29          | 33       |
| Rn | 10.748 | 36          | -        |
| Br | 11.814 | 3           | 5        |
| C  | 11.260 | 3           | 5        |
| Xe | 12.130 | 5           | 8.5      |
| Cl | 12.967 | 0.5         | 0.9      |
| O  | 13.618 | 0.04        | 0.1      |
| Kr | 13.999 | 0.2         | 0.6      |
| N  | 14.534 | 0.04        | 0.1      |
| Ar | 15.759 | 0.01        | 0.04     |
| F  | 17.422 | 0.0002      | 0.0009   |
| Ne | 21.564 | 0.000005    | 0.000006 |
| He | 24.587 | 0.000000001 | -        |

\*1 by Furuta,  $T_{ion} (Ar) = 6680 K$  and  $n_e = 1.47 \times 10^{14} cm^{-3}$

\*2 by Houk,  $T_{ion} (Ar) = 7500 K$  and  $n_e = 1 \times 10^{15} cm^{-3}$



The degree of ionization  $\alpha$ , can be determined from the following relationship:

$$\alpha = n_i / (n_a + n_i) = S_n / (n_e + S_n) \quad (3)$$

Calculation of  $\alpha$  from the above relationships by various authors [12,14-16] reveals that most elements are efficiently ionized in the ICP. The degrees of ionization calculated by Furuta [16] and Houk [15] are shown in Table 1. In general, elements with ionization potentials  $\leq 8$  eV are more than 90 % ionized in the plasma. Therefore, the ICP is an excellent ion source as it can produce a high concentration of positive ions of most of the elements in the periodic table.

### C. Ion Sampling of the ICP

The plasma gas is extracted into the mass spectrometer by means of a plasma sampling interface whose arrangement is shown in Figure 2. The plasma sampling interface consists of two water cooled sampling cones. The first cone is called the sampler and the second cone is called the skimmer. The differentially pumped region between the two sampling cones is maintained at a pressure of 1-2 torr using a mechanical pump. Similar interfaces have been used previously by various workers to generate high intensity molecular beams [17, 18] and for atmospheric pressure sampling of flames [19, 20].

Plasma gas from the core of the discharge is drawn through the first orifice and undergoes supersonic expansion in the 1 torr region. A small fraction of the expanded gas is further extracted into the mass spectrometer through the skimmer while the bulk of the plasma gas is pumped away. In

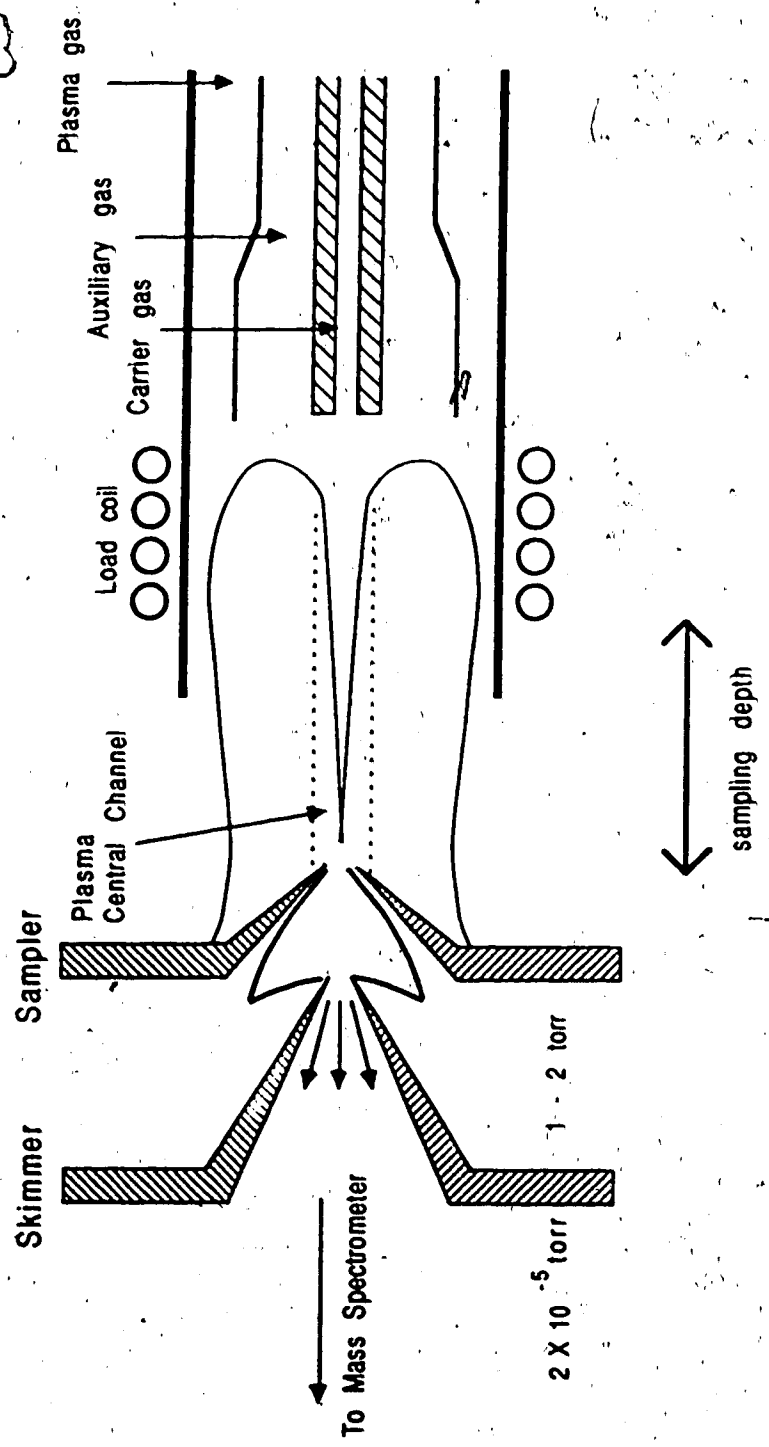


Figure 2. Ion sampling of the Inductively Coupled Plasma

the low pressure ( $10^{-5}$  torr) mass spectrometer, the plasma gas experiences another supersonic expansion. The resulting ion beam is then focussed by electrostatic ion lenses and analysed by the quadrupole mass spectrometer.

The sampling of the plasma ions in ICP-MS has been observed to follow behavior consistent with molecular beam sampling [21, 22]. The subject of molecular beam sampling has been extensively studied and its theory has been well developed [23-26]. A qualitative discussion of the basic principles involved in the sampling of ions from an ICP through a double cone interface will now be given.

In a supersonic expansion, the plasma gas expands free of the nozzle wall, molecules in the expanding jet undergo collisions and adiabatic cooling occurs. For an inviscid and isentropic flow, the quantity of gas passing through a nozzle,  $F_N$  (molecules/s) is directly proportional to the gas number density, the flow velocity at the nozzle and the cross sectional area of the orifice [22, 26]:

$$F_N = \frac{\pi D_0^2 N_A P_0 f(\gamma)}{4 (mRT_0)^{1/2}} \quad (4)$$

- where
- $f(\gamma) = \gamma^{1/2} [2/(\gamma+1)]^{(\gamma+1)/2(\gamma-1)}$
  - $\gamma =$  specific heat ratio,  $c_p/c_v$  ( $= 5/3$  for argon)
  - $D_0 =$  diameter of the sampler orifice
  - $N_A =$  Avogadro number
  - $P_0 =$  ICP source pressure
  - $m =$  mean molecular weight of the plasma gas
  - $R =$  gas constant
  - $T_0 =$  gas temperature of the ICP

The gas density of the expanding beam in the 1 torr region decreases with increasing distance from the sampler nozzle. The plasma gas flow through the skimmer,  $F_S$ , can be determined from the equation:

$$F_S = F_N f(\gamma) (D_S / X_S)^2 \quad (5)$$

where  $D_S$  = diameter of the skimmer orifice  
 $X_S$  = distance between the sampler and the skimmer

Continued expansion of the plasma gas through the skimmer in the low pressure mass spectrometer will eventually lead to free molecular flow. The gas is said to experience free molecular flow when molecular collisions become infrequent and the gas can no longer achieve equilibrium. At this point the thermodynamic parameters of the gas become frozen. Intermediate between continuum flow and free molecular flow is the transition flow regime. In ICP-MS, ion focussing of the supersonic beam by the input lenses occurs in the transition flow regime [22].

During supersonic expansion, adiabatic cooling of the plasma gas takes place and the random thermal motion of atoms is converted to a motion oriented in the direction of the expanding jet. Consequently, the velocity distribution of the supersonic jet is narrowed and the directed kinetic energy of the plasma beam is increased. Several authors have measured the ion kinetic energy distribution in the ICP-MS [4, 21, 27]. Fulford and Douglas [21] found that in the absence of a secondary discharge between the plasma and the sampling orifice, the kinetic energy spread of ions in the plasma is small.

(~ 2- 3 eV) and analyte ions have ion energies directly proportional to their masses plus a potential of about 2 V which was thought to derive from residual plasma potential or space charge effects in the ion beam. The decrease in the temperature of the expanding gas can be estimated from the following equation [28]:

$$T(z) = T_0 [2/(\gamma+1)] [(\gamma-1)/(\gamma+1)]^{(\gamma-1)/2} (D_0/z)^{2\gamma} \quad (6)$$

where  $z$  = distance from the sampler nozzle

$T(z)$  = temperature at distance  $z$

High background pressure in the differentially pumped region interferes with the expanding supersonic jet. Negligible interference from background gases will be observed only if the background pressure is less than  $10^{-3}$  torr. As a result, residual gas in the 1 torr chamber interacts with the expanding supersonic jet to form shock patterns as shown in Figure 3a. The shock wave that is formed perpendicular to the beam axis is referred to as the Mach disk and the remaining shock wave enveloping the beam is the barrel shock wave. Olivares and Houk [22] have determined the optimum distance between the sampler and the skimmer where a maximum ion intensity is obtained. They found that maximum ion intensity was obtained when the skimmer is attached to the Mach disk; that is when  $X_S = X_M$  where  $X_M$  corresponds to distance from the sampler nozzle at which the Mach disk was formed.  $X_M$  can be determined from the following equation [26]:

$$X_M = 0.67 D_0 (P_0/P_B)^{1/2} \quad (7)$$

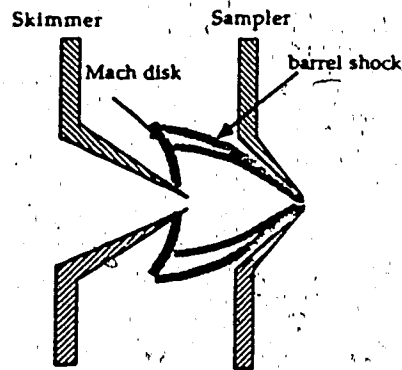


Figure 3a. Skimmer cone sampling at Mach disk

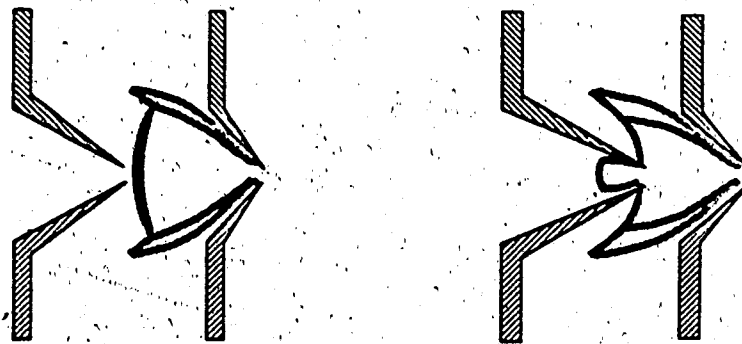


Figure 3b. Skimmer cone sampling after Mach disk

Figure 3c. Skimmer cone sampling before Mach disk

where  $P_B$  is the background pressure in the differentially pumped region. If the skimmer is positioned after the Mach disk, a low signal intensity is obtained due to extensive scattering of the expanding beam by the background gas. Similarly, if the skimmer is placed before the Mach disk, a shock wave will be formed downstream of the skimmer orifice thus scattering ions at the skimmer cone. These two conditions are shown in Figures 3b and 3c.

The plasma gas is actually a mixture of gases with the major component being the argon species. The minor components are background species such as H, O, O<sub>2</sub>, NO, OH and analyte elements. During supersonic expansion, with sufficiently high frequency of collisions, the minor components in the plasma will eventually attain the velocity of the bulk argon gas. When this occurs the kinetic energy of analyte species in the plasma is given by;

$$E_M = (m_M/m_{Ar}) E_{Ar} \quad (9)$$

where  $E_{Ar} = 5/3 kT_0$  which is the translational energy of the argon gas.

The result is that heavy molecules in the plasma could be accelerated to the mean velocity of the lighter argon gas. Thus, the plasma gas is similar to the so called seeded beam. Seeded molecular beams [29-32] have been widely used to produce molecular beams of high energies for applications in the study of solid state, nuclear and plasma physics.

#### D. Quadrupole Mass Spectrometer

The ion beam, after being extracted through the skimmer, is focussed by electrostatic optic lenses and directed into the mass filter to be analysed.

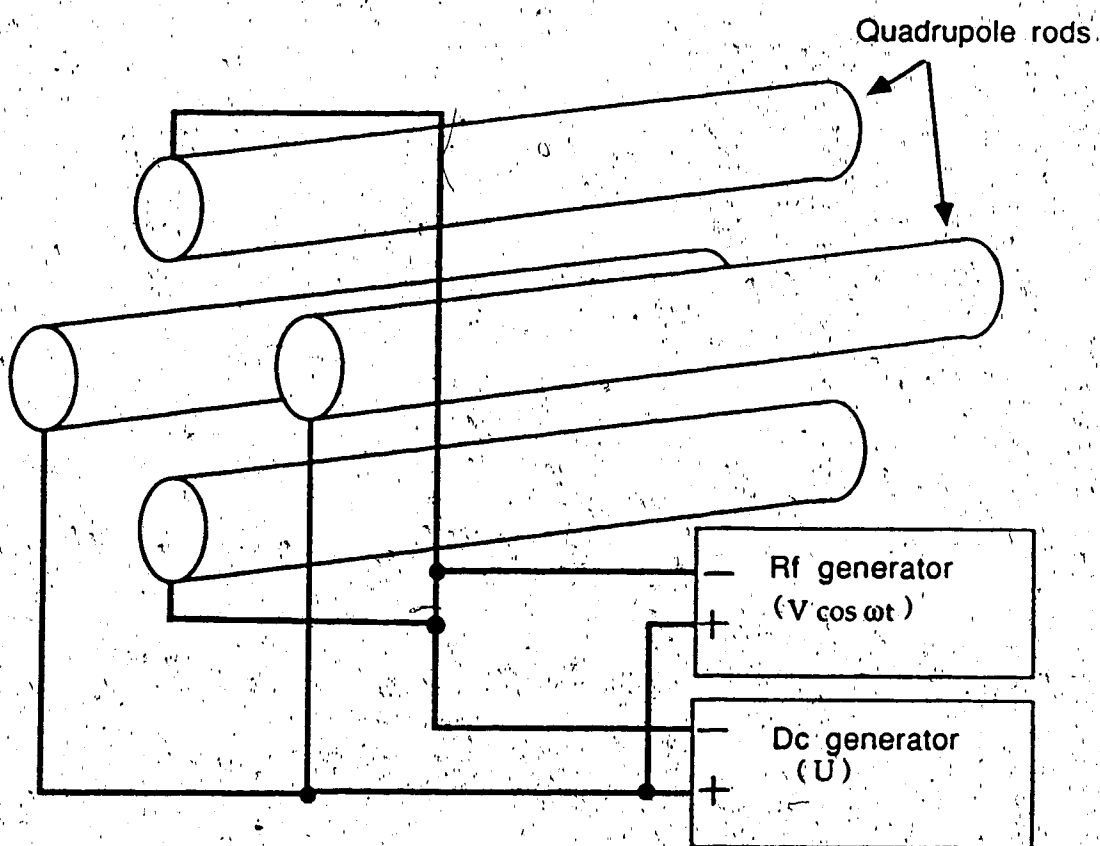


Figure 4. Schematic layout of quadrupole mass filter and its power supply



The mass filter consists of four parallel conducting cylindrical rods arranged in a precise square. A quadrupole field is established in the mass filter by application of a dc voltage and a rf voltage as shown in Figure 4. Ions from the plasma beam enter the mass filter axially and undergo oscillations in the quadrupole field governed by Mathieu type equations;

$$\frac{d^2x}{dt^2} + \frac{(a + 2q \cos\omega t) \omega^2 x}{4} = 0 \quad (10)$$

$$\frac{d^2y}{dt^2} + \frac{(a + 2q \cos\omega t) \omega^2 y}{4} = 0 \quad (11)$$

$$\frac{d^2z}{dt^2} = 0 \quad (12)$$

where

$$a = \frac{8eU}{m r_0^2 \omega^2} ; \quad q = \frac{4eV}{m r_0^2 \omega^2}$$

U = dc voltage

V = rf peak voltage

$\omega = 2\pi f$ ; f is the rf frequency

$r_0 =$  half of the closest separation between opposite rods

Equations 10 and 11 describe the ion motions in the x and y planes. Equation 12 represents the ion motion in the z direction; since there is no axial field gradient, the axial velocity of any ion is constant. In order for an ion to have

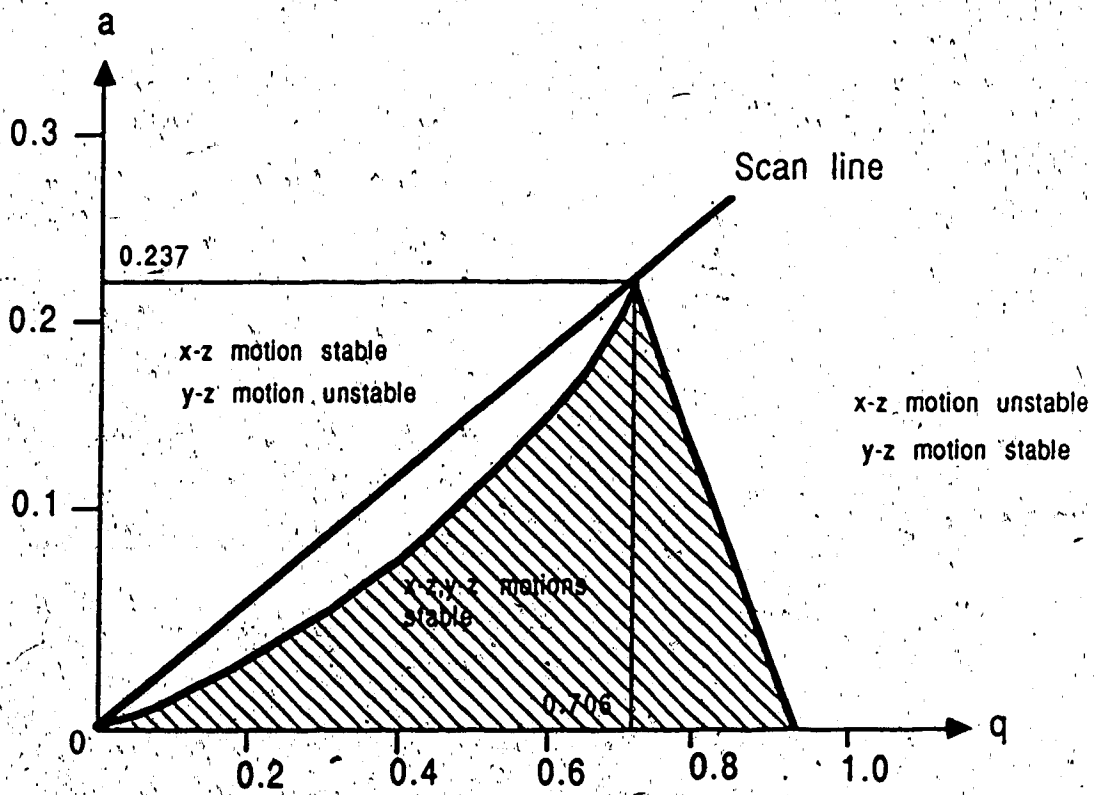


Figure 5. Stability diagram showing x and y stability envelope and scan line

a stable trajectory through the entire length of the mass filter, both equations 10 and 11 must have stable solutions which are given by only certain values of  $a$  and  $q$ . The stability diagram in Figure 5 shows pairs of  $a$ ,  $q$  values for which the ion trajectories are stable in the  $x$  and  $y$  planes. For a given ratio of the dc and rf potentials, the working points of the quadrupole rods fall on a straight line through the origin known as the scan line which has a slope of  $a/q = 2U/V$ . For optimum resolution of mass, the scan line is chosen to be close to the apex of the stable trajectory region. As a result, only ions of a certain mass-to-charge ratio corresponding to the  $a$ ,  $q$  values where the scan line crosses the stability envelope will be transmitted. All other ions in the beam will have unstable trajectories and collide with the quadrupole poles. Mass scanning is normally carried out by varying the dc and rf potentials, with a constant ratio between them and maintaining the rf frequency constant. More detailed discussions of the principles of the quadrupole mass filter can be found in the references [33, 34].

#### E. ICP-MS Literature Review

The development of ICP-MS has been well documented and a number of good overview articles have appeared [35-38]. The first paper on ICP-MS originated from the Ames Laboratory by Houk in collaboration with Fassel and Gray [2]. With their home-made ICP-MS instrument, the authors demonstrated the feasibility of the method and its associated advantages such as low detection limits, wide linear dynamic concentration range of 3 to 4 orders of magnitude and its capability for rapid isotopic abundance determination. Prior to this work, Gray had successfully coupled a dc capillary arc source to a quadrupole mass filter [39, 40]. He also showed that the technique had many advantages which included high sensitivity, speed of

analysis and inherent isotope ratio information. However, the dc capillary arc source used was found to suffer from severe inter-element and matrix effects due to the low temperature of the dc arc and inefficient sample introduction.

In the early work with ICP-MS, plasma species were extracted through small pinhole size orifices between 50-70  $\mu\text{m}$  in diameter. An aerodynamically stagnant layer of gas was formed between the plasma gas and the sampler tip. Ion extraction into the vacuum system therefore occurred only after transport through this cooled boundary layer which could take 1-2 ms. In this time, unwanted reactions such as ion-molecule reactions, ion-electron recombination and charge exchange could take place. As a result, the sampled gas was not representative of the bulk plasma gas. Extensive formation of molecular species such as oxides and hydroxides, and severe suppression of analyte signal in the presence of concomitant salts were observed. Another problem which arose because of the small diameter sampling orifice was serious signal drift due to solid condensation at the orifice surface. This limits solution concentration to lower than 10  $\mu\text{g}/\text{ml}$ . Attempts were made to use larger orifice diameters ( $> 70 \mu\text{m}$ ) so that the plasma could be directly sampled by puncturing the boundary layer. However, when a large sampling orifice was used, an arc discharge was produced between the plasma and the sampling cones [2, 3, 12]. This phenomenon gave rise to high background noise, erosion of the sampling orifice and in severe cases, loss of the instrument vacuum.

In the meanwhile, Douglas and French [42, 43] explored the use of a microwave induced plasma (MIP) as an ion source. The MIP is also a viable ion source for the mass spectrometer and has most of the advantages associated with the ICP but it is more susceptible to matrix effects.

Nevertheless, the most significant outcome from their work was the successful use of a large sampling orifice with a diameter  $\geq 0.4$  mm without the formation of a discharge at the interface. They extended the same approach to ICP-MS [42, 43]. Subsequently, Gray et al. [3, 44-46] were also successful in building an interface which employed a large sampling orifice with virtually no deleterious arc discharge formation. All subsequent work in ICP-MS has been performed with a large sampling orifice in which the plasma gas is extracted directly into the vacuum as a bulk fluid. This form of ion sampling is known as continuum sampling.

In 1983, the ICP-MS was made available commercially by two manufacturers, SCIEX Ltd. and V.G. Isotopes Ltd. These manufacturers were closely associated with the researchers mentioned before, Gray et al. with V.G. Isotopes Ltd., and Douglas et al. with SCIEX Ltd. Our instrument was the second instrument from SCIEX, delivered in May, 1984. Currently, about 80 instruments have been delivered world wide with sales about evenly split between the two manufacturers.

In the last two years there have been an increasing number of papers dealing with the application of the technique to trace element determinations in a wide variety of samples. A large number of the determinations have involved geological samples. Date and Hutchison [47] determined 20 trace elements in six US Geological Survey Geochemical Exploration standard reference samples and found reasonable agreement between their results and previously published results. Date et al. [48] also measured trace elements at different concentration levels in limestones and manganese nodules and evaluated the effectiveness of correction procedures for polyatomic ion interferences. Macleod et al. [49] determined various trace elements in nickel-base alloys and observed spectral interferences from matrix metal oxide ions.

McLaren et al. assessed the accuracy in the determination of trace elements in marine sediments and reported that good accuracy could be obtained if standard addition [50] or isotope dilution [51] were employed. ICP-MS has also been used to measure lead isotope ratios for the purpose of typing gold and base metal occurrences [52].

Boomer and Powell [53] determined the concentrations of Al, Mn, Fe and Zn in acid precipitation samples. They discussed the use of plasma operating parameters to minimize matrix effects and oxide formation, and reported spectral interferences from  $\text{ArO}^+$  and  $\text{CaO}^+$  on the determination of Fe. McLaren and co-workers [54] determined trace metals in seawater by standard addition and isotope dilution techniques. The trace elements in seawater were separated and concentrated by adsorption on silica-immobilized 8-hydroxyquinoline. Ting and Janghorbani [55] employed ICP-MS with stable isotope dilution method for isotopic analysis of Fe in human fecal matter. Date and Gray [7] also applied ICP-MS for isotope ratio measurement of stable tracer Zn 67 in blood plasma and fecal extracts, and Pb in galena samples. The potential use of the ICP-MS for the measurement and identification of polar organic compounds was investigated by Houk et al. [56].

Olivares and Houk have studied ion sampling of the plasma discharge in ICP-MS [22]. They found that ion sampling in ICP-MS is similar to neutral beam and ion sampling from other types of plasmas and flames. Olivares and Houk also measured ion energy distribution in ICP-MS using a retarding potential on the quadrupole mass filter [27]. In this study, ion kinetic energies were found to be dependent on plasma operating parameters and this feature was attributed to the presence of an induced discharge between the plasma and sampling orifice. Similarly, Fulford and Douglas measured the ion kinetic energies in the Sciex Elan 250 ICP-MS system [21]. The authors

reported the absence of an induced discharge in their system and hence ion energies were found to have values consistent with those expected from molecular beam sampling from a high temperature plasma with a residual potential of about 2 V.

Our group at the University of Alberta has published several papers on ICP-MS. In the first paper, Horlick and co-workers [57] reported the effect of plasma operating parameters on ion signals of a wide range of elements. Vaughan and Horlick [58] presented results on oxide, hydroxide and doubly charged species in ICP-MS. Tan and Horlick [59] reported background spectral features associated with distilled/deionized water, nitric acid, hydrochloric acid and sulfuric acid. In reference [60], Gray discussed the formation of oxides, doubly charged and molecular species in ICP-MS. He also discussed their effects on detection limits in ICP-MS.

Houk and et. al [61] studied suprathreshold ionization in the plasma using ICP-MS and showed that calculated  $T_{ion}$  values were greater than those expected from  $T_{exc}$ . They also presented mass spectra and ionization temperatures of a mixed gas Ar-N<sub>2</sub> plasma [62]. Olivares and Houk [63] investigated the suppression of Co ion signal by the presence of five concomitants; NaCl, MgCl<sub>2</sub>, NH<sub>4</sub>I, NH<sub>4</sub>Br and NH<sub>4</sub>Cl. Brown and co-workers [64] studied the effects of mineral acids, an easily ionized element and organic acids on In ion signals. They observed a suppression of analyte signal with mineral acids and Na, and an enhancement of analyte signal with the organic acids.

Another area of research in ICP-MS concerns the development of different types of sample introduction systems besides conventional pneumatic and ultrasonic nebulizers. Houk and Thompson [8] have developed a method for introducing small discrete volumes of solution into

the ICP for biological samples. For solid samples, Gray [65] presented preliminary results on laser ablation into the ICP-MS. Poor precision for the technique was obtained with BGS mineral samples. Arrowsmith [66] also reported the direct determination of NBS standard steel samples by laser ablation. With internal standardization he was able to obtain quantitative results with precision and accuracy of about  $\pm 5\%$ . Another interesting method of introducing solid samples is by arc nebulization [67]. This method only works with conducting solid samples.

#### F. -- Thesis Objective

The aim of this work is to study this new technique and characterize the ICP-mass spectrometer with regards to the instrument operating parameters so that proper operating conditions can be selected for subsequent experiments. This includes the determination of background mass spectra and the study of the quantitative behavior of various elements.

A major part of the research work concerns a study of the effects of the presence of a high concentration of matrix elements on analyte signals. Since almost all real samples contain at least some form of matrix elements in high concentrations, these studies are significant for the future development of analytical procedures for real sample analyses.

---



## CHAPTER 2

### EFFECTS OF PLASMA OPERATING PARAMETERS ON ANALYTE ION SIGNALS IN ICP- MS

#### A. ICP-MS Instrumentation

All the work in this thesis was carried out using the Sciex Elan Model 250 inductively coupled plasma-mass spectrometer. A block diagram of the instrument is shown in Figure 6. The basic components of the instrument are an ICP, a plasma sampling interface and a mass spectrometer. The ICP sub-system consists of an ICP torch and a sample introduction unit. The sample introduction unit is most commonly a pneumatic nebulizer and a spray chamber. In the mass spectrometer, there are the input ion optics, a quadrupole mass filter which can analyze masses up to 300 amu and a detector. The plasma sampling interface is a double cone ion beam inlet system which extracts a small portion of the plasma gas into the mass spectrometer.

A schematic diagram of the Sciex Elan 250 ICP-MS is shown in Figure 7. The ICP is a standard Plasma Therm 2.5 kW system. The plasma torch is, however, oriented to operate in a horizontal position in order to facilitate ion extraction into the mass spectrometer. The sample introduction part consists of a Meinhard nebulizer and a Scott type spray chamber. The plasma torch box is housed on top of the impedance matching network box. This housing may be moved manually back and forth to provide the appropriate sampling depth. It was also adapted to move laterally and vertically so that the plasma can be aligned with the sampling orifice. The plasma torch is run with a center tap grounded load coil to prevent the formation of a discharge at the sampling interface [43]. The plasma torch used initially was a Fassel type

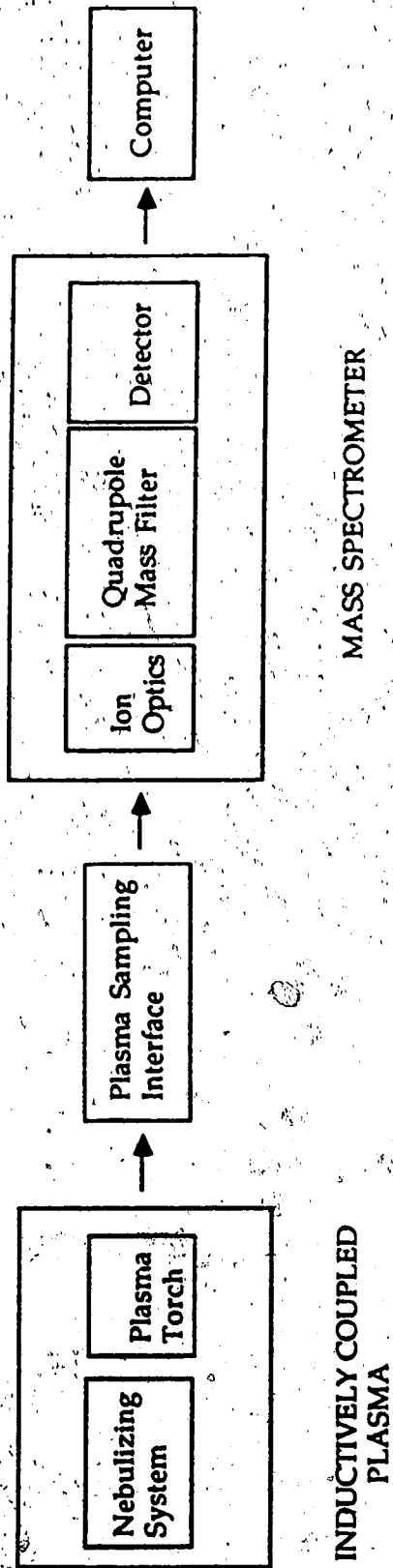


Figure 6. Block diagram of the ICP-MS.

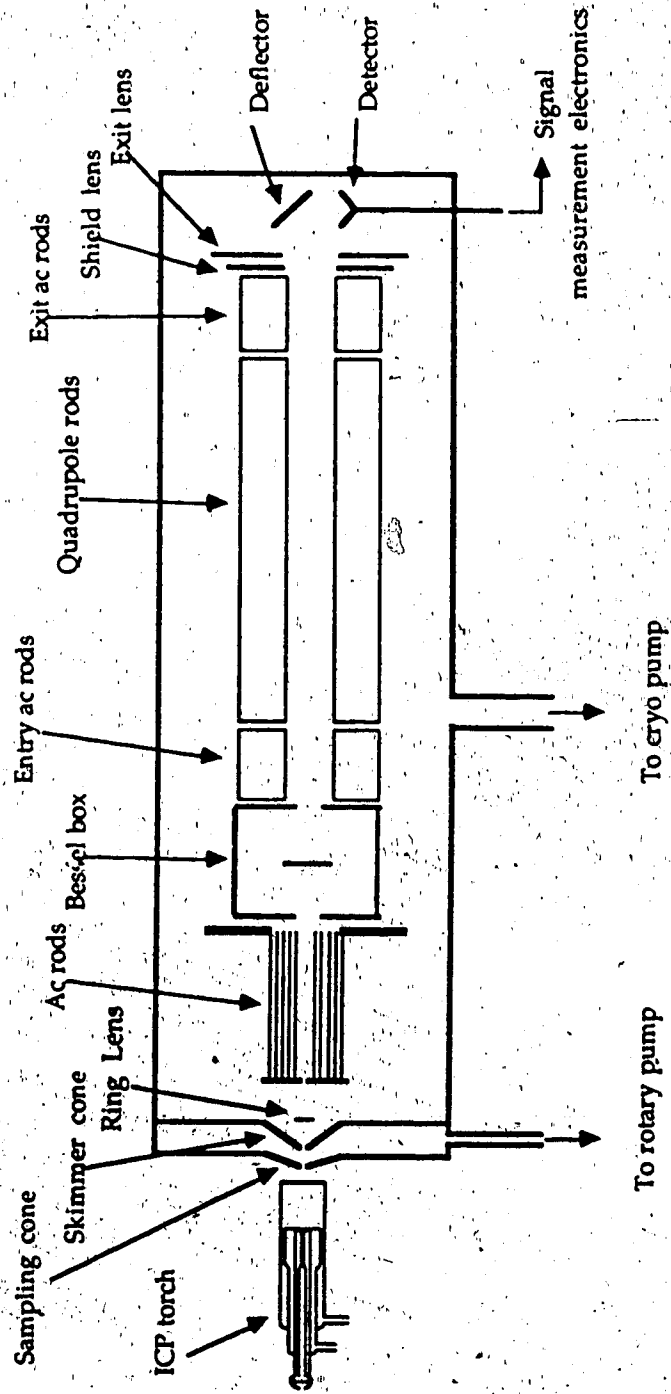


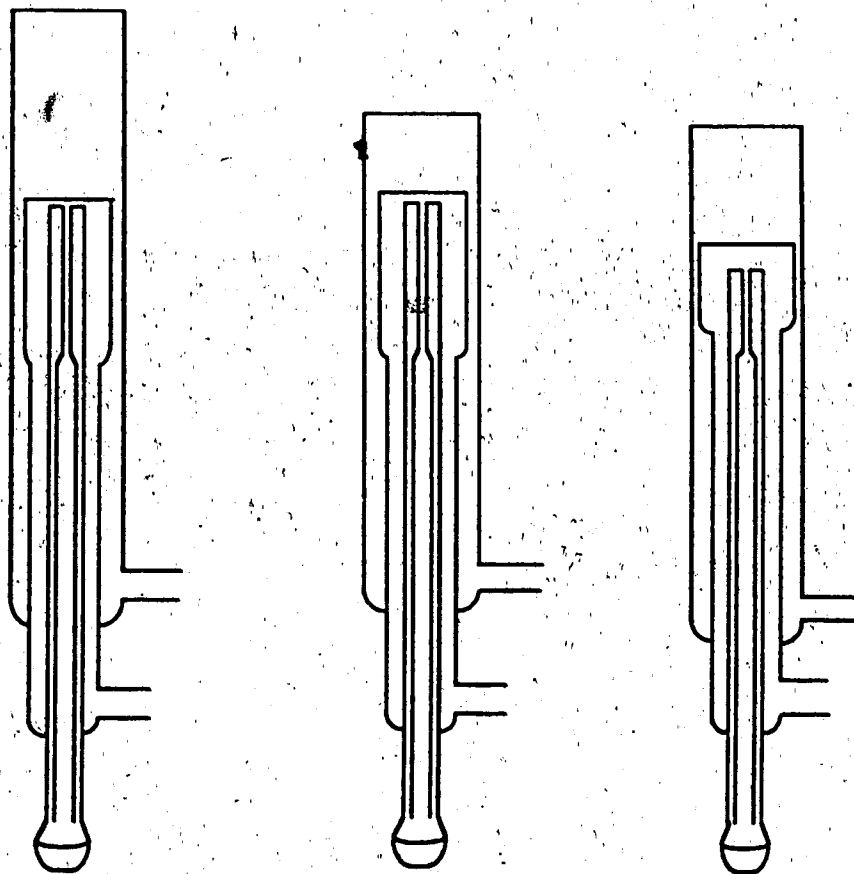
Figure 7. Schematic diagram of the Sciex Elan 250 ICP-MS

extended torch in which the length of the outer coolant tube is 20 mm longer than the regular torch. The extended torch was replaced later by a MAK torch. The relative dimensions for the torches are shown in Figure 8.

The plasma discharge is sampled through a set of metallic cones into the mass spectrometer. The first cone, called the sampler cone, is mounted on a copper block and the second cone, called the skimmer cone, is mounted on a stainless steel block. In the present interface configuration the tip of the skimmer is positioned about 5 mm behind that of the sampler. Both the copper and stainless steel blocks are water cooled and designed to move as a single piece to avoid alignment problems. When the instrument is not in operation, the interface block is positioned off-axis so that the mass spectrometer chamber is sealed. This interface block moves down into position during operation and is actuated by a water operated piston. The region between the two metal blocks is evacuated by an Edwards roughing pump and is maintained at a pressure of 1-2 torr during operation.

The diameters of the orifices of the sampler and the skimmer are about 1 mm and both the orifices are machined to a knife edge. The sampler material is usually Ni or Cu. The sampler cone has to be cleaned daily and under routine everyday use, it is replaced every 2-3 months. The skimmer cone is made of either stainless steel or Cu, and since it is not subjected directly to the high temperature of the argon plasma, it needs only to be replaced about once a year.

The front end of the mass spectrometer consists of a set of input ion lenses whose function is to shape and direct ions into the quadrupole mass filter. The initial version of the input ion optics is shown in Figure 9. They consist of a ring lens, two sets of hollow rods and a Bessel box. The ring lens has a negative voltage and thus will repel electrons. Positive ions



Extended torch

Cut-off torch

MAK torch

Figure 8. ICP torches

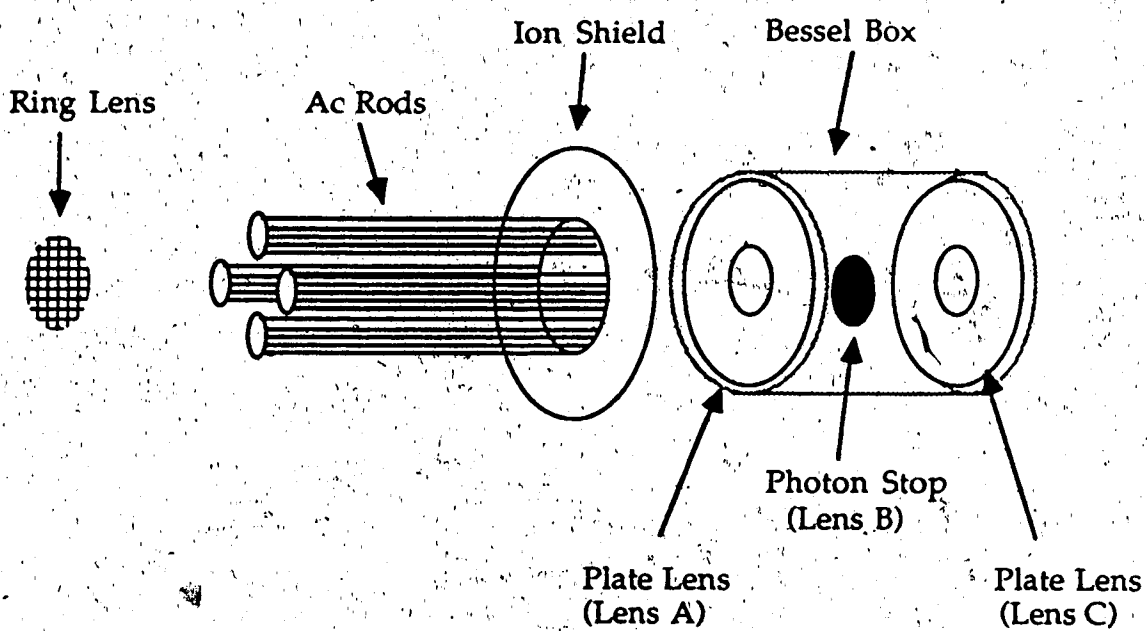


Figure 9. Original input ions optics of the mass spectrometer

however, are accelerated into the ac rods. When transversing the ac rods, ions experience the oscillating ac field and thus are collimated. There is no mass filtering of ions in the ac rod sets. In the Bessel box, the first plate lens (lens A) causes ions to diverge around the photon stop (lens B) and the second plate lens (lens C) focuses the ions into the entry ac rods that are mounted in front of the quadrupole rods. The function of the entry and exit ac rods is to reduce the fringe field effect at both ends of the quadrupole rods. In the mass filter, ions of the appropriate mass-to-charge ratios are selected and then transmitted. When exiting the mass filter, the ions are deflected by the deflector and detected by the off-axis channel electron multiplier (CEM).

The input ion optics were recently modified by the manufacturer and the new configuration is shown in Figure 10. All the data in this chapter except those in Section F were obtained with the original ion optics. With the change of the ion lenses the sensitivity of the instrument was improved by about a factor of 10. However, all the data acquired indicate that the dependence of the analyte signals on the plasma operating parameters are similar for both sets of ion optics.

The computer used in the Sciex ICP-MS system is an Intel, 16 bit microprocessor with a 10 Mbyte Winchester hard disk drive and one flexible disk drive. The computer is connected to an Envision colour graphics control console and a dot matrix printer. The dot matrix printer was later replaced by a Macintosh computer. Raw data from the ICP-MS computer were dumped into the Macintosh where they were reformatted and plotted using commercially available programs such as Multiplan, Microchart and Excel. An eight colour plotter from Houston Instrument is also available for plotting spectra such as those shown in Chapter 3.

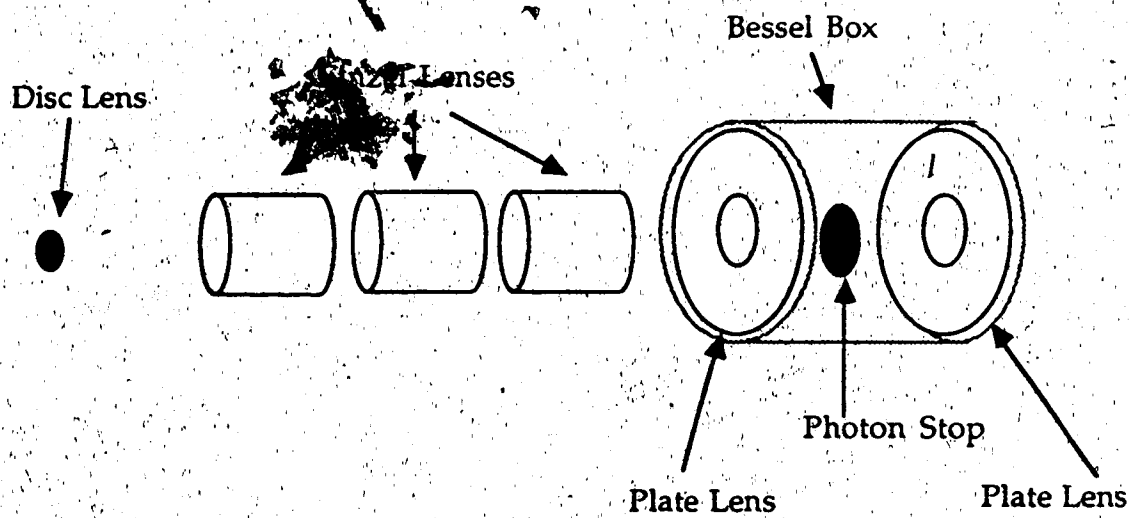


Figure 10. New input ion optics of the mass spectrometer



A summary of the instrumental variables is listed in Table 2. They are principally divided into the inductively coupled plasma, extraction interface, input ion optics and mass spectrometer parameters. For this first study, no attempts were made to change the extraction interface geometry. The mass spectrometer quadrupole parameters were optimized by the manufacture and their values were left as recommended. Voltages for the ion lenses were easily accessible, and they were optimized to transmit maximum ion count at mass 63 for Cu. Initial studies indicate that lens B, which corresponds to the voltage on the photon stop of the besel box is the most important parameter. The variation of the ion signal with the voltage on lens B is dependent on the mass of the analyte. However, the data presented in this chapter will be devoted to a study of the dependence of analyte signals on the plasma operating parameters.

The first set of experiments carried out on the ICP-MS was to investigate how the inductively coupled plasma parameters affect the ion signals of different elements. Up to 1984, there were essentially no literature reports on this area as most reports only dealt with instrument design developments and basic analytical capability of the technique. Clearly, in order to use the ICP-MS instrument with any reasonable amount of efficiency, the performance of these operating parameters has to be evaluated so that optimum instrumental operating conditions may be selected. The ICP parameters investigated are the rf power, intermediate (auxiliary) gas flowrate, aerosol carrier (nebulizer) gas flowrate and sampling depth. The elements studied included the alkali metals and the first row transition elements. Some of the results presented here have been already published [57].

Table 2. A summary of the ICP-MS instrumental parameters

A. Inductively Coupled Plasma

1. Rf power
2. Outer (plasma) gas flowrate
3. Intermediate (auxiliary) gas flowrate
4. Aerosol carrier (nebulizer) gas flowrate
5. Sampling depth

B. Extraction Interface

1. Sampler geometry
2. Skimmer geometry
3. Sampler - Skimmer separation
4. Pressure

C. Input Ion OpticsOld configuration

Ring Lens

Ac Rods

Bessel Box (lenses A, B, C)

New configuration

Disc Lens

Einzel Lenses

Bessel Box

D. Mass Spectrometer

1. Quadrupole rod voltages
2. Output ion optics
3. Deflector voltage
4. CEM detector voltage

## B. Experimental

The alkali metals studied were Li, Na, Rb and Cs and the first row transition metals studied were Sc, Ti, V, Cr, Mn, Fe, Co, Ni and Cu. Overlap from the intense ion signal at mass 40 due to  $^{40}\text{Ar}^+$  gave rise to considerable background ion counts at mass 39, thus potassium was not studied. The alkali metals have low ionization potentials and large differences in masses. The first row transition elements however, have intermediate ionization potentials and similar masses. The ionization potentials and masses for these two groups of elements are shown in Table 3. The ion signals were measured at the most abundant isotope of each element and since non-structured background was less than 10 ion counts/s, the ion signals were not corrected for background. The ion signals were determined in the low resolution mode where each mass was measured for 1 s (that is 0.1s per data point and 10 data points per amu) and an average of 6 repeat measurements was taken.

The plasma operating parameters study was initially carried out with an extended torch supplied by Sciex which was later replaced by a MAK torch. Data in Sections C. 1 and C. 2 were obtained with an extended torch; in Sections D and E with a cut-off torch; and in Section F with a MAK torch. The plasma gas flowrate and the auxiliary gas flowrate used with the extended torch were 14 l/min and 1.8 l/min and for the MAK torch were 11 l/min and 1.4 l/min respectively unless otherwise stated. The flow meter provided with the instrument for measuring the aerosol flow rate was not precise or accurate enough, thus all variations of this parameter were set initially with the nebulizer pressure gauge. Two mass flow controllers (Matheson Model 8240-0423) were acquired later and installed on the aerosol and auxiliary gas flow lines. A calibration table for nebulizer pressure vs aerosol carrier gas

Table 3. Ionization potentials, isotopic masses and natural abundances for alkali and first row transition elements.

| <u>Elements</u> | <u>Isotope Masses</u> | <u>Isotope Abundances(%)</u> | <u>First IP (eV)</u> |
|-----------------|-----------------------|------------------------------|----------------------|
| Li              | 6                     | 7.5                          | 5.39                 |
|                 | 7                     | 92.5                         |                      |
| Na              | 23                    | 100.0                        | 5.14                 |
| Rb              | 85                    | 72.2                         | 4.18                 |
|                 | 87                    | 27.8                         |                      |
| Cs              | 133                   | 100.0                        | 3.89                 |
| <hr/>           |                       |                              |                      |
| Sc              | 45                    | 100.0                        | 6.54                 |
| Ti              | 46                    | 8.0                          | 6.82                 |
|                 | 47                    | 7.5                          |                      |
|                 | 48                    | 73.7                         |                      |
|                 | 49                    | 5.5                          |                      |
|                 | 50                    | 5.3                          |                      |
| V               | 50                    | 0.3                          | 6.74                 |
|                 | 51                    | 99.7                         |                      |
| Cr              | 50                    | 4.3                          | 6.76                 |
|                 | 52                    | 83.8                         |                      |
|                 | 53                    | 9.5                          |                      |
|                 | 54                    | 2.4                          |                      |
| Mn              | 55                    | 100.0                        | 7.43                 |
| Fe              | 54                    | 5.8                          | 7.87                 |
|                 | 56                    | 91.7                         |                      |
|                 | 57                    | 2.2                          |                      |
|                 | 58                    | 0.3                          |                      |
| Co              | 59                    | 100.0                        | 7.86                 |
| Ni              | 58                    | 67.8                         | 7.63                 |
|                 | 60                    | 26.4                         |                      |
|                 | 61                    | 1.2                          |                      |
|                 | 62                    | 3.7                          |                      |
|                 | 64                    | 0.9                          |                      |
| Cu              | 63                    | 69.1                         | 7.72                 |
|                 | 65                    | 30.9                         |                      |

Table 4. Calibration of Nebulizer Pressure Vs Aerosol Carrier Gas Flowrate

| <u>Nebulizer Pressure ( psi )</u> | <u>Aerosol Flowrate ( l/min )</u> |
|-----------------------------------|-----------------------------------|
| 4                                 | 0.22                              |
| 6                                 | 0.34                              |
| 8                                 | 0.43                              |
| 10                                | 0.51                              |
| 12                                | 0.59                              |
| 14                                | 0.65                              |
| 16                                | 0.73                              |
| 18                                | 0.80                              |
| 20                                | 0.86                              |
| 22                                | 0.93                              |
| 24                                | 1.00                              |
| 26                                | 1.06                              |
| 28                                | 1.13                              |
| 30                                | 1.20                              |
| 32                                | 1.26                              |
| 34                                | 1.32                              |
| 36                                | 1.39                              |
| 38                                | 1.46                              |

flowrate measured by the Matheson mass flow controller is presented in Table 4.

C. Dependence of Analyte Ion Signals on Aerosol Carrier (Nebulizer) Gas Flowrate and Plasma Power

C.1 First Row Transition Metals

A mass spectrum of the first row transition elements is shown in Figure 11. During initial work with the instrument, it was found that the analyte ion signals were strongly dependent on both the nebulizer pressure and power. All the data in this section were measured at a plasma sampling depth of 27 mm from the load coil and a solution concentration of 1 ppm. The dependence of the ion signal for Cr on nebulizer pressure and rf power is shown in Figure 12. The plot format shown in this figure was found to be most informative. In this format the analyte ion signal is plotted against the nebulizer pressure for a particular plasma power setting and then a family of such curves is plotted on the same axis for different powers. Such a plot will be referred to as a nebulizer pressure-power parameter behavior plot. It can be seen that at a particular plasma power, the ion count rate for Cr increases to a maximum and then decreases when the nebulizer pressure is varied from 22 psi to 36 psi. When the rf power is increased from 1.1 kW to 1.5 kW, the nebulizer pressure must be increased correspondingly to achieve the maximum ion count level. In addition, the peak ion signals are higher at higher plasma power.

The variation of the ion signals of first row elements as a function of the nebulizer pressure at a particular power setting (1.3 kW) is shown in Figure 13. It is obvious that all the elements behaved very similarly and have maximum ion counts at the nebulizer pressure of about 32 psi. The ion

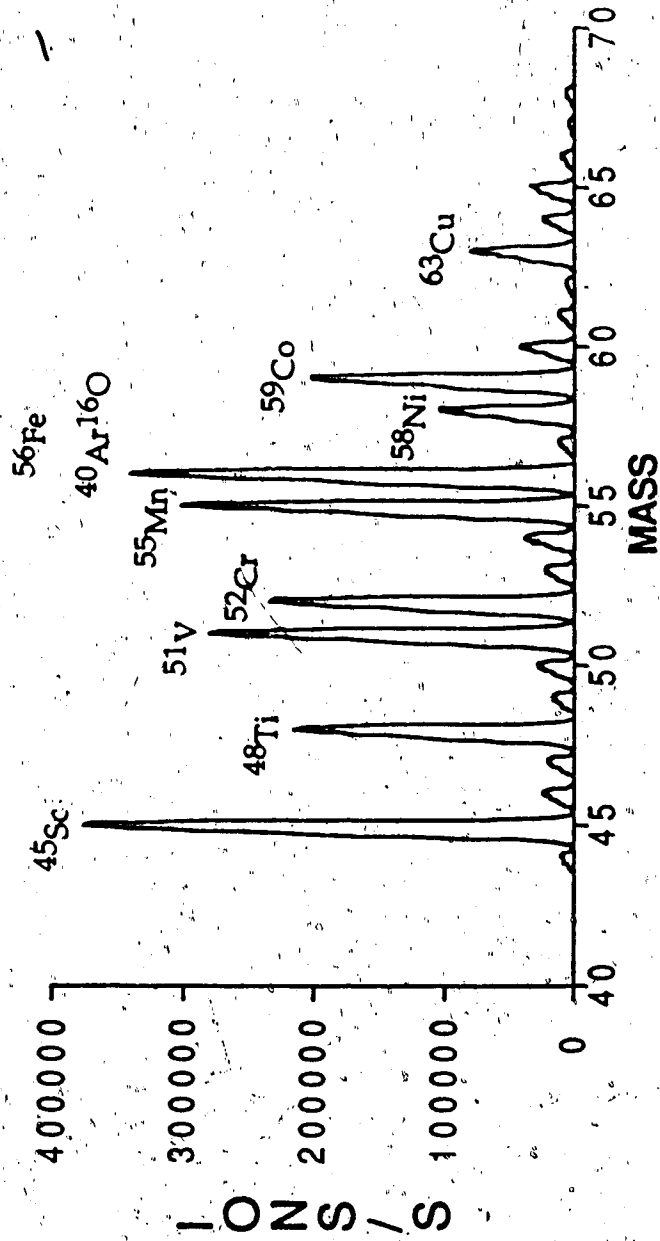


Figure 11. Mass spectrum of First Row Transition Elements

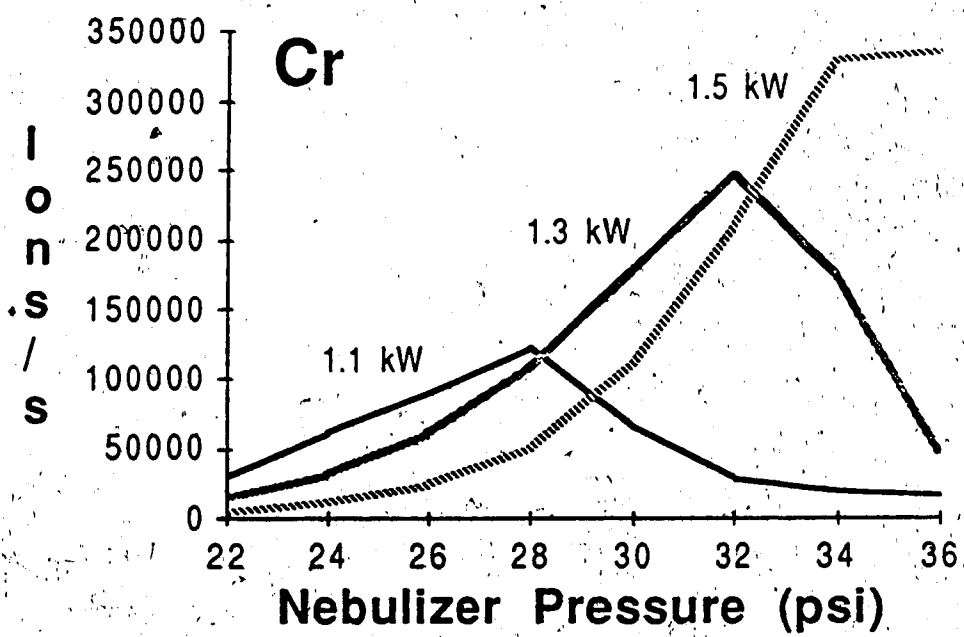


Figure 12. Nebulizer pressure-power parameter behavior plot for Cr



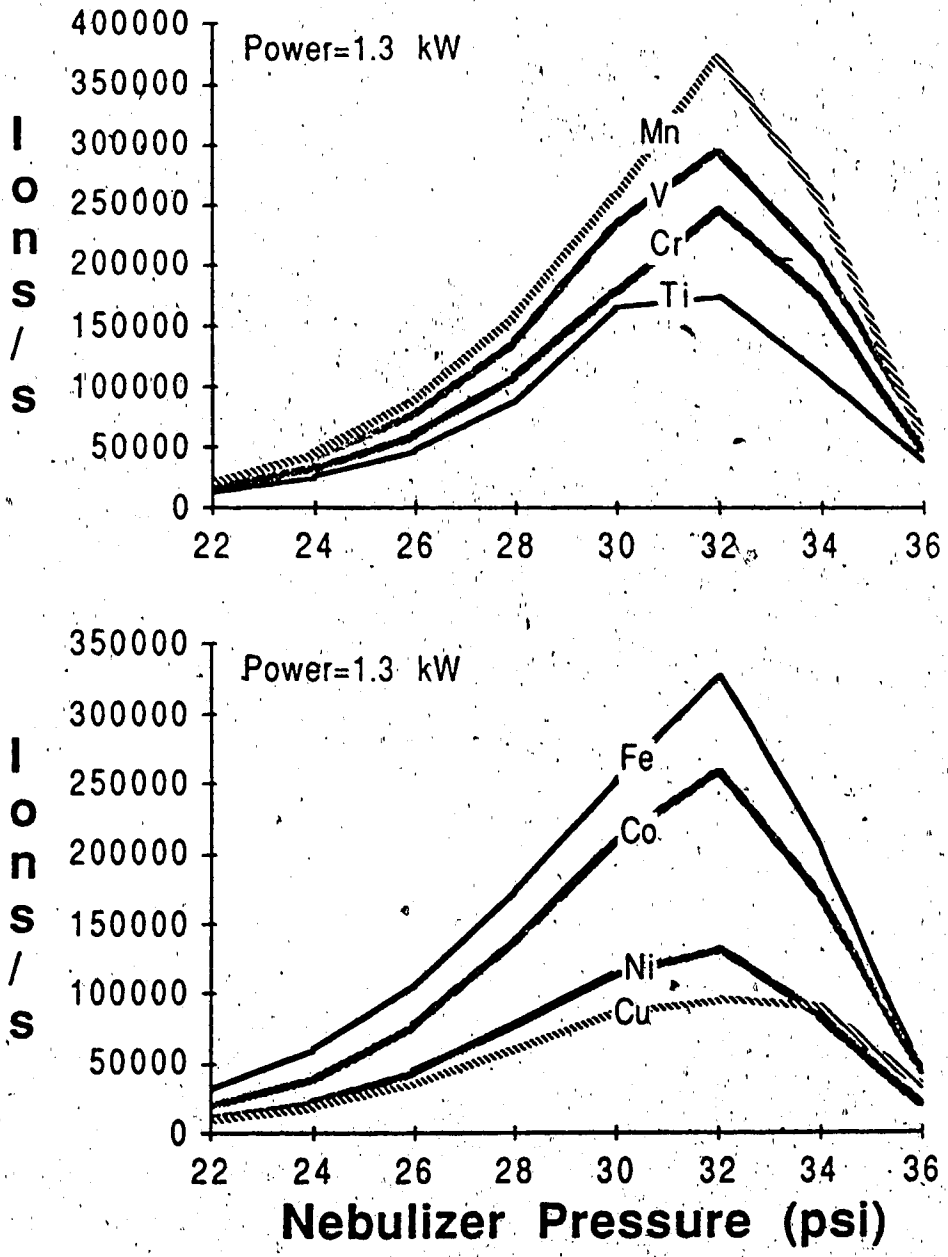


Figure 13. Dependence of ion count on nebulizer pressure (power 1.3 kW) for Mn, V, Cr, Ti, Fe, Co, Ni and Cu

counts were measured at the major isotopes of these elements and were not normalized to 100 % abundancies. An averaged and normalized set of parameter plots for the first row transition elements is shown in Figure 14. These data clearly show that the transition elements have the same characteristic nebulizer pressure-power behavior.

It can be seen from these plots that the signal is very sensitive to changes in the nebulizer pressure. For Mn, as shown in Figure 13, a 0.001 l/min (1ml/min) change in aerosol flowrate (see Table 4) corresponds to 0.5 % change in the ion signal near to the maximum. Thus, a mass flow controller is absolutely necessary to improve precision in the data. The Matheson mass flow controller that we have purchased can only control flowrate to  $\pm 0.01$  l/min, hence a precision not better than 5 % can be expected for ion counts near to the maximum.

## C.2 Alkali Metals

The nebulizer pressure-power parameter behavior plots for the alkali metals are shown in Figure 15. The concentration of these elements is 10  $\mu$ M. It is obvious from these data that the alkali metals exhibit different parameter behavior plots. From these plots, it is observed that at one power setting, increasingly higher nebulizer flowrates are required to maximize the signal in moving from Li to Cs and in the case of Cs, the signal never actually peaks out. This is more clearly illustrated in Figure 16 which shows the normalized ion count plots for Li, Na, Rb and Cs at 1.2 kW. In addition, the plots are broader as one moves from Li to Cs. Finally, the data reveal that there is no one truly optimal nebulizer flowrate for the alkali elements and a compromise setting has to be chosen. In this case, 32 psi would be an appropriate choice.

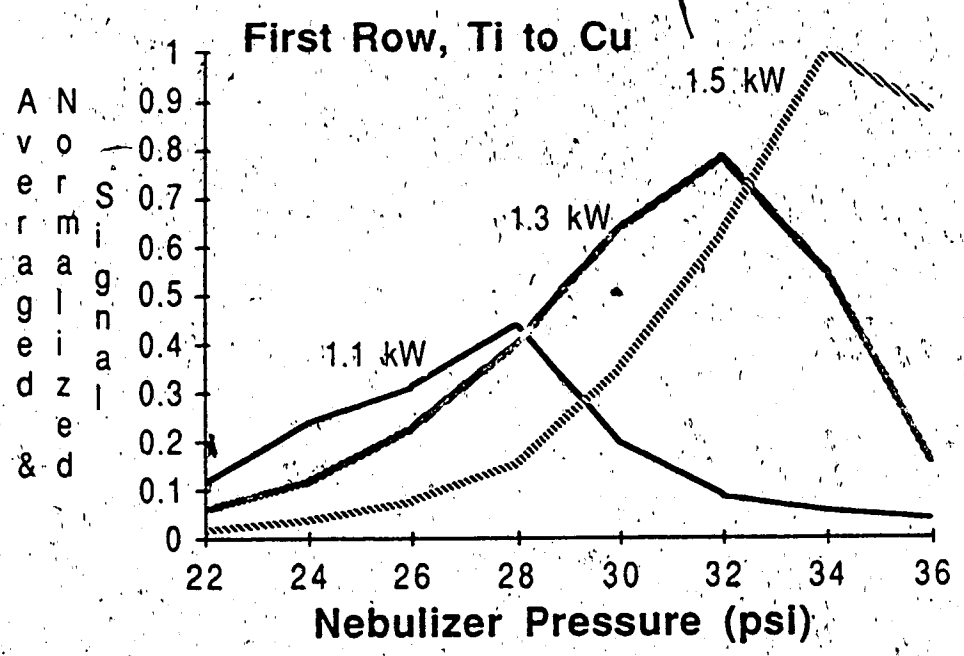


Figure 14. Averaged and normalized nebulizer pressure-power parameter behavior plots for Ti, V, Cr, Mn, Fe, Co, Ni and Cu

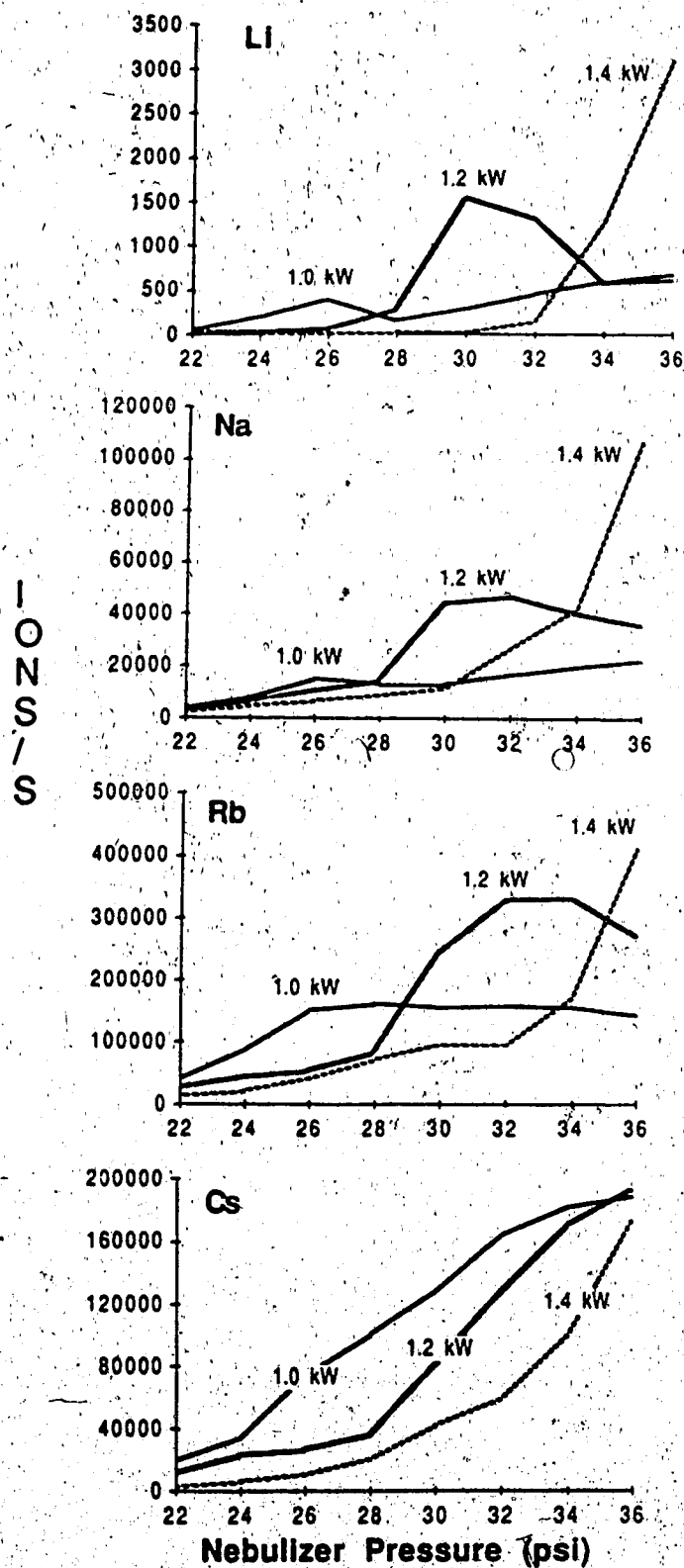


Figure 15. Nebulizer pressure-power parameter behavior plots for Li, Na, Rb and Cs

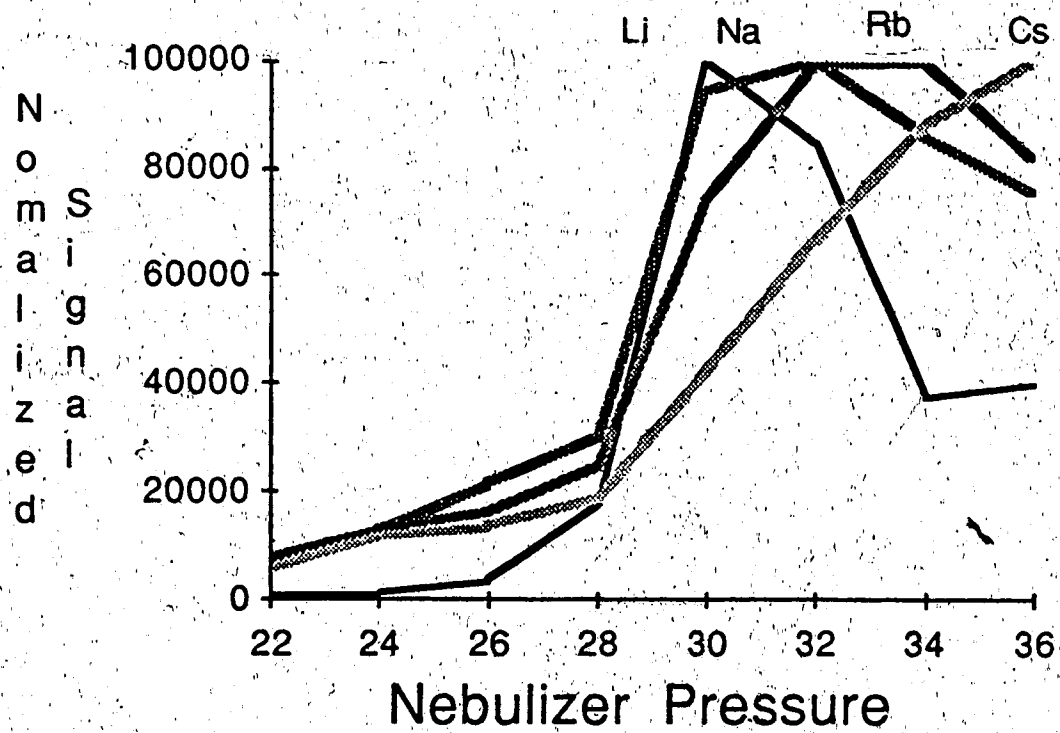


Figure 16. Normalized ion count vs nebulizer pressure plots for Li, Na, Rb and Cs at 1.2 kW

D. Dependence of Analyte Ion Signals on Sampling Depth

The experiments in this section were carried out with a cut-off extended torch which is similar to a standard optical emission ICP torch. This allowed a study of the effect of the sampling depth on the analyte ion signal. Due to the configuration of the plasma shield box housing the torch, the nearest sampling depth possible was 17 mm. Modifications of this component, which included the installation of a new load coil, now enable the plasma discharge to be sampled down to 5 mm from the load coil. The ion count-nebulizer flowrate plots for the alkali metals at 1.1kW are shown in Figure 17 for sampling depths ranging from 17 to 29mm from the load coil. It can be seen that these plots possess the general characteristics of the parameter behavior plots discussed before in Section C. 2 except for the fact that maximum signal now occurs at 26 psi rather than at 30 psi as a consequence of the shorter torch. The highest signals were obtained at a sampling depth of 17 mm, and these signals decrease when the plasma is moved away from the sampling orifice.

The dependence of the ion signals on sampling depth for V, Mn, Zn and Cd is presented in Figure 18. Again, the basic behavior of the parameter plots is identical to that observed before in Section C. 1 with the peak signals occurring at a nebulizer flowrate of 28 psi rather than 32 psi, again due to the shorter torch. However, the changes in the ion signal with respect to the sampling depth are different from those observed with the alkali metals. The best signal obtained at any sampling depth is generally similar if the nebulizer pressure is varied in order to maintain the maximum ion count as sampling depth is changed.

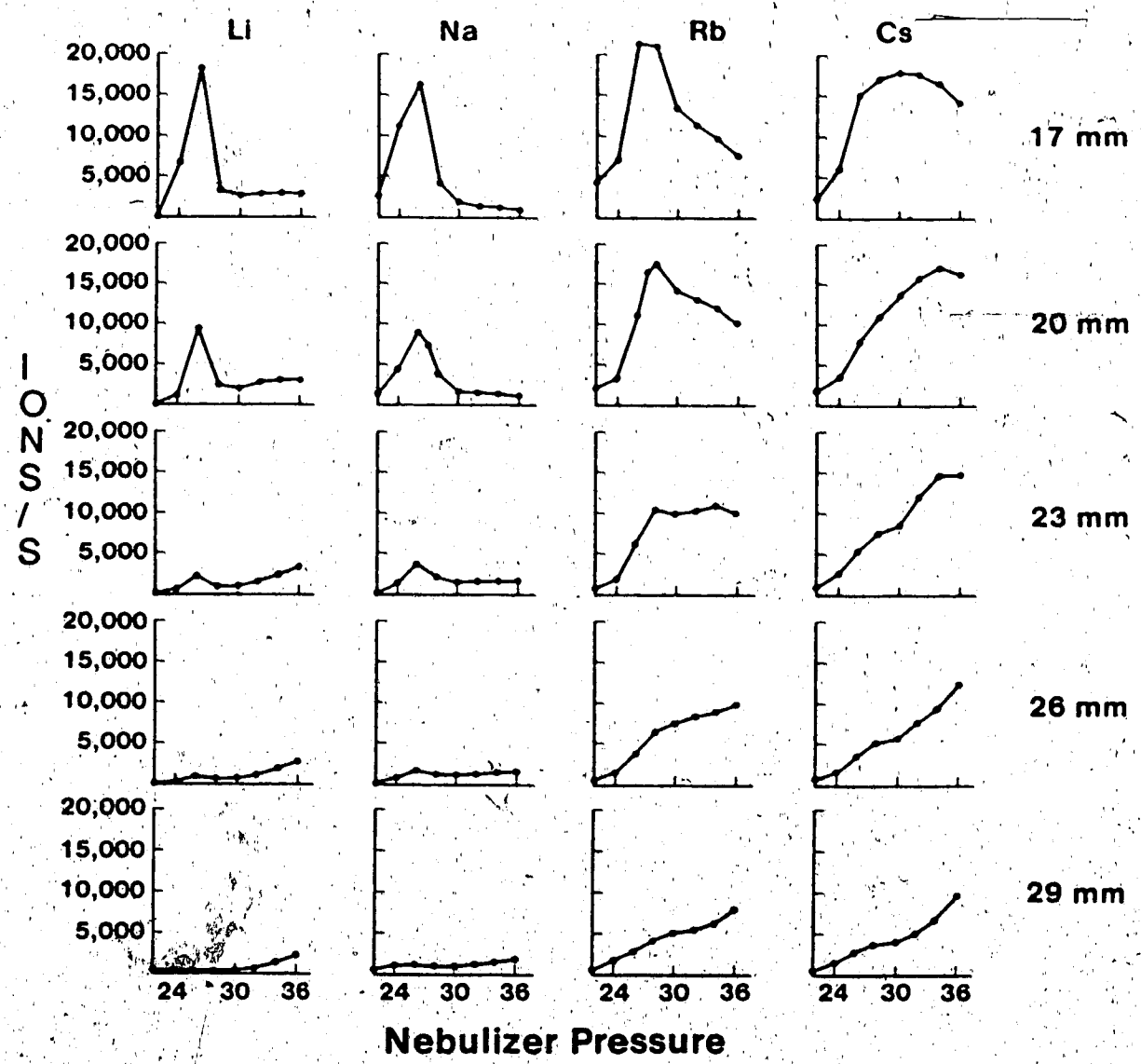


Figure 17. Dependence of ion count on nebulizer pressure for Li, Na, Rb and Cs at sampling depths of 17, 20, 23, 26 and 29 mm from the load coil

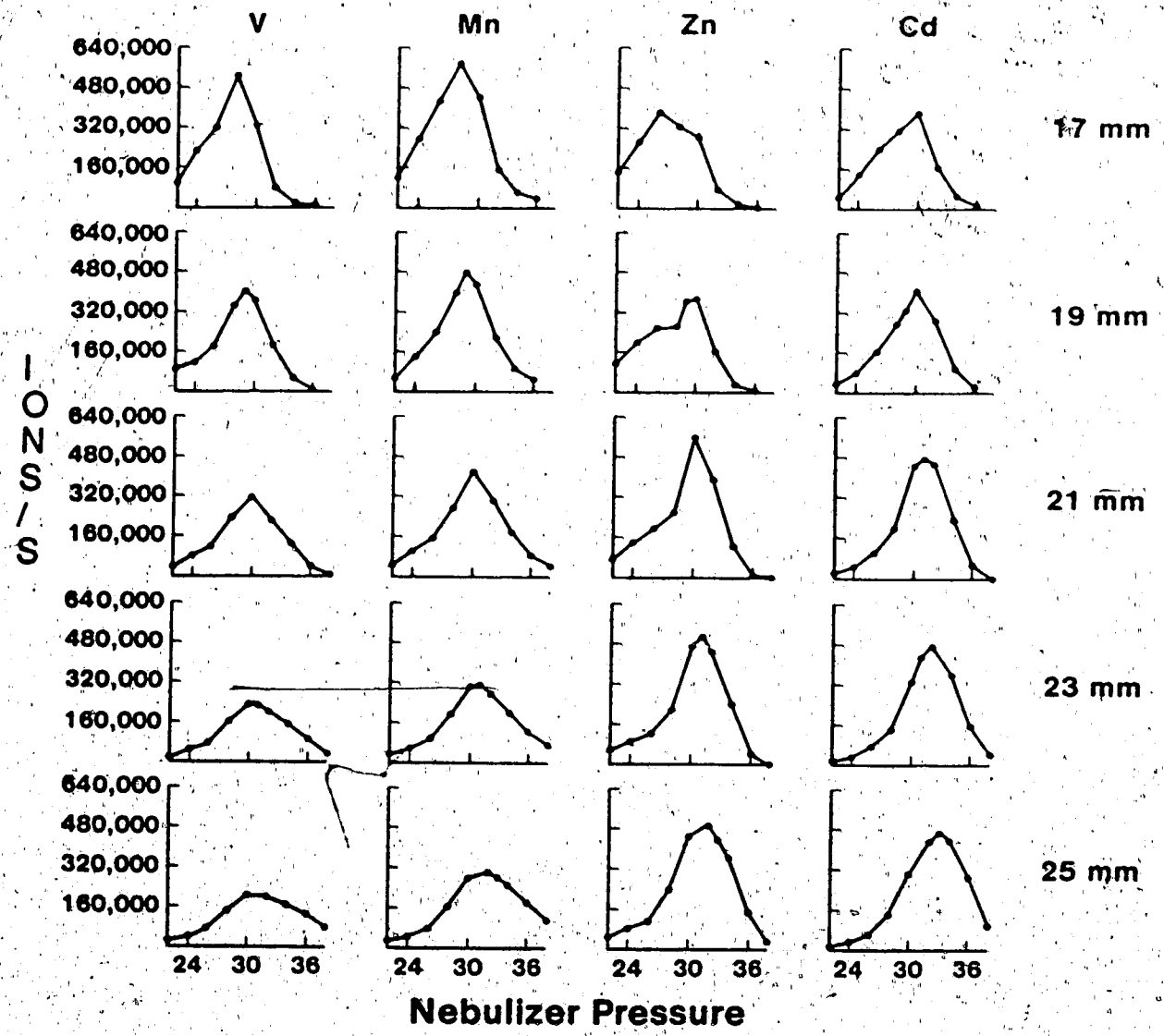


Figure 18. Dependence of ion count on nebulizer pressure for V; Mn, Zn and Cd at sampling depths of 17, 19, 21, 23 and 25 mm from the load coil



Zn is very similar in mass to the first row transition elements but has a higher ionization potential which is close to that of Cd (see Table 3). Zn and Cd have similar parameter behavior plots, like those of the first row transition elements, but the best ion signals for Zn and Cd occurred at the sampling depths of 21mm to 23 mm. The peak ion count continued to shift to higher nebulizer flowrates at all the sampling depths. Also, the peak ion signal for Cd at a certain depth is obtained at a slightly higher nebulizer flowrate than for Zn.

The data presented in Figure 18 clarified some confusing data reported by other ICP-MS users who have observed ion signal behavior at limited parameter settings. For example, let's look at the effect of sampling depth on the ion signal for Zn. If one started at 25 mm with the signal maximized by setting the nebulizer pressure at 32 psi, the observation would be that the ion signal decreased as the torch is moved closer to the sampling orifice. However, if one started at a sampling depth of 17 mm and the ion signal was maximized at 28 psi, it would be observed that the ion signal increases as the sampling depth was moved closer to the load coil.

From these data, it is also possible to see that the best ion signal for the alkali metals is found lower in the plasma especially for the lighter elements whereas the ion signal for the first row elements does not vary much between 17 mm to 25 mm with appropriate adjustment of the nebulizer pressure. Therefore, such parameter study is useful for providing a guideline for selection of sampling depth for different elements.

#### E. Dependence of Analyte Ion Signals on Intermediate (Auxiliary) Gas Flowrate

The effect of auxiliary gas flowrate for the first row transition elements

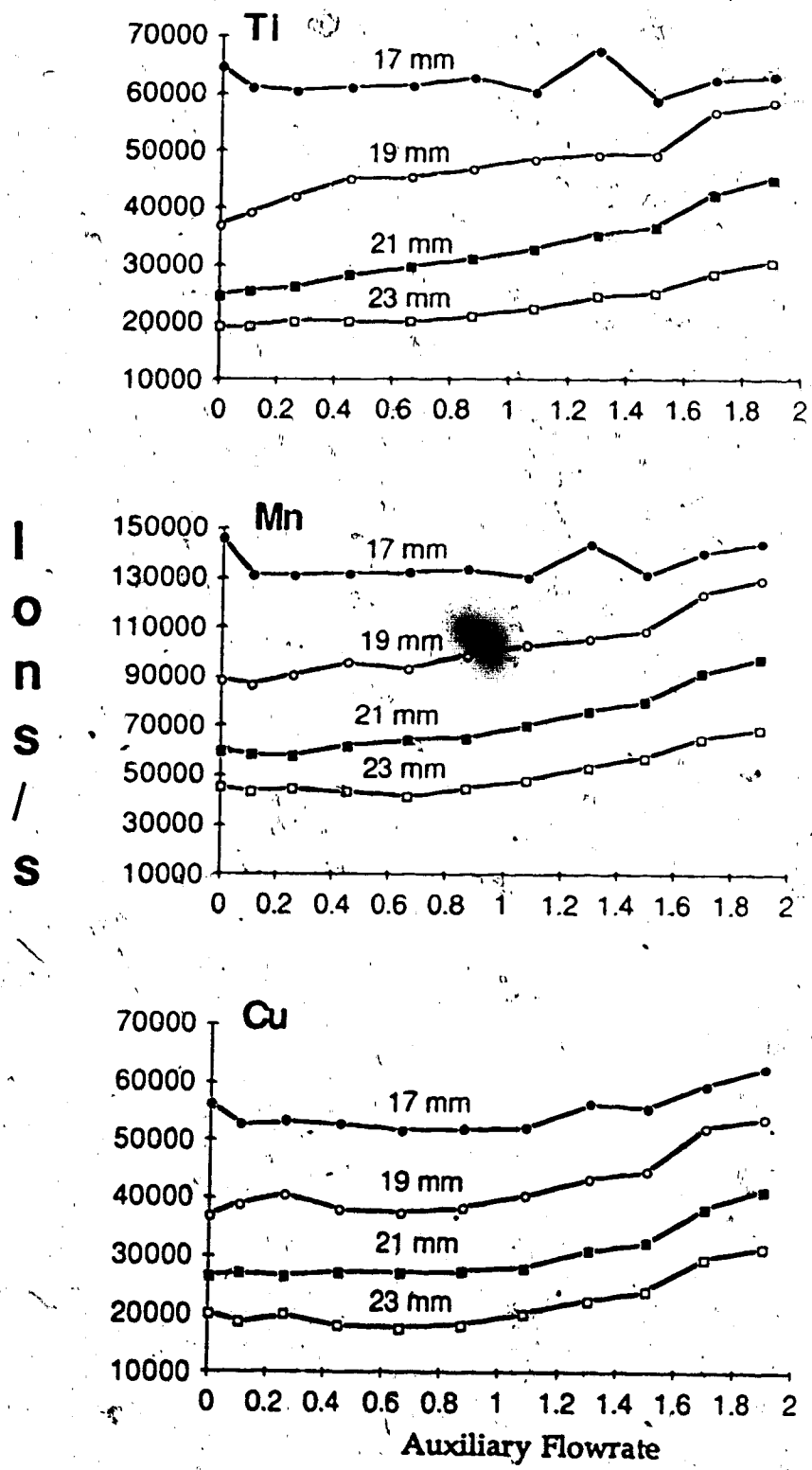


Figure 19. Dependence of ion count on auxiliary flowrate for Ti, Mn and Cu at sampling depths of 17, 19, 21 and 23 mm from the load coil

(Ti, Mn, Cu) at sampling depths of 17 mm to 23 mm is shown in Figure 19. The rf power used was 1.2 kW and the ion signal was first maximized at the sampling depth of 17 mm by setting the nebulizer flowrate at 27 psi. It can be seen from this figure that as the torch was moved away from the sampling orifice the ion counts for these elements steadily decrease. However, at each sampling depth, except at 17 mm, the ion signals slowly increase as the auxiliary gas flowrate is increased. Notice for example the curves for 21 mm and 23 mm. The ion signal near the end of the 23 mm curves at the auxiliary flowrate of 1.8 l/min is about the same as that for the 21 mm curves at 0.1 l/min auxiliary gas flowrate. This implies that increasing the auxiliary gas flowrate from 0.1 l/min to 1.8 l/min has the same effect on the ion signal as shifting the plasma about 2 mm towards the sampling orifice. The same kind of behavior is seen in the ICP-AES system where the auxiliary gas shifts the plasma up and down. A similar trend is observed for all other curves except those at 17 mm for Ti and Mn which show almost no change in ion signal as a function of auxiliary gas flowrate. This indicates that the signal is most likely optimum at 17 mm for these two elements and moving the torch closer than 17 mm will not increase the ion signal as it likely would for Cu.

Similar plots showing the variation of the ion signal for the alkali metals (Li, Na, Rb, Cs) are shown in Figure 20. These plots can be interpreted in the same manner as those of the transition elements. From these data, it can be seen that at sampling depths of 21 mm to 23 mm, the ion signals do not change very much as the auxiliary gas flowrate is increased. At the sampling depths of 17 mm to 19 mm however, the effect is much greater; this indicates that higher signals can be obtained at closer sampling depths. For Li, at 17 mm, the ion signal increases to a maximum at about 1.4 l/min and then

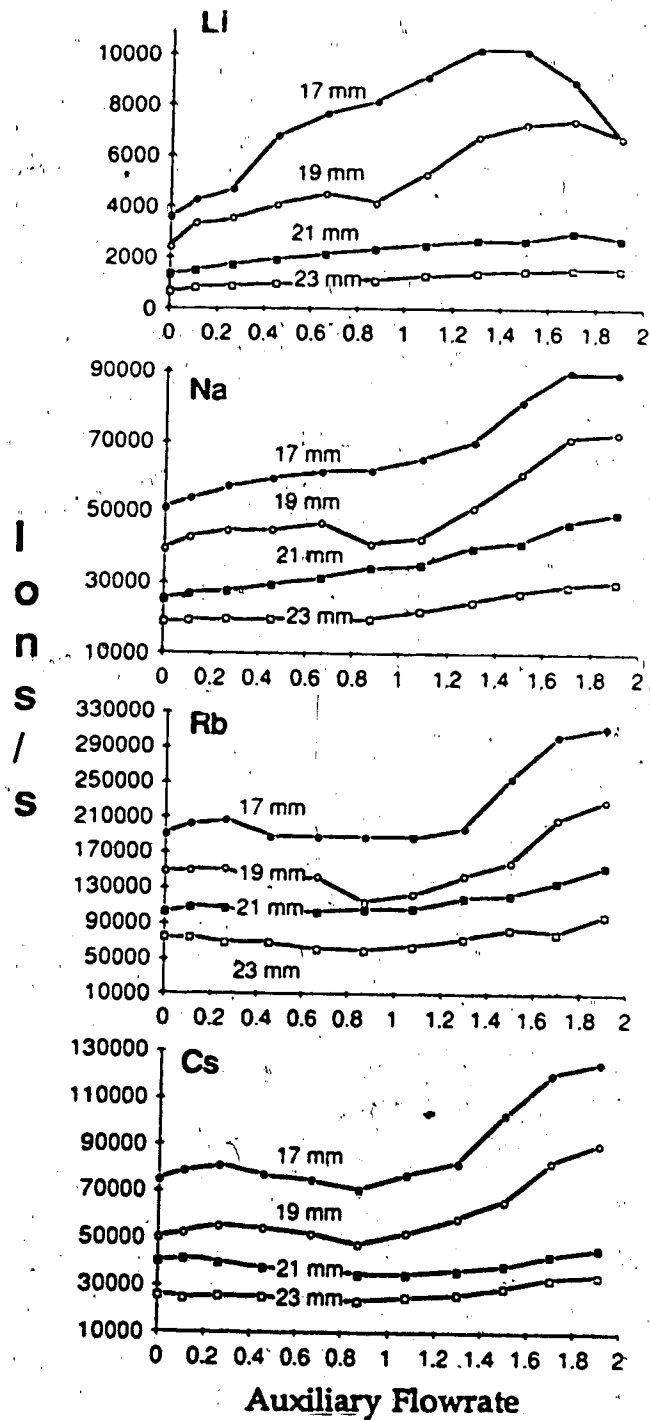


Figure 20. Dependence of ion count on auxiliary flowrate for Li, Na, Rb and Cs at sampling depths of 17, 19, 21 and 23 mm from the load coil

decreases, this indicates that moving the plasma discharge nearer than 17mm would result in a lower signal.

#### F. Parameter Behavior Plots at 5mm to 20 mm using a MAK Torch

In this section, the dependence of the ion signals on the nebulizer flowrate and plasma power at sampling depths between 5mm to 20 mm for the alkalis and the first row transition elements is illustrated. As was mentioned before, the initial setup of the plasma box did not allow the plasma torch to be moved closer than 17 mm from the sampling orifice to the load coil. In order to sample deeper into the plasma, the original center tap grounded load coil was removed and replaced by another load coil which extended further out from the plasma box, consequently, the plasma torch can be positioned nearer to the interface. The new load coil was similar in design to the original. A standard MAK torch was used in this experiment. The nebulizer flowrate-power parameter plots for the Li, Na, Rb and Cs are shown in Figures 21a, b, c and d for sampling depths of 5, 10, 15 and 20 mm. It can be seen from these data that all these elements have similar behavior. The best signals for these elements are observed at 5 mm. For Li and Na, the peak ion signals increase steadily with the increase in the plasma power at all the sampling depths measured. For Rb and Cs at 5 mm, the peak signals have about the same intensity when the plasma power is increased. The ion intensities for Li and Na drop off more rapidly than Rb and Cs as the sampling depth is increased.

Figures 22a and 22b illustrate the nebulizer flowrate-power parameter plots for Sc and Cu, which were chosen to represent the first row transition elements. Unlike the alkalis, the best ion signals occur at a sampling depth of around 10 mm to 15 mm. A possible reason is because the transition

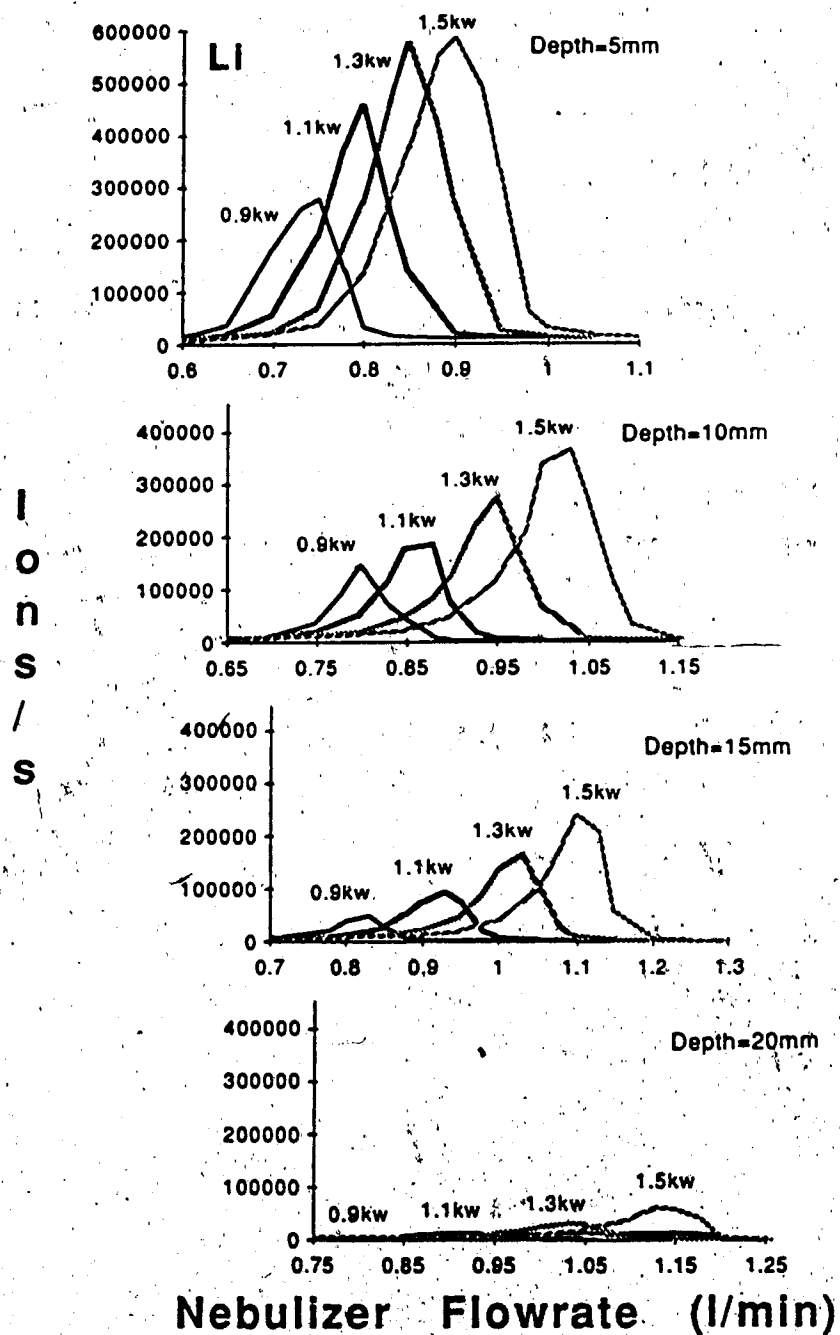


Figure 21a. Nebulizer flowrate-power parameter behavior plots for Li at sampling depths of 5, 19, 15 and 20 mm from the load coil

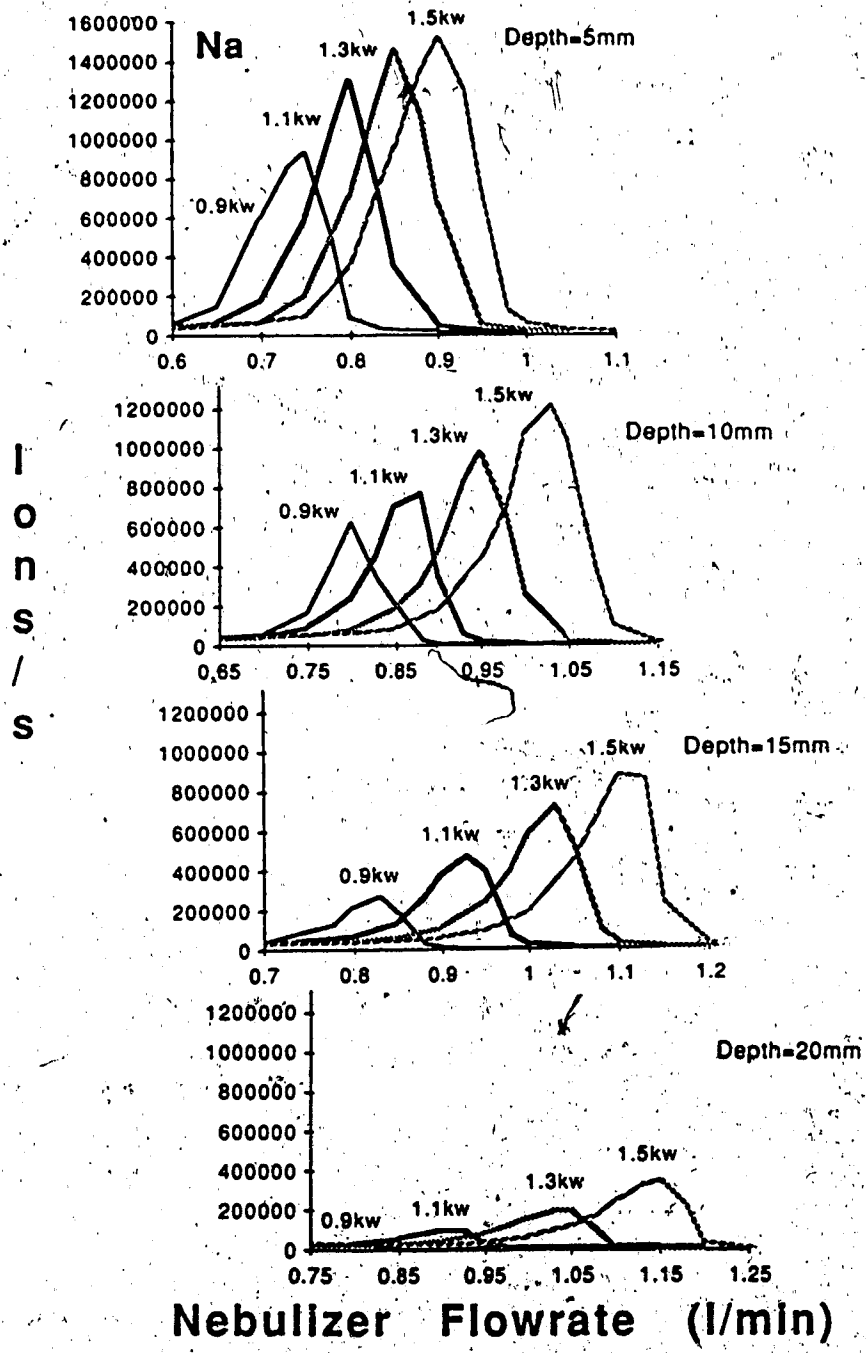


Figure 21b. Nebulizer flowrate-power parameter behavior plots for Na at sampling depths of 5, 10, 15 and 20 mm from the load coil.

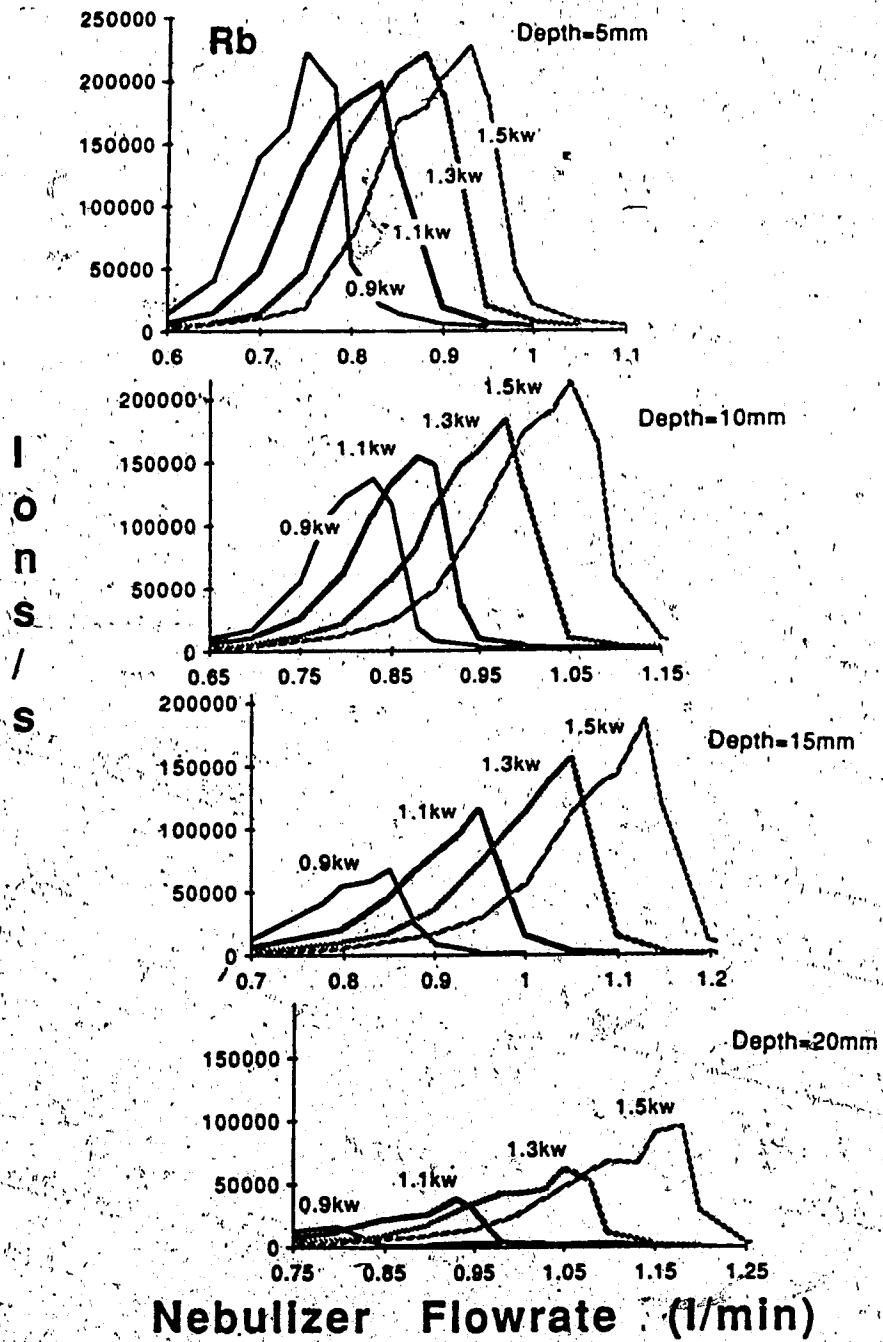


Figure 21c. Nebulizer flowrate-power parameter behavior plots for Rb at sampling depths of 5, 19, 15 and 20 mm from the load coil



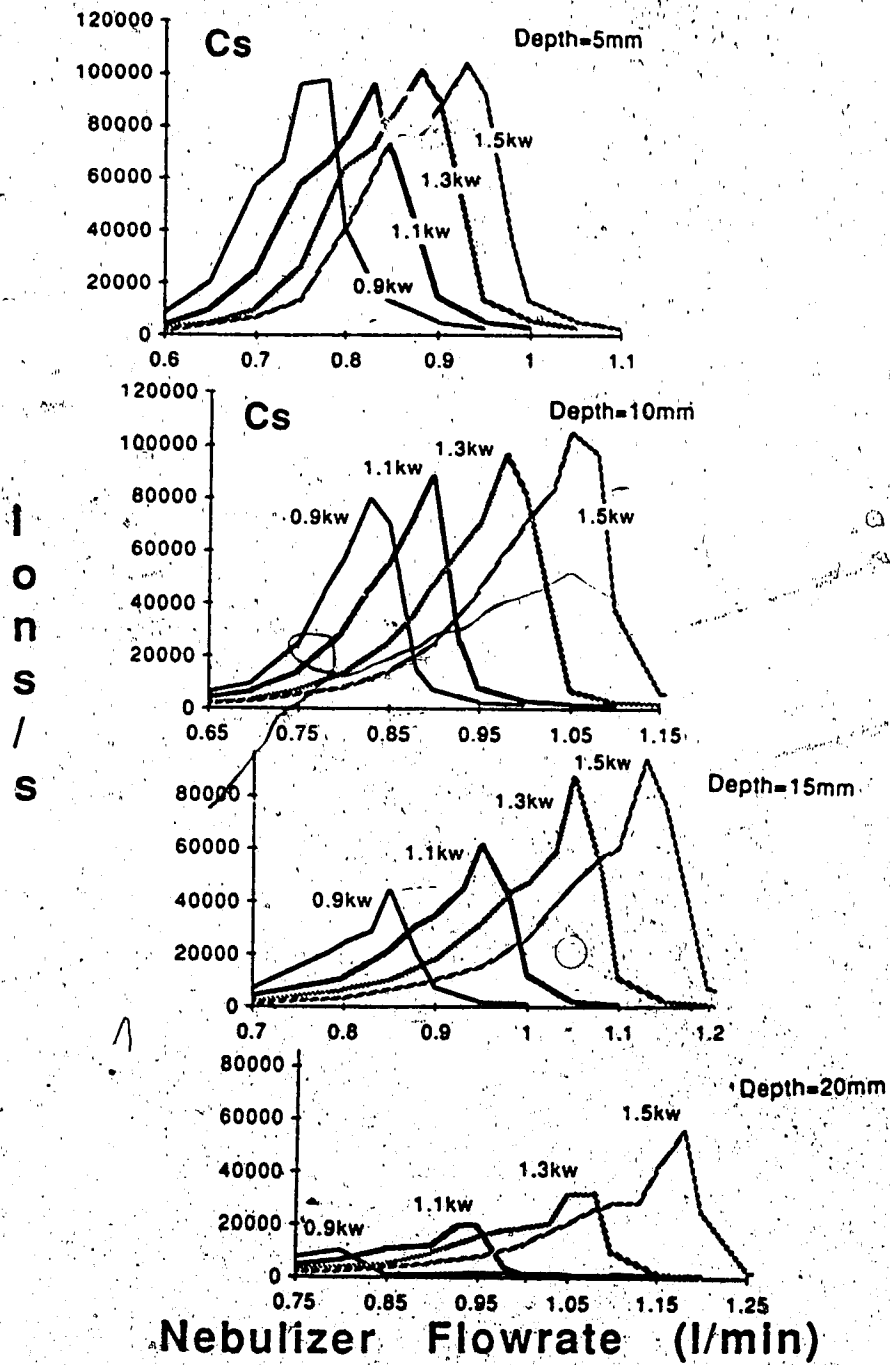


Figure 21d. Nebulizer flowrate-power parameter behavior plots for Cs at sampling depths of 5, 19, 15 and 20 mm from the load coil

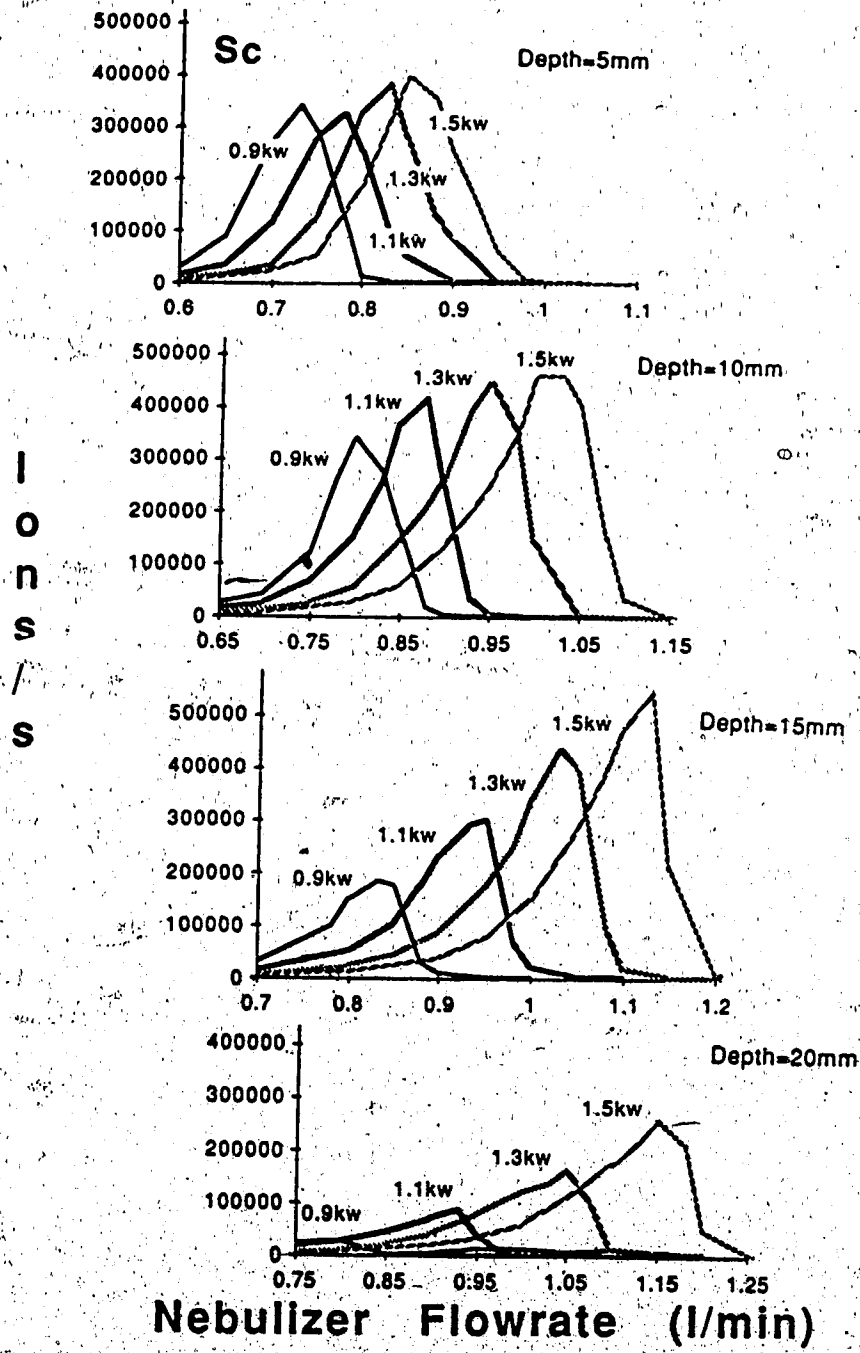


Figure 22a. Nebulizer flowrate-power parameter behavior plots for Sc at sampling depths of 5, 19, 15 and 20 mm from the load coil

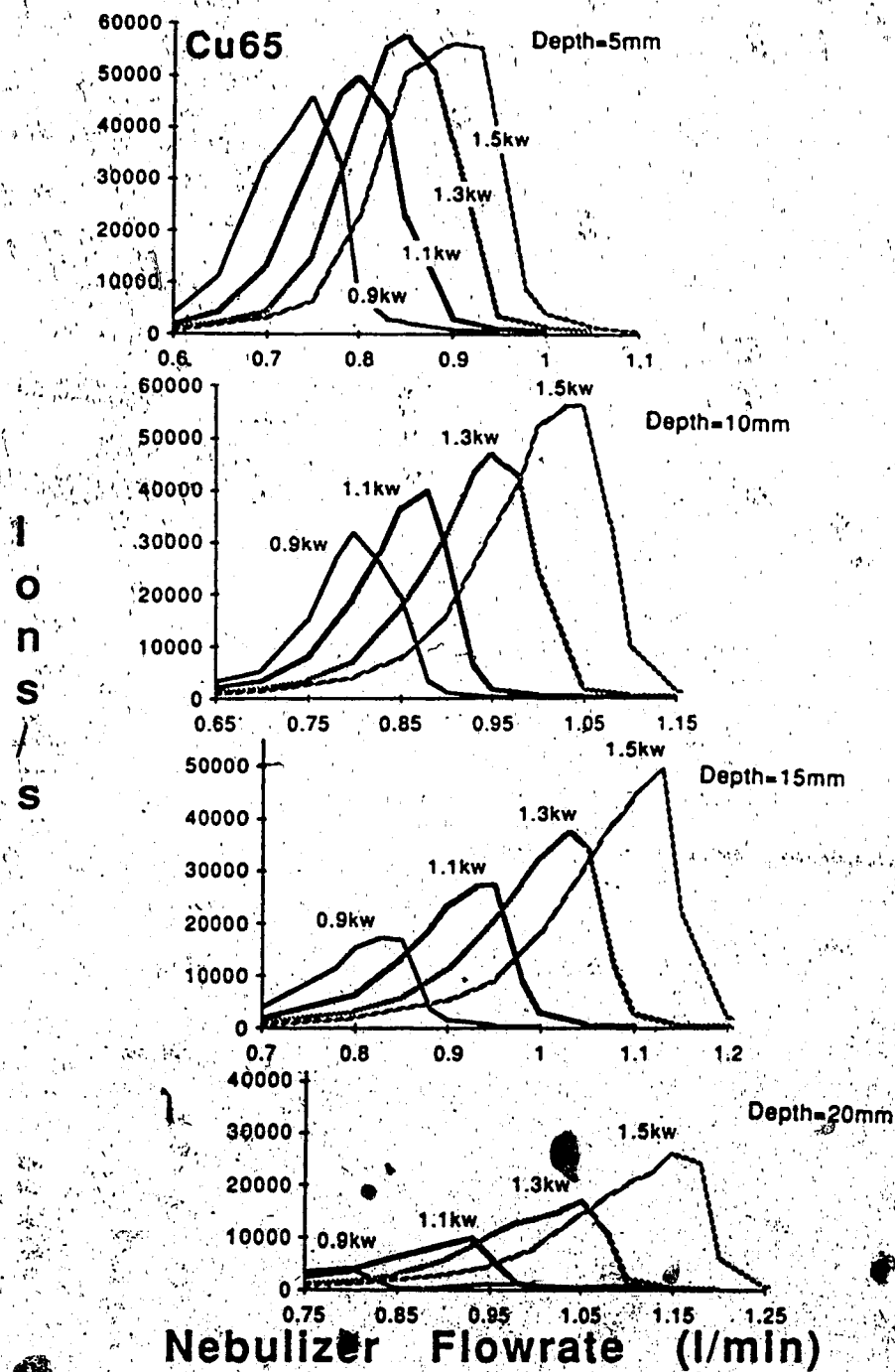


Figure 22b. Nebulizer flowrate-power parameter behavior plots for Cu65 at sampling depths of 5, 10, 15 and 20 mm from the load coil

elements have higher ionization potentials than the alkalis, hence are ionized higher in the plasma. As observed with Rb and Cs at 5 mm, the peak ion signal for the transition elements does not increase significantly with an increase in the rf power. However, at sampling depths of 10 mm to 20 mm, a corresponding increase of the peak ion count is observed with an increase in the plasma power. These observations are very different from the spatial dependence of ion emission in ICP-AES. In emission measurements, for most elements under most operating conditions, the maximum signal is obtained in the region between 15 to 20 mm above the load coil. At 25 mm above the load coil, very small ion emission is detected. Ion emission is also not as critically dependent on the aerosol flowrate and signal intensity cannot be recovered by increasing the aerosol flowrate after increasing the rf power [68, 69]. However, these data seem to correlate very well with similar data observed in ICP-atomic fluorescence spectrometry [70, 71].

#### G. Discussion

This study of the effect of plasma operating parameters on analyte signals in ICP-MS provides some interesting information regarding the factors involved in generating the ion signals in ICP-MS. Although the two groups of elements studied possess the same basic parameter behavior plots, they are different from each other in many aspects and these differences allow one to speculate on possible mechanisms involved in ion signal production in ICP-MS.

At a particular power and sampling depth, the ion signal increases to a maximum and then decreases as the nebulizer flowrate is steadily increased. The increase in the ion signal could be accounted for by; a) an increase in the amount of solution uptake, which is about 20 % even though a peristaltic

pump was used and, b) an increase in the amount of ions entering the sampling orifice due to a change in the spatial zone of the plasma that is sampled by the sampling cone. As the nebulizer flowrate is increased further, the analyte signal decreases because the central axial channel is excessively cooled by the larger amount of nebulizer gas and also the analyte residence time is shortened. An interplay of these opposing factors results in a peaking of the ion signal with respect to the nebulizer flowrate. When the plasma power is increased, the peak ion signal increases in intensity and shifts to higher flowrate. This is because as the rf power increases, the amount of energy available for heating also increases, therefore more of the analyte species in undissociated and atomic states are converted into the ionic form. In addition, the central channel can tolerate a higher nebulizer flowrate at higher rf power before being excessively cooled to the extent that ionization is reduced.

According to the nomenclature system proposed by Koirtzmann et al. [72] the axial channel of the plasma discharge can be divided into zones as shown in Figure 23. The location of these zones is strongly dependent on rf power and nebulizer gas flowrate. The initial radiation zone (IRZ) corresponds to the bullet-shaped yellow emission of sodium or the red emission of yttrium oxide in the discharge. In ICP-MS, a maximum ion count is measured when the tip of the initial radiation zone (IRZ) is sampled. In contrast, the best emission signal for ICP-AES is obtained at the normal analytical zone (NAZ). When the nebulizer flowrate is increased, the tip of the IRZ is pushed closer and closer to the sampling orifice until ion sampling finally occurs in the IRZ region. When this happens the signal decreases.

It is evident from the data that torch geometry is important and affects the ion signal behavior. Parameter behavior plots of the same elements are

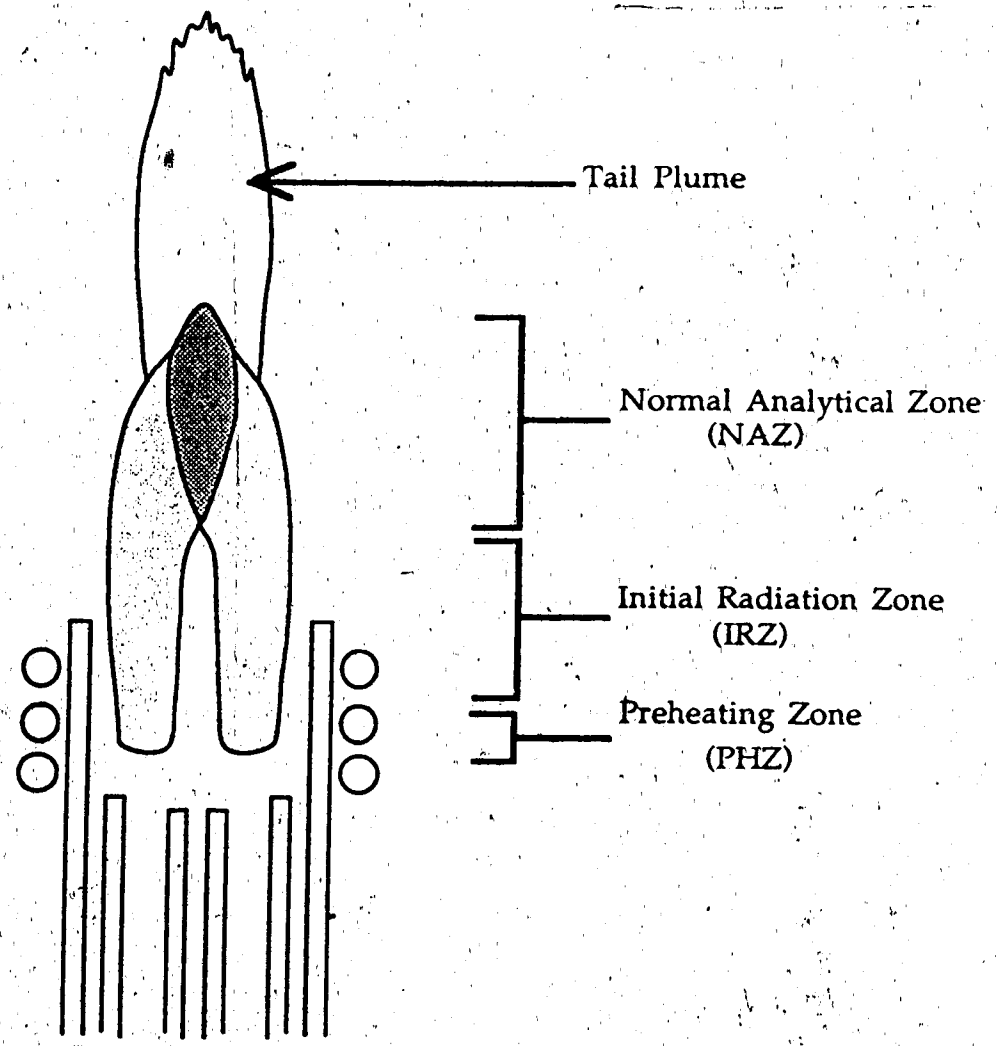


Figure 23. Zones of the ICP discharge.

slightly different for different torches. Results obtained with the extended torch show that elements with similar masses (first row elements) have very similar parameter behavior; same shape profile, peak at same nebulizer pressure and same sampling depth behavior. Elements having different masses (alkali metals) have somewhat different parameter behavior whereby the lighter elements Li and Na peak at lower nebulizer pressure than the heavier elements Rb and Cs. With the MAK torch however, the parameter behavior plots are the same for all elements. This is clearly shown by the normalized ion count plots for Li, Na, Rb, Cs and Sc in Figure 24. The sampling depth behavior is also different when different type of torches are used. With the extended torch, ion signal intensity is still reasonably high at a sampling depth of 30 mm whereas for a regular Fassel torch (cut-off extended torch), the best ion signal is obtained at around 17 mm. In contrast, the best ion signal is found at sampling depths less than 15 mm for the MAK torch. Therefore, one has the impression that the MAK torch produces a shorter, more confined plasma discharge and thus ions are generated lower in the plasma discharge. Furthermore, there is evidence [73] that elements with lighter masses undergo lateral diffusion in the axial channel at a faster rate than heavier elements. This certainly would explain why ion signals for Li and Na drop off much sooner than ion signals for Rb, Cs and the transition elements when the torch is moved away from the sampling orifice.

Another interesting feature is that at a sampling depth of 5 mm, an increase in the power does not result in a parallel increase in the peak ion intensity for the transition elements and the heavier alkali elements such as Rb and Cs. In fact, the peak ion count remains quite constant with power variation when nebulizer flowrate is adjusted. For some elements such as Pd, and Pt, this levelling of ion signal with power was observed to occur at a

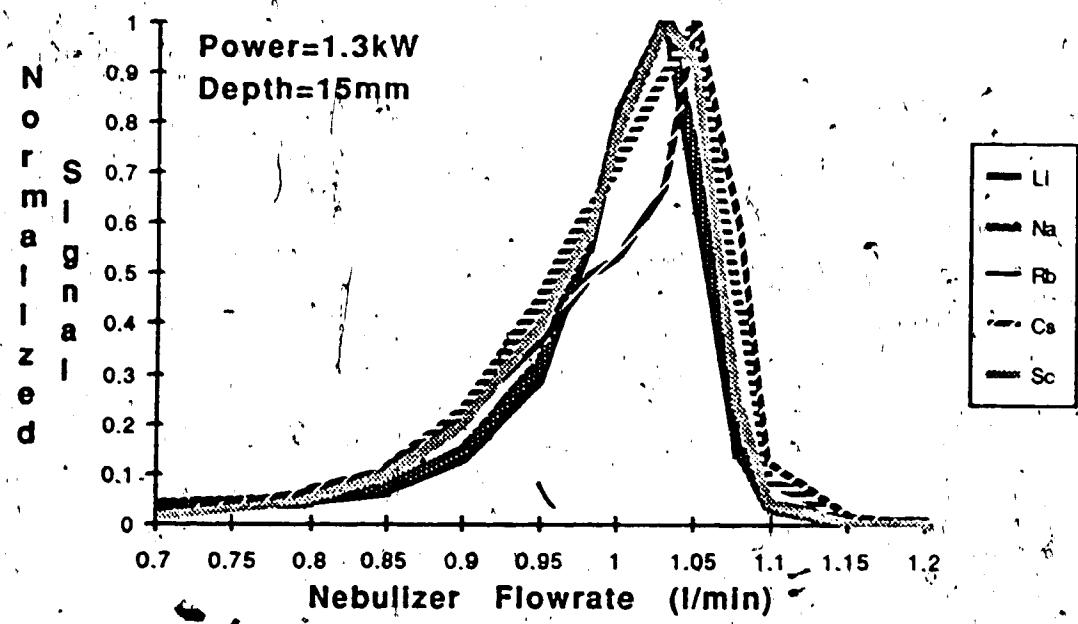


Figure 24. Normalized ion count vs nebulizer pressure plots for Li, Na, Rb, Cs and Sc for MAK torch



larger sampling depth [38, 57]. At sampling depth smaller than this, the increase of power decreased the peak ion signal. For light elements such as Li and Na, no levelling of peak ion count with power was observed even at 5 mm. This levelling of ion count behavior cannot be directly correlated to the ionization potential, but it seems to depend on the mass of the element. However, the exact nature of how these factors interact to give rise to such parameter behavior is not known at this stage. Parameter studies including those of the mass spectrometer would be tremendously helpful in further understanding the processes involved.

#### H. Conclusion

It is evident from the data presented that the ion signals in ICP-MS depend in a complex manner on ICP operating parameters. Nebulizer flowrate-power-sampling depth plots such as those in Figure 21 and 22 are very useful in grouping elements with similar trends and could help to clarify misleading data obtained with limited parameter settings. They also serve as a guide for selecting compromise plasma parameter settings for carrying out other ICP-MS experiments such as those in Chapters 3 and 4. From these parameter behavior plots, insights into the important processes involved in ion sampling of the plasma discharge are obtained. Finally, the experimental approaches used in this study are also useful with regards to investigation of the effect of high concentrations of concomitant salts on ion signals in ICP-MS and the results are presented in Chapter 5.

## CHAPTER 3

### BACKGROUND SPECTRAL FEATURES IN ICP-MS

#### A. Introduction

In this chapter the background spectral features observed in inductively coupled plasma-mass spectrometry are presented. A knowledge of background spectral features is important in order to recognize potential spectral interferences that can occur with particular analyte masses. To date, only limited background spectra and spectra tables have been published in the literature for ICP-MS [3, 4, 45, 60]. The background spectral features of distilled/deionized water and 5 % solutions (volume/volume) of some common acids were systematically studied and the background species observed were tabulated for easy reference. The acids studied were nitric acid, hydrochloric acid, sulfuric acid and phosphoric acid. Water and these dilute acid solutions are usually the most common and simplest matrices encountered when sample solutions are prepared for analysis, and, as such, provide baseline data on background spectral features. Most of the results in this chapter have already been reported in reference [59].

#### B. Experimental

The distilled/deionized water used was obtained by feeding "house" distilled water through a Millipore Milli-Q water purification system. The 5 % solutions (v/v) were made up from concentrated nitric, hydrochloric and sulfuric acids from Pfaltz and Bauer that were doubly distilled from Vycor.

Laboratory reagent hydrochloric acid and phosphoric acid were obtained from Baker and Adamson.

The plasma operating conditions were: rf power, 1.2 kW; nebulizer gas flowrate, 1.06 l/min; plasma gas flowrate, 12 l/min; and auxiliary gas flowrate, 1.4 l/min. The sampling depth was 15 mm from the load coil. These are normal operating conditions for the determination of first row transition elements. The background spectra were acquired with the mass spectrometer run in the high resolution mode (peak width ~ 0.6 amu at 10 % off the baseline), the measurement time was 1.0 s/point with a scan increment of 0.05 amu (20 points/peak). The background spectra were measured for the mass ranges 1 to 43 amu and 42 to 84 amu. In general, there were no significant background features observed above mass 84.

#### C. Distilled/Deionized Water and 5 % Nitric Acid

The background spectra of distilled/deionized water for the mass regions of 1 to 43 amu and 42 to 84 amu are shown in Figures 25 and 26 respectively. The basic background spectrum is shown in the top frame of each figure and each succeeding frame down is scale expanded at the ion count axis by a factor of 10 from the frame immediately above. An exception is Figure 26 where the bottom frame is scale expanded by a factor of 20 from the corresponding middle frame. Analogous plots are presented for all other acids in this chapter.

The background spectra for 5 % nitric acid are shown in Figures 27 and 28. On comparison to Figures 25 and 26, it can be seen that the background spectra of nitric acid are essentially the same as those of distilled water. Notice that a gap appears at mass 40 in these spectra. This is because the instrument is programmed to hop over  $\text{Ar}^+$  during scanning in order to protect the CEM detector from excessive currents. The background species for distilled water and nitric acid are derived basically from five elements; H, O,

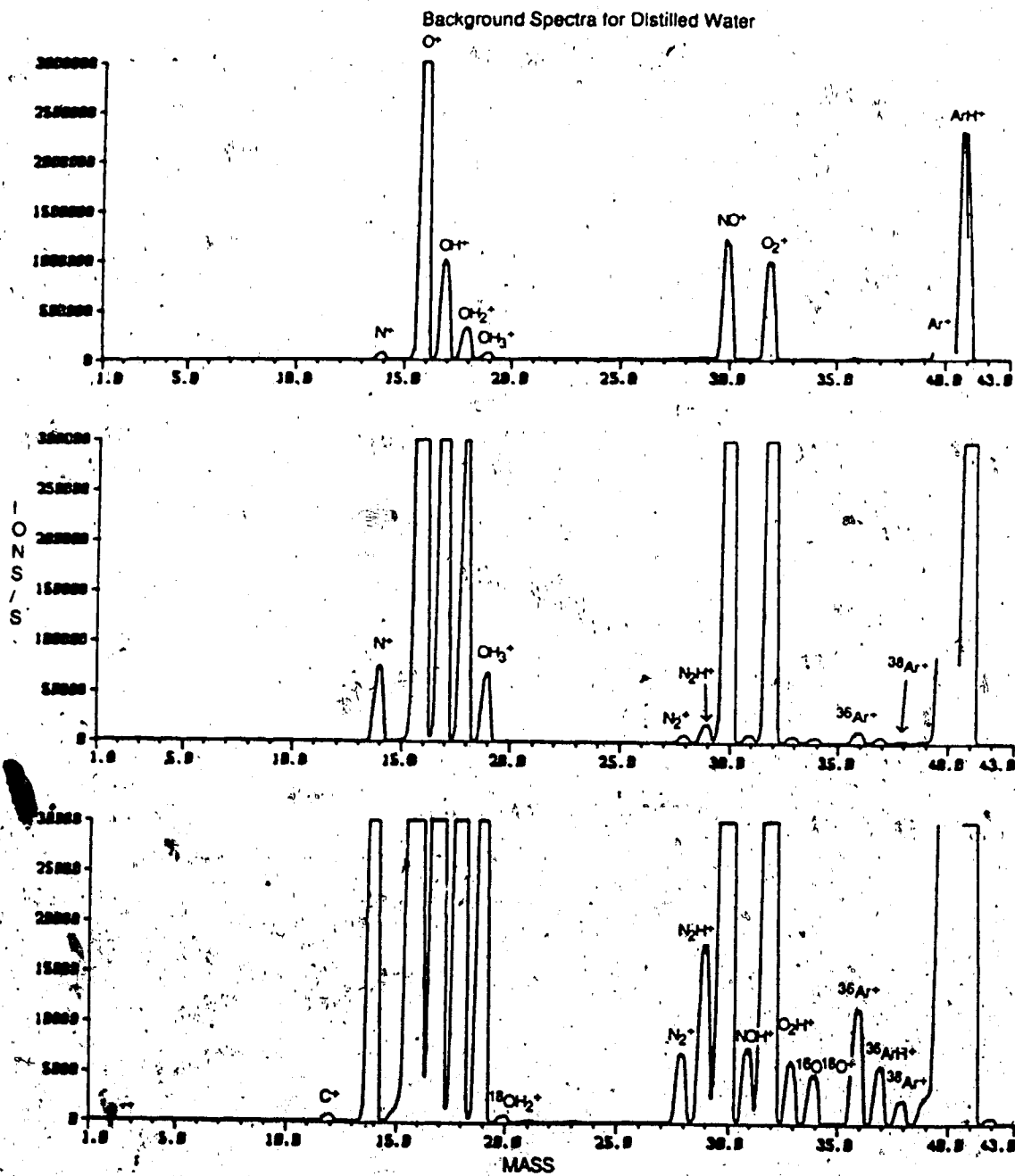


Figure 25. Background spectra for water for the mass range 1 to 43 amu

## Background Spectra for Distilled Water

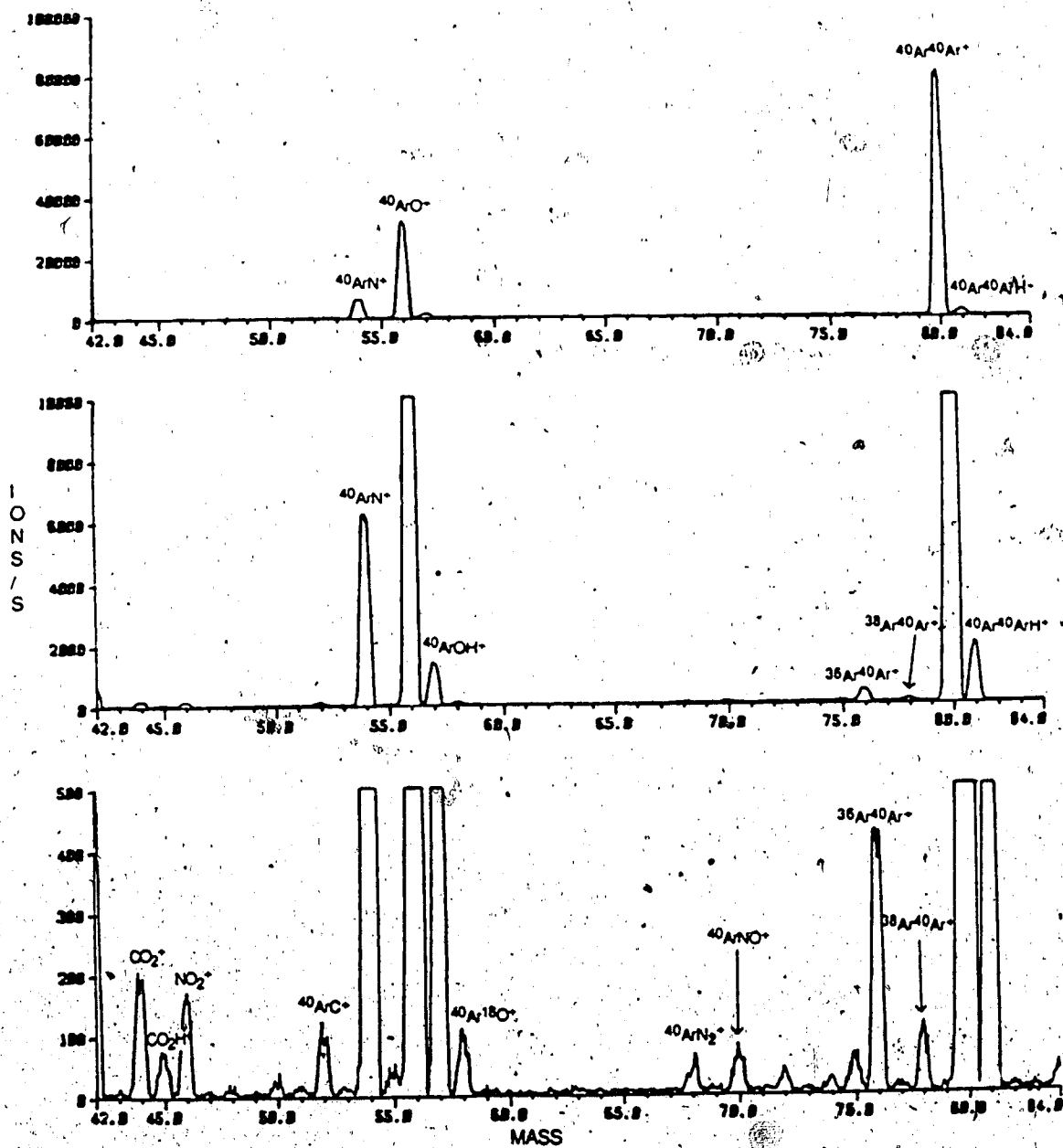


Figure 26. Background spectra for water for the mass range 42 to 84 amu

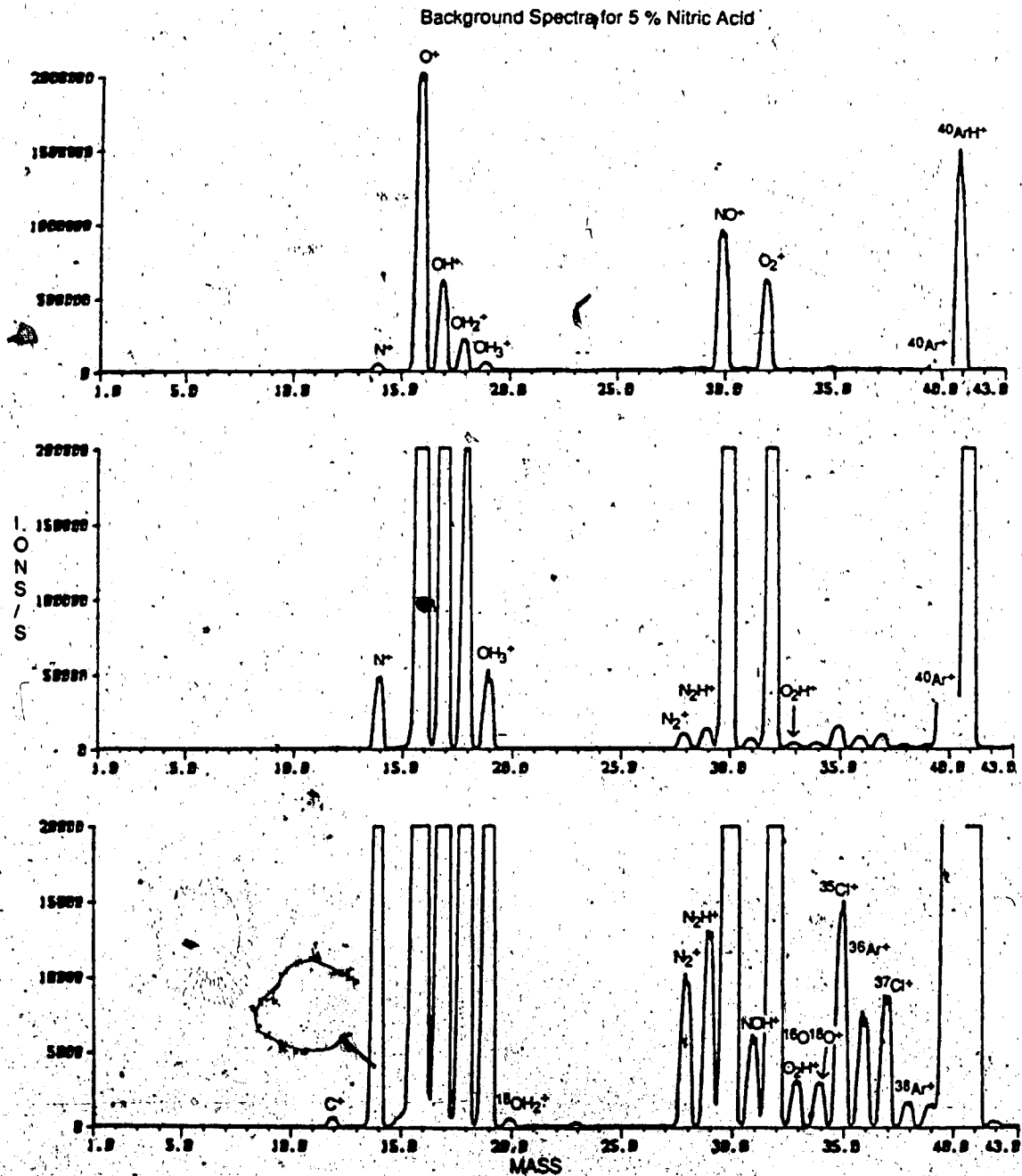


Figure 27. Background spectra for 5 % nitric acid for the mass range 1 to 43 amu

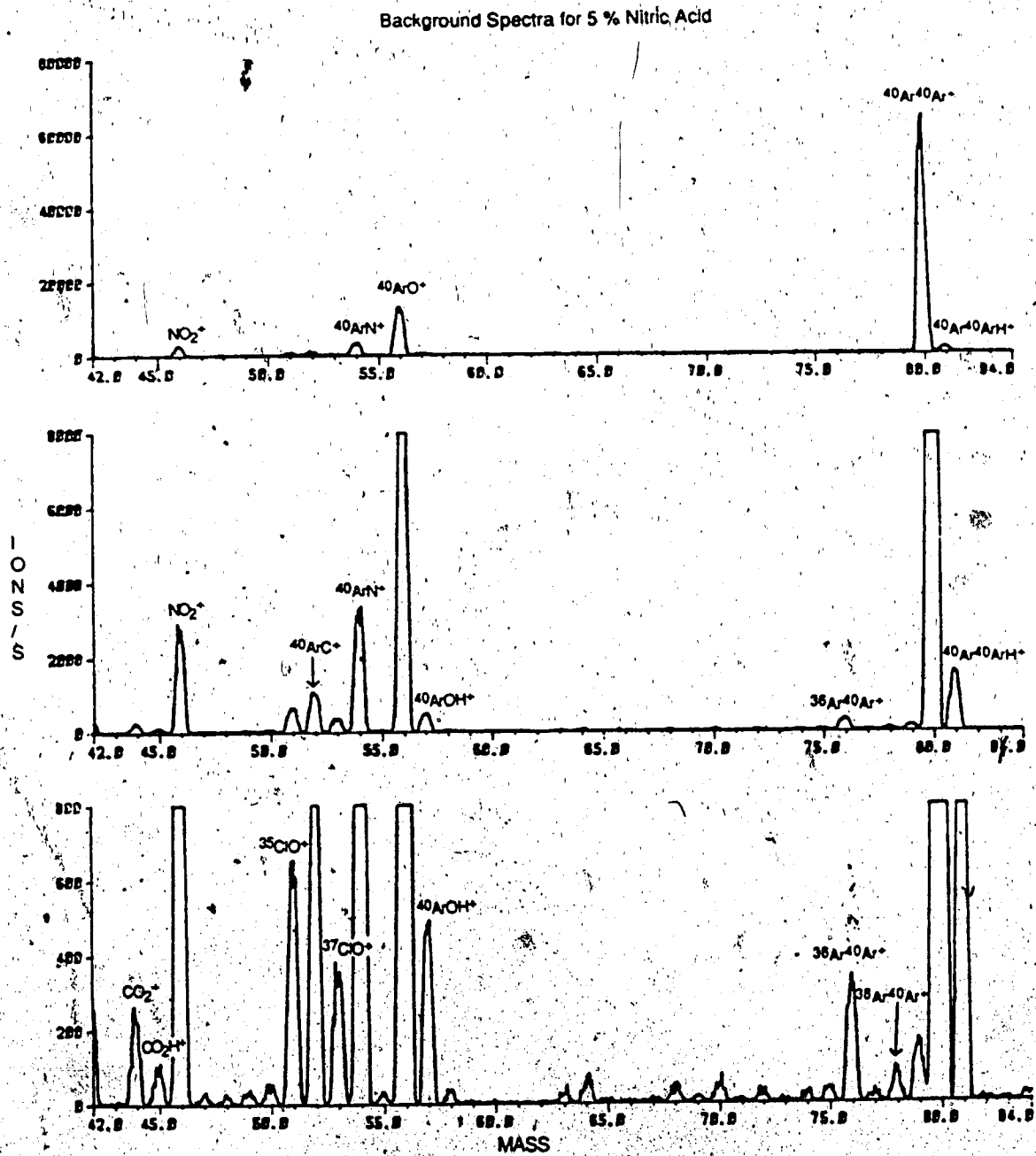


Figure 28. Background spectra for 5 % nitric acid for the mass range 42 to 84 amu

C, N and Ar. Assignment of molecular species to each mass is mostly deductive in nature, however, certain assignments can be verified. For example, for the peak at mass 46, the species  $\text{NO}_2^+$  was assigned. The ion intensity of this peak increased about ten times with 5 % nitric acid, which indicates that it is a nitrogen based species. The peak at mass 52 was attributed to  $\text{ArC}^+$  and its ion intensity increased dramatically when a few percent of methanol was added to distilled water.

Table 5 shows in greater detail the contributions from all other isotopic combinations of the background species. The major species are highlighted in boldface. The elements located at each mass are listed in the left hand column and the major isotope is highlighted in boldface. It can be seen that the background spectra in ICP-MS are generally simple but when all isotopic combinations are considered, it may be specifically complex. Unstructured background however is very small, usually less than 10 ions/s. Some of the more obvious and serious spectral overlap problems arise from the background peaks  $^{14}\text{N}^{14}\text{N}^+$ ,  $^{14}\text{N}^{16}\text{OH}^+$  and  $^{40}\text{Ar}^{40}\text{Ar}^+$  with  $^{28}\text{Si}^+$ ,  $^{31}\text{P}^+$  and  $^{80}\text{Se}^+$ . In addition,  $\text{ArO}^+$  not only interferes with  $^{56}\text{Fe}^+$  but to a lesser degree with V, Cr, Mn, Ni and Co as well when all its isotopic combinations and hydride forms are considered (see Table 5). Although background peaks derived from minor isotopic combinations may be very small, they can be significant especially when analyte measurements are being performed at sub-ppb levels. For example at mass 51, a distinct peak of about 30-40 ions/s, which is thought to be due to a combination of  $^{36}\text{Ar}^{15}\text{N}^+$  and  $^{36}\text{Ar}^{14}\text{N}^+$ , posed a problem when carrying out ultra-trace level determinations of vanadium. Therefore, the presence of such small structured background often degrades the detection limits of many low mass elements.



Table 5. Background species for water and 5 % nitric acid with corresponding element masses

| MASS | ELEMENTS  | DISTILLED WATER (5 % NITRIC ACID)   |
|------|-----------|---|
| 1    | H(99.985) | $^1\text{H}$  |
| 2    | H(0.015)  | $^2\text{H}$  |
| 3    |           |   |
| 4    | He(100)   |   |
| 5    |           |   |
| 6    | Li(7.5)   |   |
| 7    | Li(92.5)  |   |
| 8    |           |   |
| 9    | Be(100)   |   |
| 10   | B(19.91)  |   |
| 11   | B(80.09)  |   |
| 12   | C(98.89)  | $^{12}\text{C}$   |
| 13   | C(1.11)   | $^{13}\text{C}$   |
| 14   | N(99.63)  | $^{14}\text{N}$   |
| 15   | N(0.37)   | $^{15}\text{N}$   |
| 16   | O(99.76)  | $^{16}\text{O}$   |
| 17   | O(0.04)   | $^{17}\text{O}$ , $^{16}\text{OH}$  |
| 18   | O(0.20)   | $^{18}\text{O}$ , $^{17}\text{OH}$ , $^{16}\text{OH}_2$   |
| 19   | F(100)    | $^{18}\text{OH}$ , $^{17}\text{OH}_2$ , $^{16}\text{OH}_3$  |
| 20   | Ne(90.92) | $^{18}\text{OH}_2$ , $^{17}\text{OH}_3$   |
| 21   | Ne(0.26)  | $^{18}\text{OH}_3$  |
| 22   | Ne(8.82)  |   |
| 23   | Na(100)   |   |
| 24   | Mg(78.8)  |   |
| 25   | Mg(10.15) |   |
| 26   | Mg(11.05) |   |
| 27   | Al(100)   |   |
| 28   | Si(92.21) | $^{14}\text{N}^{14}\text{N}$ , $^{12}\text{C}^{16}\text{O}$   |
| 29   | Si(4.7)   | $^{14}\text{N}^{15}\text{N}$ , $^{14}\text{N}^{14}\text{NH}$ , $^{13}\text{C}^{16}\text{O}$ , $^{12}\text{C}^{17}\text{O}$ , $^{12}\text{C}^{16}\text{OH}$  |
| 30   | Si(3.09)  | $^{15}\text{N}^{15}\text{N}$ , $^{14}\text{N}^{15}\text{NH}$ , $^{14}\text{N}^{16}\text{O}$ , $^{12}\text{C}^{18}\text{O}$ , $^{13}\text{C}^{17}\text{O}$   |
| 31   | P(100)    | $^{15}\text{N}^{15}\text{NH}$ , $^{14}\text{N}^{16}\text{OH}$ , $^{15}\text{N}^{16}\text{O}$ , $^{14}\text{N}^{17}\text{O}$ , $^{13}\text{C}^{18}\text{O}$  |
| 32   | S(93.02)  | $^{14}\text{N}^{18}\text{O}$ , $^{15}\text{N}^{17}\text{O}$ , $^{14}\text{N}^{17}\text{OH}$ , $^{15}\text{N}^{16}\text{OH}$ , $^{16}\text{O}^{16}\text{O}$  |
| 33   | S(0.75)   | $^{15}\text{N}^{18}\text{O}$ , $^{14}\text{N}^{18}\text{OH}$ , $^{15}\text{N}^{17}\text{OH}$ , $^{16}\text{O}^{17}\text{O}$ , $^{16}\text{O}^{16}\text{OH}$ |
| 34   | S(4.21)   | $^{15}\text{N}^{18}\text{OH}$ , $^{16}\text{O}^{18}\text{O}$ , $^{17}\text{O}^{17}\text{O}$ , $^{16}\text{O}^{17}\text{OH}$                                 |

Table 5. Continued

| MASS | ELEMENTS                     | DISTILLED WATER (5% NITRIC ACID)   |
|------|------------------------------|--|
| 35   | Cl(73.77)                    | $^{17}\text{O}^{18}\text{O}$ , $^{16}\text{O}^{18}\text{OH}$ , $^{17}\text{O}^{17}\text{OH}$   |
| 36   | Ar(0.34), S(0.02)            | $^{36}\text{Ar}$ , $^{18}\text{O}^{18}\text{O}$ , $^{17}\text{O}^{18}\text{OH}$  |
| 37   | Cl(24.23)                    | $^{36}\text{ArH}$ , $^{18}\text{O}^{18}\text{OH}$  |
| 38   | Ar(0.06)                     | $^{38}\text{Ar}$   |
| 39   | K(93.08)                     | $^{38}\text{ArH}$  |
| 40   | Ar(99.6), Ca(96.97), K(0.01) | $^{40}\text{Ar}$   |
| 41   | K(6.91)                      | $^{40}\text{ArH}$  |
| 42   | Ca(0.64)                     | $^{40}\text{ArH}_2$  |
| 43   | Ca(0.14)                     |  |
| 44   | Ca(2.06)                     | $^{12}\text{C}^{16}\text{O}^{16}\text{O}$  |
| 45   | Sc(100)                      | $^{12}\text{C}^{16}\text{O}^{16}\text{OH}$   |
| 46   | Ti(7.99), Ca(0.003)          | $^{14}\text{N}^{16}\text{O}^{16}\text{O}$  |
| 47   | Ti(7.32)                     |  |
| 48   | Ti(73.98), Ca(0.19)          |  |
| 49   | Ti(5.46)                     |  |
| 50   | Ti(5.25), Cr(4.35), V(0.24)  | $^{36}\text{Ar}^{14}\text{N}$  |
| 51   | V(99.76)                     | $^{36}\text{Ar}^{15}\text{N}$ , $^{36}\text{Ar}^{14}\text{NH}$   |
| 52   | Cr(83.76)                    | $^{38}\text{Ar}^{14}\text{N}$ , $^{36}\text{Ar}^{15}\text{NH}$ , $^{40}\text{Ar}^{12}\text{C}$ , $^{36}\text{Ar}^{16}\text{O}$                                   |
| 53   | Cr(9.51)                     | $^{38}\text{Ar}^{15}\text{N}$ , $^{38}\text{Ar}^{14}\text{NH}$ , $^{36}\text{Ar}^{17}\text{O}$ , $^{36}\text{Ar}^{16}\text{OH}$                                  |
| 54   | Fe(5.82), Cr(2.38)           | $^{38}\text{Ar}^{15}\text{NH}$ , $^{40}\text{Ar}^{14}\text{N}$ , $^{36}\text{Ar}^{18}\text{O}$ , $^{38}\text{Ar}^{16}\text{O}$ , $^{36}\text{Ar}^{17}\text{OH}$  |
| 55   | Mn(100)                      | $^{40}\text{Ar}^{15}\text{N}$ , $^{40}\text{Ar}^{14}\text{NH}$ , $^{38}\text{Ar}^{17}\text{O}$ , $^{36}\text{Ar}^{18}\text{OH}$ , $^{38}\text{Ar}^{16}\text{OH}$ |
| 56   | Fe(91.66)                    | $^{40}\text{Ar}^{15}\text{NH}$ , $^{38}\text{Ar}^{18}\text{O}$ , $^{40}\text{Ar}^{16}\text{O}$ , $^{38}\text{Ar}^{17}\text{OH}$                                  |
| 57   | Fe(2.19)                     | $^{40}\text{Ar}^{17}\text{O}$ , $^{40}\text{Ar}^{16}\text{OH}$ , $^{38}\text{Ar}^{18}\text{OH}$  |
| 58   | Ni(67.77), Fe(0.33)          | $^{40}\text{Ar}^{18}\text{O}$ , $^{40}\text{Ar}^{17}\text{OH}$   |
| 59   | Co(100)                      | $^{40}\text{Ar}^{18}\text{OH}$   |
| 60   | Ni(26.16)                    |  |
| 61   | Ni(1.25)                     |  |
| 62   | Ni(3.66)                     |  |
| 63   | Cu(69.1)                     |  |
| 64   | Zn(68.89), Ni(1.16)          |  |
| 65   | Cu(30.9)                     |  |
| 66   | Zn(27.81)                    |  |
| 67   | Zn(4.11)                     |  |
| 68   | Zn(18.57)                    | $^{40}\text{Ar}^{14}\text{N}^{14}\text{N}$   |
| 69   | Ge(60.16)                    |  |
| 70   | Ge(20.51), Zn(0.62)          | $^{40}\text{Ar}^{14}\text{N}^{16}\text{O}$   |
| 71   | Ge(39.84)                    |  |
| 72   | Ge(27.4)                     | $^{36}\text{Ar}^{36}\text{Ar}$   |
| 73   | Ge(7.76)                     | $^{36}\text{Ar}^{36}\text{ArH}$  |
| 74   | Ge(36.36), Se(0.87)          | $^{36}\text{Ar}^{38}\text{Ar}$   |
| 75   | As(100)                      | $^{36}\text{Ar}^{38}\text{ArH}$  |
| 76   | Ge(7.77), Se(9.02)           | $^{36}\text{Ar}^{40}\text{Ar}$ , $^{38}\text{Ar}^{38}\text{Ar}$  |
| 77   | Se(7.58)                     | $^{36}\text{Ar}^{40}\text{ArH}$ , $^{38}\text{Ar}^{38}\text{ArH}$  |
| 78   | Se(23.52), Kr(0.35)          | $^{38}\text{Ar}^{40}\text{Ar}$   |
| 79   | Br(50.54)                    | $^{38}\text{Ar}^{40}\text{ArH}$  |
| 80   | Se(69.82), Kr(2.27)          | $^{40}\text{Ar}^{40}\text{Ar}$   |
| 81   | Br(49.46)                    | $^{40}\text{Ar}^{40}\text{ArH}$  |

A more subtle problem can arise concerning the application of correction procedures for isobaric spectra overlaps. For example at mass 58, a minor isotope of Fe coincides with the major isotope of Ni. When Ni is to be determined in the presence of Fe, a correction procedure can be implemented the software provided by Sciex. The correction procedure consists of measuring the signal at mass 56 and, assuming it to come completely from  $^{56}\text{Fe}^+$ , subtracting 0.0036 times the measured ion count from the ion count at mass 58, thus correcting for the contribution of  $^{58}\text{Fe}^+$  to the total count at that mass. However, the ion signal at mass 56 consists of a major contribution from  $^{40}\text{Ar}^{16}\text{O}^+$  and, depending on the actual relative and absolute concentrations of Ni and Fe present, an erroneous correction could result.

As mentioned before, nitric acid has background spectra which are very similar to those of distilled water, however the ion intensity of most background species with the exception of nitrogen containing species are decreased as much as by a factor of two. This could be due to the suppression of these background species in the presence of 5 % nitric acid (15,000 ppm of N). Nitrogen containing species, except for  $\text{NO}_2^+$  at mass 46, have about the same intensity as in distilled water spectrum.  $\text{NO}_2^+$  is different in that it is about 10 times more intense in 5 % nitric acid background spectrum as compared to water background spectrum.

Two unexpected peaks at masses 35 and 37 in the ratio of about 3:1 are observed in nitric acid and are most likely from  $^{35}\text{Cl}^+$  and  $^{37}\text{Cl}^+$ . Another set of peaks occurring at masses 51 and 53 are also observed (see bottom frame in Figure 28) which are most likely  $^{35}\text{ClO}^+$  and  $^{37}\text{ClO}^+$  species. The doubly distilled nitric acid is apparently contaminated with chloride. The  $^{35}\text{ClO}^+$  peak at mass 51 represents a serious spectral interference for  $^{51}\text{V}^+$  which is the major V isotope; the only other isotope,  $^{50}\text{V}^+$ , is only 0.24 % in

abundance. Therefore, this particular batch of nitric acid cannot be used in conjunction with trace vanadium determinations. Of course, hydrochloric acid and other matrices containing large amount of chlorides will also have the same background interference problems.

Trace amounts of sodium, potassium and chromium are also found in the nitric acid. The peak at mass 52 is attributed to  $^{52}\text{Cr}^+$  as well as to  $^{40}\text{Ar}^{12}\text{C}^+$ . In Figures 26 and 28, the  $\text{CO}_2^+$  and  $\text{CO}_2\text{H}^+$  peaks have about the same intensity, therefore the peak at mass 52 is too intense to be due to  $^{40}\text{Ar}^{12}\text{C}^+$  alone. Thus, from the ICP-MS point of view, care must be taken to monitor stock acids for contaminants which could sometimes cause serious errors in analysis. Some contaminants such as the chloride case mentioned above would not even warrant passing notice if the nitric acid was used in ICP-AES applications, but when used for ICP-MS, serious spectral interference with the most abundant isotope of vanadium occurred.

#### D. 5 % Hydrochloric Acid

The background spectra for 5 % hydrochloric acid in the same basic format are shown in Figures 29 and 30. Similar to what was observed with 5 % nitric acid, the ion intensity of most background species common to distilled water and hydrochloric acid are suppressed by about a factor of two in the hydrochloric acid spectrum. The concentration of Cl in 5 % hydrochloric acid is about 57,000 ppm. In addition to all the background species that are observed in distilled water, the new peaks are  $\text{Cl}^+$ ,  $\text{ClO}^+$ ,  $\text{ClN}^+$ ,  $\text{Cl}_2^+$ ,  $\text{ClO}_2^+$  and  $\text{ArCl}^+$ . The molecular species significantly increase the complexity of the background for the determination of first row transition elements, especially when all the isotopic combinations are considered. The isotopic combinations of these species are listed in Table 6.

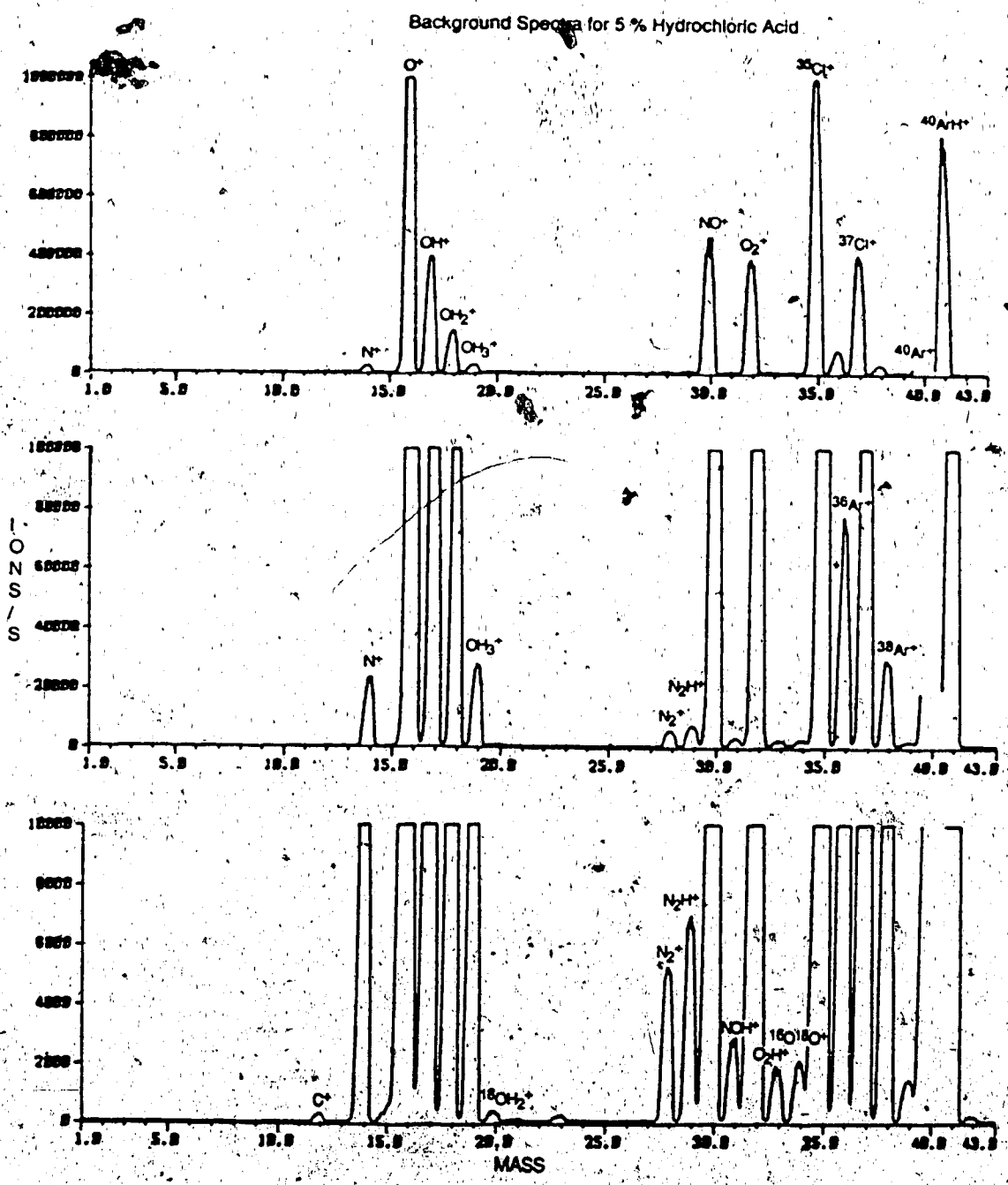


Figure 29. Background spectra for 5 % hydrochloric acid for the mass range 1 to 43 amu. Source of stock acid: Pfaltz and Bauer

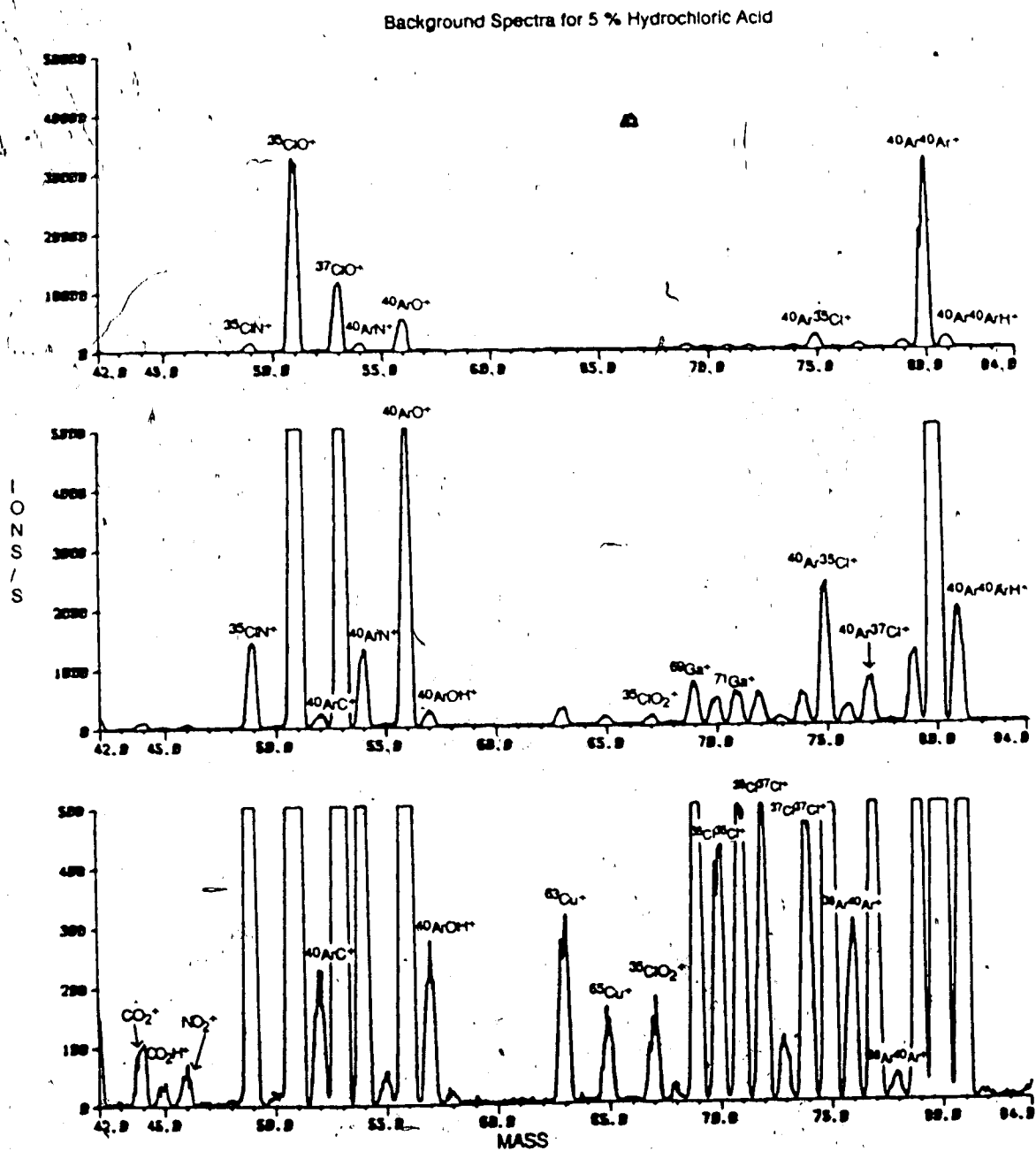


Figure 30. Background spectra for 5 % hydrochloric acid for the mass range 42 to 84 amu. Source of stock acid: Pfaltz and Bauer

The most intense peak is due to  $^{35}\text{Cl}^+$  which in 5 % HCl has an intensity of about  $10^6$  counts/s. This translates to about 20 ions/s/ppm of  $\text{Cl}^+$ . There is some interference at mass 35 from the minor isotopic combinations of oxygen species, but it is still possible to determine chloride at the ppm level using this positive chloride ion. The second most intense peak is due to  $^{35}\text{ClO}^+$  which is about 30 times less sensitive.

As stated before, the molecular chlorine species cause serious spectral interferences in the determination of the first row transition elements. It can be seen from Table 6 that the  $\text{ClN}^+$  and  $\text{ClO}^+$  species affect several first row transition elements. The most serious interference is that of  $^{35}\text{Cl}^{16}\text{O}^+$  on  $^{51}\text{V}^+$ . The only other isotope of vanadium,  $^{50}\text{V}^+$ , is only 0.24% abundant and has interference problems from  $^{35}\text{Cl}^{15}\text{N}^+$  and the minor isotopes of titanium and chromium. This means that in ICP-MS, trace vanadium cannot really be determined in a solution matrix containing chloride or other chlorine compounds. Note also that problems could arise with low concentration determinations of Mn and Cr. Manganese, which is mono-isotopic, has interference from  $^{37}\text{Cl}^{18}\text{O}^+$ , and all chromium isotopes have interferences from various isotopic combinations of  $\text{ClN}^+$  and  $\text{ClO}^+$ .

In the mass range of 67 to 77 amu,  $\text{ClO}^+$  and  $\text{Cl}_2^+$  and  $\text{ArCl}^+$  species also interfere with the determinations of Ga, Ge, Se and As. The interference of  $^{40}\text{Ar}^{35}\text{Cl}^+$  on  $^{75}\text{As}^+$  is a major problem since the  $^{40}\text{Ar}^{35}\text{Cl}^+$  peak is quite intense and arsenic is mono-isotopic. Similar to vanadium, As determinations by ICP-MS cannot be carried out in solution matrices containing chlorine species. In effect, these spectral interference problems dictate the type of sample dissolution and solution work-up conditions, reagents and procedures that can be used if analysis by ICP-MS is anticipated. And

Table 6. Background species for 5 % hydrochloric acid with corresponding element masses

| MASS | ELEMENTS                    | 5 % HYDROCHLORIC ACID   |
|------|-----------------------------|---|
| 35   | Cl(75.77)                   | $^{35}\text{Cl}$  |
| 36   | Ar(0.34), S(0.02)           | $^{35}\text{ClH}$   |
| 37   | Cl(24.23)                   | $^{37}\text{Cl}$  |
| 38   | Ar(0.06)                    | $^{37}\text{ClH}$   |
| 49   | Ti (5.46)                   | $^{35}\text{Cl}^{14}\text{N}$   |
| 50   | Ti(5.25), Cr(4.35), V(0.24) | $^{35}\text{Cl}^{15}\text{N}$   |
| 51   | V(99.76)                    | $^{37}\text{Cl}^{14}\text{N}$ , $^{35}\text{Cl}^{16}\text{O}$   |
| 52   | Cr(83.76)                   | $^{37}\text{Cl}^{15}\text{N}$ , $^{35}\text{Cl}^{17}\text{O}$ , $^{35}\text{Cl}^{16}\text{OH}$  |
| 53   | Cr(9.51)                    | $^{37}\text{Cl}^{16}\text{O}$ , $^{35}\text{Cl}^{17}\text{OH}$ , $^{35}\text{Cl}^{18}\text{O}$  |
| 54   | Fe(5.82), Cr(2.38)          | $^{37}\text{Cl}^{16}\text{OH}$ , $^{37}\text{Cl}^{17}\text{O}$  |
| 55   | Mn(100)                     | $^{37}\text{Cl}^{18}\text{O}$ , $^{37}\text{Cl}^{17}\text{OH}$  |
| 56   | Fe(91.66)                   | $^{37}\text{Cl}^{18}\text{OH}$  |
| 67   | Zn(4.11)                    | $^{35}\text{Cl}^{16}\text{O}^{16}\text{O}$  |
| 68   | Zn(18.57)                   | $^{35}\text{Cl}^{16}\text{O}^{17}\text{O}$  |
| 69   | Ga(60.16)                   | $^{35}\text{Cl}^{16}\text{O}^{18}\text{O}$ , $^{35}\text{Cl}^{17}\text{O}^{17}\text{O}$ , $^{37}\text{Cl}^{16}\text{O}^{16}\text{O}$                                  |
| 70   | Ge(20.51), Zn(0.62)         | $^{35}\text{Cl}^{17}\text{O}^{18}\text{O}$ , $^{37}\text{Cl}^{16}\text{O}^{17}\text{O}$ , $^{35}\text{Ar}^{35}\text{Cl}$  |
| 71   | Ga(39.84)                   | $^{35}\text{Cl}^{18}\text{O}^{18}\text{O}$ , $^{37}\text{Cl}^{16}\text{O}^{18}\text{O}$ , $^{37}\text{Cl}^{17}\text{O}^{17}\text{O}$ , $^{36}\text{Ar}^{35}\text{Cl}$ |
| 72   | Ge(27.4)                    | $^{37}\text{Cl}^{17}\text{O}^{18}\text{O}$ , $^{35}\text{Cl}^{37}\text{Cl}$   |
| 73   | Ge(7.76)                    | $^{37}\text{Cl}^{18}\text{O}^{18}\text{O}$ , $^{36}\text{Ar}^{37}\text{Cl}$ , $^{38}\text{Ar}^{35}\text{Cl}$  |
| 74   | Ge(36.56), Se(0.87)         | $^{37}\text{Cl}^{37}\text{Cl}$  |
| 75   | As(100)                     | $^{38}\text{Ar}^{37}\text{Cl}$ , $^{40}\text{Ar}^{35}\text{Cl}$   |
| 77   | Se(7.58)                    | $^{40}\text{Ar}^{37}\text{Cl}$  |



hydrochloric acid is obviously not an acid of choice for the determination of As or certain first row transition elements, especially V.

The background spectra shown in Figures 29 and 30 were obtained using the doubly distilled hydrochloric acid purchased from Pfaltz and Bauer. As can be seen from the spectra (bottom frame in Figure 29), the acid shows contaminations from Cu, Ga and Ge. The presence of  $Ge^+$  causes the ratio of  $Cl_2^+$  at masses 70, 72 and 74 to be different from the expected values. The estimated concentration of these contaminants is about 0.5 to 1 ppb in the 5% hydrochloric acid solution. A certain amount of bromine could also be present, as indicated by the peak at mass 79.

Background spectra of 5 % hydrochloric acid prepared from off the shelf laboratory reagent grade hydrochloric acid (Baker & Adamson) are shown in Figures 31 and 32. As can be seen from the bottom frame in Figure 32, the laboratory reagent grade acid also has contaminations from Cu and a very small amount of Br but Ga and Ge are absent. Thus, the spectrum gives a better picture of the hydrochloric acid background pattern in this mass region than in the corresponding spectrum in Figure 30. A certain amount of sulfate contamination is also found in this batch of acid as indicated by the peaks at masses 48 and 50, which are most likely  $^{32}S^{16}O^+$  and  $^{34}S^{16}O^+$ , and the increase in the peak intensities at 32, 34 and 46, which are most likely due to  $^{32}S^+$ ,  $^{34}S^+$  and  $^{32}SN^+$ .

#### E. 5 % Sulfuric Acid

The background spectra for 5 % sulfuric acid solution are shown in Figures 33 and 34. The spectrum format is the same as that used for previous spectra except that four frames of decade scale expanded spectra are shown. The intensity of distilled water background peaks (oxygen, hydroxyls and

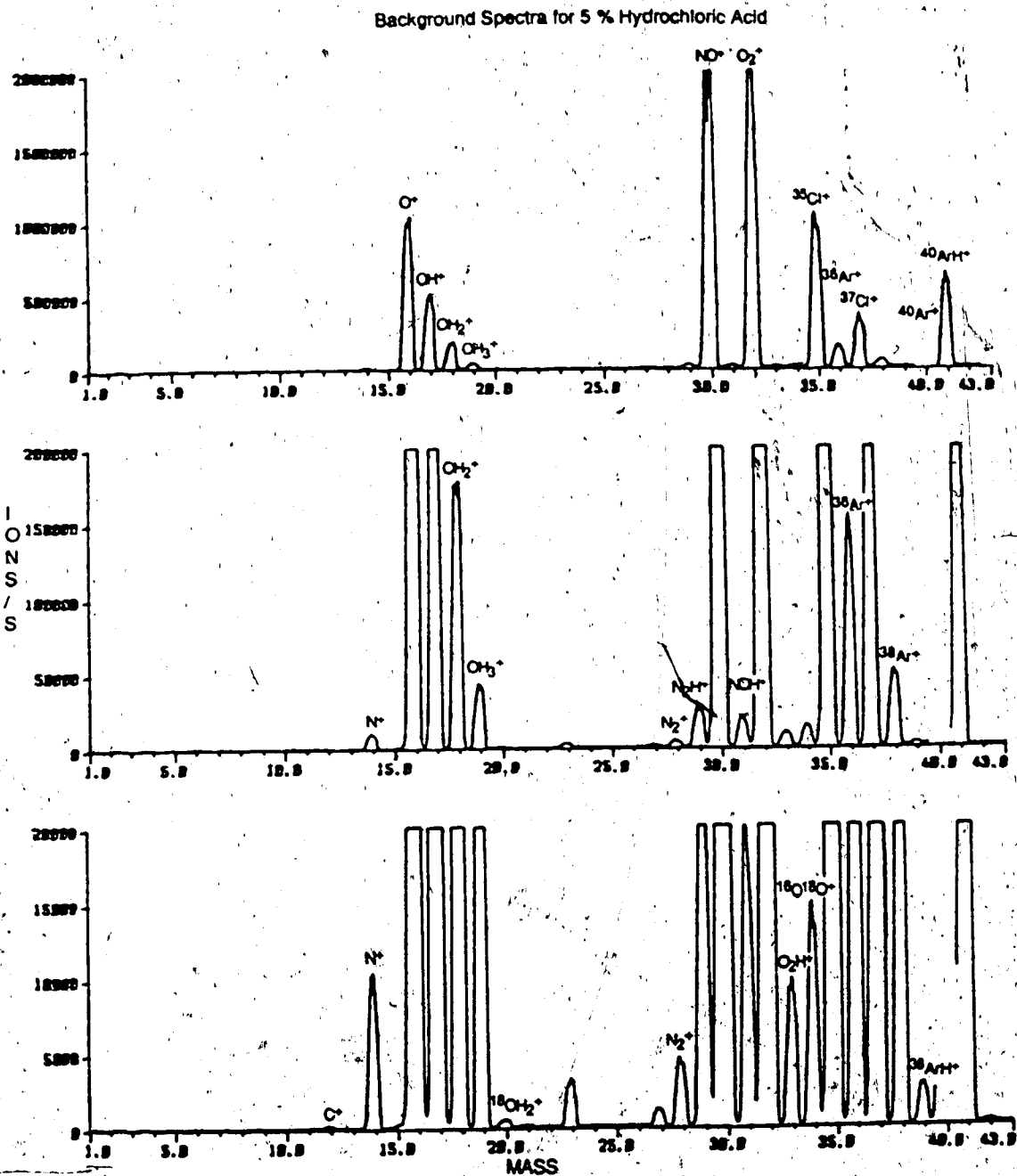


Figure 31. Background spectra for 5 % hydrochloric acid for the mass range 1 to 43 amu. Source of stock: Baker and Adamson

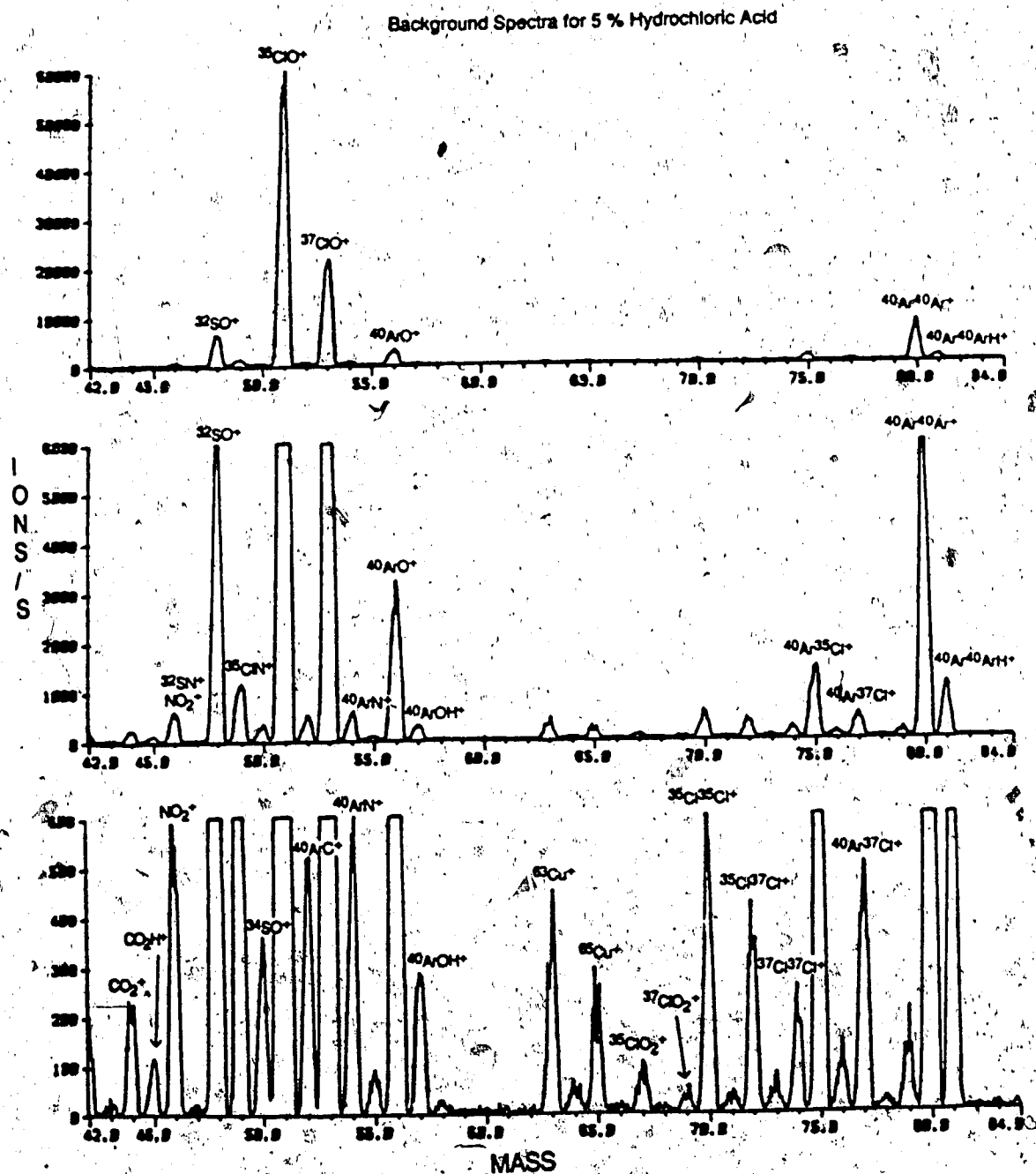


Figure 32. Background spectra for 5 % hydrochloric acid for the mass range 42 to 84 amu. Source of stock: Baker and Adamson

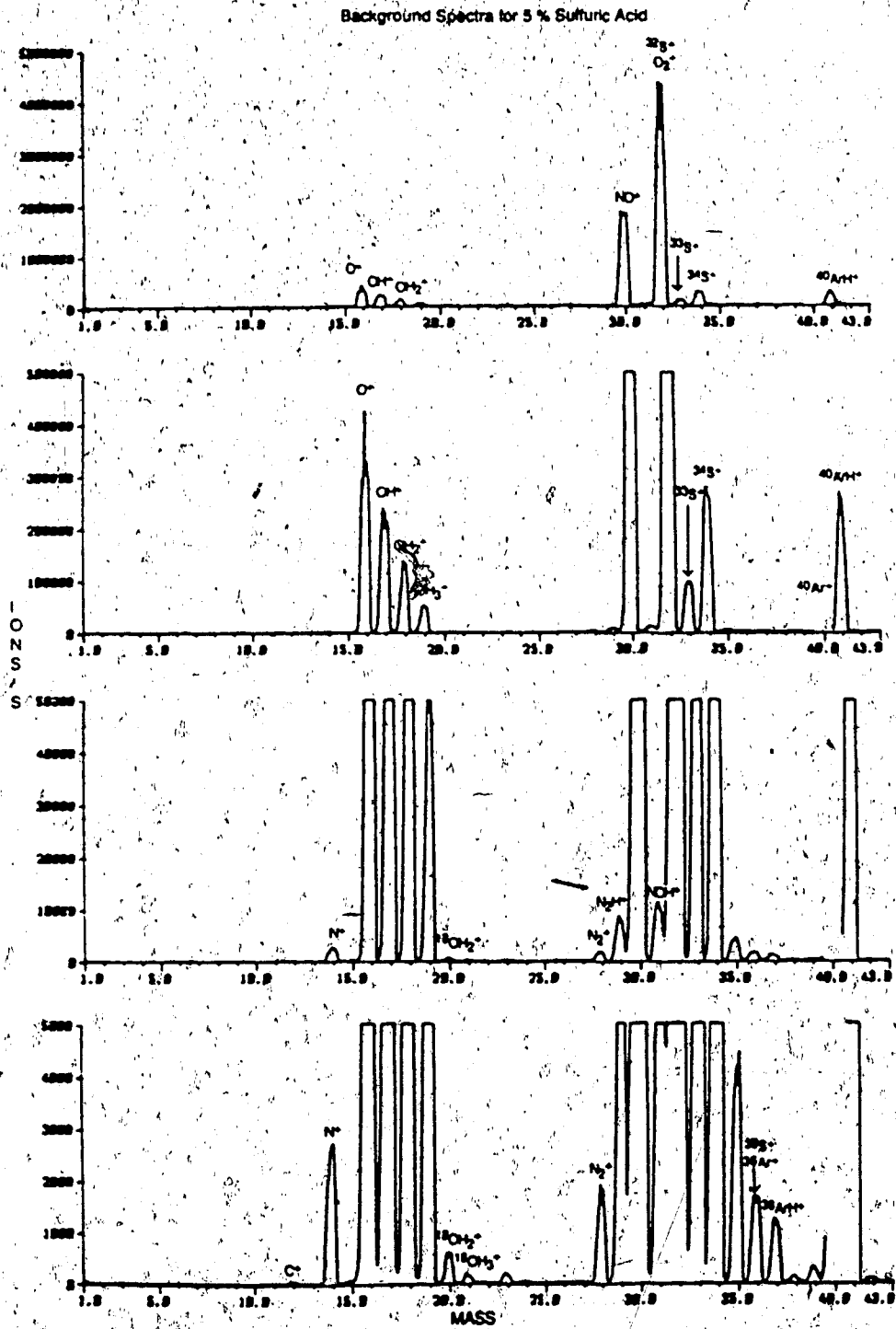


Figure 33: Background spectra for 5 % sulfuric acid for the mass range 1 to 43 amu

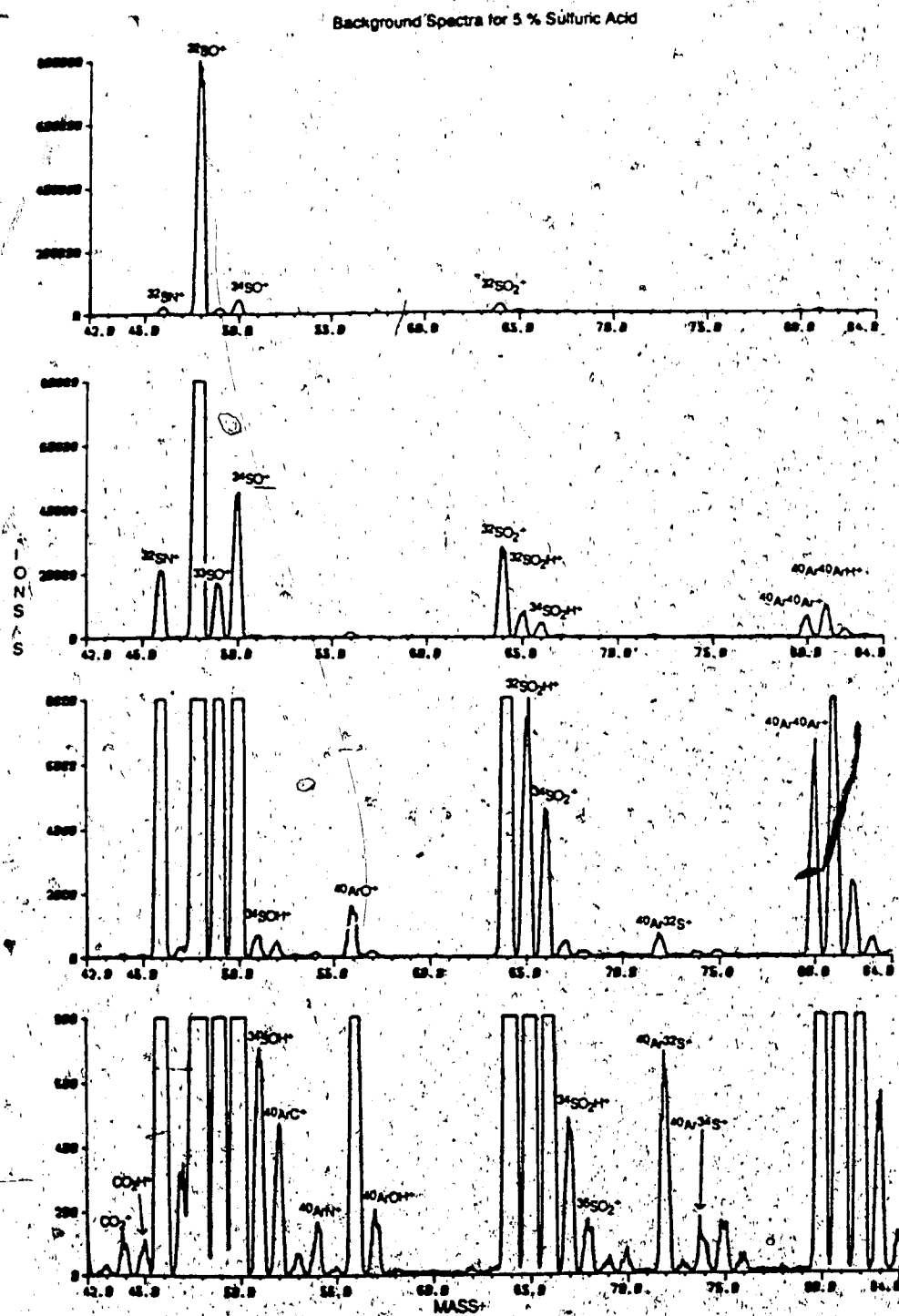


Figure 34. Background spectra for 5 % sulfuric acid for the mass range 42 to 84 amu.

argon species) is suppressed by more than a factor of five in the presence of 5 % sulfuric acid. The concentration of sulfur in the 5 % sulfuric acid is about 30,000 ppm. The new background peaks for sulfuric acid comprise  $S^+$ ,  $SO^+$ ,  $SN^+$ ,  $S_2^+$ ,  $SO_2^+$ , and  $ArS^+$ . Most of these species also form corresponding monohydrogenated species. The major sulfur species in 5 % sulfuric acid are presented in Table 7. The hydrogenated molecular species are not included in the table in order to obtain a more readable table. The  $S_2^+$  and  $SO_2^+$  have similar masses and isotopic ratios for the various isotopic combinations, therefore, it is difficult to definitely assign the correct species to each mass. However, as evident in nitric acid and hydrochloric acid, both species are most likely formed. The peaks in the spectra are labeled as  $SO_2^+$  but both species are possible, as has been listed in Table 7. The peaks occurring at masses 81 and 82 which were attributed to  $Ar_2H^+$  and  $Ar_2H_2^+$  have higher intensities than those observed in water and other acids. Peaks are also found at masses 83 and 84. These peaks are most likely due to the formation of  $SO_3^+$  and  $SO_3H^+$  species.

The most intense peak in 5 % sulfuric acid is  $^{32}S^+$  which coincides with the intense peak of  $O_2^+$ . The other less intense peak is  $SO^+$  at mass 48, which has an intensity of 800,000 ions/s. The sensitivity of this peak is about 27 ions/ppm of sulfur. Therefore, sulfur may be determined from its positive sulfur oxide ions at concentration levels of 1 ppm or more. However, since it is a molecular species, the amount which is formed is dependent on the mechanism of its formation as well as its original chemical form in solution. Thus, it may not be so suitable for quantitative analytical use.

From Table 7, it can be seen that numerous interference problems could occur for the determination of some first row transition elements and other elements like Zn, Ga and Ge, especially when the hydrogenated species

Table 7. Background species for 5 % sulfuric acid with corresponding element masses

| MASS | ELEMENTS                    | 5 % SULFURIC ACID  |
|------|-----------------------------|--|
| 32   | S(95.02)                    | $^{32}\text{S}$  |
| 33   | S(0.75)                     | $^{33}\text{S}$ , $^{32}\text{SH}$   |
| 34   | S(4.21)                     | $^{34}\text{S}$ , $^{33}\text{SH}$   |
| 35   | Cl(75.77)                   | $^{34}\text{SH}$   |
| 36   | Ar(0.34), S(0.02)           | $^{36}\text{S}$  |
| 37   | Cl(24.23)                   | $^{36}\text{SH}$   |
| 46   | Ti(7.99), Ca(0.003)         | $^{32}\text{S}^{14}\text{N}$   |
| 47   | Ti(7.32)                    | $^{32}\text{S}^{15}\text{N}$ , $^{33}\text{S}^{14}\text{N}$  |
| 48   | Ti(73.98), Ca(0.19)         | $^{33}\text{S}^{15}\text{N}$ , $^{34}\text{S}^{14}\text{N}$ , $^{32}\text{S}^{16}\text{O}$   |
| 49   | Ti(5.46)                    | $^{34}\text{S}^{15}\text{N}$ , $^{32}\text{S}^{17}\text{O}$ , $^{33}\text{S}^{16}\text{O}$   |
| 50   | Ti(5.25), Cr(4.35), V(0.24) | $^{36}\text{S}^{14}\text{N}$ , $^{32}\text{S}^{18}\text{O}$ , $^{33}\text{S}^{17}\text{O}$ , $^{34}\text{S}^{16}\text{O}$  |
| 51   | V(99.76)                    | $^{36}\text{S}^{15}\text{N}$ , $^{33}\text{S}^{18}\text{O}$ , $^{34}\text{S}^{17}\text{O}$   |
| 52   | Cr(83.76)                   | $^{34}\text{S}^{18}\text{O}$ , $^{36}\text{S}^{16}\text{O}$  |
| 53   | Cr(9.51)                    | $^{36}\text{S}^{17}\text{O}$   |
| 54   | Fe(5.82), Cr(2.38)          | $^{36}\text{S}^{18}\text{O}$   |
| 64   | Zn(48.89), Ni(1.16)         | $^{32}\text{S}^{16}\text{O}^{16}\text{O}$ , $^{32}\text{S}^{32}\text{S}$   |
| 65   | Cu(30.9)                    | $^{32}\text{S}^{16}\text{O}^{17}\text{O}$ , $^{33}\text{S}^{16}\text{O}^{16}\text{O}$ , $^{32}\text{S}^{33}\text{S}$   |
| 66   | Zn(27.81)                   | $^{32}\text{S}^{16}\text{O}^{18}\text{O}$ , $^{32}\text{S}^{17}\text{O}^{17}\text{O}$ , $^{33}\text{S}^{16}\text{O}^{17}\text{O}$ , $^{32}\text{S}^{34}\text{S}$ , $^{33}\text{S}^{33}\text{S}$ ,<br>$^{34}\text{S}^{16}\text{O}^{16}\text{O}$   |
| 67   | Zn(4.11)                    | $^{32}\text{S}^{17}\text{O}^{18}\text{O}$ , $^{33}\text{S}^{16}\text{O}^{18}\text{O}$ , $^{33}\text{S}^{17}\text{O}^{17}\text{O}$ , $^{33}\text{S}^{34}\text{S}$ ,<br>$^{34}\text{S}^{16}\text{O}^{17}\text{O}$  |
| 68   | Zn(18.57)                   | $^{32}\text{S}^{18}\text{O}^{18}\text{O}$ , $^{33}\text{S}^{17}\text{O}^{18}\text{O}$ , $^{34}\text{S}^{16}\text{O}^{18}\text{O}$ , $^{32}\text{S}^{36}\text{S}$ ,<br>$^{34}\text{S}^{17}\text{O}^{17}\text{O}$ , $^{36}\text{S}^{16}\text{O}^{16}\text{O}$ , $^{34}\text{S}^{34}\text{S}$ , $^{36}\text{Ar}^{32}\text{S}$ |
| 69   | Ga(60.16)                   | $^{33}\text{S}^{18}\text{O}^{18}\text{O}$ , $^{34}\text{S}^{17}\text{O}^{18}\text{O}$ , $^{36}\text{S}^{16}\text{O}^{17}\text{O}$ , $^{33}\text{S}^{36}\text{S}$ , $^{36}\text{Ar}^{33}\text{S}$   |
| 70   | Ge(20.51), Zn(0.62)         | $^{34}\text{S}^{18}\text{O}^{18}\text{O}$ , $^{36}\text{S}^{16}\text{O}^{18}\text{O}$ , $^{36}\text{S}^{17}\text{O}^{17}\text{O}$ , $^{34}\text{S}^{36}\text{S}$ , $^{36}\text{Ar}^{34}\text{S}$ , $^{38}\text{Ar}^{32}\text{S}$   |
| 71   | Ga(39.84)                   | $^{36}\text{S}^{17}\text{O}^{18}\text{O}$ , $^{38}\text{Ar}^{33}\text{S}$  |
| 72   | Ge(27.4)                    | $^{36}\text{S}^{18}\text{O}^{18}\text{O}$ , $^{36}\text{S}^{36}\text{S}$ , $^{36}\text{Ar}^{36}\text{S}$ ,<br>$^{38}\text{Ar}^{34}\text{S}$ , $^{40}\text{Ar}^{32}\text{S}$  |

Table 7. continued

| <u>MASS</u> | <u>ELEMENTS</u>     | <u>5 % SULFURIC ACID</u>  |
|-------------|---------------------|---|
| 73          | Ge(7.76)            |   |
| 74          | Ge(36.56), Se(0.87) |   |
| 75          | As(100)             |   |
| 76          | Ge(7.77), Se(9.02)  |   |
| 80          | Se(49.82), Kr(2.27) | $^{32}\text{S}^{16}\text{O}^{16}\text{O}$   |
| 81          | Br(49.46)           | $^{33}\text{S}^{16}\text{O}^{16}\text{O}$ , $^{32}\text{S}^{16}\text{O}^{16}\text{O}^{16}\text{OH}$ |
| 82          | Kr(11.56), Se(9.19) | $^{34}\text{S}^{16}\text{O}^{16}\text{O}$ , $^{33}\text{S}^{16}\text{O}^{16}\text{O}^{16}\text{OH}$ |
| 83          | Kr(11.53)           | $^{34}\text{S}^{16}\text{O}^{16}\text{O}^{16}\text{OH}$   |
| 84          | Kr(56.9), Sr(0.56)  | $^{36}\text{S}^{16}\text{O}^{16}\text{O}$   |

 $^{40}\text{Ar}^{33}\text{S}$   
 $^{38}\text{Ar}^{36}\text{S}$ ,  $^{40}\text{Ar}^{34}\text{S}$ 
 $^{40}\text{Ar}^{36}\text{S}$



are also taken into consideration. The interference of  $\text{SO}_2^+/\text{S}_2^+$  species on zinc can be a major problem since the  $^{32}\text{S}^{16}\text{O}^{16}\text{O}^+ / ^{32}\text{S}^{32}\text{S}^+$  peak is quite intense. It affects zinc at its most abundant isotope, at mass 64, and all other minor isotopes of zinc are also affected by their isotopic combinations. Other major interferences include  $^{32}\text{S}^{16}\text{O}^+$  on  $^{48}\text{Ti}^+$ ,  $^{36}\text{S}^{16}\text{O}^+$  on  $^{52}\text{Cr}^+$  and  $^{40}\text{Ar}^{34}\text{S}^+$  on  $^{74}\text{Ge}^+$ .

#### F. 5 % Phosphoric Acid

Background spectra for 5 % phosphoric acid are shown in Figures 35 and 36. The background spectra for phosphoric acid are different from previous spectra in that they were acquired using the low resolution mode (peak width is 1.0 amu at 10% above baseline) and the mass ranges are 1 to 42 amu and 42 to 82 amu. Since phosphorus is mono-isotopic, the background spectra of phosphoric acid are considerably simpler. The background species observed for 5 % phosphoric acid are presented in Table 8. Comparing the four common acids that were studied, phosphoric acid is next to nitric acid in having simple background spectrum. The presence of the peak at mass 45 which is due to  $^{31}\text{P}^{14}\text{N}^+$  interferes with the determination of scandium which is mono-isotopic and  $^{31}\text{P}^{16}\text{OH}^+$  at mass 48 interferes with the determination of  $^{48}\text{Cr}^+$ . Peaks 63, 64 and 65 are most likely due to  $\text{PO}_2^+$  species and will interfere with the determinations of Cu and Zn at sub-ppb levels. However, their peak intensities are different from the expected ratios, therefore, it is possible that trace amounts of copper and zinc are present in this batch of phosphoric acid.

#### G. Conclusion

A summary of the major background species for distilled water/nitric acid, hydrochloric acid, sulfuric acid and phosphoric acid is presented in Table

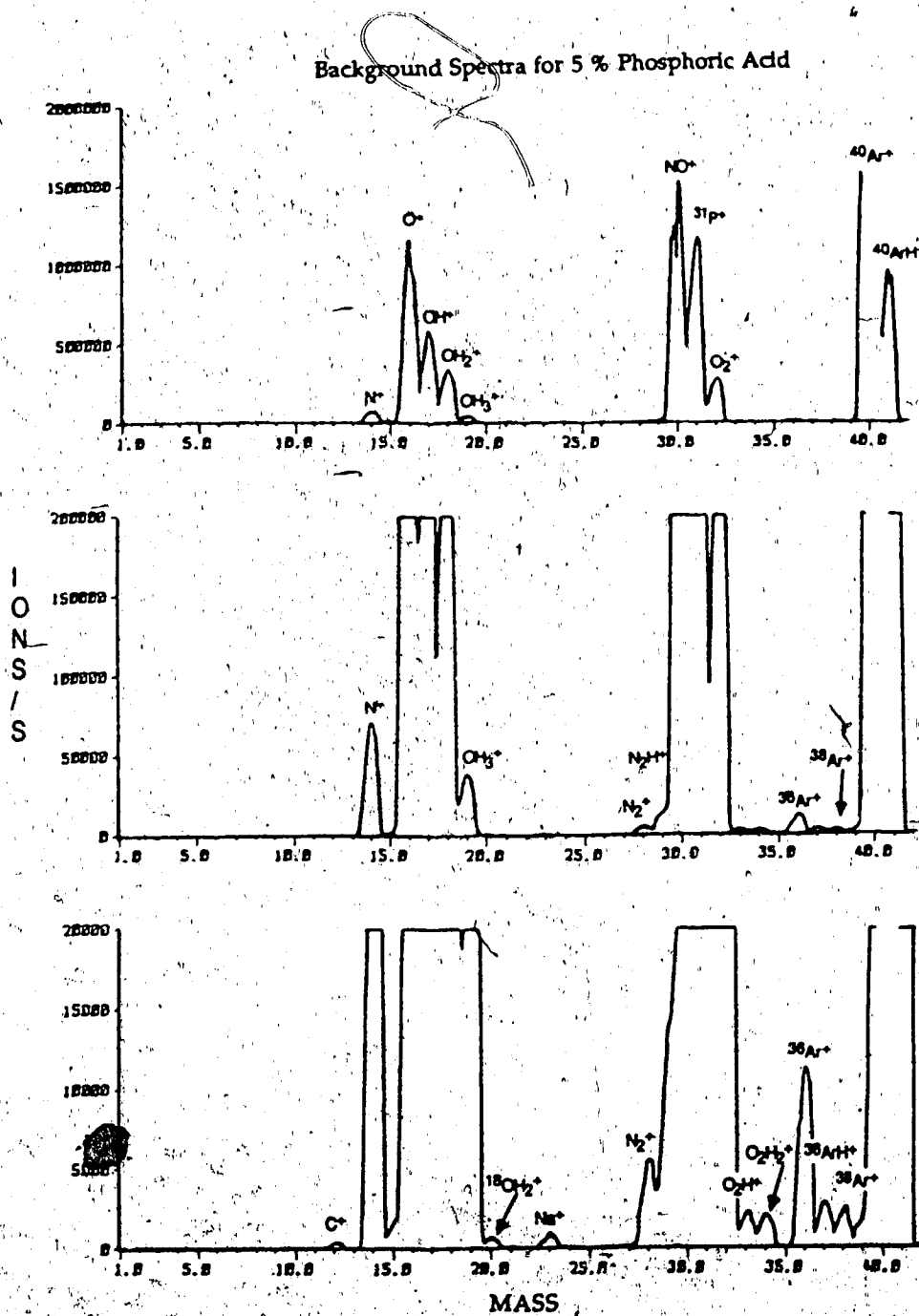


Figure 35. Background spectra for 5 % phosphoric acid for the mass range 1 to 42 amu

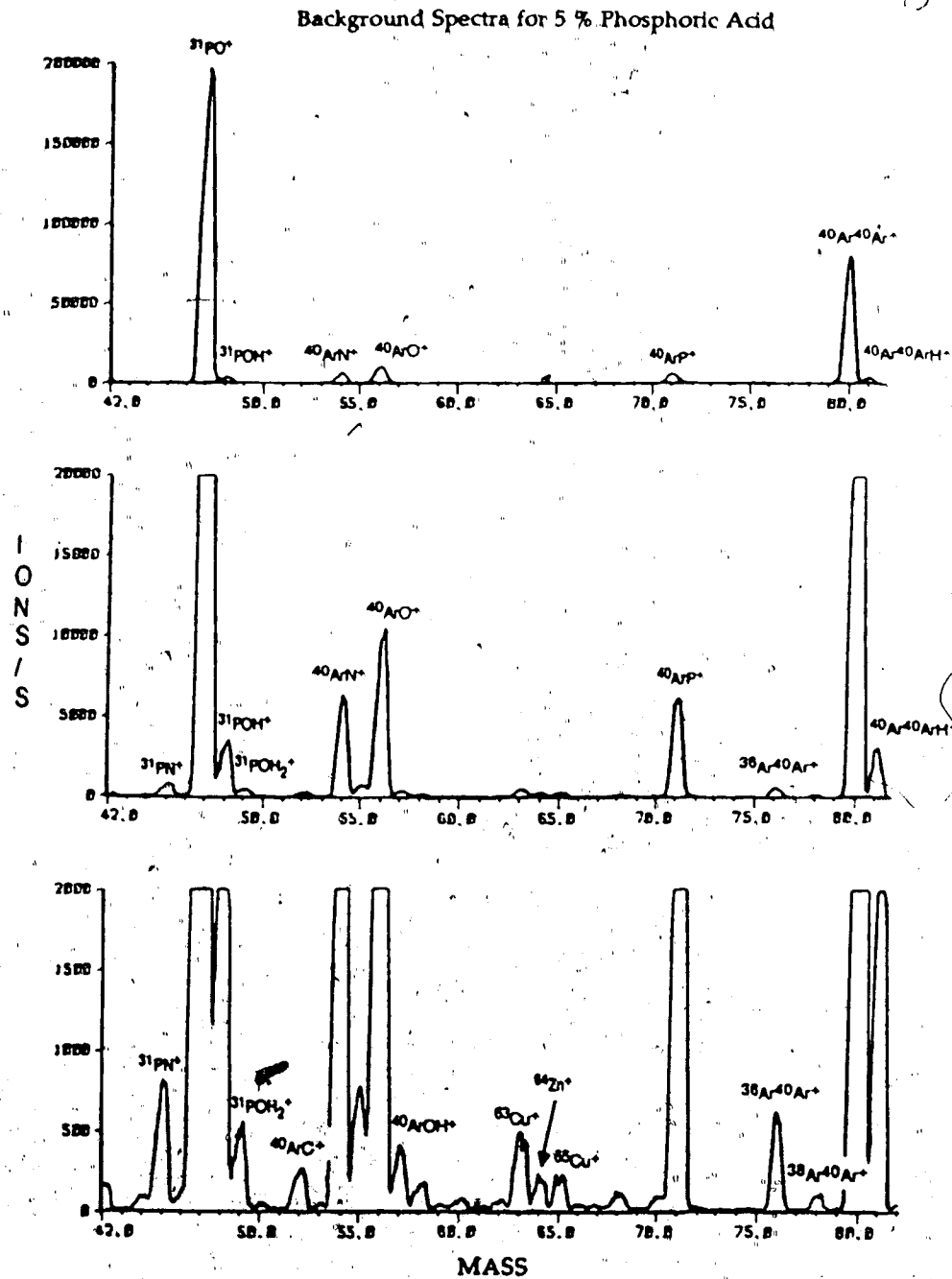


Figure 36. Background spectra for 5 % phosphoric acid for the mass range 42 to 82 amu

Table 8. Background species for 5 % phosphoric acid with corresponding element masses

| <u>MASS</u> | <u>ELEMENTS</u>             | <u>5 % PHOSPHORIC ACID</u>                                   |
|-------------|-----------------------------|--|
| 31          | P(100)                      | $^{31}\text{P}$  |
| 32          | S(95.02)                    | $^{31}\text{P}\text{H}$                                      |
| 45          | Sc(100)                     | $^{31}\text{P}\text{N}$                                      |
| 46          | Ti(7.99), Ca(0.003)         |  |
| 47          | Ti(7.32)                    | $^{31}\text{P}^{16}\text{O}$                                 |
| 48          | Ti(73.98), Ca(0.19)         | $^{31}\text{P}^{17}\text{O}$ , $^{31}\text{P}^{16}\text{OH}$ |
| 49          | Ti(5.46)                    | $^{31}\text{P}^{18}\text{O}$ , $^{31}\text{P}^{17}\text{OH}$ |
| 50          | Ti(5.25), Cr(4.35), V(0.24) | $^{31}\text{P}^{18}\text{OH}$                                |
| 63          | Cu(69.1)                    | $^{31}\text{P}^{16}\text{O}^{16}\text{O}$                    |
| 64          | Zn(48.89), Ni(1.16)         | $^{31}\text{P}^{16}\text{O}^{17}\text{O}$                    |
| 65          | Cu(30.9)                    | $^{31}\text{P}^{16}\text{O}^{18}\text{O}$                    |
| 66          | Zn(27.81)                   |  |
| 67          | Zn(4.11)                    | $^{36}\text{Ar}^{31}\text{P}$                                |
| 68          | Zn(18.57)                   |  |
| 69          | Ga(60.16)                   | $^{38}\text{Ar}^{31}\text{P}$                                |
| 70          | Ge(20.51), Zn(0.62)         |  |
| 71          | Ga(39.84)                   | $^{40}\text{Ar}^{31}\text{P}$                                |

9. It is obvious that great care has to be taken in choosing appropriate solution matrices in the determination of elements with masses less than mass 80. In many cases, sample preparation procedures for ICP-MS will require completely new approaches from that used in ICP-AES, that is, "zero base design" of the entire sample preparation procedure may be necessary.

It is found that on closer scrutiny, the spectral background is quite complex, especially for sulfuric acid and hydrochloric acid, when all the isotopic species are taken into account. The minor isotopic species of the background cannot be ignored because these species will interfere with elemental analysis at sub-ppb levels.

Nitric acid has the least complex background spectrum of the acids studied and fortunately, most background species are only found below mass 82. Finally, although phosphoric acid is not commonly used in solution preparation, it should perhaps be considered as the next acid of choice after nitric acid since it has a background spectrum that is considerably less complex than that of hydrochloric acid and sulfuric acid.

Table 9. Summary of major background species for water/5 % nitric, 5 % sulfuric acid, 5 % hydrochloric acid and 5 % phosphoric acid

| MASS | ELEMENTS          | H <sub>2</sub> O (5% HNO <sub>3</sub> )                            | 5% H <sub>2</sub> SO <sub>4</sub> | 5% HCL | 5% H <sub>3</sub> PO <sub>4</sub> |
|------|-------------------|--|-----------------------------------|--------|-----------------------------------|
| 1    | H(99.985)         | <sup>1</sup> H   |                                   |        |                                   |
| 2    | H(0.015)          | <sup>2</sup> H   |                                   |        |                                   |
| 3    |                   |  |                                   |        |                                   |
| 4    | He(100)           |  |                                   |        |                                   |
| 5    |                   |  |                                   |        |                                   |
| 6    | Li(7.5)           |  |                                   |        |                                   |
| 7    | Li(92.5)          |  |                                   |        |                                   |
| 8    |                   |  |                                   |        |                                   |
| 9    | Be(100)           |  |                                   |        |                                   |
| 10   | B(19.91)          |  |                                   |        |                                   |
| 11   | B(80.09)          |  |                                   |        |                                   |
| 12   | C(98.89)          | <sup>12</sup> C  |                                   |        |                                   |
| 13   | C(1.11)           | <sup>13</sup> C  |                                   |        |                                   |
| 14   | N(99.63)          | <sup>14</sup> N  |                                   |        |                                   |
| 15   | N(0.37)           | <sup>15</sup> N  |                                   |        |                                   |
| 16   | O(99.76)          | <sup>16</sup> O  |                                   |        |                                   |
| 17   | O(0.04)           | <sup>16</sup> OH   |                                   |        |                                   |
| 18   | O(0.20)           | <sup>16</sup> OH <sub>2</sub>                                      |                                   |        |                                   |
| 19   | F(100)            | <sup>16</sup> OH <sub>3</sub>                                      |                                   |        |                                   |
| 20   | Ne(90.92)         | <sup>18</sup> OH <sub>2</sub>                                      |                                   |        |                                   |
| 21   | Ne(0.26)          | <sup>18</sup> OH <sub>3</sub>                                      |                                   |        |                                   |
| 22   | Ne(8.82)          |  |                                   |        |                                   |
| 23   | Na(100)           |  |                                   |        |                                   |
| 24   | Mg(78.8)          |  |                                   |        |                                   |
| 25   | Mg(10.15)         |  |                                   |        |                                   |
| 26   | Mg(11.05)         |  |                                   |        |                                   |
| 27   | Al(100)           |  |                                   |        |                                   |
| 28   | Si(92.21)         | <sup>14</sup> N <sup>14</sup> N, <sup>12</sup> C <sup>16</sup> O   |                                   |        |                                   |
| 29   | Si(4.7)           | <sup>14</sup> N <sup>14</sup> NH, <sup>12</sup> C <sup>16</sup> OH |                                   |        |                                   |
| 30   | Si(3.09)          | <sup>14</sup> N <sup>16</sup> O                                    |                                   |        |                                   |
| 31   | P(100)            | <sup>14</sup> N <sup>16</sup> OH                                   |                                   |        | <sup>31</sup> P                   |
| 32   | S(93.02)          | <sup>16</sup> O <sup>16</sup> O                                    | <sup>32</sup> S                   |        |                                   |
| 33   | S(0.75)           | <sup>16</sup> O <sup>16</sup> OH                                   | <sup>33</sup> S, <sup>32</sup> SH |        |                                   |
| 34   | S(4.21)           | <sup>16</sup> O <sup>18</sup> O                                    | <sup>34</sup> S, <sup>33</sup> SH |        |                                   |
| 35   | Cl(73.77)         | <sup>16</sup> O <sup>18</sup> OH                                   | <sup>34</sup> SH                  |        | <sup>35</sup> Cl                  |
| 36   | Ar(0.34), S(0.02) | <sup>36</sup> Ar   | <sup>36</sup> S                   |        | <sup>35</sup> ClH                 |
| 37   | Cl(24.23)         | <sup>36</sup> ArH  | <sup>36</sup> SH                  |        | <sup>37</sup> Cl                  |
| 38   | Ar(0.06)          | <sup>38</sup> Ar   |                                   |        | <sup>37</sup> ClH                 |
| 39   | K(93.08)          | <sup>38</sup> ArH  |                                   |        |                                   |

Table 9. Continued

| MASS ELEMENTS                   | H <sub>2</sub> O (5% HNO <sub>3</sub> ) 5% H <sub>2</sub> SO <sub>4</sub> | 5% HCl   | 5% H <sub>3</sub> PO <sub>4</sub>                                  |
|---------------------------------|---|--|--|
| 40 Ar(99.6), Ca(0.697), K(0.01) | <sup>40</sup> Ar  |  |  |
| 41 K(6.91)                      | <sup>40</sup> ArH   |  |  |
| 42 Ca(0.64)                     | <sup>40</sup> ArH <sub>2</sub>  |  |  |
| 43 O(0.14)                      |   |  |  |
| 44 Ca(2.06)                     | <sup>12</sup> C <sup>16</sup> O <sup>16</sup> O                           |  |  |
| 45 Sc(100)                      | <sup>12</sup> C <sup>16</sup> O <sup>16</sup> OH                          |  |  |
| 46 Ti(7.99), Ca(0.003)          | <sup>14</sup> N <sup>16</sup> O <sup>16</sup> O                           | <sup>32</sup> S <sup>14</sup> N  | <sup>31</sup> P <sup>14</sup> N                                    |
| 47 Ti(7.32)                     |   | <sup>33</sup> S <sup>14</sup> N  |  |
| 48 Ti(73.98), Ca(0.19)          |   | <sup>34</sup> S <sup>14</sup> N, <sup>32</sup> S <sup>16</sup> O                 | <sup>31</sup> P <sup>16</sup> O                                    |
| 49 Ti(5.46)                     |   | <sup>33</sup> S <sup>16</sup> O  | <sup>31</sup> P <sup>16</sup> OH                                   |
| 50 Ti(5.25), Cr(4.35), V(0.24)  | <sup>36</sup> Ar <sup>14</sup> N  | <sup>34</sup> S <sup>16</sup> O  |  |
| 51 V(99.76)                     |   |  |  |
| 52 Cr(83.76)                    | <sup>40</sup> Ar <sup>12</sup> C, <sup>36</sup> Ar <sup>16</sup> O        | <sup>36</sup> S <sup>16</sup> O  | <sup>37</sup> Cl <sup>14</sup> N, <sup>35</sup> Cl <sup>16</sup> O |
| 53 Cr(9.51)                     |   |  | <sup>35</sup> Cl <sup>16</sup> OH                                  |
| 54 Fe(5.82), Cr(2.38)           | <sup>40</sup> Ar <sup>14</sup> N  |  | <sup>37</sup> Cl <sup>16</sup> O                                   |
| 55 Mn(100)                      | <sup>40</sup> Ar <sup>14</sup> NH   |  | <sup>37</sup> Cl <sup>16</sup> OH                                  |
| 56 Fe(91.66)                    | <sup>40</sup> Ar <sup>16</sup> O  |  |  |
| 57 Fe(2.19)                     | <sup>40</sup> Ar <sup>16</sup> OH   |  |  |
| 58 Ni(67.77), Fe(0.33)          |   |  |  |
| 59 Co(100)                      |   |  |  |
| 60 Ni(26.16)                    |   |  |  |
| 61 Ni(1.25)                     |   |  |  |
| 62 Ni(3.66)                     |   |  |  |
| 63 Cu(69.1)                     |   |  |  |
| 64 Zn(68.89), Ni(1.16)          |   | <sup>32</sup> S <sup>16</sup> O <sup>16</sup> O, <sup>32</sup> S <sup>32</sup> S |  |
| 65 Cu(30.9)                     |   | <sup>33</sup> S <sup>16</sup> O <sup>16</sup> O, <sup>32</sup> S <sup>33</sup> S |  |
| 66 Zn(27.81)                    |   | <sup>34</sup> S <sup>16</sup> O <sup>16</sup> O, <sup>32</sup> S <sup>34</sup> S |  |
| 67 Zn(4.11)                     |   |  | <sup>35</sup> Cl <sup>16</sup> O <sup>16</sup> O                   |
| 68 Zn(18.57)                    | <sup>40</sup> Ar <sup>14</sup> N <sup>14</sup> N                          | <sup>36</sup> S <sup>16</sup> O <sup>16</sup> O, <sup>33</sup> S <sup>36</sup> S |  |
| 69 Ga(60.16)                    |   |  | <sup>37</sup> Cl <sup>16</sup> O <sup>16</sup> O                   |
| 70 Ge(20.51), Zn(0.62)          | <sup>40</sup> Ar <sup>14</sup> N <sup>16</sup> O                          |  |  |
| 71 Ga(39.84)                    |   |  | <sup>36</sup> Ar <sup>35</sup> Cl                                  |
| 72 Ge(27.4)                     | <sup>36</sup> Ar <sup>36</sup> Ar   | <sup>40</sup> Ar <sup>32</sup> S   | <sup>40</sup> Ar <sup>31</sup> P                                   |
| 73 Ge(7.26)                     |   | <sup>40</sup> Ar <sup>33</sup> S   | <sup>36</sup> Ar <sup>37</sup> Cl                                  |
| 74 Ge(34.56), Se(0.87)          | <sup>36</sup> Ar <sup>38</sup> Ar   | <sup>40</sup> Ar <sup>34</sup> S   |  |
| 75 As(100)                      |   |  | <sup>40</sup> Ar <sup>35</sup> Cl                                  |
| 76 Ge(7.77), Se(9.02)           | <sup>36</sup> Ar <sup>40</sup> Ar   | <sup>40</sup> Ar <sup>36</sup> S   |  |
| 77 Se(7.58)                     | <sup>36</sup> Ar <sup>40</sup> ArH  |  | <sup>40</sup> Ar <sup>37</sup> Cl                                  |
| 78 Se(23.52), Kr(0.35)          | <sup>38</sup> Ar <sup>40</sup> Ar   |  |  |
| 79 Br(50.54)                    | <sup>38</sup> Ar <sup>40</sup> ArH  |  |  |
| 80 Se(69.82), Kr(2.27)          | <sup>40</sup> Ar <sup>40</sup> Ar   | <sup>32</sup> S <sup>16</sup> O <sup>16</sup> O <sup>16</sup> O                  |  |
| 81 Br(69.46)                    | <sup>40</sup> Ar <sup>40</sup> ArH  | <sup>32</sup> S <sup>16</sup> O <sup>16</sup> O <sup>16</sup> OH                 |  |
| 82 Kr(11.56), Se(9.19)          |   | <sup>34</sup> S <sup>16</sup> O <sup>16</sup> O <sup>16</sup> O                  |  |
| 83 Kr(11.55)                    |   | <sup>34</sup> S <sup>16</sup> O <sup>16</sup> O <sup>16</sup> OH                 |  |
| 84 Kr(34.9), Sr(0.56)           |   | <sup>36</sup> S <sup>16</sup> O <sup>16</sup> O <sup>16</sup> O                  |  |

## CHAPTER 4

### QUANTITATIVE PERFORMANCE IN ICP-MS

#### A. Introduction

In this chapter the general quantitative performance of ICP-MS is investigated. It is well-known that the ICP is an excellent source for quantitative elemental analysis by atomic emission spectroscopy. As stated in chapter 1, it has a wide linear dynamic range, low detection limits and is relatively free from matrix interferences. In addition, samples in different physical forms can be directly analysed. In ICP-MS, all these advantages should also be realized and because of the additional sensitivity associated with mass-detection, the detection limits should be lower.

Applications of ICP-MS for the determination of minor and trace elements in a broad range of samples have been carried out by various authors [47-53]. In this chapter only a preliminary study of the general quantitative characteristics of the ICP-MS is carried out including analytical calibration curves and detection limits of a wide range of elements in single and multi-element solutions.

#### B. Experimental

All the solutions used for establishing analytical curves were freshly prepared in distilled/deionized water either from their respective salts or by appropriate dilution of the 1000 ppm commercial solution standards. In most cases the calibration solutions contain more than one element. Since the data for the calibration curves were acquired from many different experiments performed over a long period of time, the experimental conditions were not the same in each case. The plasma operating parameters normally used were;



rf power, 1.2-1.3 kW; plasma gas flowrate, 10-11 l/min and auxiliary gas flowrate, 1.4-2.0 l/min. For all the experiments the nebulizer flowrate was adjusted to obtain the maximum ion count for the analyte of interest unless otherwise stated and it varied between 1.00 to 1.15 l/min depending on the exact settings of other plasma operating conditions (see chapter 2). The plasma sampling depth was about 15-17 mm from the load coil.

The mass spectrometer ion optics were optimized to give a maximum ion count for Cu (voltages for lens A, B, C and ring lens were -4.0 V, +5.4 V, -6.0 V and -15.0 V respectively). Data were acquired with the mass spectrometer run in the low resolution mode and peak hopping mode. For each mass, seven to ten data points were determined per peak. A measurement time of 0.5 or 1.0 s per data point was used. All signals were an average of six repetitive measurements at each mass.

In determining the detection limits, the background noise was measured using a distilled/deionized water blank. The measurement time was 5 s per peak (0.5 s per data point and 10 data points per peak) and the standard deviation for the background was calculated from 10 repetitive measurements at the mass of interest. A one ppm analyte solution was used to obtain the ion signal at the mass of interest. An average of 6 measurements was obtained.

In order to assess the nature of the noise in the system and how it might affect the quantitative measurements, the variation of signal-to-noise ratio with signal measurement time was investigated for Cu. The Cu ion signal measured was the average peak area ion signal. Ten data points were sequentially measured around mass 63 (from 62.5 amu to 63.4 amu at 0.1 amu increments) and the ion signals for these ten data points were summed and divided by 10 to give an average peak area ion signal for Cu. All standard

deviations and signal-to-noise ratios were estimated from 10 replicate scans of each mass. The measurement time per peak was varied from 0.1 s to 80 s. The data for signal-to noise ratio and standard deviation versus measurement time are shown in Figure 37. It can be seen that signal-to-ratio is independent of the measurement time and the log-log plot for the standard deviation of Cu signal has unity slope. These data are consistent with those obtained by Belchamber and Horlick [74] for ICP-AES for which the limiting noise was analyte flicker noise.

The dependence of standard deviation and signal-to-noise ratio on ion signal over a wide dynamic concentration range are shown for V in Figure 38. At low analyte ion signal, the standard deviation is independent of the ion signal and the signal-to-noise ratio increases in direct proportion to the ion signal. This indicates that the limiting noise in this region is background shot noise. At high ion signal levels (above 10,000 ions/s), the slope of the standard deviation plot approaches unity and the signal-to-noise ratio of vanadium become independent of the signal level. This indicates that the predominating noise of the system is analyte flicker noise when ion signal is high. Again, these results are in agreement with those obtained by Salin and Horlick [75].

### C. Detection Limits

Detection limits are dependent on background noise and the sensitivity of the instrument for a certain element. The background noise is determined from a distilled/deionized water blank. Nonstructured background ion signal is normally less than 10 ions/s and is fairly uniform across the entire mass range. The ion signal of a 1 ppm solution is typically about  $10^5$ - $10^6$  counts/s. Detection limit is defined as the concentration of the element which gives

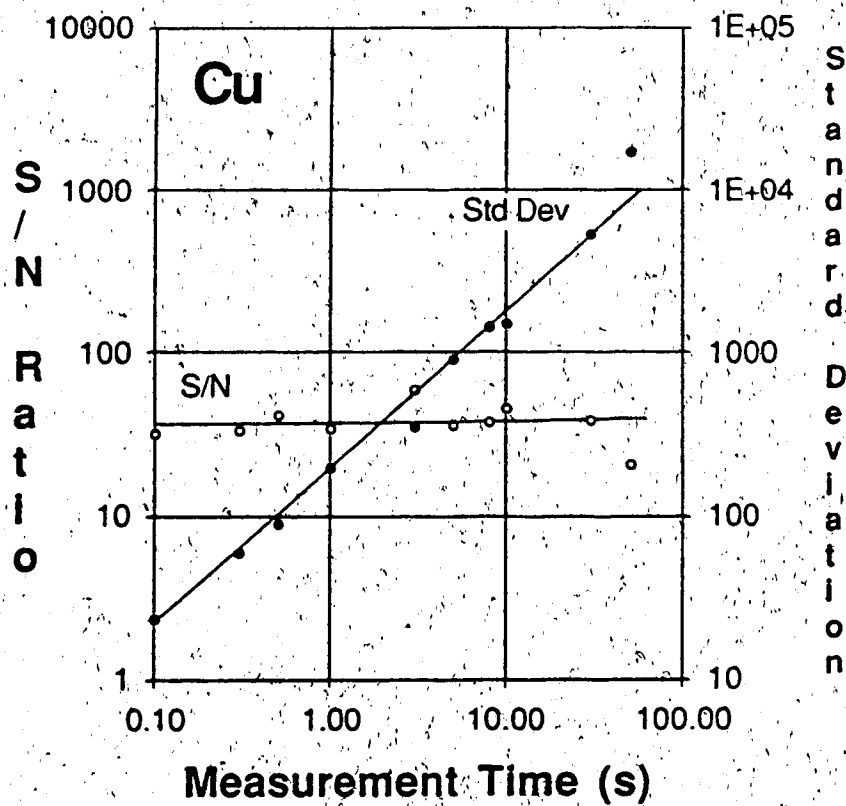


Figure 37. Signal-to-noise ratio and standard deviation vs measurement time for Cu.

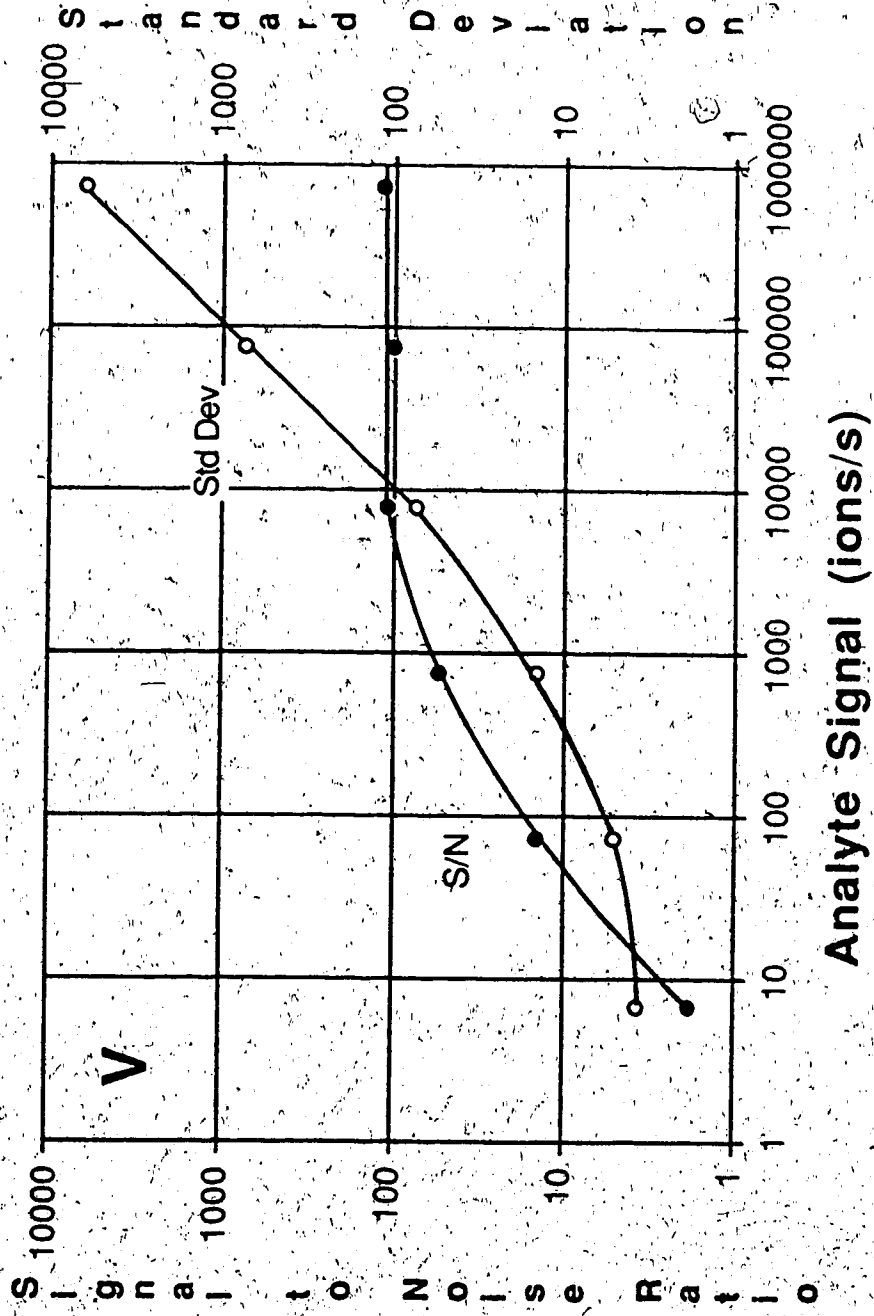


Figure 38. Signal-to-noise ratio and standard deviation vs ion signal intensity for V

rise to an ion signal equivalent to 3 times the standard deviation ( $3\sigma$ ) of the background signal.

Detection limits for the first row transition elements and the alkali metals are shown in Table 10. It can be seen from these data that the detection limits for all these elements are excellent and in the range of tens of parts per trillion (pg/ml) except for the elements Fe and K. At mass 56, an intense background peak due to  $^{40}\text{Ar}^{16}\text{O}^+$  is present (see Chapter 3). Since the noise level associated with this intense peak is correspondingly larger, the detection limit of Fe is degraded. Similarly, the detection limit of an element with its mass adjacent to a large background peak is poorer because of the overlap from the wing of the background peak. This occurred with K at mass 39 which is adjacent to the huge  $^{40}\text{Ar}^+$  peak. Overlap from the  $^{40}\text{Ar}^+$  peak can be minimized by increasing the resolution of the instrument but this will also decrease the sensitivity for potassium. For both Fe and K, using an alternative minor isotope does not improve their detection limits due to the relatively low abundance of the second most abundant isotopes. Also, all the minor isotopes of Fe and K have interferences from background peaks. Therefore, detection limits of less than 0.1 ppb are only achievable provided that the mass of interest has no spectral interferences.

When acquiring the detection limit data for the first row elements, the plasma operating parameters were optimized to obtain maximum ion counts for all the first row elements. For the alkali metals however, compromise plasma operating conditions were selected (see Table 10). The detection limits for a broad range of elements determined under a single set of compromise plasma operating conditions are listed in Table 11. Under these operating conditions the ion signals for the light mass elements Li and Na are low, hence their detection limits are poorer. The detection limits for all other

Table 10. Detection limits for the first row elements and the alkali metals

| <u>First row transition elements</u> *1 | <u>Detection Limits (ng/ml)</u> |
|---|---------------------------------|
| Ti                                      | 0.05                            |
| V                                       | 0.01                            |
| Cr                                      | 0.06                            |
| Mn                                      | 0.07                            |
| Fe                                      | 2.8                             |
| Co                                      | 0.01                            |
| Ni                                      | 0.06                            |
| Cu                                      | 0.02                            |

| <u>Alkali metals</u> *2 |      |
|-------------------------|------|
| Li                      | 0.04 |
| Na                      | 0.08 |
| K                       | 0.2  |
| Rb                      | 0.04 |
| Cs                      | 0.04 |

Plasma operating conditions; \*1 plasma power, 1.4 kW; nebulizer flowrate, 1.12 l/min

\*2 plasma power, 1.1 kW; nebulizer flowrate, 1.26 l/min

Table 11. Detection limits at compromise plasma operating conditions (power, 1.2 kW and nebulizer flowrate, 1.1 l/min)

| <u>Elements</u>  | <u>Detection Limits (ng/ml)</u> |
|------------------|---------------------------------|
| Li               | 0.13                            |
| Na               | 0.33                            |
| Rb               | 0.003                           |
| Cs               | 0.07                            |
| Cu               | 0.04                            |
| Rh               | 0.03                            |
| Ce               | 0.008                           |
| Ir               | 0.04                            |
| Pb               | 0.03                            |
| Th               | 0.04                            |
| V 50 (0.24%)*    | 1.7                             |
| V 51 (99.76%)*   | 0.02                            |
| Cd 106 (1.22%)*  | 2.9                             |
| Cd 113 (12.26%)* | 0.25                            |
| Cd 114 (28.86%)* | 0.16                            |

\* Values in parenthesis are the natural isotopic abundances

elements are excellent. The detection limits for vanadium and cadmium measured at their minor isotopes are shown in Table 11. As expected the detection limits vary according to the isotopic abundances of V and Cd.

#### D. Analytical Calibration Curves

##### D. 1 Linearity and Dynamic Range

Typical concentration calibration curves are shown in Figure 39 for vanadium. In this figure the calibration plots for the major vanadium isotope at mass 51 (99.7 %) and its minor isotope at mass 50 (0.3 %) are illustrated. It can be seen that the log-log plots are linear with unity slopes for 4 to 5 orders of magnitude. The maximum ion signal that can be measured at the detector is limited to  $3.2 \times 10^6$  ions/s. This is because the lifetime of the CEM is considerably shortened by excessive ion bombardment. Therefore, circuitry is built into the instrument whereby the lens voltages are altered to lower the ion count reaching the CEM if the average ion signal exceeds  $3.2 \times 10^6$  ions/s, thus preventing excessive wear of the CEM at any one time. Consequently, the upper concentration range of the calibration curve for V 51 is limited by this feature. The use of the minor isotope of vanadium at mass 50 extends linearity at the upper concentration range by an order of magnitude; a negative deviation from linearity beyond 10 ppm is observed. At concentrations less than 5 ppb, the ion signal for V 50 is very small and not distinguishable from the background noise. These data show that the major isotope of an element should be used when determining trace concentration levels whereas a minor isotope can be chosen to extend measurements to higher concentration levels.

##### D. 2 Analytical Curves with Internal Standard



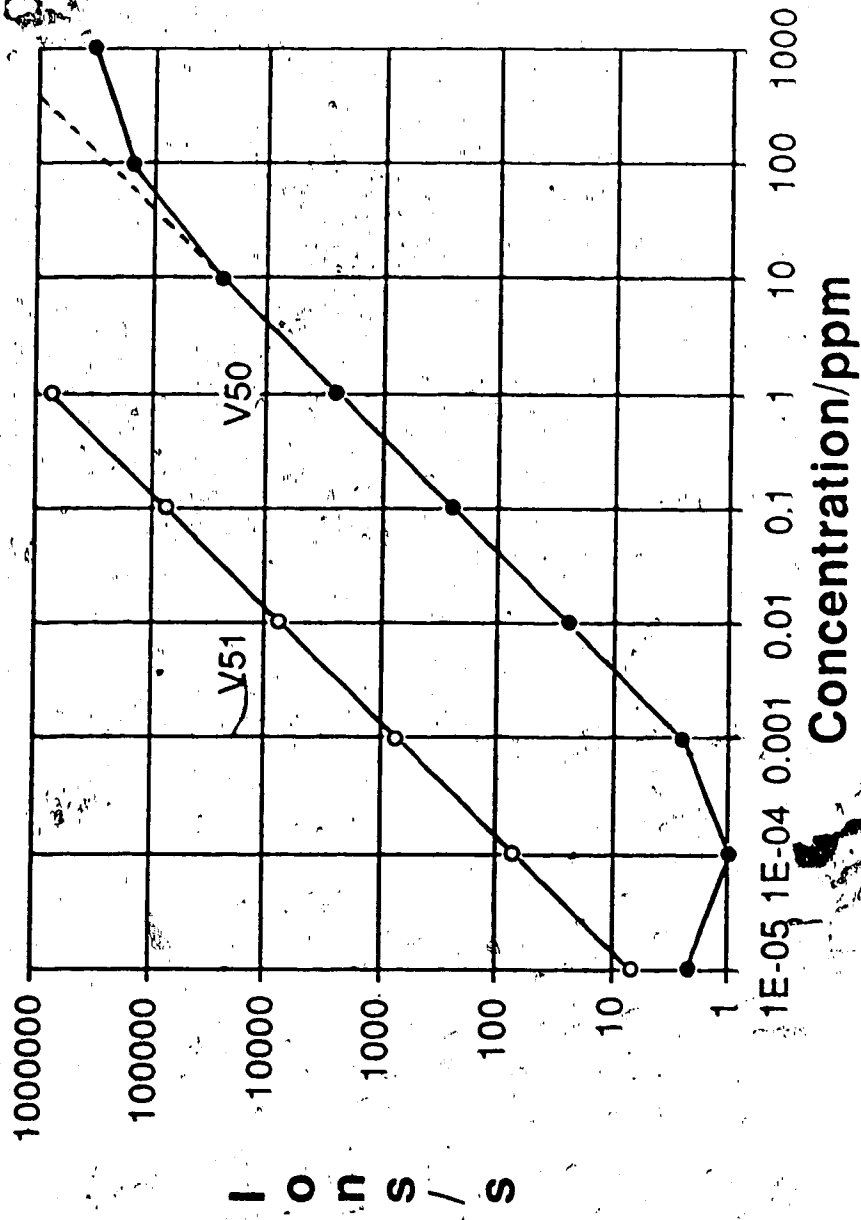


Figure 39. Calibration plots for V51 and V50

In this experiment, the selection of an internal standard is based on the data obtained in Chapter 2. The internal standard should be as similar as possible to the analyte in terms of plasma operating parameter behavior and also should have a similar mass. In Figure 40 the analytical calibration curves for Zn 67 with and without an internal standard are presented. Since the first row transition elements have very similar parameter behavior to zinc, cobalt was selected to be the internal standard. With the application of an internal standard the linear dynamic range of zinc is extended by at least an order of magnitude at the high concentration end. The same feature can be observed for Cd 111 in Figure 41 where the internal standard used was Rh. When the analyte concentration exceeds 10 ppm, the ion signal of the internal standard is suppressed to the same degree as the ion signal of analyte. Therefore, normalizing the ion signal of the analyte to that of the internal standard extends the linear range of the calibration plots beyond 10 ppm.

There are several possible explanations for the negative deviation observed at high concentrations. Firstly, when a solution containing a relatively high salt concentration is aspirated, gradual clogging of the orifice occurs which reduces the amount of ions entering the mass spectrometer. But since the analyte concentration is usually less than 100 ppm, salt deposition at the orifice is relatively small and will not account for the loss of ion signal in the above cases. The other possible explanation is matrix suppression of the analyte signal. Negative deviation always seems to occur at an analyte concentration of 10 ppm for every element. If the concentration scale is converted from ppm to molar concentration, negative deviations occur between  $10^2$  to  $10^3$   $\mu\text{M}$  depending on the atomic mass of the element. Figure 42 shows the calibration plots for Cu and Li. The calibration plots deviate from linearity at about  $1.6 \times 10^2$   $\mu\text{M}$  for Cu and about  $1.4 \times 10^3$   $\mu\text{M}$  for

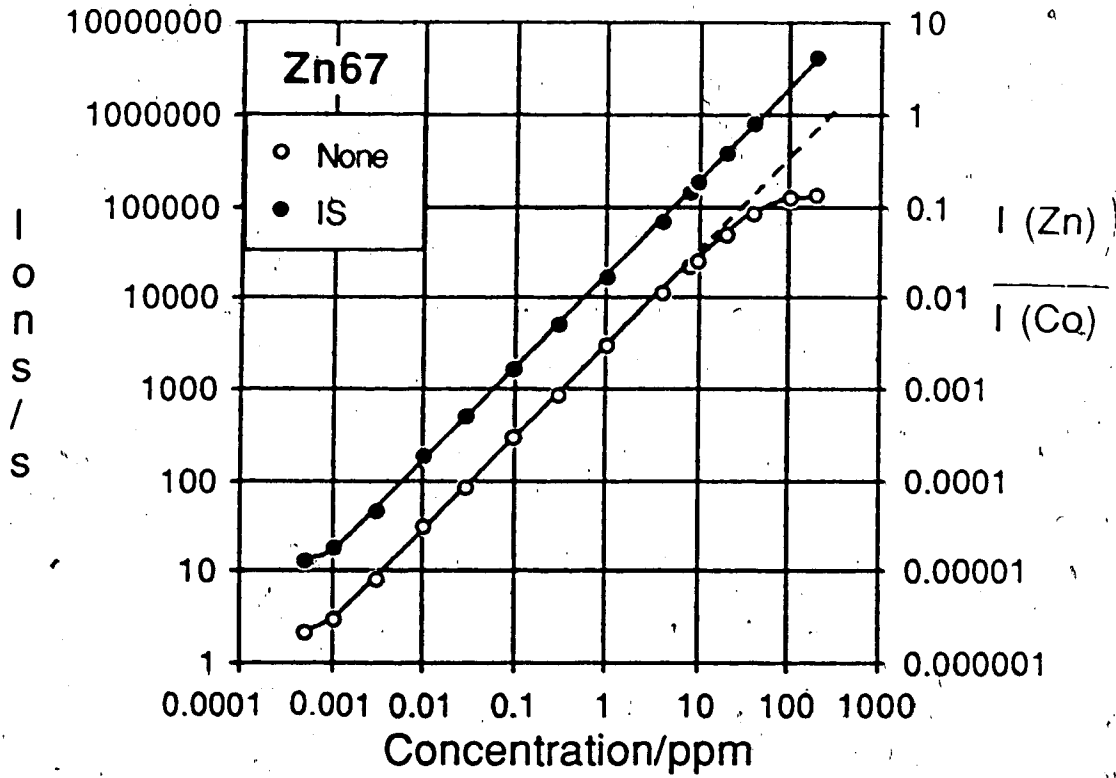


Figure 40. Calibration plots for Zn67 with and without internal standard. The internal standard was 0.4 ppm Co

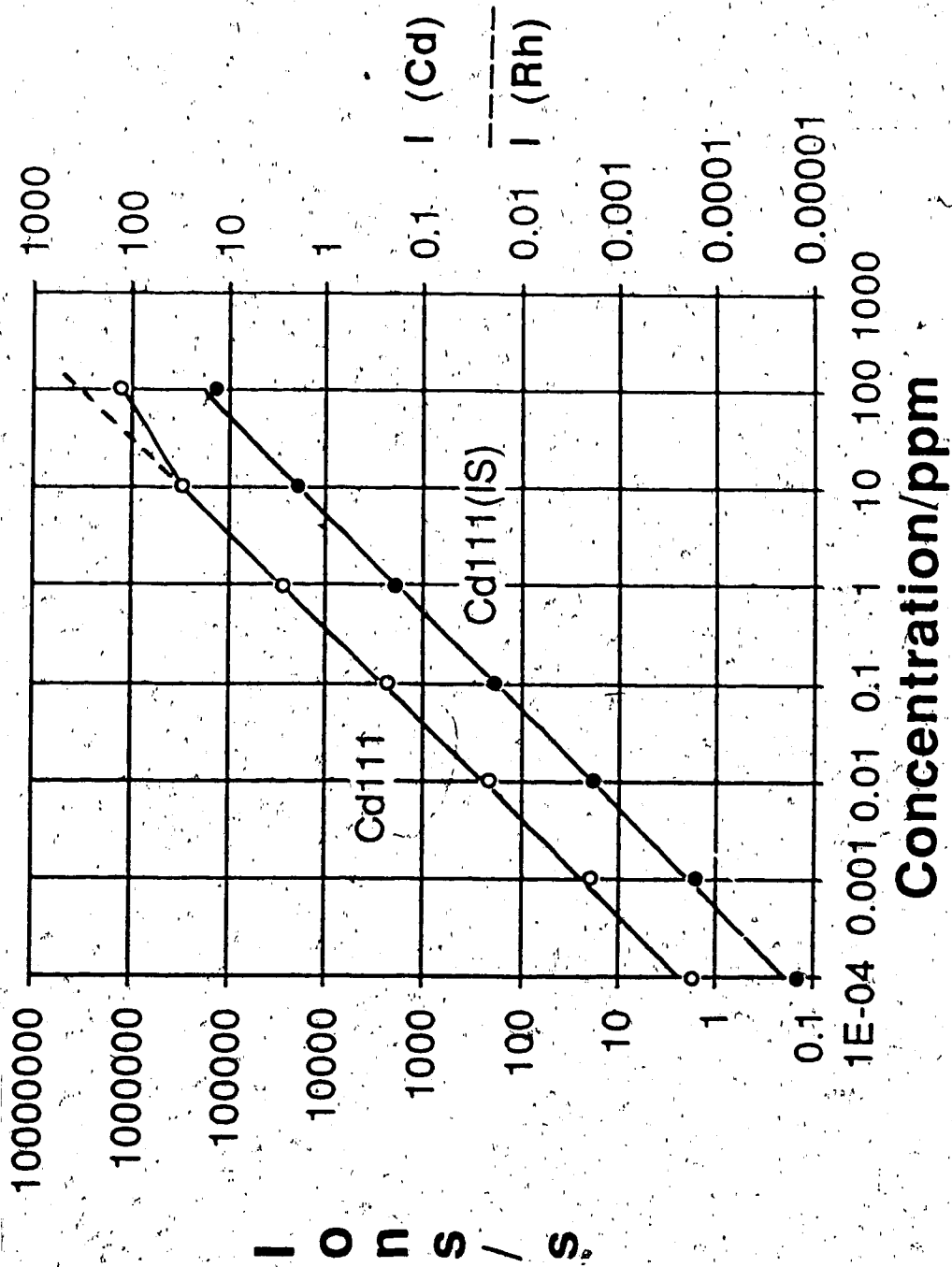


Figure 41. Calibration plots for Cd111 with and without internal standard. The internal standard was 0.5 ppm Rh.

Li. In Figure 41, the deviation occurs at about  $0.9 \times 10^2 \mu\text{M}$  for Cd.

Incidentally, despite the fact that the ion signal for Li 6 is more than 10 times lower than Li 7, the deviation occurs at the same concentration; this indicates that loss of ion signal is not due to saturation at the detector by a large ion signal. Since the solution used to acquire the data in Figure 42 contained three elements, the total salt concentration at 10 ppm is actually 30 ppm. At a concentration of 30 ppm and above, matrix suppression effects can be quite serious, especially if high nebulizer flowrates are used (see Chapter 5).

Therefore, the deviation from linearity at high concentration is most likely due to the suppression of analyte ion signal by the presence of high concentration of other concomitant salts. However, interestingly enough, negative deviation occurs regardless of whether the calibration solutions contain only a single element or more than one element. For example, for the single element solution of vanadium in Figure 39, a negative deviation is also observed at the concentration of 10 ppm for V 50. This can be rationalized as the suppression of the vanadium ion signal by a high concentration of itself. The mechanism giving rise to this observation is not clear at this time but could be related to processes occurring in the mass spectrometer. In addition, it is evident that the analyte concentration at which deviation occurs may be also dependent on the mass of the analyte element, which could be related to the mass effect phenomenon observed in Chapter 5.

### D.3 Analytical Curves of Elements forming Oxides and Doubly Charged Ions

In this section the quantitative analytical behavior of elements forming oxides and doubly charged ions is studied. Furthermore, the feasibility of

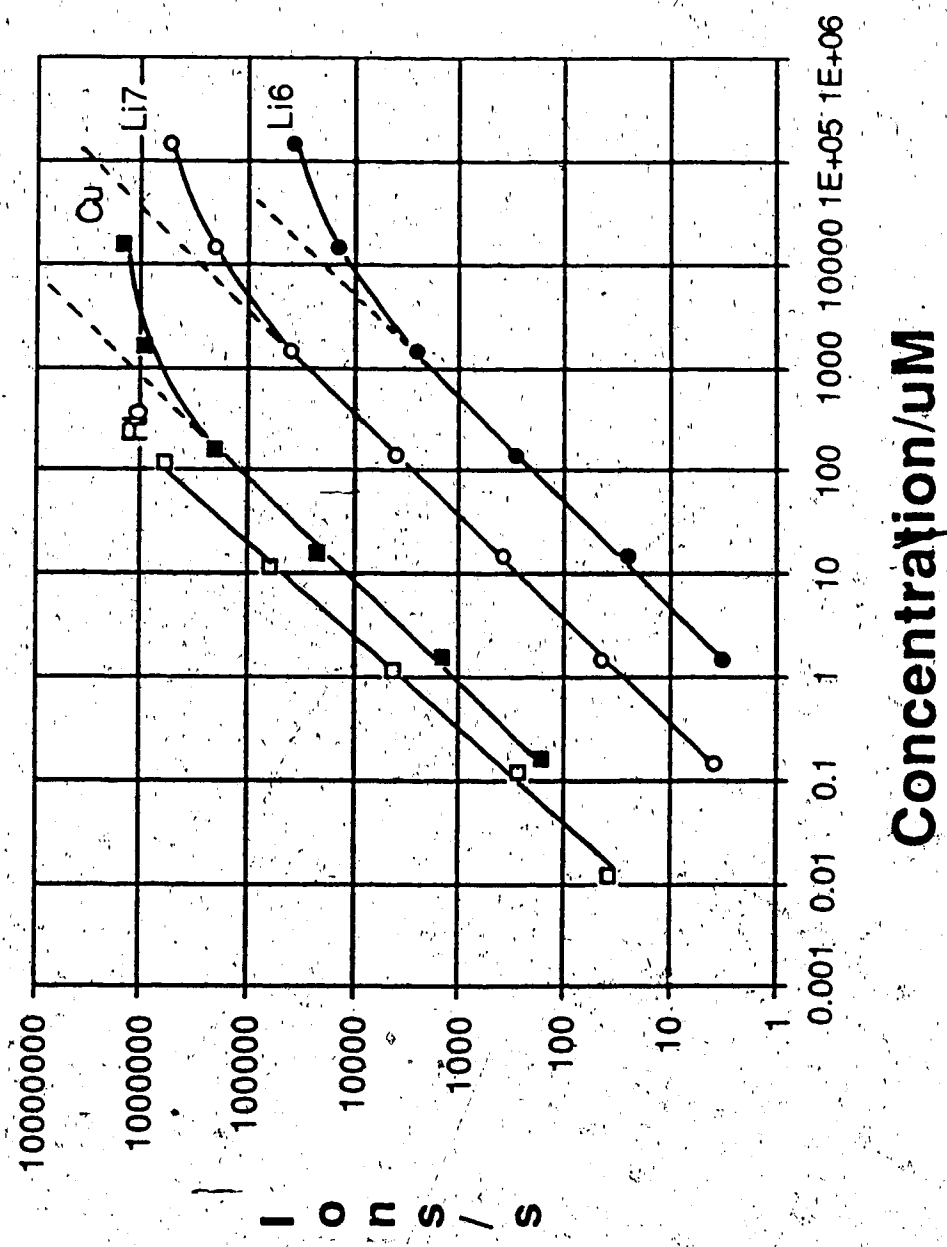


Figure 42. Calibration plots for Li6, Li7, Cu65 and Rb85

using oxide and doubly charged ions themselves for quantitative calibration is tested. The elements chosen were lanthanum and uranium. The rf power used was 1.2 kW and the nebulizer flowrate was optimized for maximum ion counts at 1.15 l/min. The calibration plots obtained for La and U are both non-linear over the concentration range studied. In Figure 43, the calibration plots for  $\text{La}^+$  and  $\text{LaO}^+$  are shown. Under the experimental conditions selected, lanthanum oxide and lanthanum ions are formed almost in equal proportion and they have almost identical calibration plots. These curves are only linear over an order of magnitude from 0.05 ppm to 1 ppm. The calibration plot for scandium is shown in Figure 44. It can be seen that the plot is linear for only about an order of magnitude and at below 0.1 ppm, the plot is not linear. Scandium is another element that formed oxide. These results were both unexpected and puzzling, therefore, another experiment using a single element solution containing only cerium and 0.5 ppm cesium as the internal standard was then carried out.

For establishing the calibration plots of cerium, the plasma power used was 1.2 kW and the nebulizer flowrates at which the maximum ion counts occurred for  $\text{Ce}^+$ ,  $\text{CeO}^+$  and  $\text{Ce}^{2+}$  species were 1.02 l/min, 1.12 l/min and 1.00 l/min respectively. A nebulizer flowrate of 1.00 l/min was used for the measurements. The analytical curves obtained for  $\text{Ce}^+$ ,  $\text{CeO}^+$  and  $\text{Ce}^{2+}$  are presented in Figures 45, 46 and 47. The calibration plots for the singly charged, oxide, and doubly charged Ce are non-linear below 0.5 ppm. The Cs internal standard used did not remove the non-linearity at low concentrations although it extends the linear range of the doubly charged ion at the high concentration end (see Figure 47).

On closer scrutiny of the data obtained for lanthanum and cerium, one can see that the nebulizer flowrate is important in affecting the linear

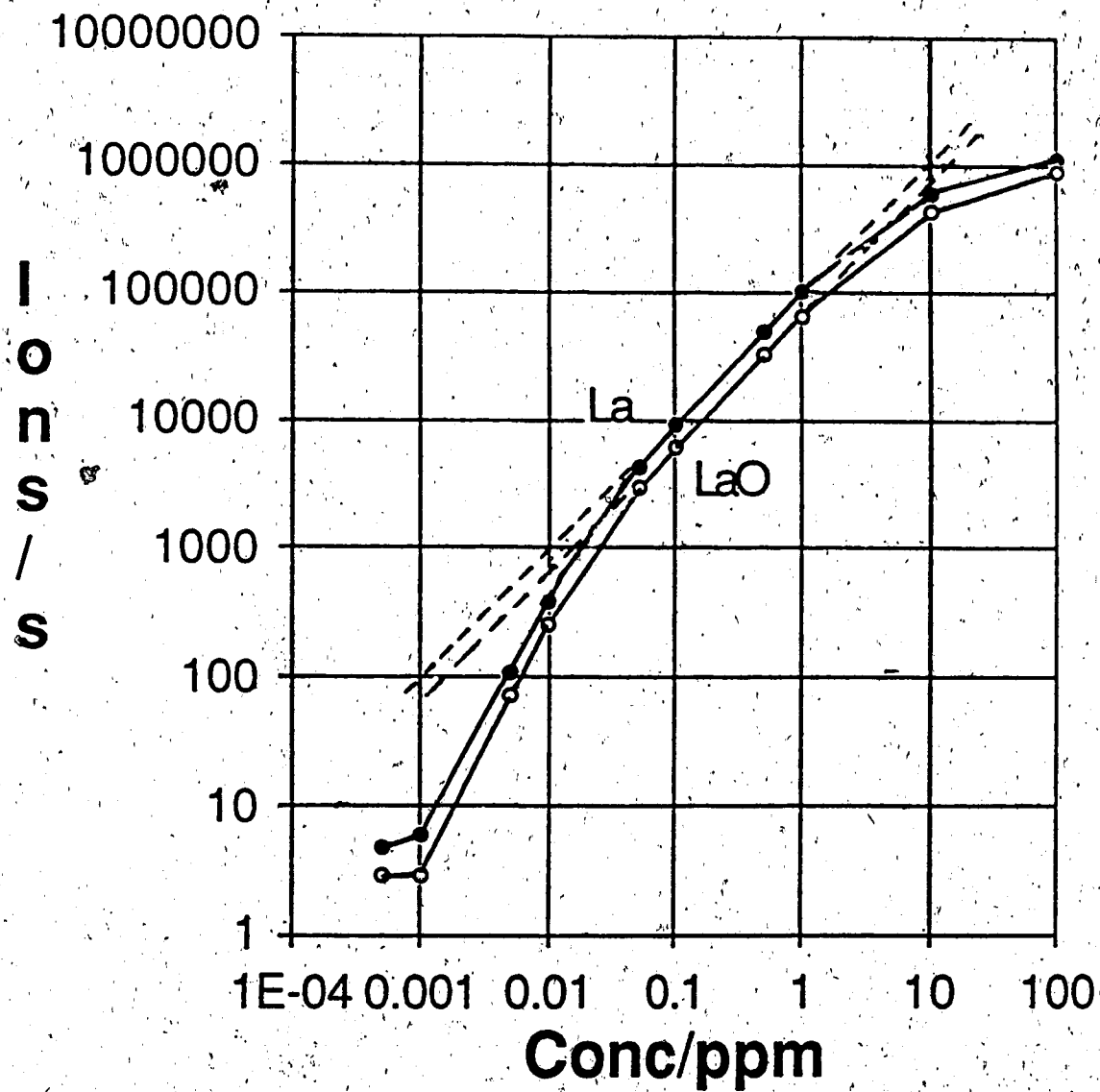


Figure 43. Calibration plots for La and LaO



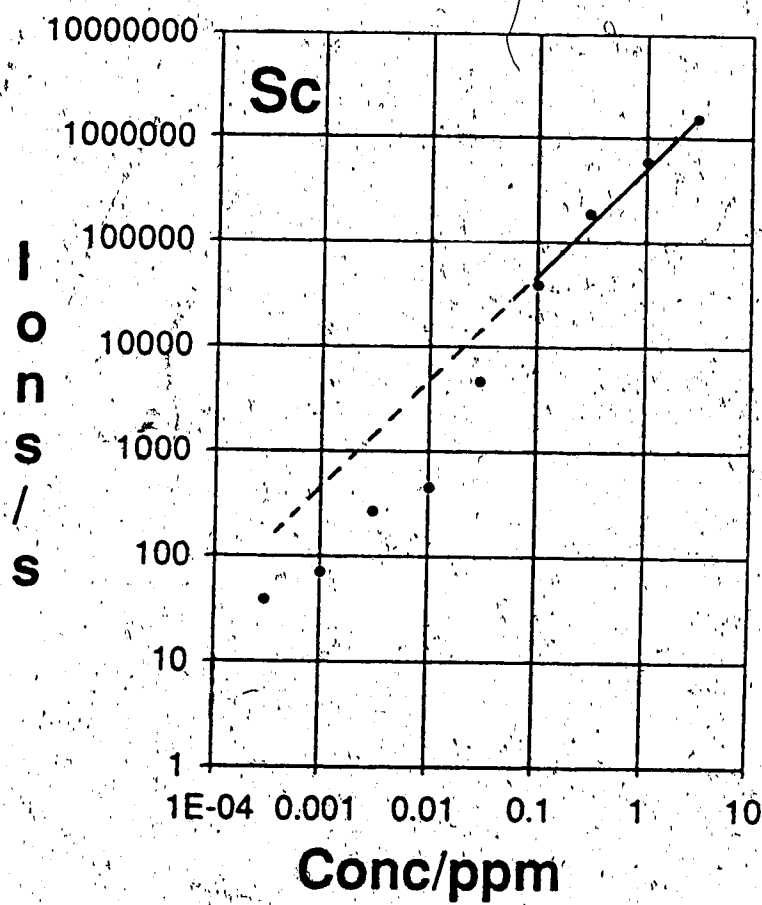


Figure 44. Calibration plot for Sc

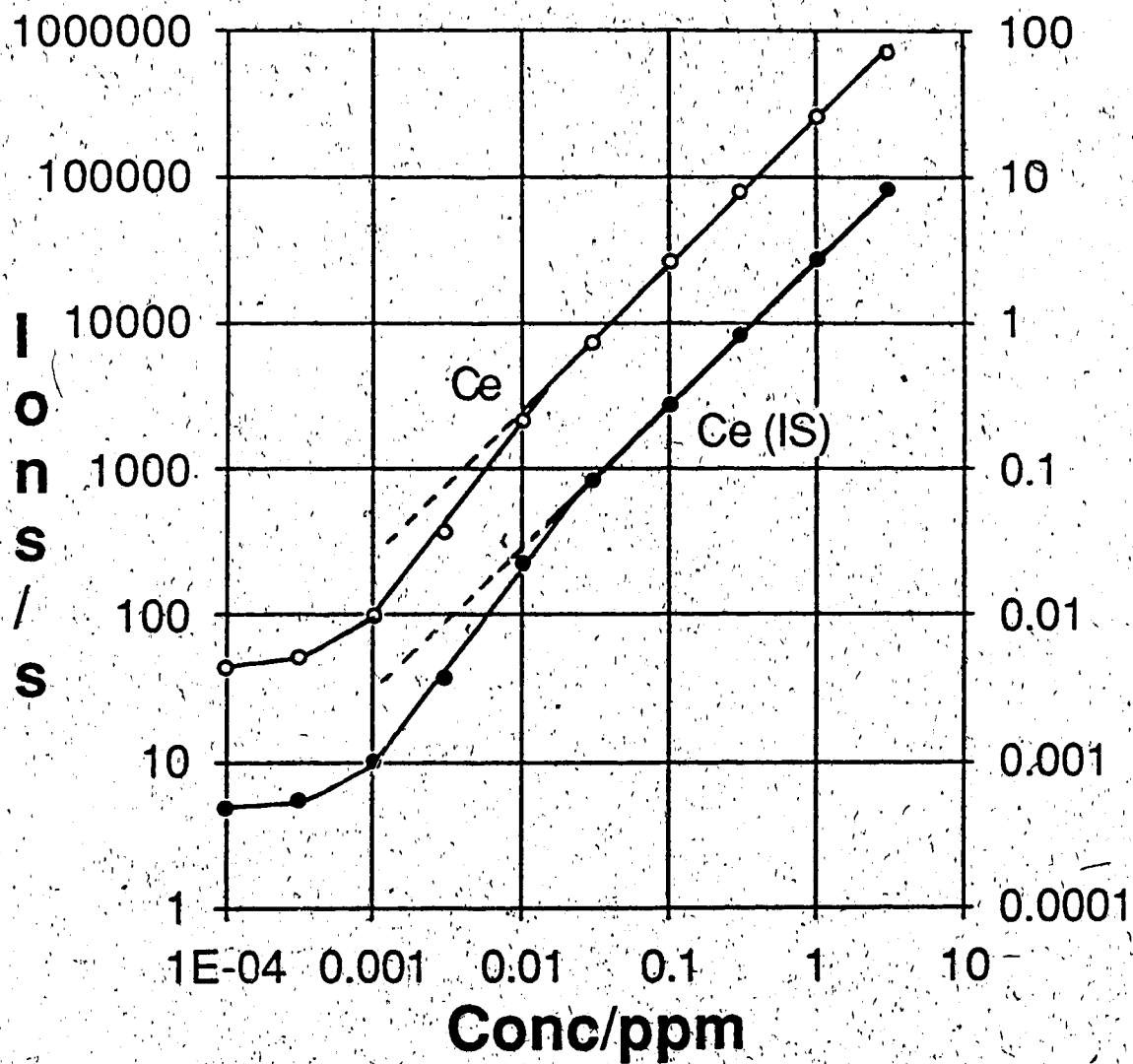


Figure 45. Calibration plots for Ce with and without internal standard. The internal standard was 0.5 ppm Cs

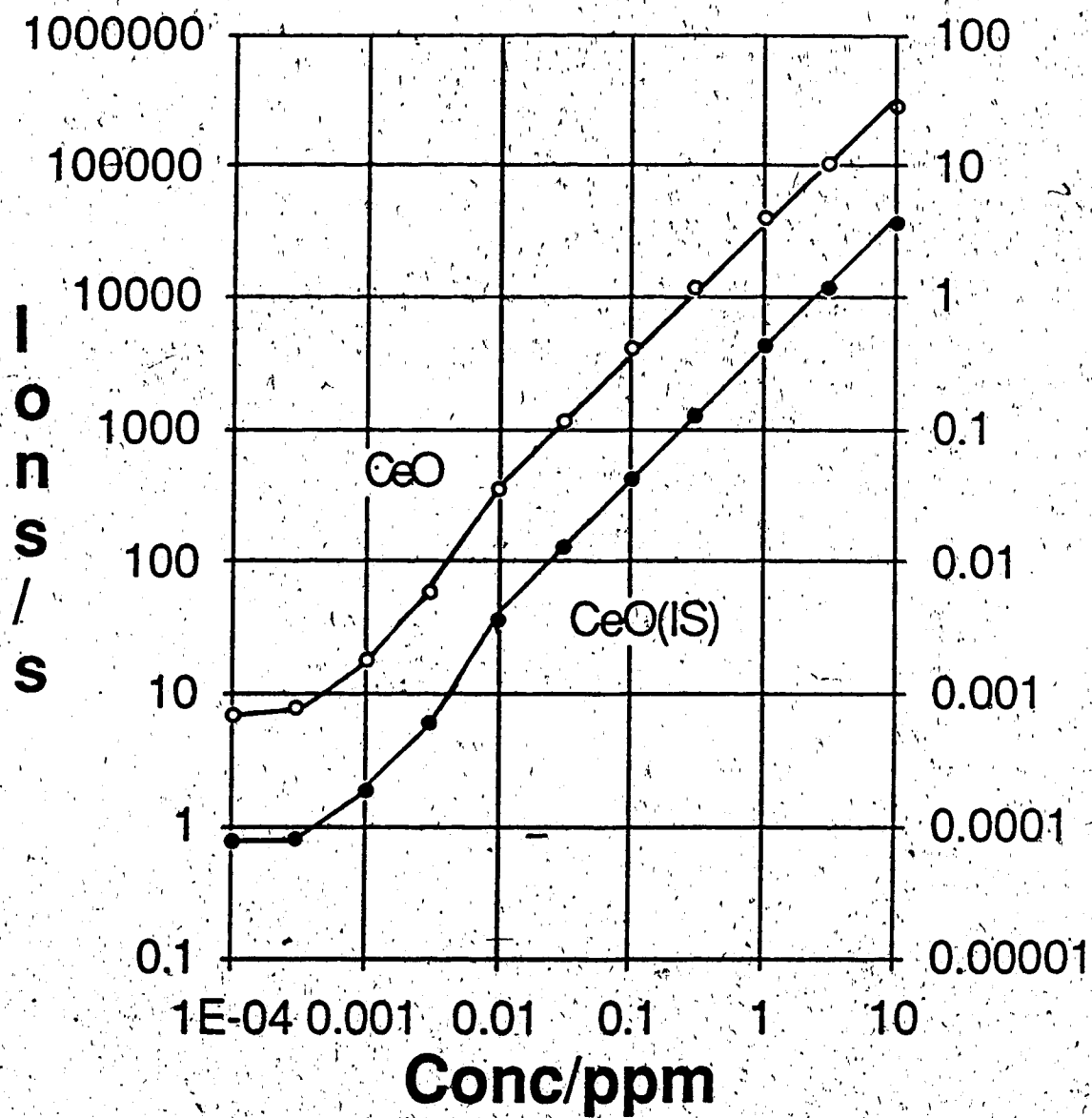


Figure 46. Calibration plots for CeO with and without internal standard. The internal standard was 0.5 ppm Cs.

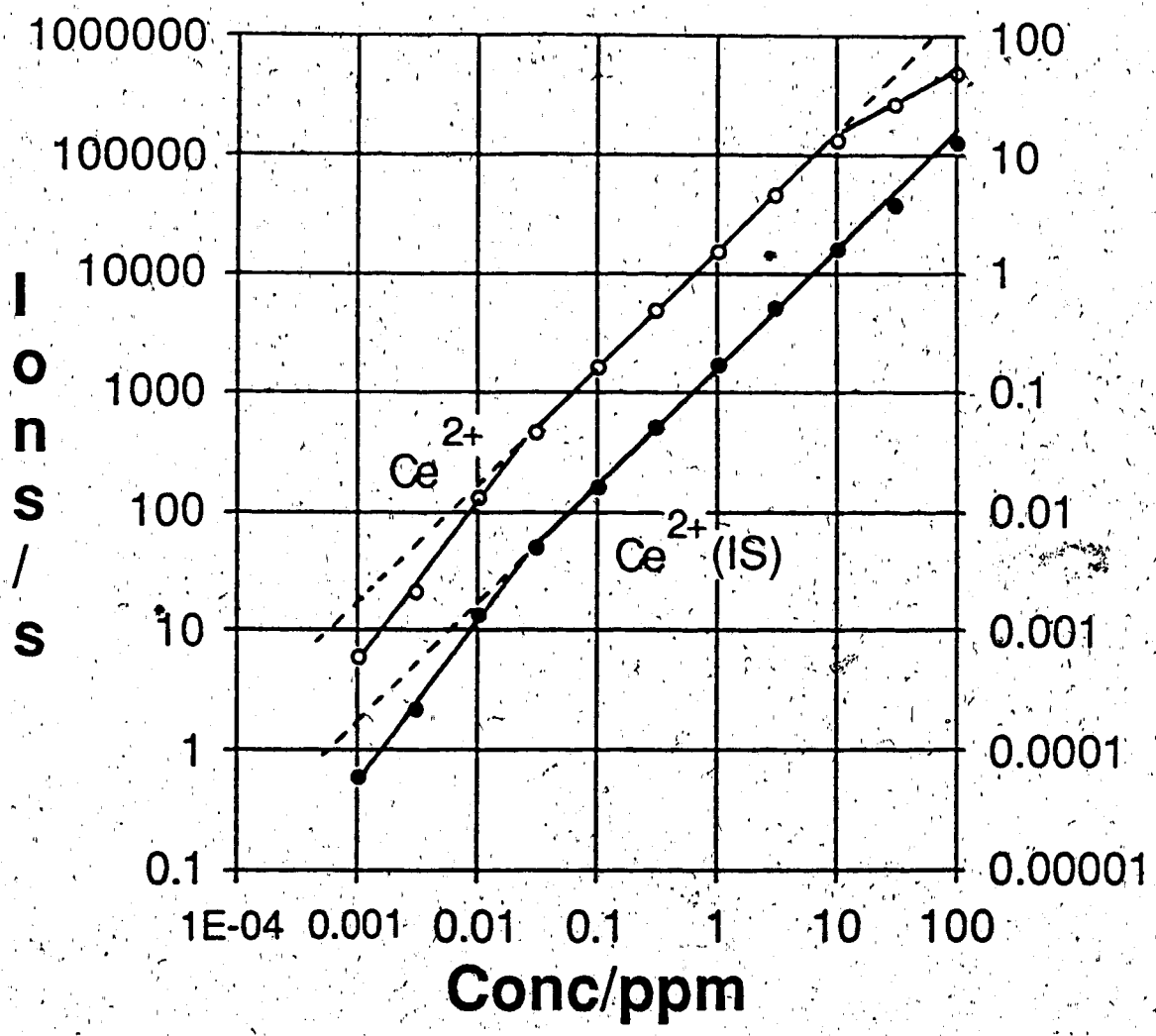


Figure 47. Calibration plot for Ce<sup>2+</sup> with and without internal standard. The internal standard was 0.5 ppm Cs

dynamic range of their analytical curves. A lower nebulizer flowrate as in the case of Ce seems to produce better analytical curves with more than two orders of magnitude of linear dynamic range. This appeared to be related to the temperature of the plasma; at lower nebulizer flowrates, the plasma is hotter, hence oxide concentration is lower [58].

The actual cause for the non-linear calibration plots is not immediately obvious, but it is clear that the formation of oxides has somehow changed the concentrations of all other ionic species of the analyte from the expected values. The oxide ratios of La and Ce, and the doubly charged ratio of Ce at different analyte concentrations, are listed in Table 12. It can be seen that the ratios in most instances remain almost constant with variation in analyte concentration except at high concentrations of La. This indicates that the loss of ion signals at low analyte concentrations could not be due to the shift in the equilibria concerning the singly charged, doubly charged and oxide ions. With the limited data available it is not possible to decipher the true mechanism involved. In addition, the mechanism for the formation of oxides in ICP-MS has not been unequivocally established. However, it is known that oxides can be formed in the initial radiation zone of the plasma discharge especially in a detuned plasma operating at high nebulizer flowrates. Or, alternatively, oxides could be formed by recombination processes in the cooling supersonic plasma jet in the 1 torr region. In any event, both processes, in varying degrees, should contribute to the oxide concentration observed. The formation of oxide will also depend on the availability of oxygen species, usually derived from water. Therefore, it can be seen that the problem not only involves equilibria governing charged and neutral analyte species but those of the matrices as well. It is interesting to note that in flame atomic absorption spectroscopy, physical occlusion of

Table 12: Lanthanum and cerium oxide ratios and cerium doubly charged ratio at different analyte concentrations

| <u>La concentration (ppm)</u> | <u>LaO<sup>+</sup>/La<sup>+</sup></u> |
|-------------------------------|---------------------------------------|
| 0.001                         | 0.53                                  |
| 0.005                         | 0.67                                  |
| 0.01                          | 0.65                                  |
| 0.05                          | 0.67                                  |
| 0.1                           | 0.68                                  |
| 0.5                           | 0.67                                  |
| 1.0                           | 0.65                                  |
| 10                            | 0.73                                  |
| 100                           | 0.81                                  |

| <u>Ce concentration (ppm)</u> | <u>CeO<sup>+</sup>/Ce<sup>+</sup></u> | <u>Ce<sup>2+</sup>/Ce<sup>+</sup></u> |
|-------------------------------|---------------------------------------|---------------------------------------|
| 0.0001                        | 0.157                                 | -                                     |
| 0.0003                        | 0.156                                 | -                                     |
| 0.001                         | 0.175                                 | 0.061                                 |
| 0.003                         | 0.165                                 | 0.058                                 |
| 0.01                          | 0.166                                 | 0.060                                 |
| 0.03                          | 0.155                                 | 0.060                                 |
| 0.1                           | 0.158                                 | 0.060                                 |
| 0.3                           | 0.154                                 | 0.061                                 |
| 1.0                           | 0.145                                 | 0.063                                 |
| 3.0                           | 0.145                                 | 0.629                                 |

analyte species in oxide particles has been reported [76], a possibility which cannot be completely discounted here particularly in the 1 torr region.

#### E. Conclusion

The detection limits of ICP-MS for most elements are excellent and are in the range of 0.01 ppb to 0.1 ppb. However, for some elements, the detection limits are degraded by the presence of background spectral interferences. Nevertheless, when taken into consideration that these detection limits are attainable for essentially every element in the periodic table, ICP-MS is superior to optical ICP systems for ultra trace elemental analysis.

The linear dynamic concentration range of the instrument is 4 to 5 orders of magnitude typically from 0.1 ppb to 10 ppm. An internal standard can be used to extend the linear dynamic range beyond 10 ppm by another one order of magnitude. Non-linearity at the upper concentration range is most likely due to matrix suppression or "self suppression" of analyte ion signal whereas the lower concentration range is limited by background noise.

Elements forming oxides may have non-linear calibration curves. Therefore, care should be taken when determining low concentrations of elements which form oxides. Data show that lower nebulizer flowrates should be preferably used to increase the linear range of the calibration plot. Analyte ion signal intensity is drastically lowered when the nebulizer flowrate is lowered. Therefore, a compromise has to be obtained where there is an adequate ion signal and minimum oxide formation. Finally, more definitive studies of the analytical characteristic of elements which form oxide have to be carried out to confirm this observation as well as to provide more conclusive data.

CHAPTER 5  
MATRIX EFFECTS IN ICP-MS (PART I)

A. Introduction

Recently, the subject of matrix interferences on analyte ion signals is receiving more attention from ICP-MS users. Preliminary matrix interference studies reveal that the technique is more susceptible to matrix interferences when compared to ICP-AES [4, 42, 44]. In ICP-AES, matrix effects may originate at various stages of the system, beginning from sample introduction to the measurement of analyte radiation. The different kinds of matrix effects in ICP-AES have been summarized by the authors in references [11, 77] and are listed in Figure 48.

In ICP-AES, sample introduction by nebulization can affect the analyte signal intensity in two different ways. Firstly, the increase in the total salt concentration alters the viscosity of the sample solution which will ultimately affect the amount of analyte reaching the plasma. The other mechanism involves the phenomenon of aerosol ionic redistribution (AIR) where nebulized droplets containing cation pairs show an enrichment in the minor component when the major component is present in high concentration. In the plasma discharge, matrix interferences of the analyte signal can arise from a number of processes such as volatilization effects, shifts in ionization equilibria, ambipolar diffusion and enhanced collisional excitation. When a solution contains a high concentration of a matrix element, the volatilization rate of a desolvated particle is different from that containing the analyte alone. Volatilization effects are manifested in the shifts of the spatial behavior of analyte emission and absorption. The presence of a high concentration of an easily ionized element (EIE) may



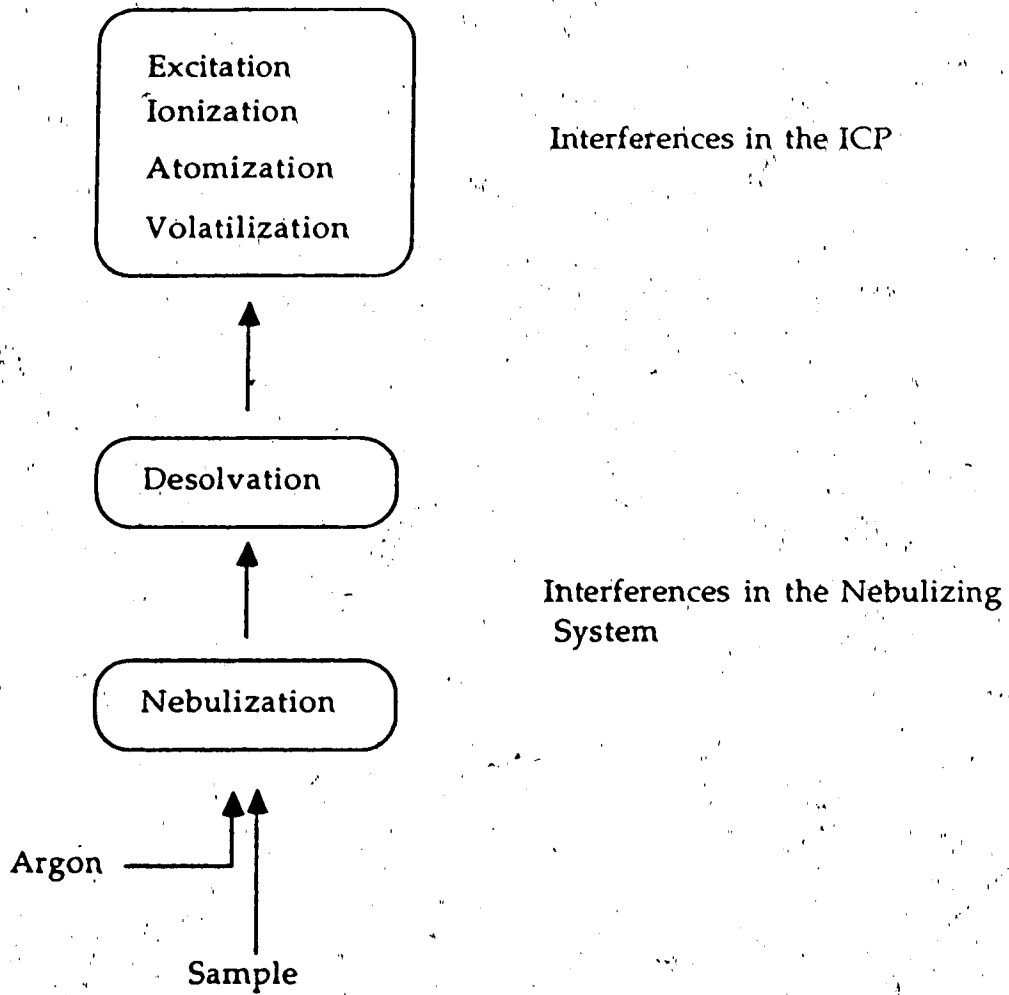


Figure 48. Types of interferences in ICP-AES

increase the electron density which can cause a shift in the ionization equilibrium towards the neutral atom species. This will cause an enhancement of neutral atom line emission and a suppression of ion line emission. Under normal plasma operating conditions, ionization interference is not a major problem. However, if exceedingly high nebulizer flowrates are used as reported by Kornblum [78], ionization interference can be quite significant. An increase in the electron density will also cause an enhancement of analyte signal as a result of the increase in collisional excitation of both the atoms and ions. This was observed by Bladeš and Horlick [77] in the lower region of the plasma-channel. In the upper region of the plasma, observed depressions in analyte signal were explained in terms of ambipolar diffusion.

Due to the intrinsic differences in the two methods of elemental analysis, some of these mechanisms may not be observable in ICP-MS; similarly, there will be other types of matrix interferences which are unique only to ICP-MS. As mentioned in Chapter 1, there are two types of commercial ICP-MS instruments currently available and a few laboratory constructed ones. Some users have reported the presence of severe matrix interferences whereas others have seen only small matrix interferences comparable to those experienced in ICP-AES. A summary of the matrix interferences in ICP-MS reported by various authors is given in the following discussion.

In the early ICP-MS instruments which utilized a pinhole size sampling orifice ( $< 50 \mu\text{m}$  in diameter), matrix suppression of analyte signal was severe because ions were sampled from the cooler boundary layer that formed in front of the sampling orifice. Clogging of the sampling orifice was also a serious problem when solution concentrations were greater than 0.01

% . Most instruments now, however, have sampling orifices with diameters greater than 0.5 mm which is large enough for the plasma to be sampled directly without the formation of a cooled boundary layer. The following papers present matrix interferences associated with large sampling orifices having the continuum mode of ion sampling.

In their earlier papers, Gray and Date [4, 44] reported a 10-20 % decrease in signals for 10 ppm Bi and Co with sodium concentrations up to 1000 ppm. Douglas et al. [42] did not find any interference from phosphate or aluminium concentrations of up to 1000 ug/ml on 2 ug/ml calcium solutions. Brown et al. [64] found that various mineral acids suppressed 0.5 ppm In ion signal by up to 50 % and organic acids caused an enhancement of the In ion signal. The authors also reported the suppression of Li, In and Pb ion signals by varying concentrations of sodium. Li, In and Pb signals were suppressed by about 30 %, 9 % and 15 % respectively in the presence of 1000 ppm Na.

Date et al. [48] investigated the effect of 500 ug/ml of Ca, Fe and Mn on a range of trace elements. The matrix effects found were small, less than  $\pm 10$  %. Macleod et al. [49] determined trace elements in Ni-base alloys and reported that, with the exception of overlaps from metal oxides, no matrix effect is observed for solutions containing 0.01% and 0.1 % dissolved solids. However, when dissolved solid content is 1 %, low results are obtained. In a recent paper, McLaren et al. [50] obtained low results for the determination of trace elements V, Mn, Co, and Ni in marine sediments. They attributed the suppression of ion signals to the presence of a high concentration of concomitant elements. They also mentioned that the matrix effect observed was affected by the ion optics of the instrument. To date, only Olivares and Houk [63] have made a more systematic study of matrix interferences in ICP-MS. They found that matrix effect was most serious for the most easily

ionized matrix elements; the order was  $\text{Na} > \text{Mg} > \text{I} > \text{Br} > \text{Cl}$ . Ion signal suppression was mainly explained by a shift in ionization equilibrium of the analyte. They concluded that the ion signals in ICP-MS are more susceptible to ionization suppression than in ICP-AES.

It is evident from the above results that matrix interferences in ICP-MS are confusing and vaguely understood. It is indeed important that a study on this subject be pursued more intently in order for the numerous advantages of the technique to be realized. In this chapter, matrix interferences from high concentrations of concomitant elements on analyte ion signals are studied at different plasma operating conditions. Matrix effects associated with varying concentrations of concomitant elements and analyte elements are also reported.

#### B. Experimental

The data acquisition and plasma operating conditions are listed below;

Resolution: Low

Measurement time/data point: 0.1 s

Data points/peak: 7-10

Repeats of measurement: 6

Plasma flowrate: 12 l/min

Auxiliary flowrate: 1.4 l/min

Sample uptake: ~ 0.9 l/min

The plasma power, nebulizer flowrate and sampling depth are varied throughout the experiments and data were acquired in a similar manner to those presented in Chapter 2.

### C. Effect of Sodium on Analyte Ion Signals at Different Plasma Operating Conditions

In this study, the analyte elements investigated were 0.1 ppm Sc, Cr, Co, Cu, Zn and Ga with Na as the matrix element. Matrix interferences were studied using 2 different concentrations of Na, 100 ppm and 1000 ppm. The plasma operating parameters varied in this study were plasma power, nebulizer flowrate and sampling depth. Plasma power and nebulizer flowrate were varied from 0.9 kW to 1.5 kW and 0.8 l/min to 1.4 l/min respectively. The sampling depth was varied from 15 mm to 27 mm.

The effect of 100 ppm Na on the Sc ion signal at different plasma powers and nebulizer flowrates is shown in Figure 49. Each frame in the figure shows the variation of the Sc ion signal with nebulizer flowrate at a certain power. The rf powers are 0.9 kW, 1.1 kW, 1.3 kW and 1.5 kW. All the data were acquired at a sampling depth of 15 mm from the load coil. It can be seen that the effect of 100 ppm Na is to shift the plot profile to higher nebulizer flowrates. As a result, the ion signal for Sc is suppressed at low flowrates and enhanced at high flowrates. This shift is less evident at the rf power of 0.9 kW. Similar plots showing the effect of 1000 ppm Na on 0.1 ppm Sc are presented in Figure 50. The data for 100 ppm Na and 1000 ppm Na were acquired on different days, hence the sensitivity for the ion signal is slightly different. In the presence of 1000 ppm Na, the ion signal for Sc is suppressed to a greater extent than that at 100 ppm Na. Suppression of Sc ion signal occurs at all nebulizer flowrates and plasma powers. However, at low nebulizer flowrates, the suppression effect is less severe than at higher nebulizer flowrates.

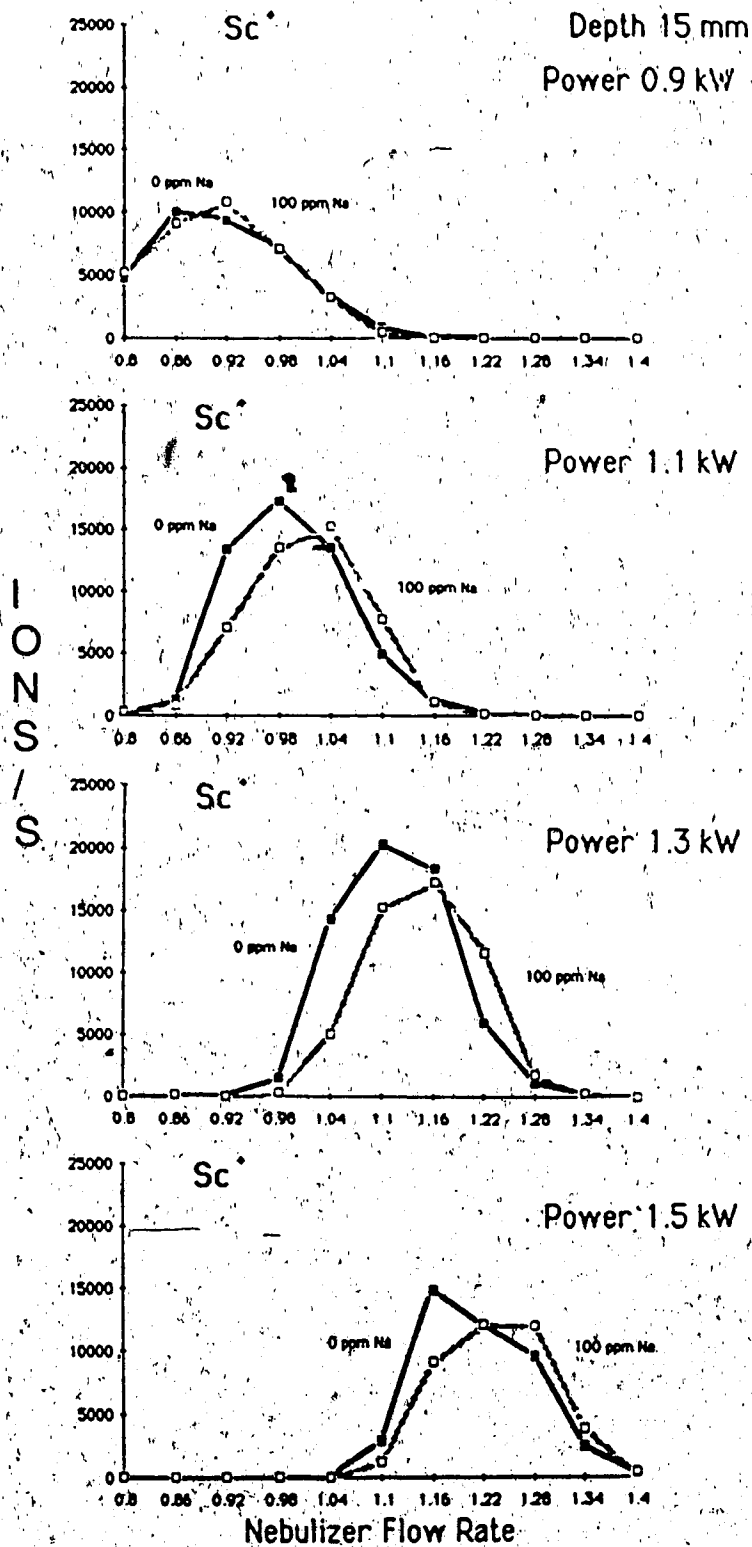


Figure 49. Effect of 100 ppm Na on the Sc signal as a function of nebulizer flowrate and power.

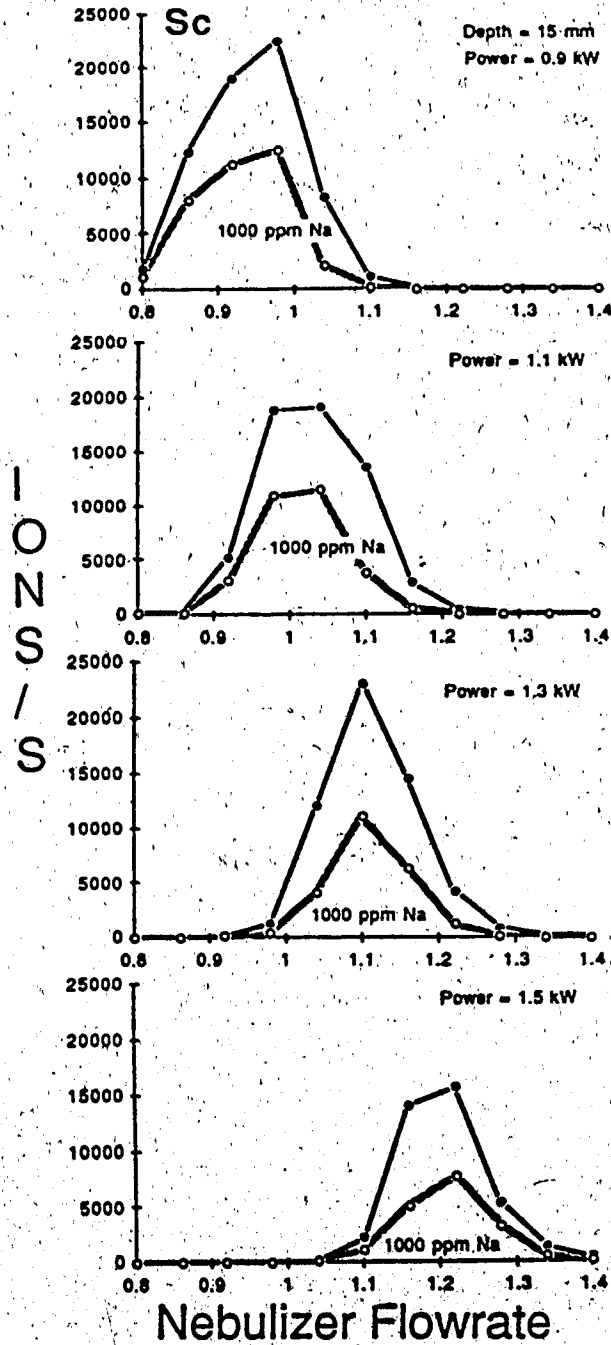


Figure 50. Effect of 1000 ppm Na on the Sc signal as a function of nebulizer flowrate and power.

The effect of sampling depth on matrix effect at a plasma power of 1.3 kW is shown in Figures 51 and 52 for Na concentrations of 100 ppm and 1000 ppm respectively. In Figure 51, it can be seen that the shift in the parameter behavior plot occurs only at the sampling depth of 15 mm. At the sampling depths of 19 mm, 23 mm and 27 mm, however, a suppression of the ion signal at all nebulizer flowrates is observed. As observed before, at low nebulizer flowrates, the ion signal is suppressed to a lesser degree. In Figure 52, an overall suppression of Sc ion signal by 1000 ppm of Na is seen and matrix suppression may be as high as 80 %.

Other analyte species are affected in the same manner as Sc in the presence of a high concentration of Na. The parameter behavior plots showing the effect of 1000 ppm Na on the ion signals of 0.1 ppm Cr, Zn, Ga and ScO are illustrated in Figure 53 at an rf power of 1.3 kW and a sampling depth of 15 mm. It is obvious that all the analyte ion signals are suppressed by the Na matrix. An interesting feature is that the ion signal for the molecular species ScO is similarly suppressed as the other analytes. However, inconsistent matrix effect behavior was obtained for Cu ion signals. An enhancement of the Cu ion signal was observed in the presence of both 100 ppm and 1000 ppm Na. The effect of 1000 ppm Na on the Cu ion signal at four plasma power settings is shown in Figure 54. The enhancement was found to be most evident at small sampling depths, therefore, data taken at the sampling depth of 15 mm were chosen to illustrate the enhancement effect. In addition, it can be seen from Figure 54 that enhancement of the ion signal is most pronounced at low powers ( $\leq 1.1$  kW). This increase in ion signal was found to be due to the formation of the molecular species  $\text{ArNa}^+$  in the presence of a high concentration of sodium. This was verified by scanning the mass spectrum of a solution containing only 100 ppm Na. A



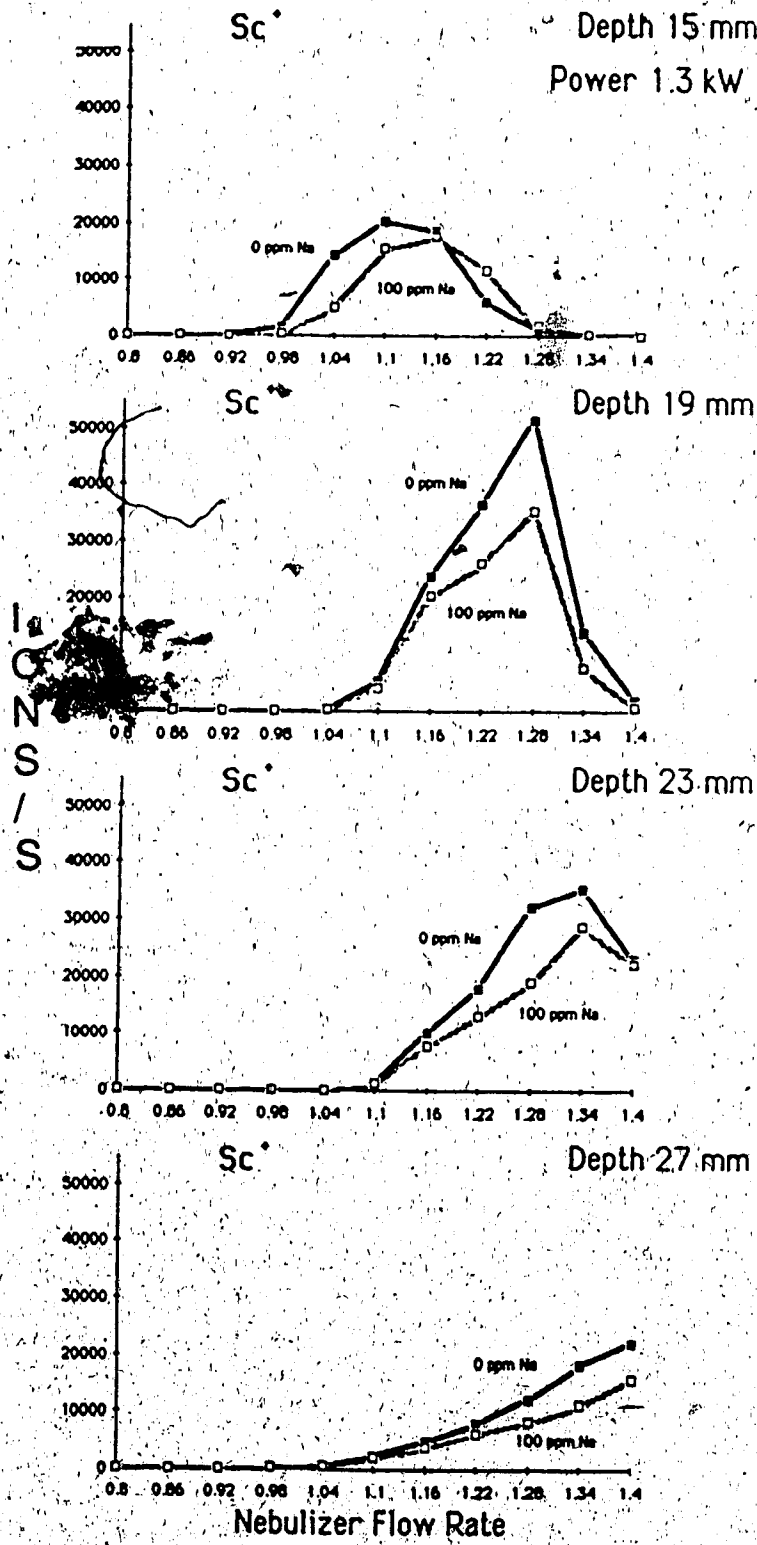


Figure 51. Effect of 100 ppm Na on the Sc signal as a function of nebulizer flowrate and sampling depth.

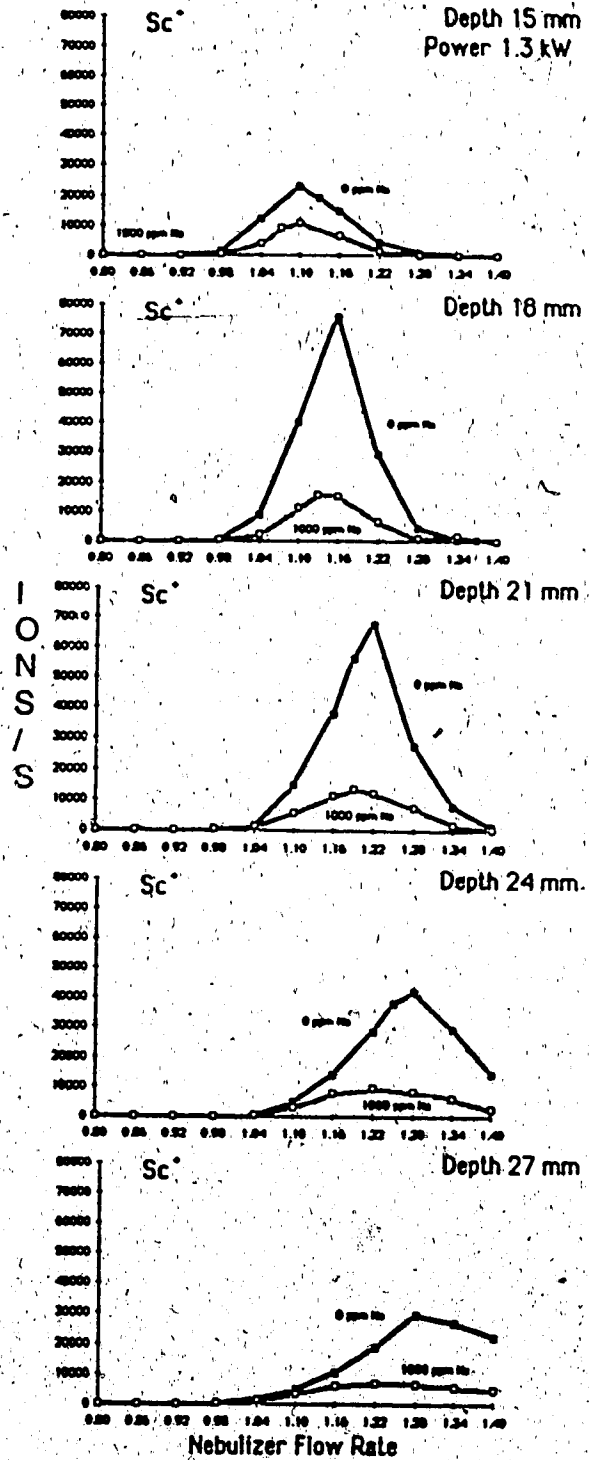


Figure 52. Effect of 1000 ppm Na on the Sc signal as a function of nebulizer flowrate and sampling depth.

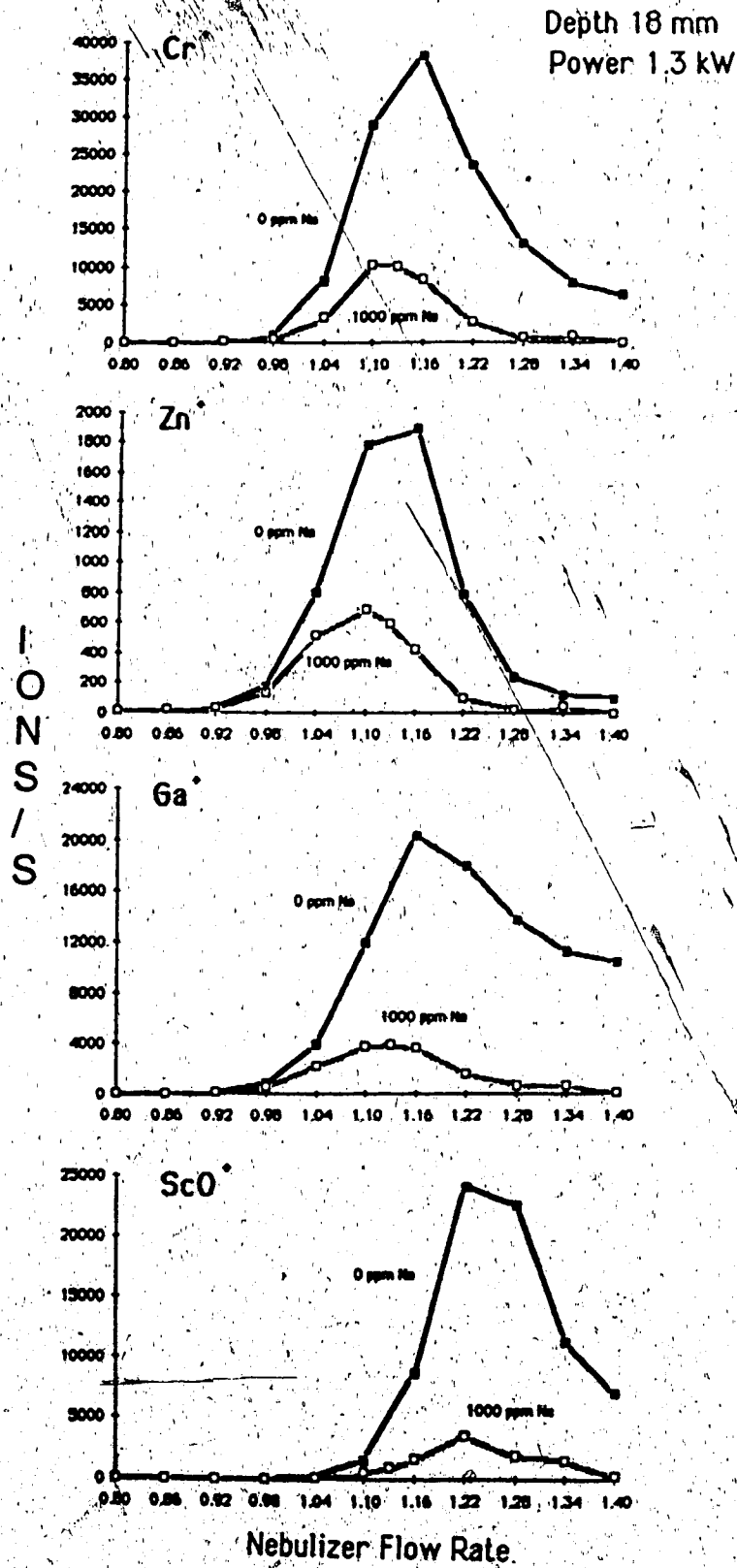


Figure 53. Effect of 1000 ppm Na on the signals for Cr, Zn, Ga, and ScO as a function of nebulizer flowrate.

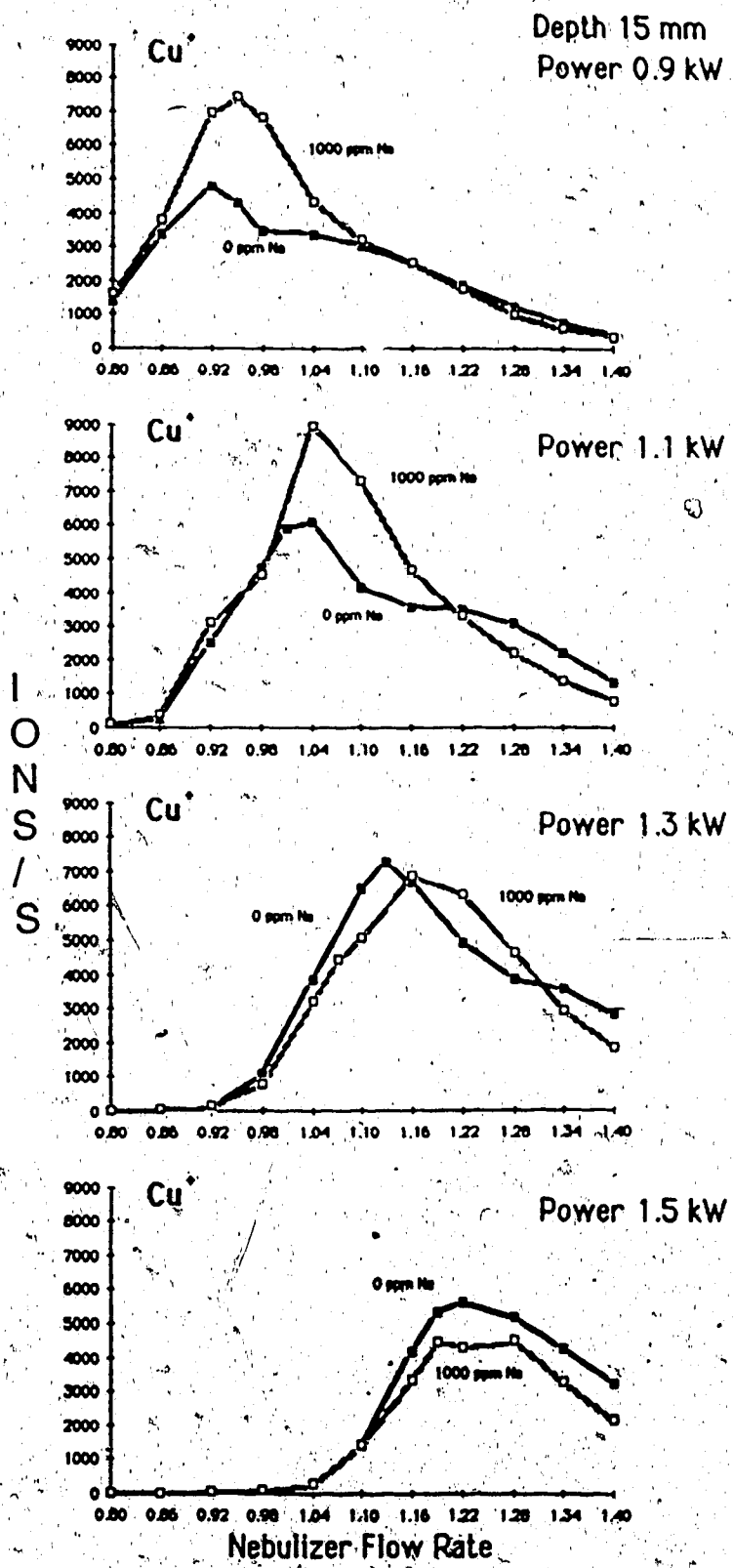


Figure 54. Effect of 1000 ppm Na on the Cu signal as a function of nebulizer flowrate and power.

peak at mass 63 was present but there was no corresponding peak at mass 65. This indicates that the ion signal at mass 63 is not derived from Cu but rather from  $^{40}\text{Ar}^{23}\text{Na}$ . When the Na concentration is varied from 0 ppm to 1000 ppm, the ion intensity at mass 63 also varies accordingly; this is shown in Figure 55. These data were acquired with the new ion lenses, thus the ion signal sensitivity is about an order of magnitude greater than that for the data in Figure 54. From the data it can be seen that the ion signal of ArNa increases in direct proportion to the Na concentration. Incidentally, another isotopic combination of ArNa is  $^{36}\text{Ar}^{23}\text{Na}$  at mass 59, which overlaps with cobalt. As the isotopic abundance of  $^{36}\text{Ar}$  is only 0.34 %, no enhancement of the Co ion signal was observed even with 1000 ppm Na. However, its contribution could be significant when determining trace levels of Co in samples containing high concentrations of sodium. Therefore, care should be taken when determining Cu and Co in samples with high concentrations of sodium.

D. Effect of High Concentrations of a Range of Matrix Elements on Analyte Ion Signals

The effect of 1000 ppm Cd on 0.1 ppm of Sc, Cr, Co, Cu, Zn and Ga at 1.3 kW is shown in Figure 56. The data were acquired at a sampling depth of 18 mm. It can be seen that ion signals are severely suppressed as was the case for the Na matrix. Severe matrix suppression of analyte signals observed so far is not found in ICP-AES and these observations are most likely unique to ICP-MS.

In the following section, interference effects from equi-molar concentrations of six matrix elements are illustrated. The concentration of the matrix elements is  $7.5 \times 10^{-3}$  M which is equivalent to 1000 ppm of Cs, 863.

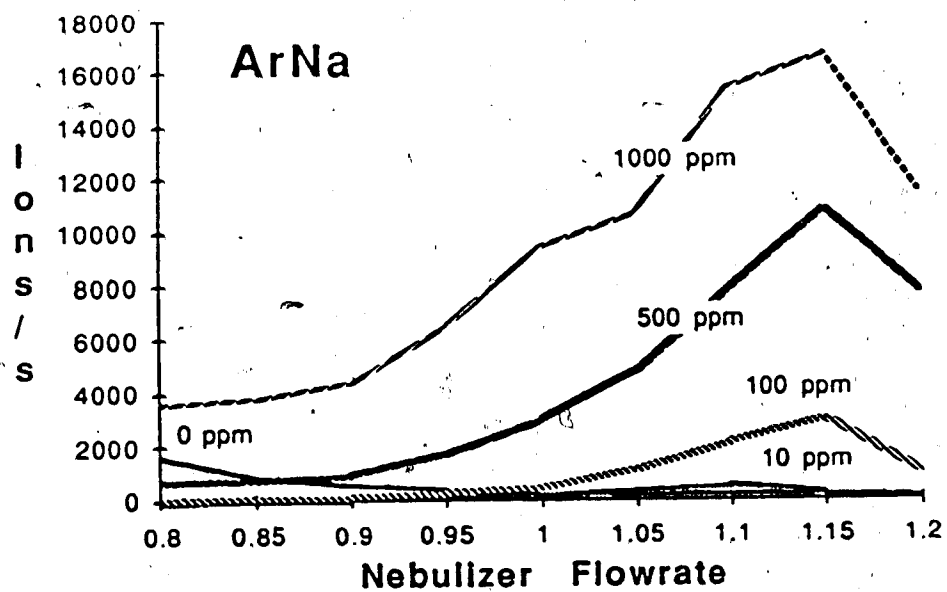


Figure 55. Dependence of ArNa ion signal on nebulizer flowrate and Na matrix concentration

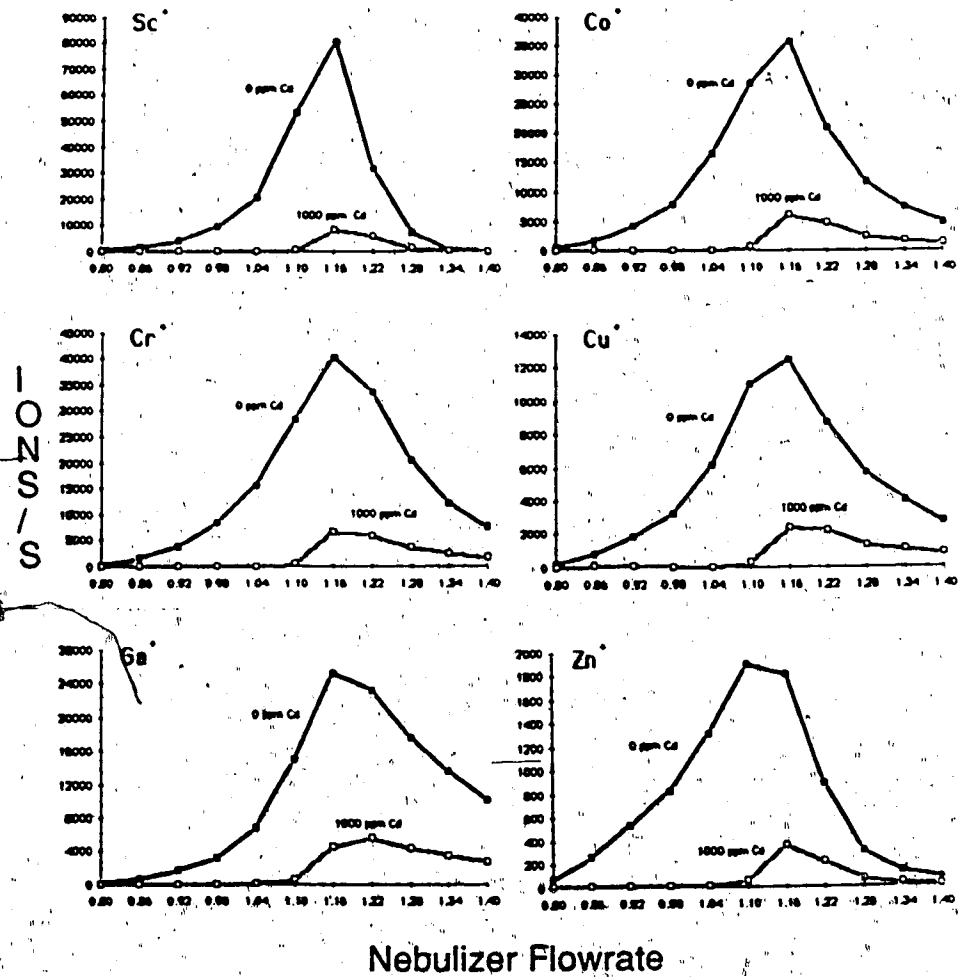


Figure 56. Effect of 1000 ppm Cd on Sc, Cr, Co, Cu, Zn and Ga as a function of nebulizer flowrate. Sampling depth was 18 mm from the load coil.

ppm of In, 845 ppm of Cd, 775 ppm of Rh, 893 ppm of Sn and 916 ppm of Sb. The analytes are 1.0 ppm Sc, Cr, Mn, Co, Cu and Zn. The rf power used was 1.3 kW and the sampling depth was 15 mm. Data for Cs, In and Cd matrices were acquired on a different day from those for Rh, Sn and Sb. Although the plasma operating conditions were essentially the same for both sets of data, the sensitivity was different because different ion lens settings were used in the two experiments.

The data obtained for Cs, In and Cd matrices are shown in Figures 57, 58 and 59. It is clear from the data presented that a high concentration of all these matrix elements causes a suppression of analyte signal. Since the solutions have the same molar concentration, it appears that the greatest matrix effect is associated with the Cs matrix which is an easily ionized element. Although still serious, a smaller suppression effect is seen for Cd. Notice too, that at the sampling depth used, the suppression effect is relatively small at nebulizer flowrates lower than 1.05 l/min. At higher nebulizer flowrates where the analyte signals are high, matrix suppression is most severe. When a low nebulizer flowrate is used, the plasma operating condition is similar to that used for analytical determination in the ICP-AES, where matrix effect is relatively small. However, the extent of signal suppression seen at all nebulizer flowrates is much higher than that observed in ICP-AES, so it is likely that mechanisms unique to ICP-MS are involved in causing the matrix effects observed. For example, in the 1 torr region, cooling of the extracted ion beam occurs during the supersonic expansion process, but because complete freezing of all chemical processes is not achieved, ion-electron recombination, charge transfer and other molecular reactions could occur. Therefore, matrix interferences in ICP-MS are likely caused by a



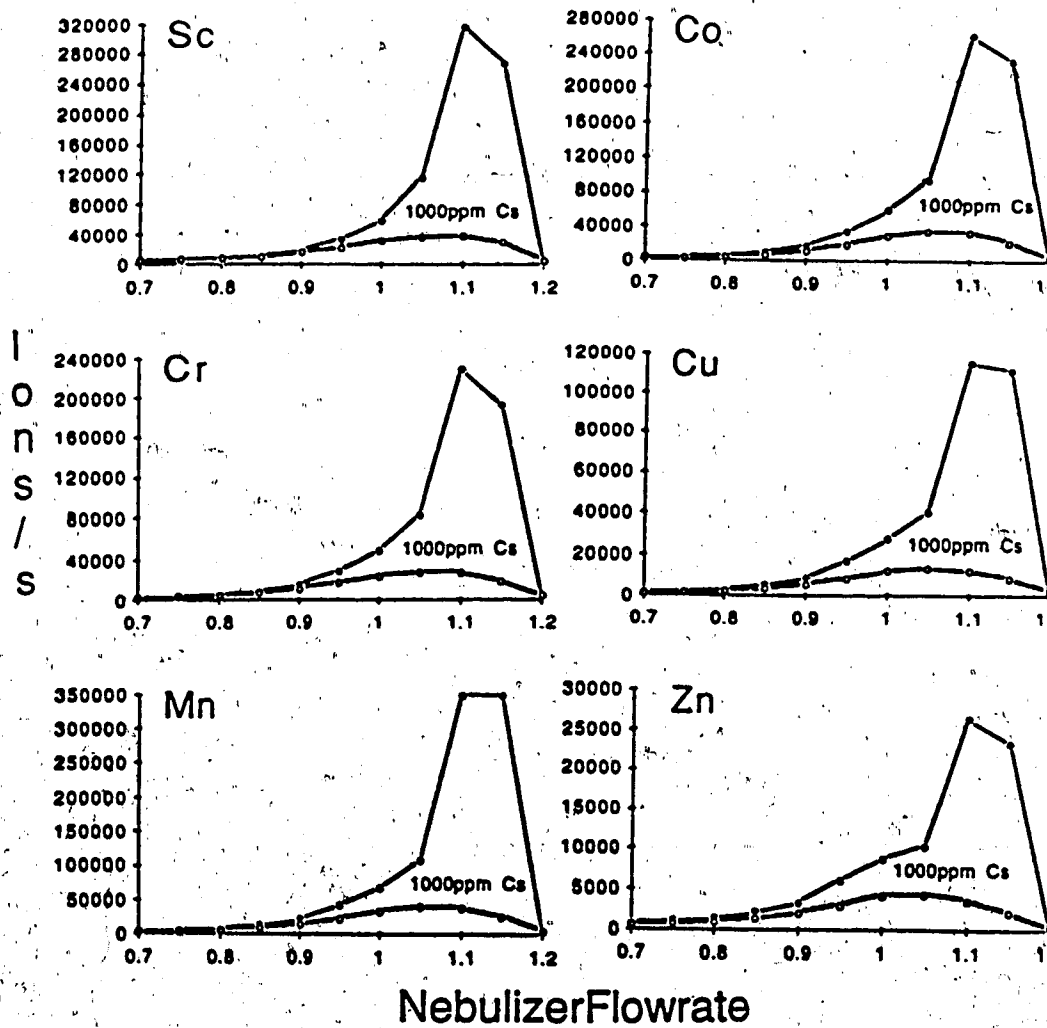


Figure 57. Effect of 1000 ppm Cs on 1 ppm Sc, Cr, Mn, Co, Cu and Zn as a function of nebulizer flowrate.

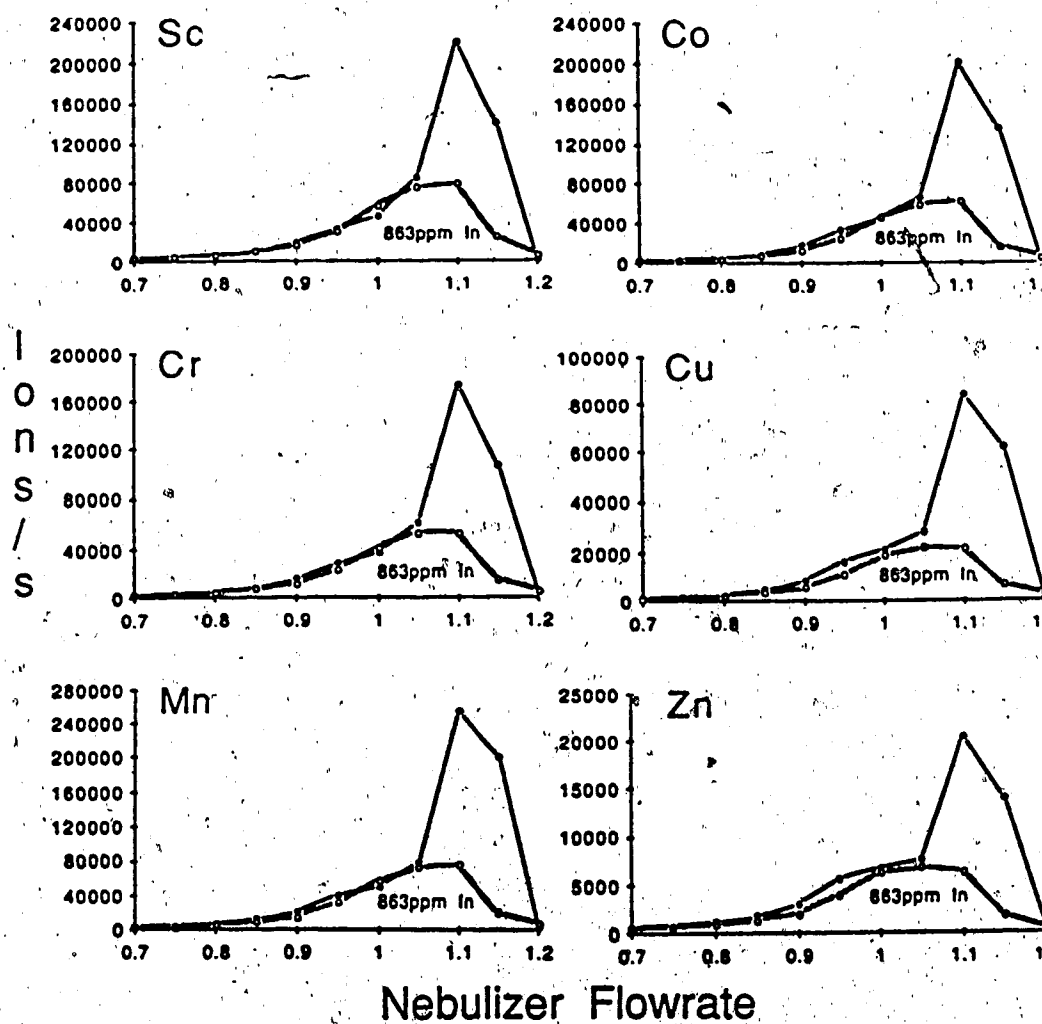


Figure 58. Effect of 863 ppm In on 1 ppm Sc, Cr, Mn, Co, Cu and Zn as a function of nebulizer flowrate.

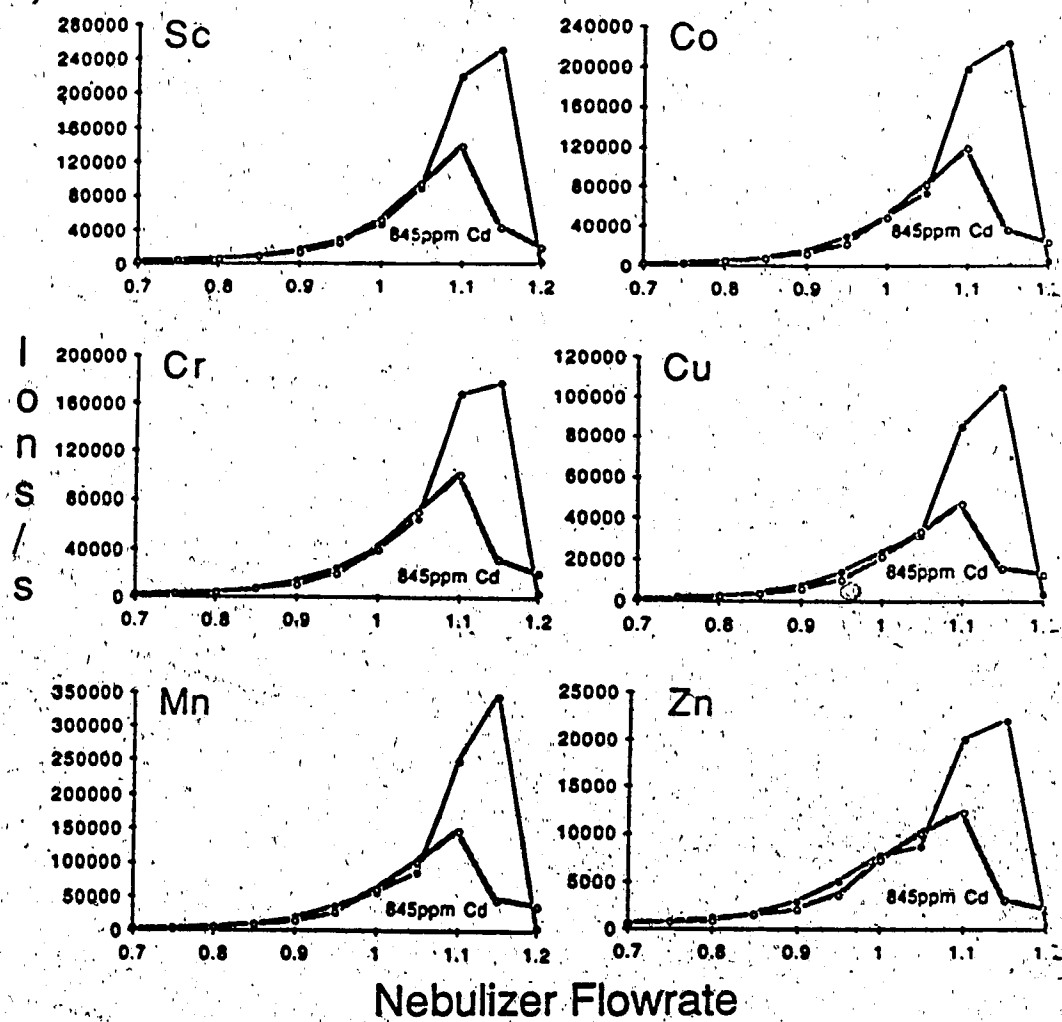


Figure 59. Effect of 845 ppm Cd on 1 ppm Sc, Cr, Mn, Co, Cu and Zn as a function of nebulizer flowrate.

combination of processes occurring in the plasma discharge itself and in other parts of the mass spectrometer.

Suppression of analyte signals by equi-molar amounts of Rh, Sn and Sb matrices are shown in Figures 60, 61 and 62. Signal suppression occurs for all analytes in the three matrices, similar to the data just shown for Cs, In and Cd. It should be noted that the anions of the three matrices were different. It was reported by Brown [64] that mineral acids with different anions suppressed analyte signal to different degrees. Therefore, in order to make valid comparisons among different matrices, it is important to make sure that the anions of the matrix elements are the same. In addition, the total salt concentration of the solution and the amount of acid added for stabilization should also be equivalent.

#### E. Effect of Photon Stop Voltage (Lens B) on the Matrix Effect

When carrying out the matrix effect experiments, the lens voltage on the photon stop (lens B) was usually adjusted at the beginning of an experiment to provide a maximum ion count for Cu. Voltage adjustment was performed at the nebulizer flowrate in which the maximum Cu ion count occurred. Set in this manner, the voltage on the photon stop normally is quite reproducible from day to day and has the value of  $5.5 \pm 0.5$  V. The  $\pm 0.5$  V is not the range associated with the precision of the voltage setting but rather the possible variation in the voltage of the photon stop from day to day.

The ion signals of Co and Cd with and without the presence of 1000 ppm Na were measured as a function of the voltage of the photon stop at 3 different nebulizer flowrates; the resulting data are plotted in Figure 63. Note that for this diagram, the designation symbols for the analyte signals with and

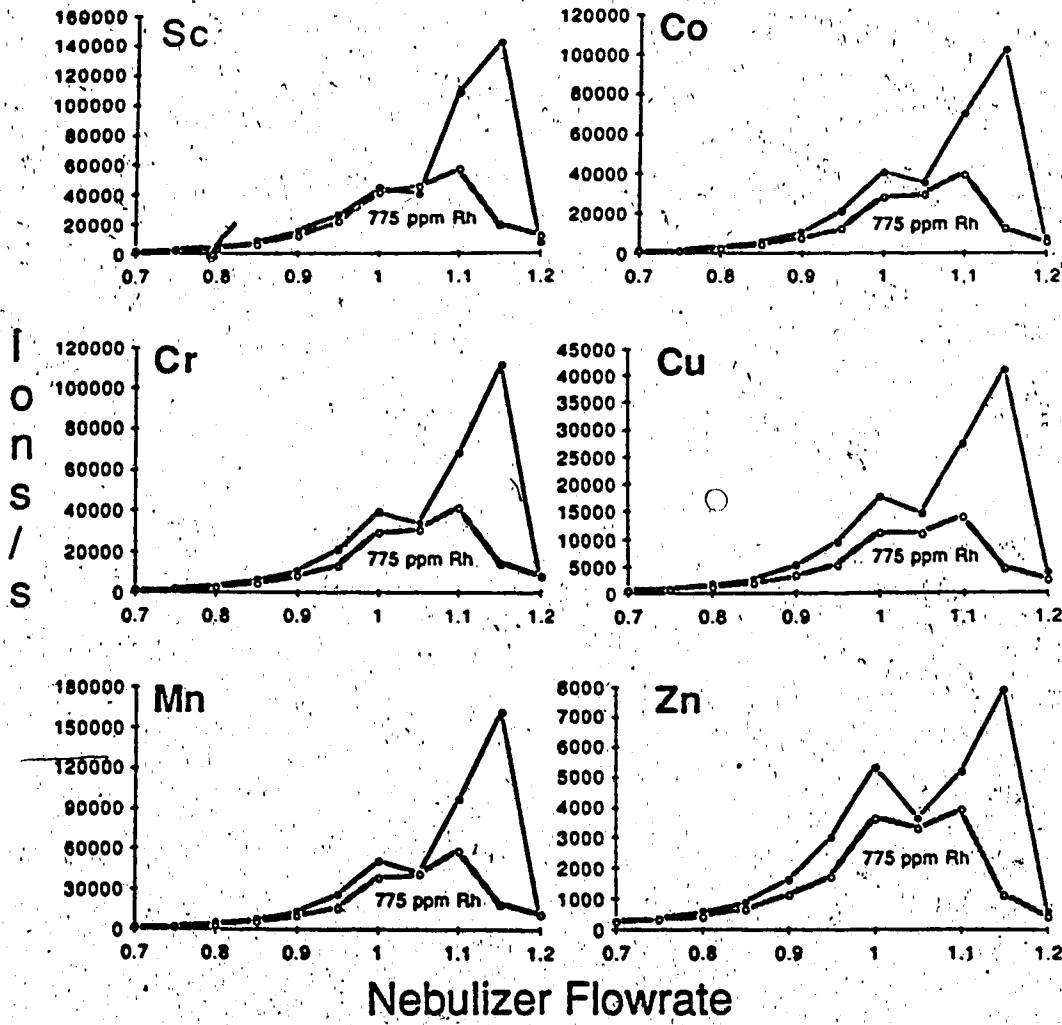


Figure 60. Effect of 775 ppm Rh on 1 ppm Sc, Cr, Mn, Co, Cu and Zn as a function of nebulizer flowrate.

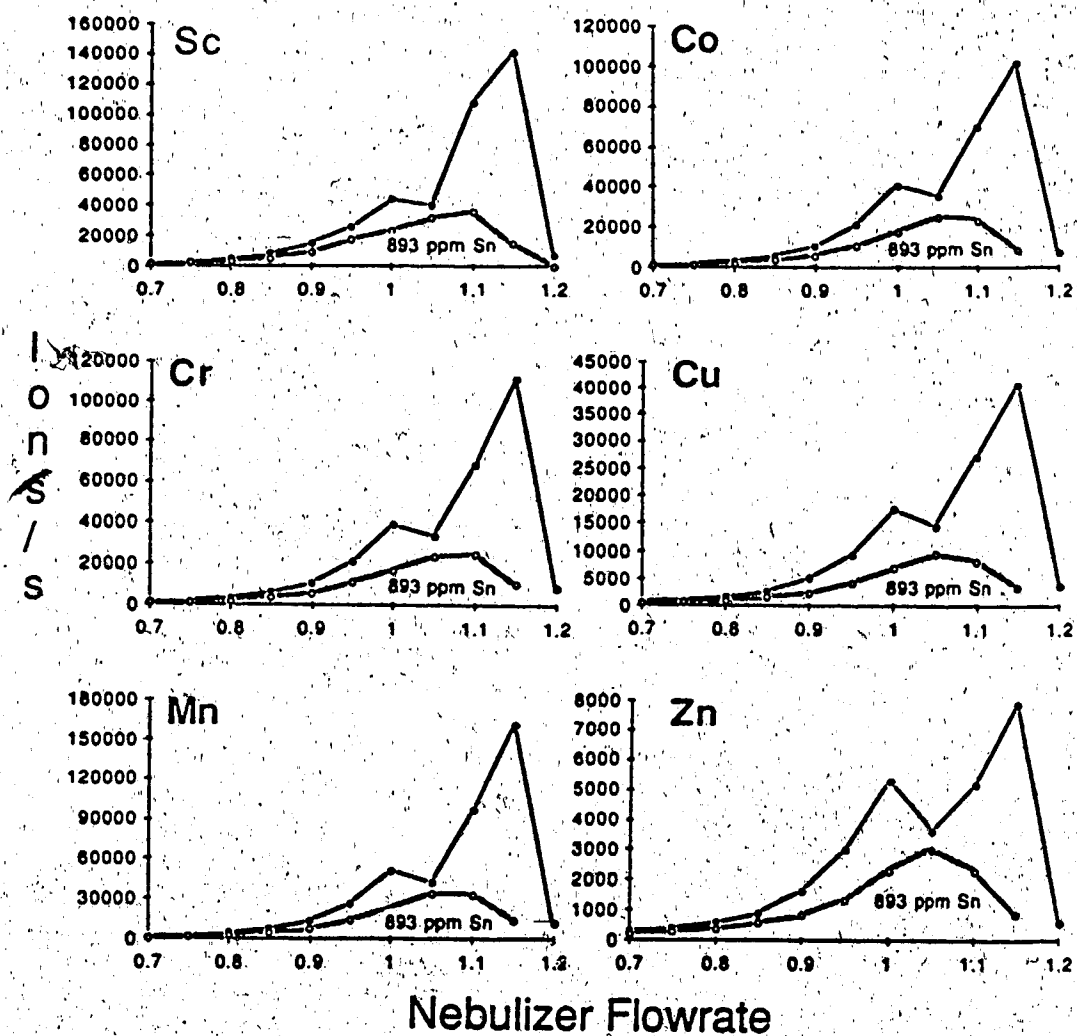


Figure 61. Effect of 893 ppm Sn on 1 ppm Sc, Cr, Mn, Co, Cu and Zn as a function of nebulizer flowrate.

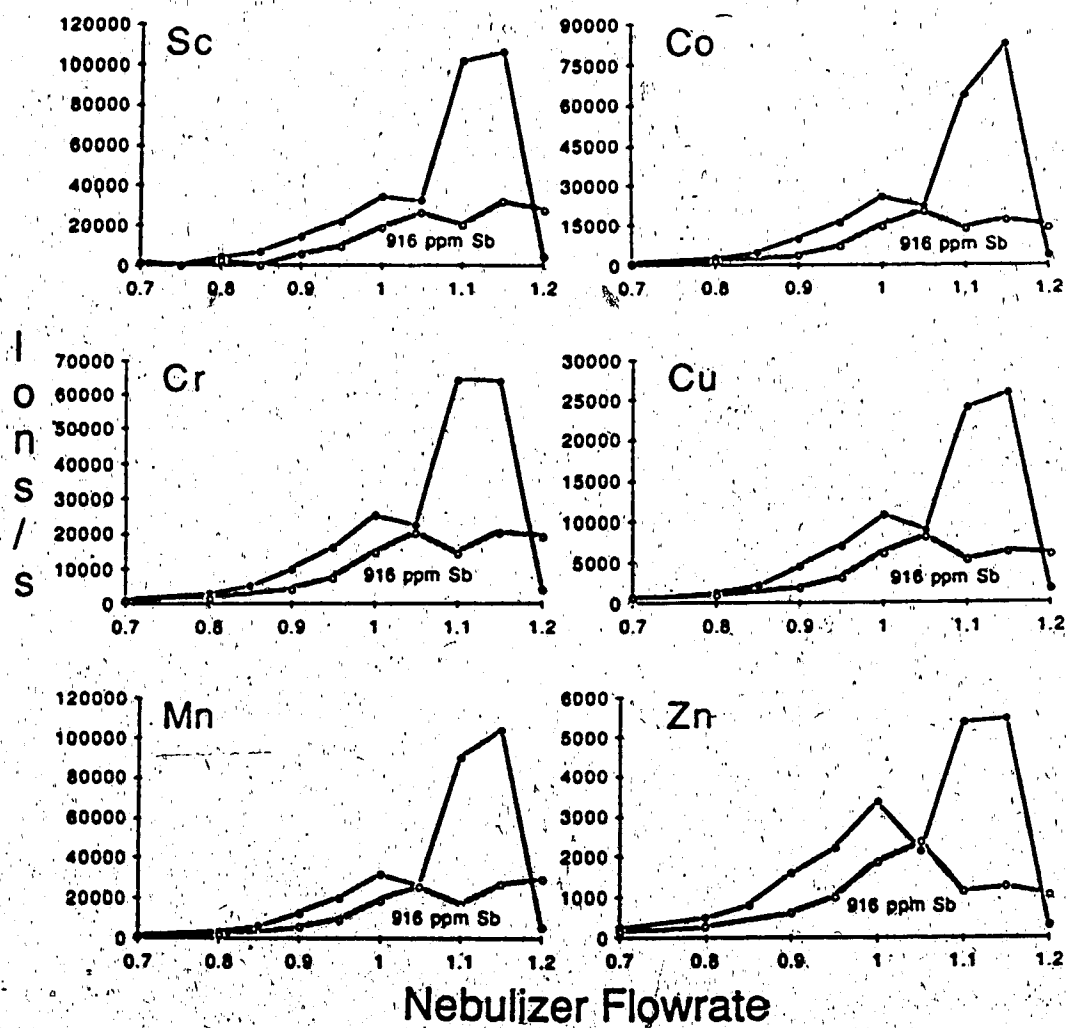


Figure 62. Effect of 916 ppm Sb on 1 ppm Sc, Cr, Mn, Co, Cu and Zn as a function of nebulizer flowrate.

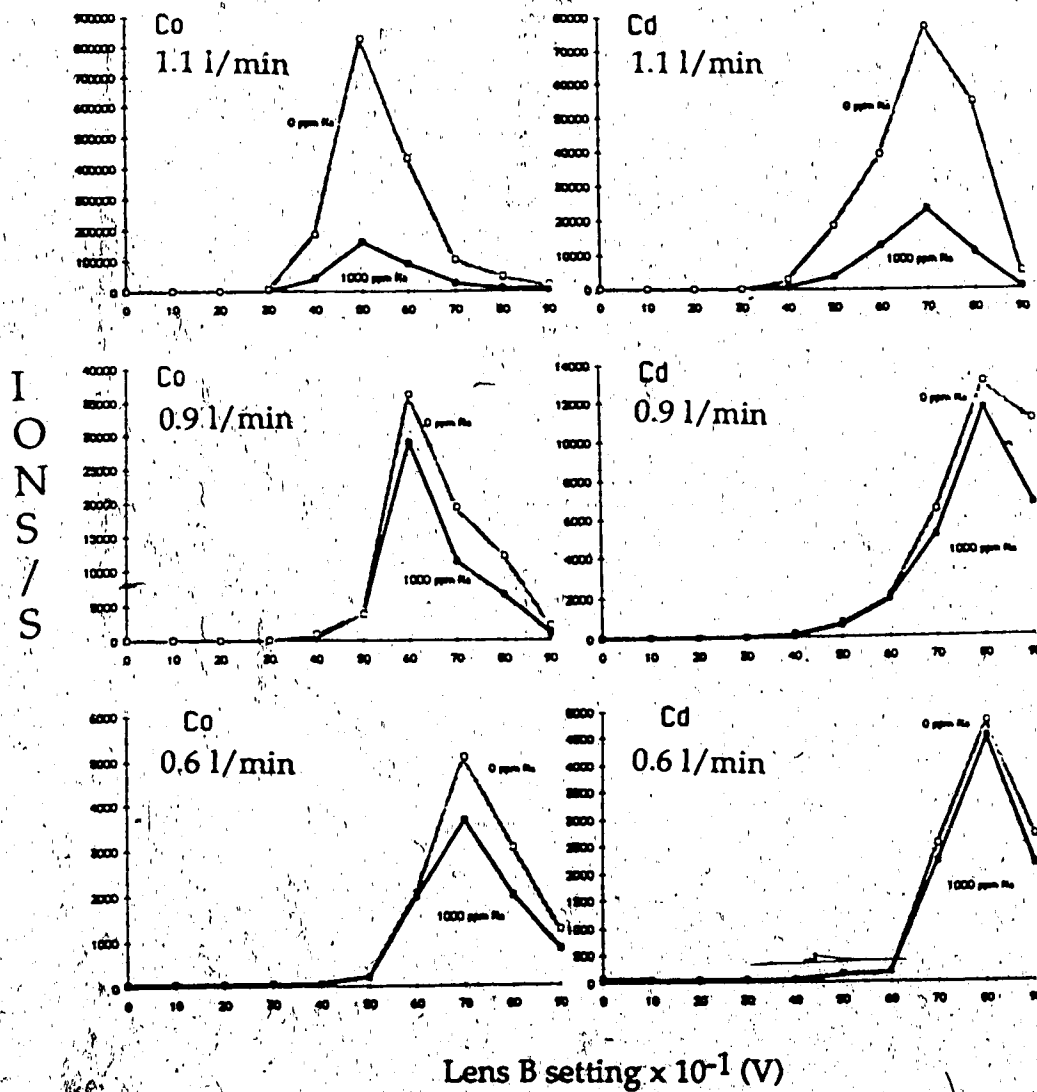


Figure 63. Dependence of matrix effect on the photon stop (lens B) for Co and Cd signals at nebulizer flowrates of 1.1, 0.9 and 0.6 l/min.

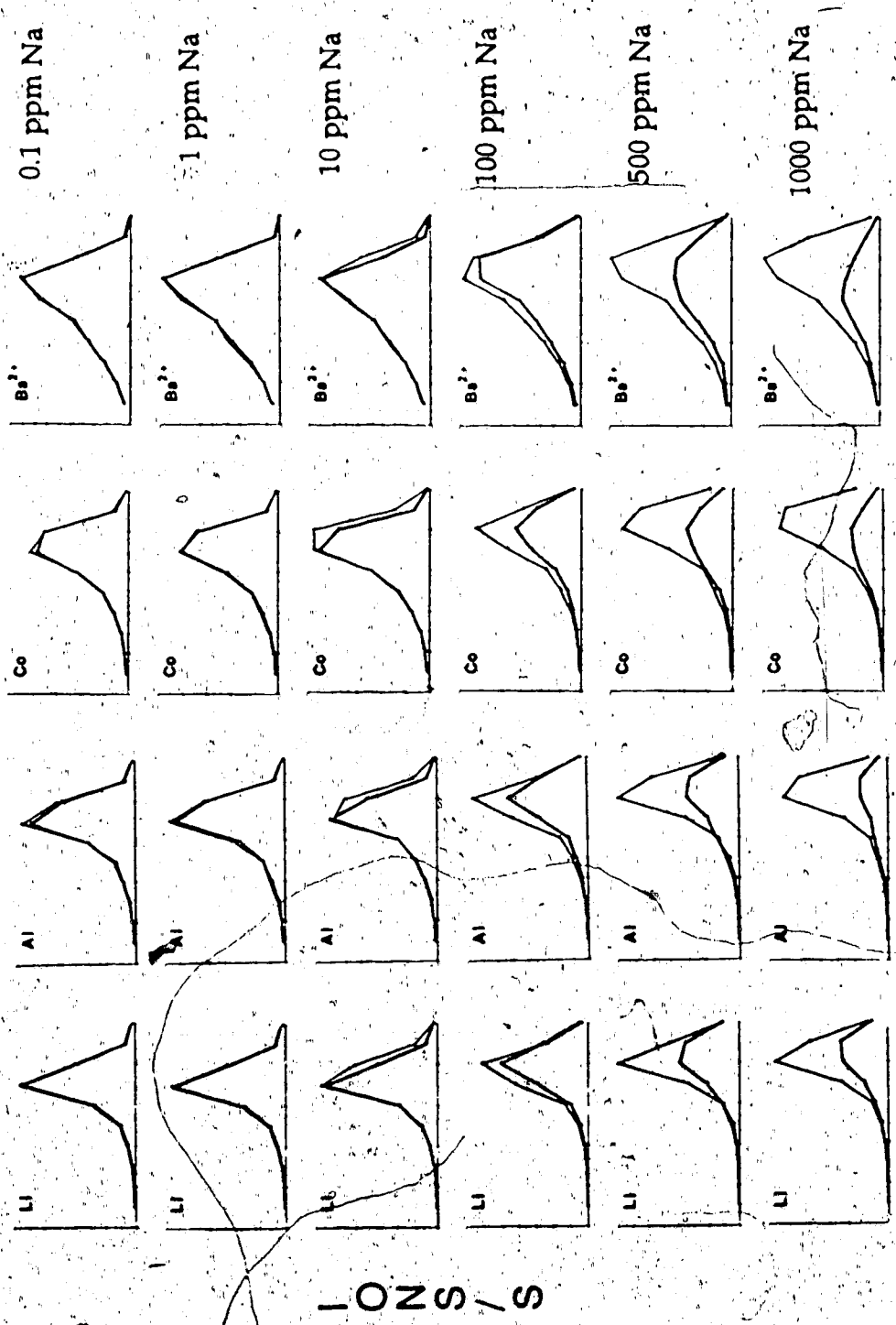


without matrix are reverse to that in other figures in this chapter. First, it can be seen that the maximum ion count for Co occurs at a lower voltage than that for Cd. At the nebulizer flowrate of 1.1 l/min, the maximum ion count for Co occurs at about 5.0 V whereas it occurs at about 7.0 V for Cd. This is because the ion kinetic energy of Co and Cd is different. For both elements, the peak signal occurs at higher lens voltage settings as the nebulizer flowrate is decreased. At a particular nebulizer flowrate setting, the amount of matrix suppression does not change significantly with changes in the photon stop voltage. The results show that even though the photon stop voltage may be set at a slightly different value for each experiment, the matrix effect observed is not significantly affected by the photon stop voltage.

#### F. Effect of Varying Concomitant Concentrations on Analyte Ion Signals

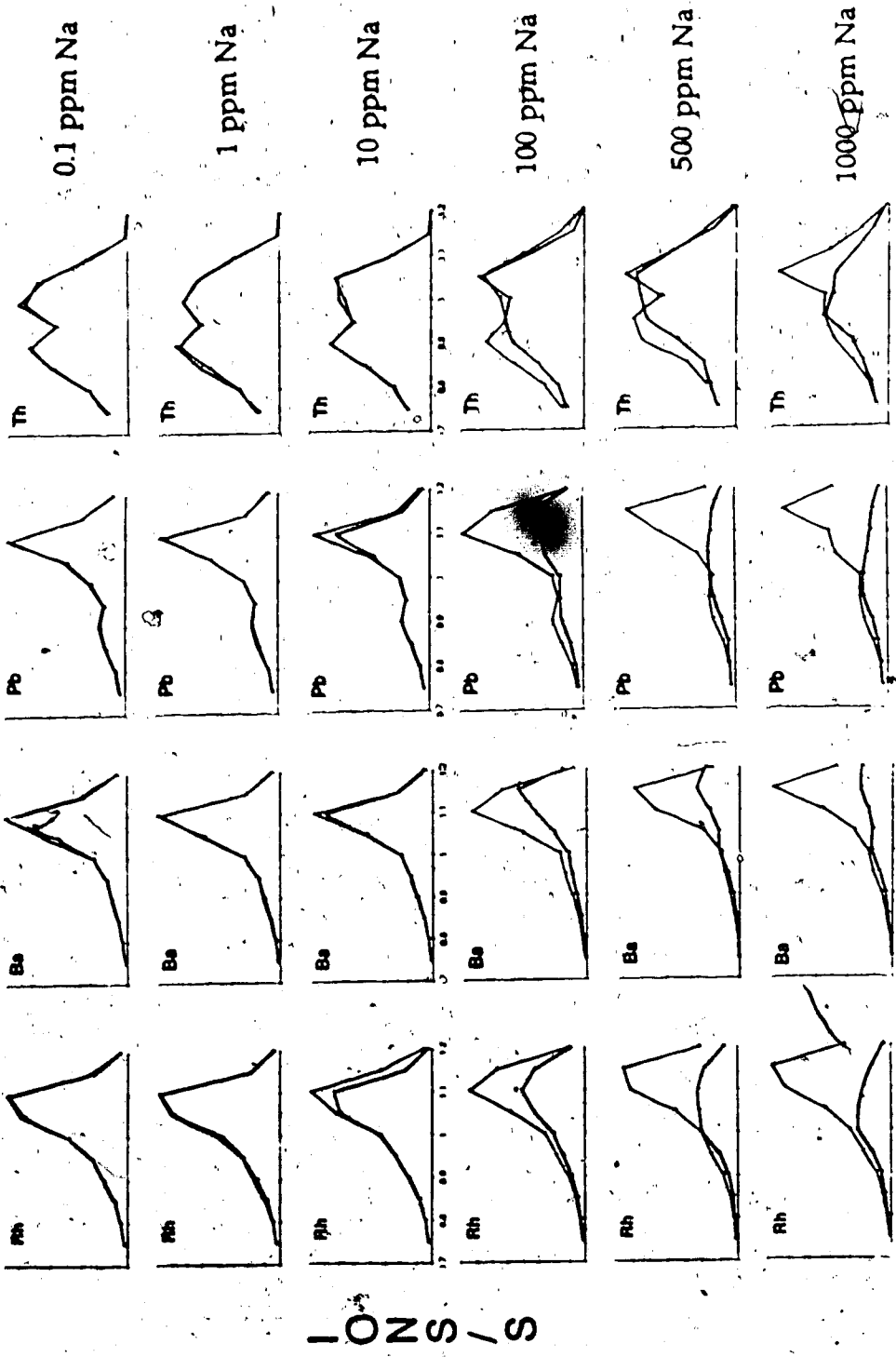
All the data in this section were acquired at a plasma power of 1.3 kW and at 15 mm from the load coil. The overall effect of different Na concentrations on 0.1 ppm Li, Al, Sc, Co, Ba<sup>2+</sup>, Ba, Pb and Th between the nebulizer flowrates of 0.7 l/min to 1.2 l/min is shown in Figures 64a and 64b. The concentrations of the Na matrix are 0.1 ppm, 1 ppm, 10 ppm, 100 ppm, 500 ppm and 1000 ppm from the top to the bottom. As expected, no matrix effect is observed for Na concentrations of 0.1 ppm and 1 ppm. An increasing matrix effect, however, is seen for Na concentrations higher than 10 ppm.

In order to have a clearer picture of the degree of the matrix effect, the percent matrix effect for the analyte elements Al, Co, Rh, Ba and Pb is plotted against Na concentration in Figure 65 for nebulizer flowrates of 0.9 l/min, 1.0 l/min and 1.1 l/min. At a nebulizer flowrate of 0.9 l/min, Na concentrations up to 10 ppm do not affect the analyte ion signal. For Na concentrations greater than 10 ppm, however, the analyte ion signals are increasingly



Nebulizer Flowrate L/min

Figure 64a. The effect of Na on 0.1 ppm Li, Al, Co and Ba<sup>2+</sup> as a function of Na concentration and nebulizer flowrate.



Nebulizer Flowrate L/min

Figure 64b. The effect of Na on 0.1 ppm Rh, Ba, Pb and Th as a function of Na concentration and nebulizer flowrate.

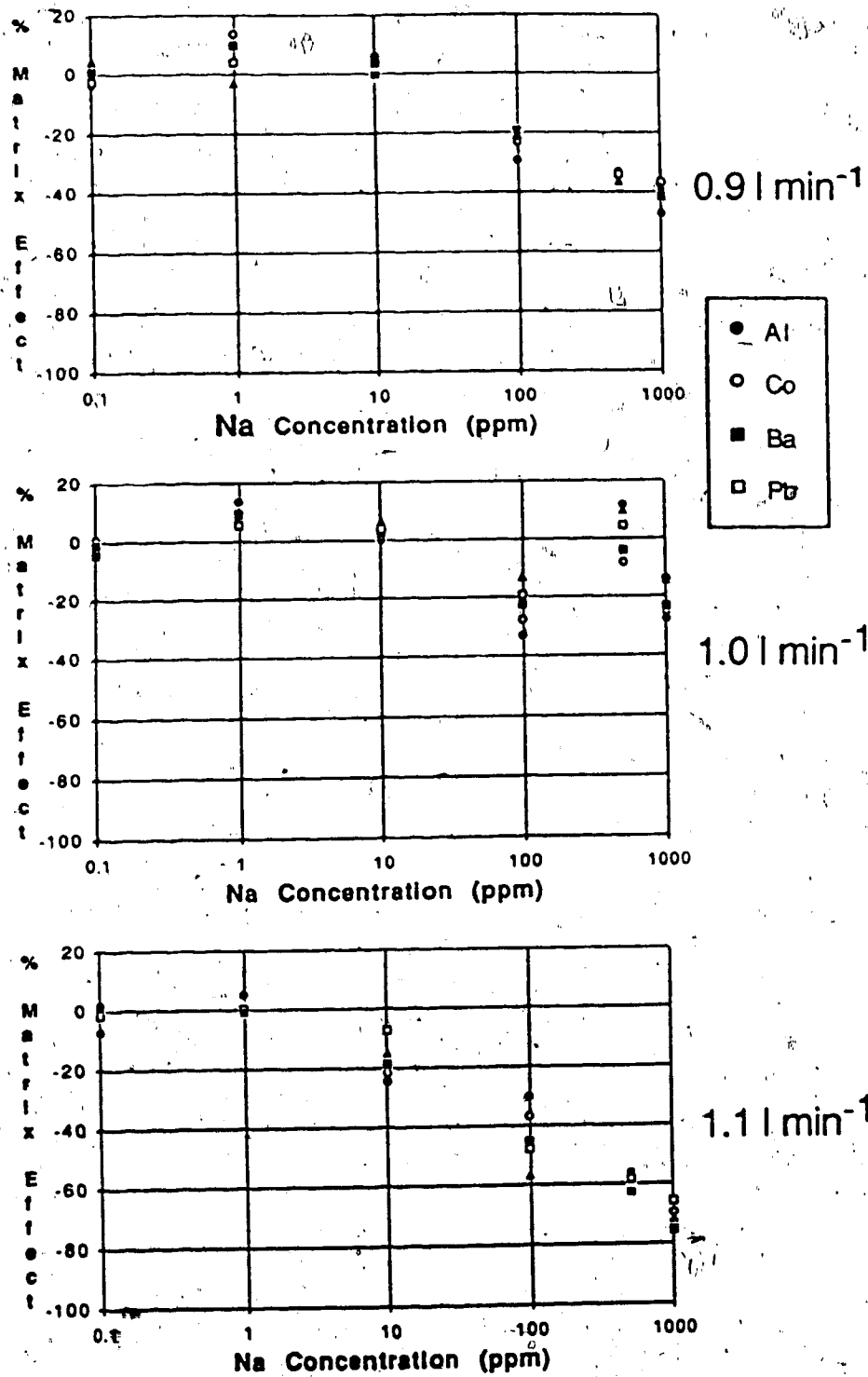


Figure 65. Matrix effect of Na on Al, Co, Ba and Pb as a function of Na concentration at nebulizer flowrates of 0.9, 1.0 and 1.1 l/min.

suppressed. The suppression effect is about 20 % at 100 ppm Na and it is about 40 % at 1000 ppm Na. All the analyte elements seem to be affected to about the same extent by different concentrations of the matrix element. Suppression of analyte ion signal is much greater at 1.1 l/min, which is the nebulizer flowrate at which maximum ion signals occurred for most elements. At this flowrate, significant matrix suppression of the analytes is observed even at 10 ppm Na and as much as 70 % suppression of the analyte signal is found with 1000 ppm Na.

Anomalous results were obtained for the nebulizer flowrate of 1.0 l/min. The matrix effects exerted by 500 ppm and 1000 ppm Na were less than that observed for 0.9 l/min. Indeed, with 500 ppm Na there is no significant matrix effect at all. Looking at Figure 64, one notices that the profiles of the parameter plots in the presence of 500 ppm and 1000 ppm Na are slightly shifted to lower nebulizer flowrates. Consequently, the suppression effects between the nebulizer flowrates of 0.95 l/min to 1.0 l/min are decreased. In other words, the absolute amount of ion count lost due to the presence of the Na matrix is about the same at all nebulizer flowrates lower than 1.0 l/min, but the ion signal detected increases with the nebulizer flowrate up to about 1.1 l/min. As a result, the percent matrix effect calculated for 1.0 l/min is lower than 0.9 l/min for 500 ppm and 1000 ppm Na.

Similar data acquired with Cs as the matrix element are shown in Figures 66a and 66b. From these data, it can be seen that there is no significant matrix effect associated with the presence of 0.1 ppm, 1.0 ppm and 10 ppm of Cs for all the three nebulizer flowrates. For matrix concentrations greater than 10 ppm, however, distinct changes in the analyte ion signals are seen. An interesting feature in this figure is that at 100 ppm Cs, there seems to be a shift in the parameter plot profiles of Li, Al, Sc, Co and Ba<sup>2+</sup> similar to that

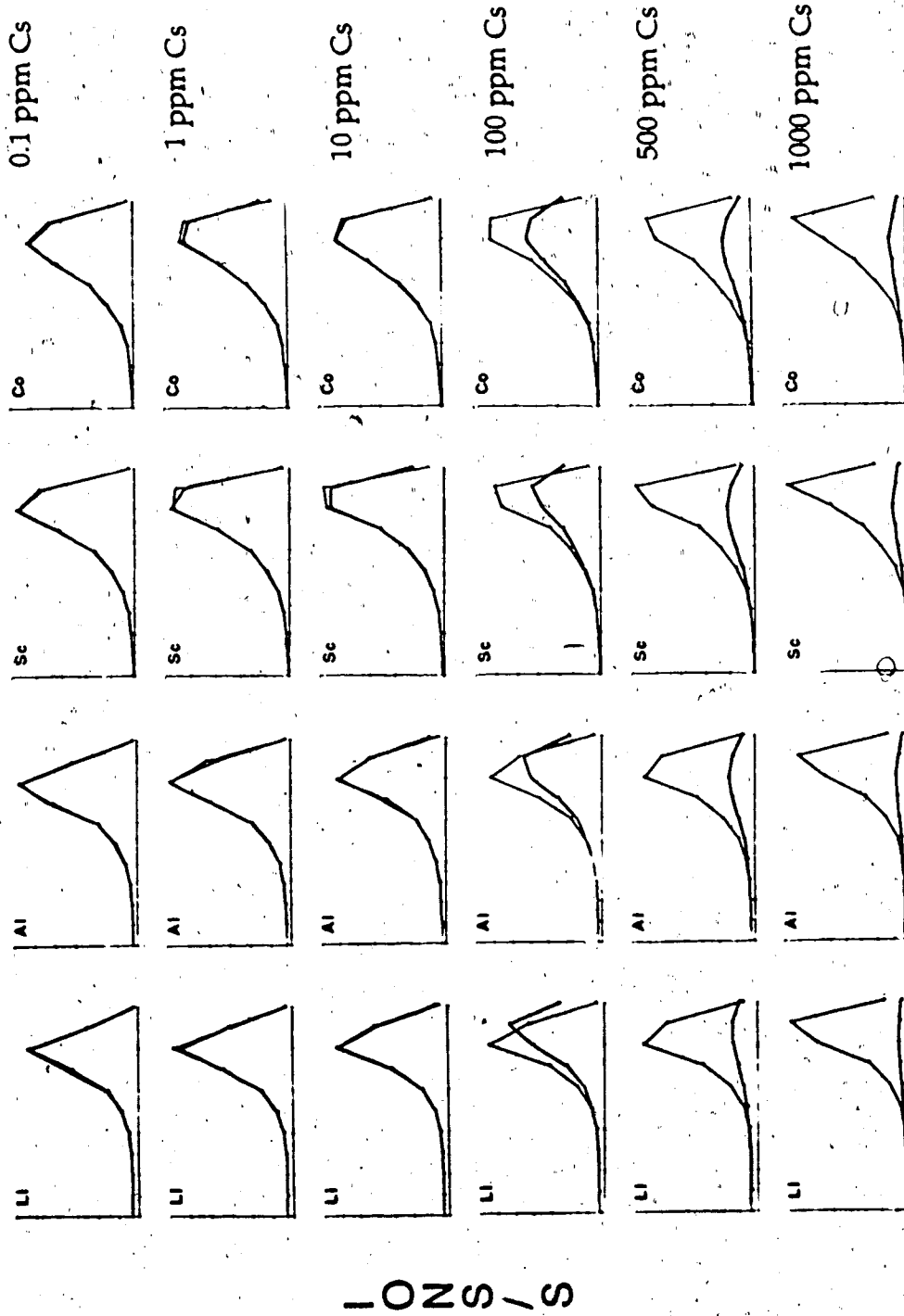
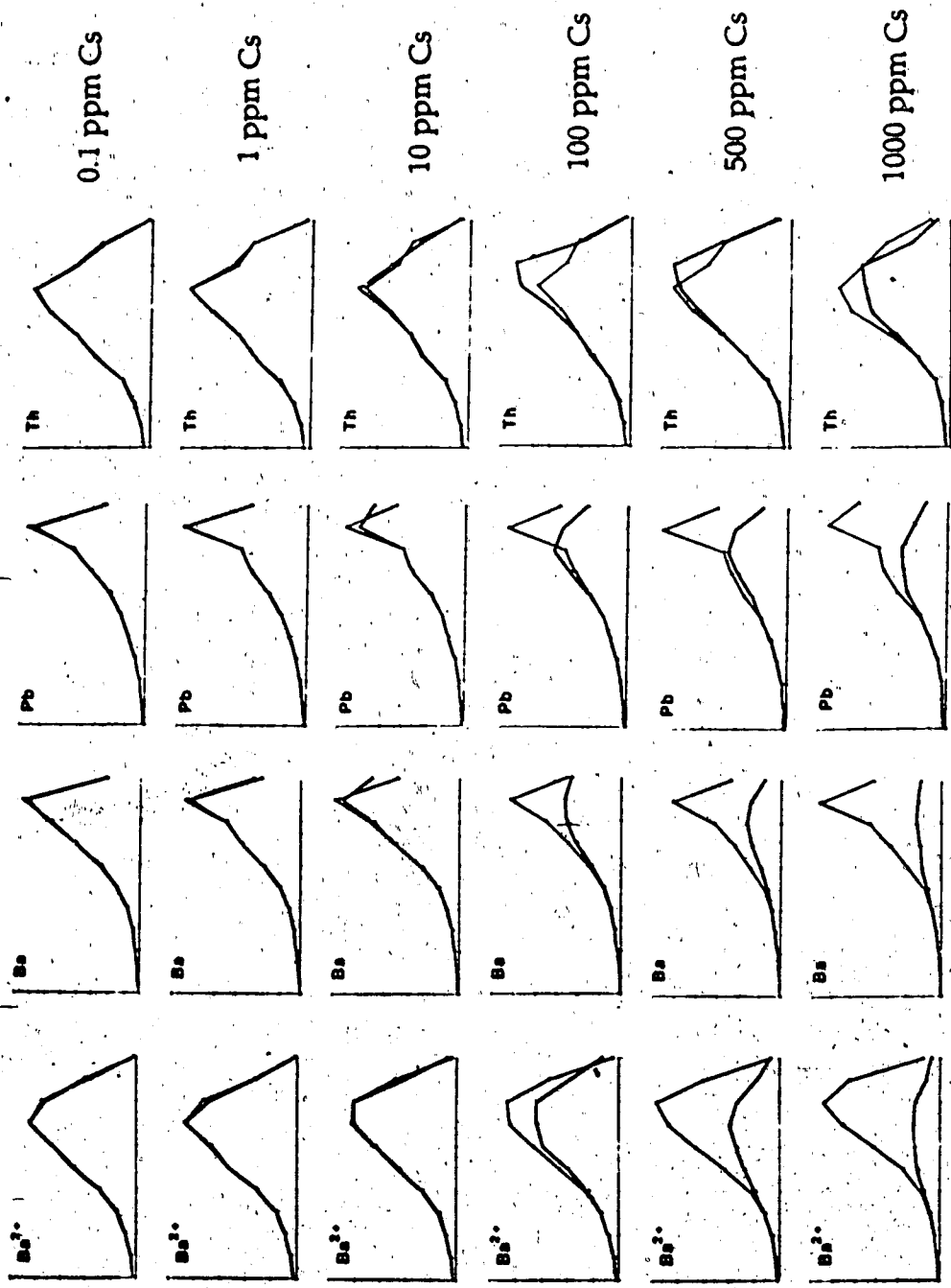


Figure 66a. The effect of Cs on 0.1 ppm Li, Al, Sc and Co as a function of Cs concentration and nebulizer flowrate.



Nebulizer Flowrate L/min

Figure 66b. The effect of Cs on 0.1 ppm Ba<sup>2+</sup>, Ba, Pb and Th as a function of Cs concentration and nebulizer flowrate.

IONS

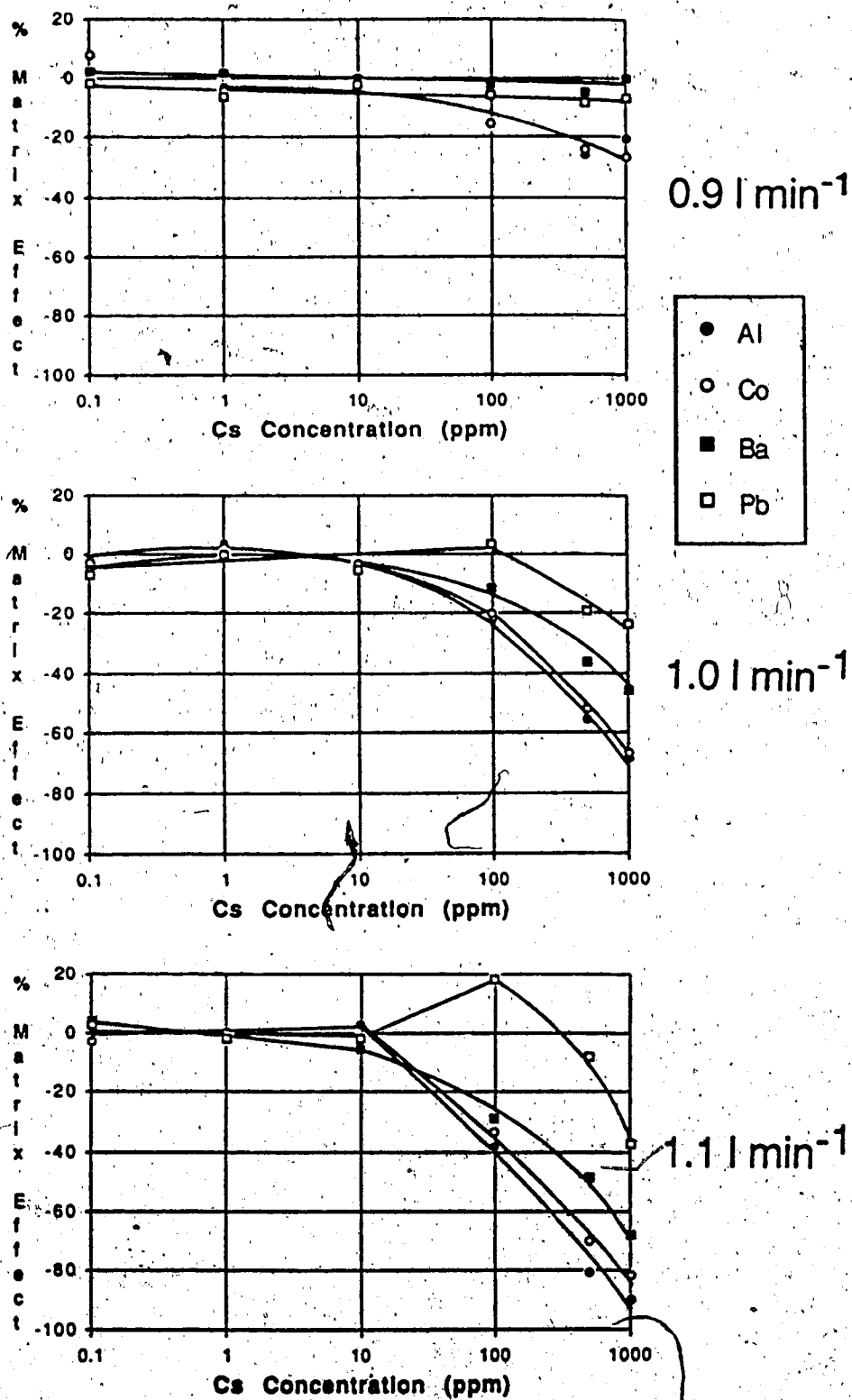


Figure 67. Matrix effect of Cs on Al, Co, Ba and Pb as a function of Cs concentration at nebulizer flowrates of 0.9, 1.0 and 1.1 l/min.



observed for Na in Figure 49. On comparison with Figures 64a and 64b, the amount of suppression exerted by equal concentrations of the matrix element seems to be greater for Cs as compared to Na. Notice too, that the matrix effect is greater for lighter analyte elements such as Li, Al, Sc and Co than for Pb and Th.

The percent matrix effect associated with the analyte elements Al, Co, Ba and Th in the presence of various concentrations of Cs are plotted in Figure 67 at nebulizer flowrates of 0.9 l/min, 1.0 l/min and 1.1 l/min. It is obvious from these data that no matrix effect is exercised on the analyte signals for matrix concentrations of less than 10 ppm Cs. In general, at Cs concentrations higher than 10 ppm, the matrix effect increases with an increase in the matrix concentration. As the nebulizer flowrate increases from 0.9 l/min to 1.1 l/min, the matrix suppression also increases steadily in severity. Unlike the Na matrix, the Cs matrix seems to affect individual analyte element differently depending on their masses. At each nebulizer flowrate, suppression of the ion signal is most severe for light elements such as Al and Co as compared to Ba and Pb. Indeed, for 0.9 l/min, no matrix effect is observed for Ba and Pb. This mass dependence of the matrix effect will be studied in greater detail in Chapter 6.

#### G. Matrix Effects for Solutions containing Constant Molar Ratio of Analyte Element to Matrix Element

The aim of this experiment was to study how the absolute salt concentration of a sample solution affects the matrix effect observed. The matrix elements studied were K and Zn. The analytes were Li, Al, Se, Co, Rh, Pt and Pb and their concentrations were  $2.2 \times 10^{-5}$  M which correspond to 1 ppm Se. The concentration of the matrix element was  $2.2 \times 10^{-2}$  M.

Therefore, the solution contained 1: 1000 molar ratio of the analyte to the matrix element. This solution was then diluted by 10 times and 100 times to obtain two other solutions. For each matrix element then, there are three sets of solutions; set 1 consisting of a  $2.2 \times 10^{-5}$  M analyte solution and a  $2.2 \times 10^{-5}$  M :  $2.2 \times 10^{-2}$  M of analyte and matrix element solution, set 2 consisting of a  $2.2 \times 10^{-6}$  M analyte solution and a  $2.2 \times 10^{-6}$  M :  $2.2 \times 10^{-3}$  M of analyte and matrix element, and set 3 consisting of a  $2.2 \times 10^{-7}$  M analyte solution and a  $2.2 \times 10^{-7}$  M :  $2.2 \times 10^{-4}$  M of analyte and matrix element solution. The three solutions containing a matrix element have different total molar concentrations but have the same constant molar ratio of analyte to matrix element. The composition of the solution in set 1 containing either K or Zn as the matrix element is listed in Table 13.

The results obtained for the K and Zn matrices are presented in Figure 68. The first column in the figure shows the matrix effects for  $2.2 \times 10^{-2}$  M K and Zn on the ion signals of  $2.2 \times 10^{-5}$  M Li, Al, Sc, Co, Rh, Pt and Pb. The concentrations of K and Zn are 860 ppm and 1430 ppm respectively. An overall suppression of ion signal is observed for all analytes at all nebulizer flowrates with K exerting more suppression effect than Zn. In the second column, the matrix effect of  $2.2 \times 10^{-3}$  M K and Zn on the analyte ion signal is illustrated. The suppression of the ion signal is not as severe for the diluted solution. In fact, at low nebulizer flowrates, there is an enhancement of ion signals. Further dilution of this solution by ten times results in an overall enhancement of analyte ion signals at all nebulizer flowrates as shown by the third column of Figure 68. The enhancement effect provided by the K matrix seems to be greater than that of the Zn matrix but the ion signals for some of the analyte elements are small, therefore, they could be more susceptible to background interferences.

Table 13. Concentration of the analytes and matrix elements used in Section G

| Analytes | $2.2 \times 10^{-5} \text{ M}$ | Matrix elements | $2.2 \times 10^{-2} \text{ M}$ |
|----------|--------------------------------|-----------------|--------------------------------|
| Li       | 0.15 ppm                       | K               | 860 ppm                        |
| Al       | 0.59 ppm                       | Zn              | 1430 ppm                       |
| Sc       | 1.0 ppm                        |                 |                                |
| Co       | 1.3 ppm                        |                 |                                |
| Rh       | 2.3 ppm                        |                 |                                |
| Ba       | 3.0 ppm                        |                 |                                |
| Pb       | 4.6 ppm                        |                 |                                |
| Th       | 5.1 ppm                        |                 |                                |

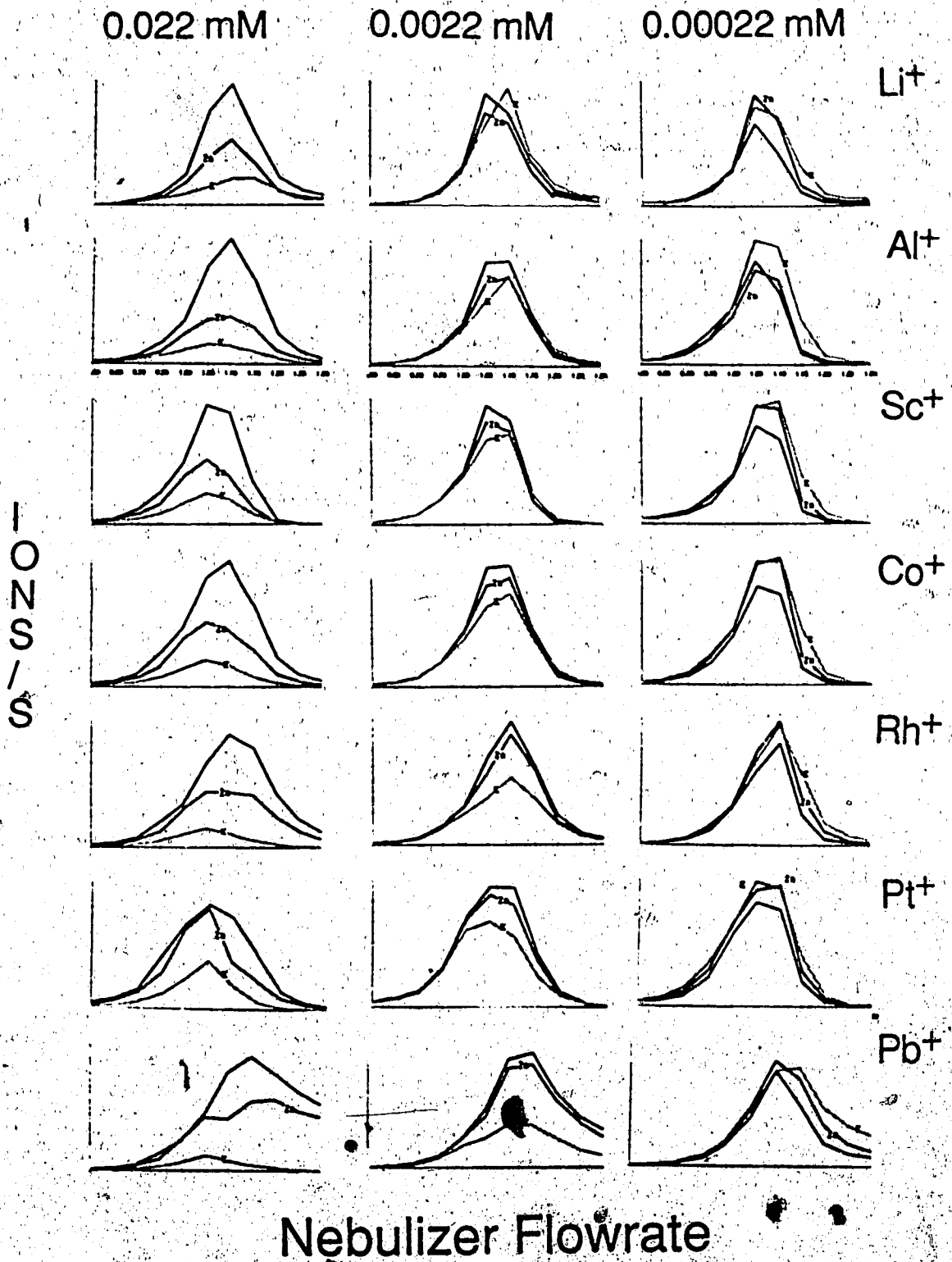


Figure 38. Effect of matrix element concentration (Zn and K) on analyte elements. Concentration listed for each column is that for the analyte element and the molar ratio of matrix to analyte is 1000:1 in all cases.

This set of data is indeed very interesting. It indicates that the matrix interference effect in ICP-MS is dependent on the total concentration of the sample solution. It appears that upon dilution, the nature of the matrix effect changes from one of major suppression to one of minor suppression and/or enhancement even though the molar ratio of analyte to matrix element remains at 1:1000.

#### H. Summary and Conclusion

From the results presented in this chapter it is clear that the presence of high concentrations of a concomitant salt in ICP-MS is a serious problem. It was seen that matrix interferences are dependent on the plasma operating conditions. For the range of sampling depths studied (15mm to 27 mm), matrix effects seem to be smallest at 15 mm. Matrix suppression is also very dependent on the nebulizer flowrate. At low flowrates (< 1.0 l/min), matrix suppression is minimal, then increases rapidly with increasing nebulizer flowrates. Therefore, in order to clarify matrix interferences in ICP-MS, it is important to study them with respect to variations in the plasma operating conditions, especially with respect to the nebulizer flowrate.

It was found that matrix suppression is dependent on the absolute matrix salt concentration and not the molar concentration ratio of the analyte to matrix element. This feature was clearly illustrated by the experiments in Sections F and G. When the concentration of the matrix element is high (>  $10^{-3}$  M), suppression of analyte ion signal is prevalent. As the absolute concentration of the matrix element is decreased to less than  $10^{-3}$  M, no matrix effect is observed even though the molar ratio of the analyte to matrix element is 1:1000. This indicates that matrix effects in ICP-MS can be minimized by dilution of the sample.

Another type of matrix interference results from the formation of the molecular species  $ArX$ , where  $X$  is any element present in high concentration in the plasma. The amount of  $ArX$  formed is dependent on the concentration of the matrix element and the plasma operating conditions.

Another important aspect in the study of matrix effects in ICP-MS is the memory effect associated with aspirating solutions containing high total salt concentrations. Memory effects in most instances appear to be due to the deposition of salt in the sampling orifices. For the experiments performed, it was found that memory effects were not a serious problem for concentrations less than 100 ppm but a 10 to 20 % unrecoverable loss of analyte ion signal may result if the total salt concentration exceeds 500 ppm. This loss of analyte ion signal is normally recovered when salt deposition is burnt off or when the sampling orifice is removed and cleaned. To estimate the memory effect in ICP-MS may prove to be a complex task, since it is dependent on several factors, such as the physical properties of the elements involved and the plasma operating conditions.

## CHAPTER 6

### MATRIX EFFECTS IN ICP-MS (PART 2)

#### A. Introduction

It is evident from Chapter 5 that ICP-MS is very susceptible to interferences from comparatively low concentrations of matrix elements. Matrix concentrations of 1000 ppm seriously suppress analyte ion signals by up to 80 %. Mechanisms giving rise to matrix interferences in ICP-MS are likely complex. Matrix interferences may not only originate from processes occurring in the ICP system but also from processes occurring in the ion sampling interface and mass spectrometer. A feature of matrix interference in ICP-MS is its dependence on the mass of analyte elements. In this chapter, the dependence of matrix effect on the mass of the matrix element and analyte element in ICP-MS is investigated in more detail. The matrix effects of 12 matrix elements on 8 analyte elements are studied. The matrix elements investigated are B, Na, K, Cr, Zn, Rb, Cd, In, Cs, Au, Tl and U. The analyte elements studied are Li, Al, Sc, Co, Rh, Ba, Pb and Th.

#### B. Experimental

The plasma operating conditions for the experiments were as follows;

Rf power : 1.3 kW

Plasma gas flowrate : 11.0 l/min

Auxiliary gas flowrate : 1.4 l/min

Nebulizer gas flowrate : 0.7 - 1.2 l/min

Sampling depth : 15 mm

The instrumental data acquisition conditions used were;

Resolution mode : low

Data points/peak : 9

Integration time/data point : 0.1 s

Repeats of measurement : 5

The lens settings on the mass spectrometer were optimized to obtain maximum Cu ion counts. As mentioned before a mass flow controller was installed on the aerosol carrier gas flow to provide precise control of this flowrate. Solutions were delivered to a Meinhard nebulizer by a peristaltic pump in order to maintain a constant uptake rate in the event that the solution viscosities changed as a result of altering the matrix concentrations.

All solutions were made up in 2 % nitric acid using distilled/deionized water. Solutions containing equi-molar concentration of the matrix elements, B, Na, K, Cr, Zn, Rb, Cd, In, Cs, Au, Tl and U were prepared. The matrix concentration used was  $4.2 \times 10^{-3} \text{ M}$  which is equivalent to 1000 ppm U. All solutions except for Tl and U were prepared from their corresponding chloride salts. The Tl solution was prepared from thallium oxide and the U solution was prepared from uranium sulfate. The chemicals used were carefully selected to minimize contamination to the analyte elements. The analyte concentration in these solutions was 1 ppm of Li, Al, Sc, Co, Rh, Ba, Pb and Th. Since the concentration of the solutions was sufficiently dilute, the uptake rate and the efficiency of the concentric nebulizer, hence, the amount of analyte that was transferred to the plasma, should not be substantially altered in these different matrices. The concentrations in ppm and some properties of the matrix elements and analytes are listed in Table 14.

The data for this study were acquired in the following manner. First, the ion signals of the analytes without matrix were measured at nebulizer flowrates beginning from 0.7 l/min to 1.2 l/min at 0.05 l/min intervals, then,



Table 14. Mass, ionization potential and degree of ionization of matrix elements and analyte elements

| <u>Matrix Elements</u> | <u>Conc</u><br>( $4.2 \times 10^{-3} M$ ) | <u>Mass</u> | <u>IP (eV)</u>    | <u>Degree of Ionization (%)</u> <sup>*1</sup> |
|------------------------|---|-------------|-------------------|---|
| B                      | 45 ppm                                    | 10.81       | 8.298             | 62.03   |
| Zn                     | 275 ppm                                   | 65.38       | 9.394             | 74.50   |
| Cd                     | 472 ppm                                   | 112.41      | 8.993             | 85.43   |
| Au                     | 827 ppm                                   | 196.97      | 9.225             | 48.87   |
| Na                     | 97 ppm                                    | 22.99       | 5.139             | 99.91   |
| K                      | 164 ppm                                   | 39.10       | 4.341             | 99.97   |
| Cr                     | 218 ppm                                   | 51.99       | 6.766             | 98.89   |
| Rb                     | 359 ppm                                   | 85.47       | 4.177             | 99.98   |
| In                     | 482 ppm                                   | 114.82      | 5.786             | 99.42   |
| Cs                     | 559 ppm                                   | 132.91      | 3.894             | 99.98   |
| Tl                     | 858 ppm                                   | 204.38      | 6.108             | 99.38   |
| U                      | 1000 ppm                                  | 238.03      | 6.3 <sup>*3</sup> | 100 <sup>*2</sup>                             |

| <u>Analyte Elements</u> | <u>Conc</u> | <u>Mass</u> | <u>IP (eV)</u>    | <u>Degree of Ionization (%)</u> <sup>*1</sup> |
|-------------------------|-------------|-------------|-------------------|---|
| Li                      | 1 ppm       | 6.94        | 5.392             | 99.85   |
| Al                      | 1 ppm       | 26.98       | 5.986             | 98.92   |
| Sc                      | 1 ppm       | 44.96       | 6.54              | 99.71   |
| Co                      | 1 ppm       | 58.93       | 7.86              | 94.83   |
| Rh                      | 1 ppm       | 102.91      | 7.46              | 95.87   |
| Ba                      | 1 ppm       | 137.33      | 5.212             | 99.96   |
| Pb                      | 1 ppm       | 207.2       | 7.416             | 97.93   |
| Th                      | 1 ppm       | 232.03      | 7.5 <sup>*3</sup> | 100 <sup>*2</sup>                             |

\*1 by Furuta from reference [16] calculated using  $T_{ion} = 6680 K$ ,  $n_e = 1.475 \times 10^{14} cm^{-3}$

\*2 by Houk from reference [15] calculated using  $T_{ion} = 7500 K$ ,  $n_e = 1 \times 10^{15} cm^{-3}$

\*3 Ionization potentials from reference [79]

the ion signals of the analytes with a matrix element present were similarly measured at nebulizer flowrates beginning from 0.7 l/min to 1.2 l/min. The above procedure was repeated for each matrix element. Each set of data measured for nebulizer flowrates of 0.7 l/min to 1.2 l/min was acquired in about 15 to 20 mins. The matrix effect at each nebulizer flowrate was then calculated as follows. An average analyte ion signal for the solution containing no matrix element was first obtained. This average ion signal was obtained by averaging the analyte signals for the solution without a matrix element measured just before and after the solution containing a matrix element. This was done in order to compensate for any drift in the ion signals. The difference between the average ion signal (with no matrix) and the ion signal (with a matrix element) was then divided by the average ion signal (with no matrix) to give the matrix effect, which is expressed as a percentage in most plots.

### C. Precision and Reproducibility of Data

In an evaluation of the errors in the data, two important factors have to be considered. They are the precision of the ion signal obtained from 5 repeat measurements at a particular nebulizer flowrate and the reproducibility of the ion signal obtained about one half hour later at the same nebulizer flowrate. In general, the relative standard deviation for 5 repeats is about 1-5% except at the low (< 0.8 l/min) or high (>1.1 l/min) nebulizer flowrates. At these two extremes, the relative standard deviation can be as high as 10% because the ions counts are low.

The reproducibility of two data points obtained about one half hour apart at the same nebulizer flowrate is dependent on the drift of the instrument and the precision in resetting to the same nebulizer flowrate with

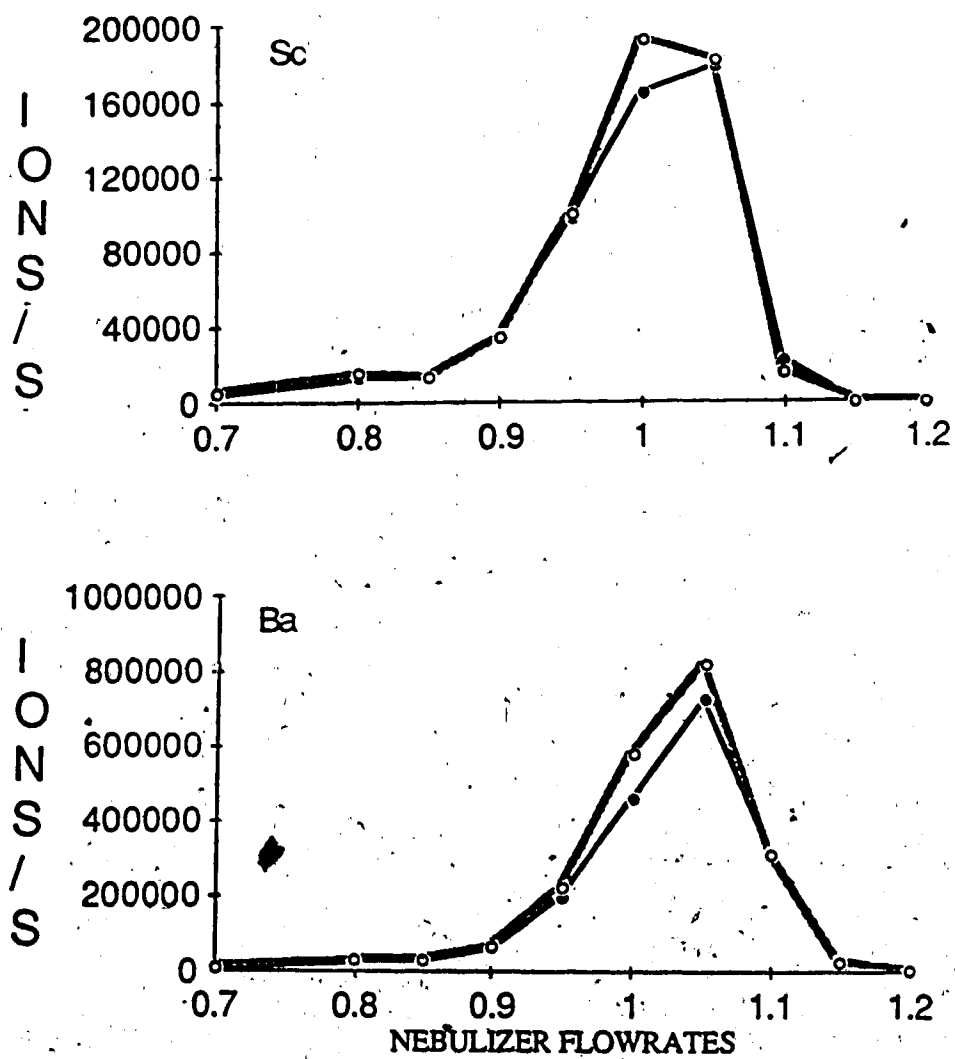


Figure 69. Reproducibility of two nebulizer flowrate parameter plots for Sc and Ba taken one-half hour apart.

the mass flow controller. Under normal working conditions the drift of the ion signal over one hour was about  $\pm 10\%$ . The mass flow controller can be reset to  $\pm 0.01$  l/min. Examples of the reproducibility of 2 sets of data are shown in Figure 69 for Sc and Ba. At low nebulizer flowrates ( $< 0.95$  l/min), reproducibility is reasonably good and is greater than 95%. At these nebulizer flowrates, the change in the ion signal with a change in the nebulizer flowrate is gradual, hence the ion signal is not affected significantly by any imprecision involved in resetting the mass flow controller. But at higher flowrates, reproducibility tends to be poor because of the steeper slope of the parameter plot. Imprecision in resetting the mass flow controller to the same nebulizer flowrate can adversely affect the reproducibility in this region. As the nebulizer flowrate cannot be reset to better than  $\pm 0.01$  l/min, an error of as much as 15% can occur between two runs at nebulizer flowrates of 1.0 l/min to 1.2 l/min where the change of ion counts with flowrate is rapid.

#### D. Matrix Effects at a Nebulizer Flowrate of 0.9 l/min

As seen from the data presented in Chapter 5, matrix effects vary significantly with nebulizer flowrate. In addition, matrix effects were also found to be dependent on the mass of the matrix element. The matrix effects exerted by  $4.2 \times 10^{-3}$  M of B, Na, Zn, Rb, Cd, Cs, Au, Tl, U on the ion signal of 1 ppm Sc are shown in Figure 70 for a nebulizer flowrate of 0.9 l/min. In this figure, the percentage matrix effect is plotted against the mass of the matrix element. It can be seen that suppression of the Sc ion signal increases with an increase of the mass of the matrix elements and a zig-zag line is obtained. If the matrix elements are separated into 2 groups, the first group with high ionization potentials (B, Zn, Cd and Au) and the second group with low ionization potentials (Na, Rb, Cs, Tl and U), two smooth distinct lines are

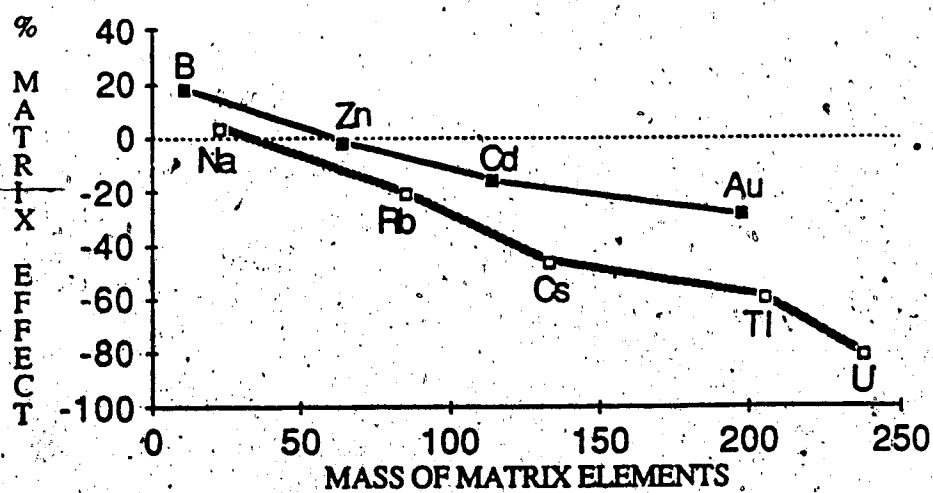
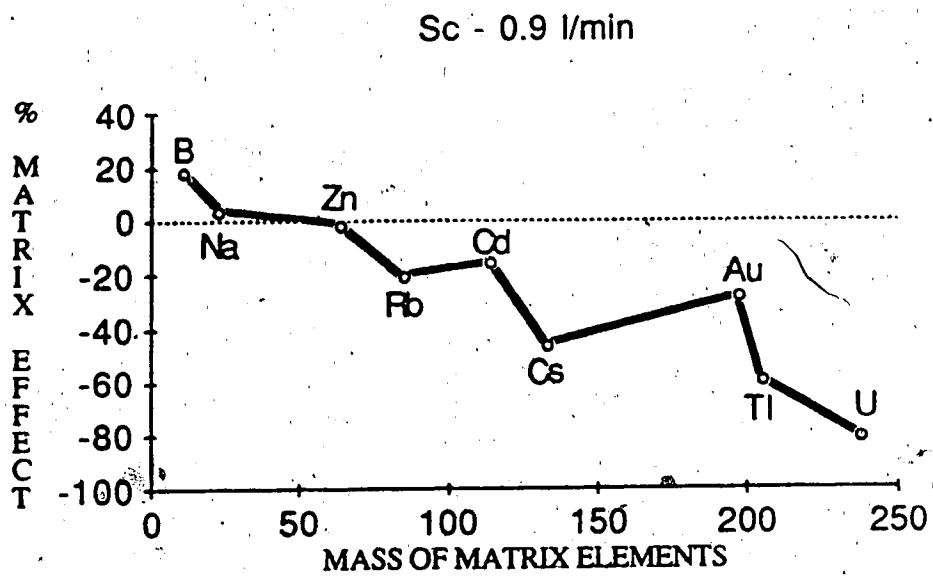


Figure 70. Matrix effects on Sc for equi-molar amounts ( $4.2 \times 10^{-3} M$ ) of the matrix elements B, Na, Zn, Rb, Cd, Cs, Au, Tl and U.

obtained. This shows that matrix elements with high ionization potentials (B, Zn, Cd, Au) cause less suppression of the Sc ion signal than the more easily ionized matrix elements (Na, Rb, Cs, Tl, U). However, for both groups of matrix elements, the suppression of the Sc ion signal increases with the mass of the matrix element. The dependence of a matrix effect on the mass of the matrix element has never been observed in ICP-AES and this mass effect most likely originates from processes occurring at the extraction interface and in the mass spectrometer.

In Figure 71, the matrix effects for all the analyte elements, Li, Al, Sc, Co, Rh, Ba, Pb and Th, are plotted against the mass of the matrix elements in the same format as for Figure 70. Each frame in Figure 71 illustrates the matrix effect for each analyte element at a nebulizer flowrate of 0.9 l/min. If one examines Figure 71 beginning with the plot for Li in the first column through Al, Sc, Co, to Rh in the second column, it can be seen that the overall matrix effect decreases with an increase in the mass of the analyte element. For analyte elements in the second column (Rh, Ba, Pb and Th), enhancement of ion signals is observed for matrix elements with a high ionization potential. It can also be seen that there is little if any suppression of the ion signals of Pb and Th in the easily ionized matrices except for uranium.

The dependence of matrix effect on the masses of the analyte and matrix element is clearly seen if the data in Figure 71 are replotted as shown in Figure 72. In the top frame of Figure 72, the matrix effects experienced by Al, Co, Rh, Ba and Th in the high ionization potential matrices are shown. In the lower frame of Figure 72, the matrix effects experienced by the same group of analytes in the easily ionized matrices are shown. The matrix elements are indicated on the mass axes at their appropriate masses. In both matrices, it is

0.9 l/min

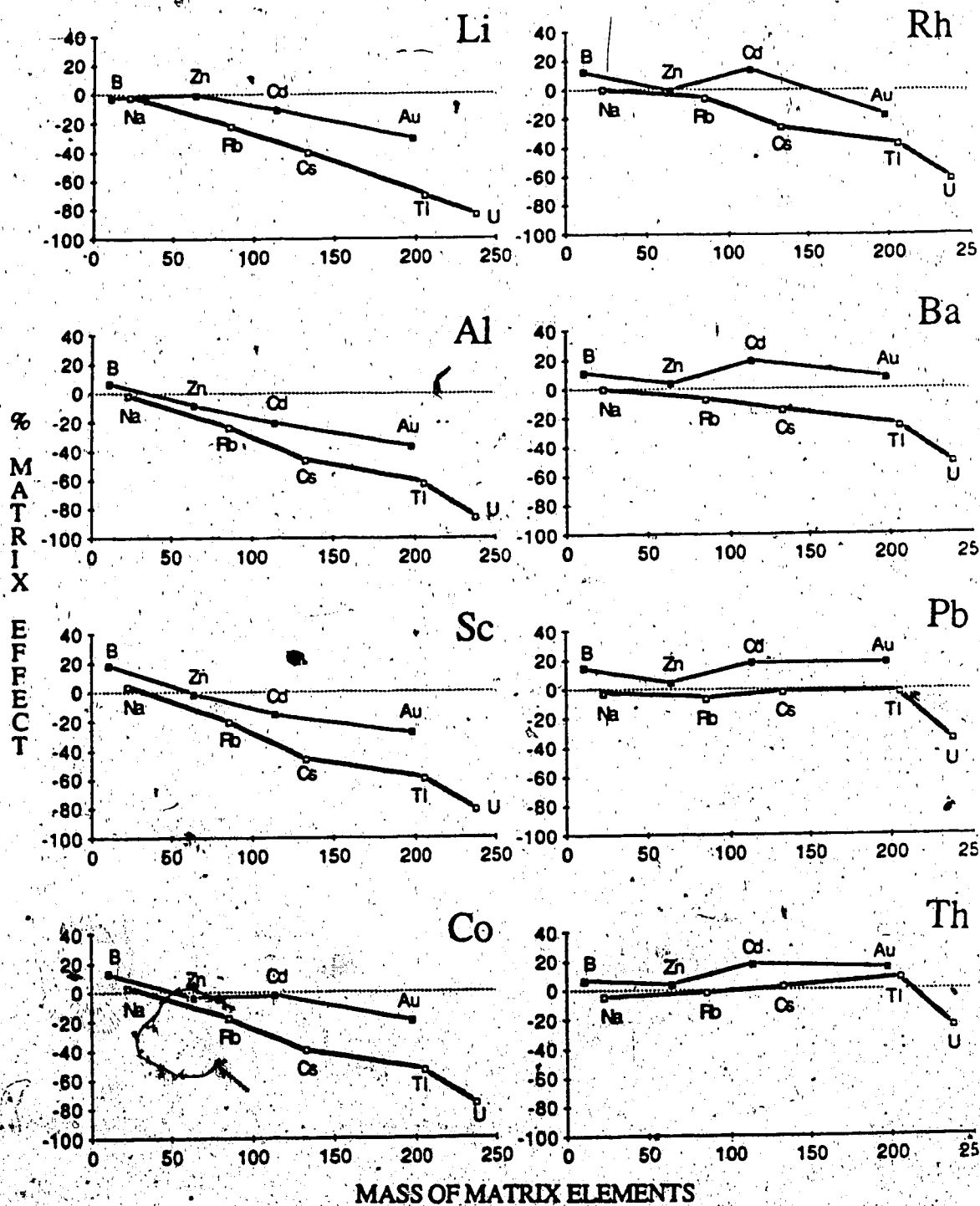


Figure 71. Matrix effects on Li, Al, Sc, Co, Rh, Ba, Pb and Th for equi-molar amounts of matrix elements.

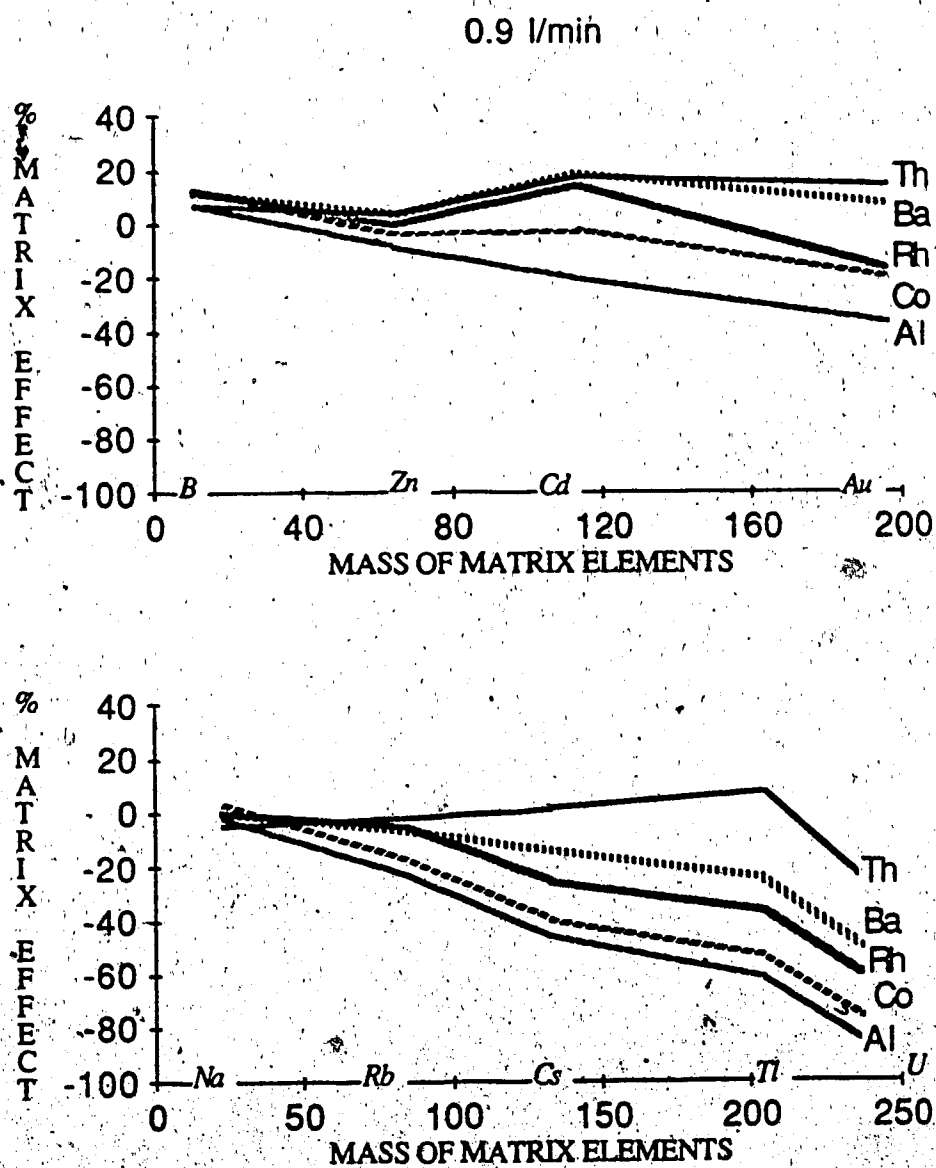


Figure 72. Matrix effect on Al, Co, Rh, Ba and Th as a function of the mass of the matrix element for high ionization potential matrices (upper graph) and for low ionization potential matrices (lower graph).



clearly seen that light analyte elements such as Al and Co are suppressed more severely than the heavier analyte elements such as Rh, Ba and Th.

Also, suppression of the analyte signals is most severe in matrices containing heavy matrix elements such as Au or U as compared to light matrix elements like Zn or Na.

In Figure 73, the variation of matrix effects with the mass of the analyte element for both classes of matrix elements is clearly illustrated. In the top diagram, the dependence of matrix effect on the mass of the analyte in the presence of the high ionization potential matrix element is shown. In the lower diagram, the dependence of the matrix effect in the lower ionization potential matrix elements is shown. Clearly, the high ionization potential matrix elements exert less suppression of all analyte ion signals as compared to the lower ionization potential matrix elements. In addition, analyte elements with a mass greater than 150 experienced relatively small matrix interference effects in both types of matrices except the U matrix.

An interesting set of data is shown in Figure 74. Data are presented that compare the mass dependency of the matrix effect for  $Ba^+$  and  $Ba^{2+}$  analyte signals. These data indicate that for analyte, it is the mass to charge ratio that is important in determining the degree of the matrix effect. The matrix effect trends observed for  $Ba^{2+}$  ( $m/z = 69$ ) as shown in the top of Figure 74 are clearly more similar to a lighter element such as  $Co^+$  ( $m/z = 59$ ) as shown in Figure 71.

E. Matrix Effects at Nebulizer Flowrates of 0.8, 0.85, 0.9, 0.95, 1.0 and 1.05 l/min

Overall matrix effects on the analytes (Li, Al, Co, Rh, Ba, Pb and Th) are plotted against the mass of the matrix elements in Figure 75 for nebulizer

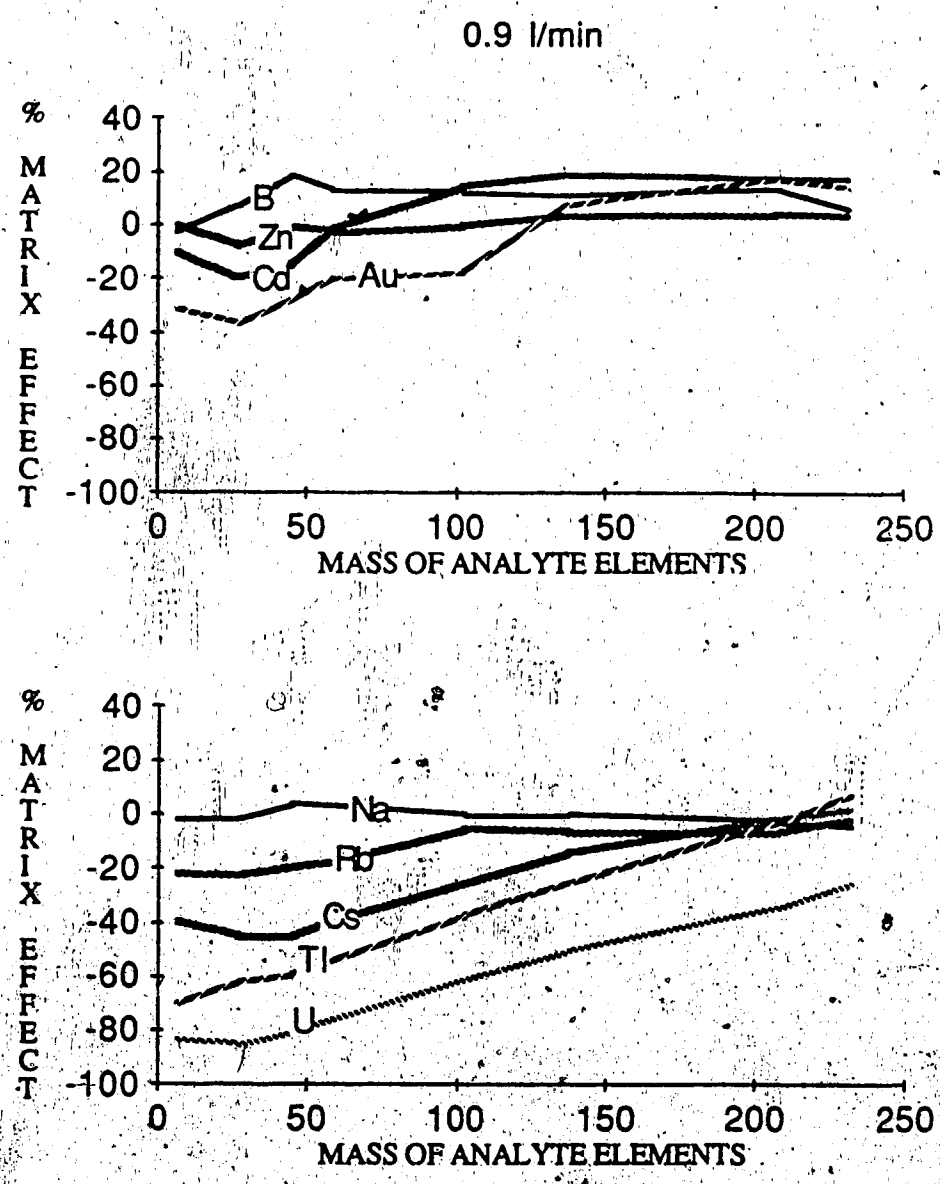


Figure 73. Matrix effect as a function of the mass of the analyte for high ionization potential matrices (upper graph) and for low ionization potential matrices (lower graph).

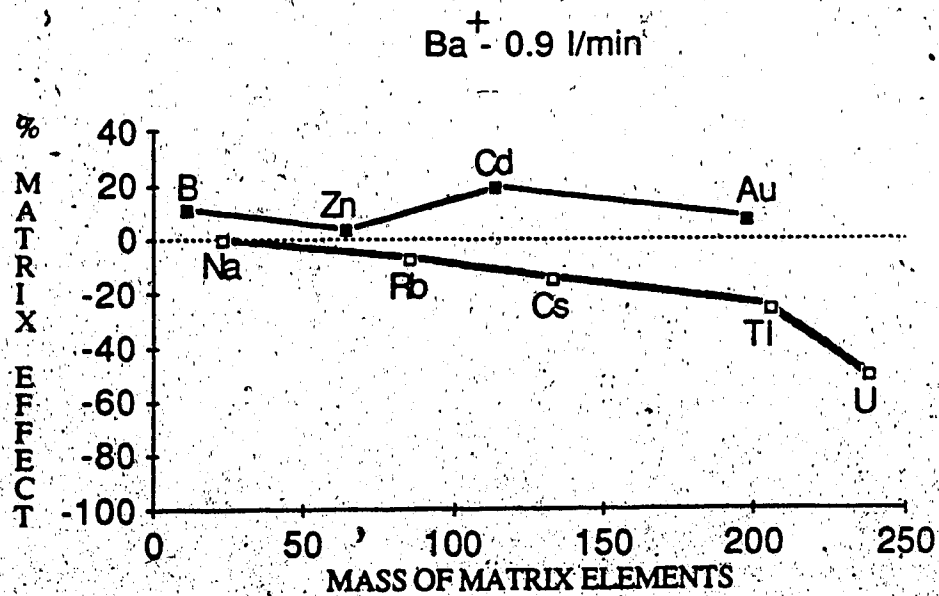
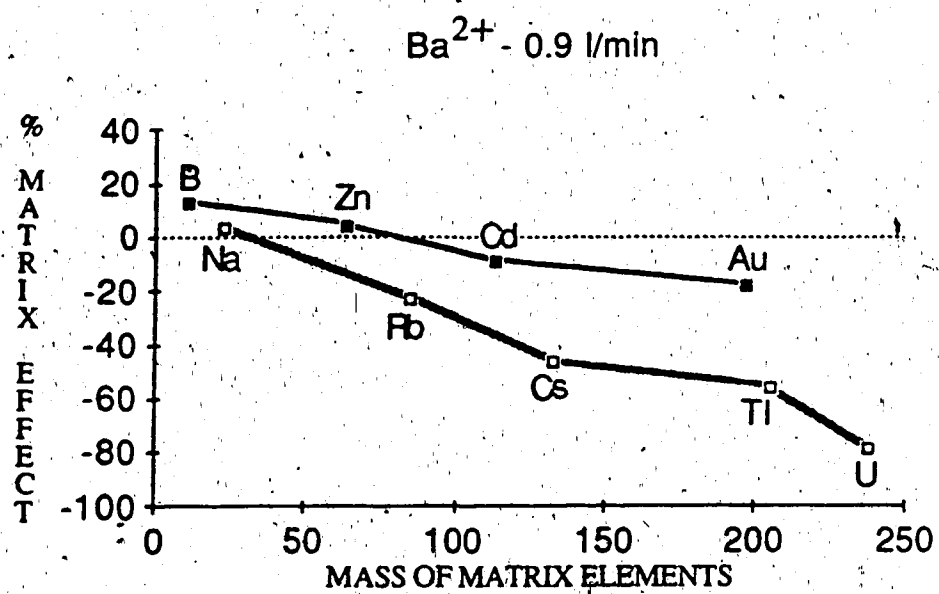
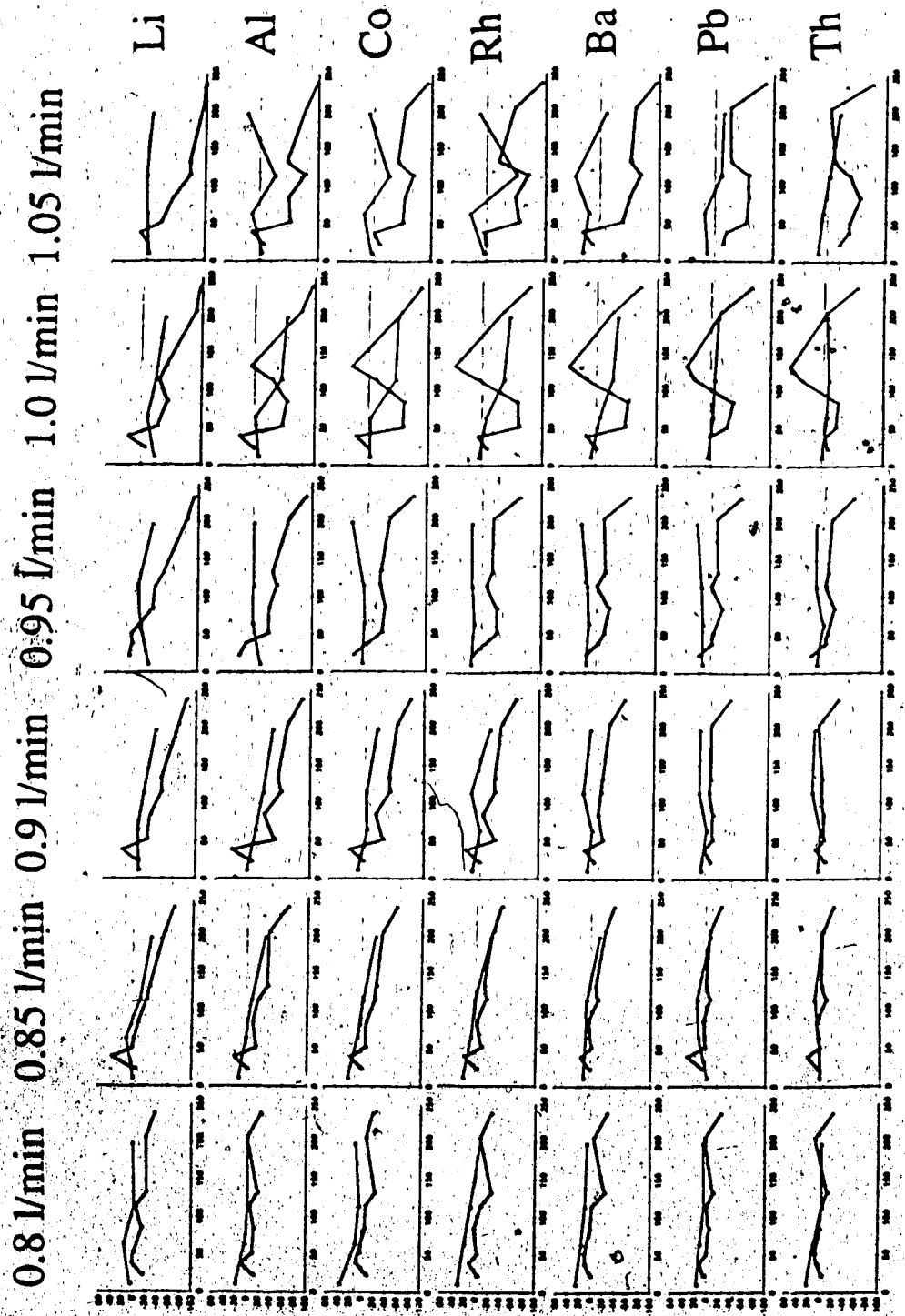


Figure 74. Mass dependency of the matrix effect for  $Ba^{2+}$  (upper graph) and  $Ba^{+}$  (lower graph).

flowrates of 0.8, 0.85, 0.9, 0.95, 1.0 and 1.05 l/min. The plot format for each frame in the figure is the same as that for Figure 70. The rows illustrate the matrix effect behaviors for the analyte elements of Li, Al, Co, Rh, Ba, Pb and Th. The plots for Sc were omitted because they are very similar to those of Co. Each column presents the matrix effects characteristic of each nebulizer flowrate. In addition to the 2 groups of matrix elements discussed previously, the matrix elements K, Cr and In are also included in this set of data. The In data fits well into the easily ionized elements group but K and Cr matrices in most instances behave differently. The anomalous behavior of the K and Cr matrices will be discussed later in the chapter.

From this rather complex diagram, several interesting features can be identified. In general, matrix effects are smaller at lower nebulizer flowrates. As the nebulizer flowrate is increased, matrix effects (suppressions and enhancements) become more severe. Dependence of the matrix effect on the mass of the matrix element is not observed at all nebulizer flowrates. The mass dependence is only clearly seen at 0.85, 0.9 l/min and 0.95 l/min for both groups of matrices. At the nebulizer flowrates of 1.0 l/min and 1.05 l/min, no smooth trend in the plots is observed. However, it can be seen that the difference in the matrix effect exerted by the 2 groups of matrices increases from 0.8 l/min to 0.95 l/min, as is indicated by the greater separation of the 2 lines in the plots as the nebulizer flowrate increases. This feature indicates that as the nebulizer flowrate increases the low ionization potential matrix elements exert more matrix effect. At higher flowrates, no clear trend can be seen for these matrices but it is still obvious that the high ionization potential elements cause less matrix effects as compared to the low ionization potential elements.



### MASS OF MATRIX ELEMENTS

Figure 75. Effect of nebulizer flowrate on the mass dependency of the matrix effect.

The data from Figure 75 are replotted for each nebulizer flowrate in Figures 76 and 77. In both these figures, matrix effects for the high ionization potential matrix elements are shown in the first column and those for the low ionization potential matrix elements are shown in the second column. In Figure 76, the matrix effect is plotted against the mass of the matrix element, whereas in Figure 77 the matrix effect is plotted against the mass of the analyte element. From these data, it can be seen that although matrix effects at a nebulizer flowrate of 0.8 l/min are relatively small, the separation of the matrix elements into 2 groups is still evident; however, the dependence of matrix effect on the mass of analyte element is not observed for this flowrate. For the high ionization potential matrices, at nebulizer flowrates 0.85, 0.9 and 1.0 l/min, the dependence of the matrix effect on the mass of matrix element and analyte element is clearly observed. Unexpected behavior is observed at 0.95 l/min, where a minimal matrix effect is obtained. For low ionization potential matrices, the dependence on mass is observed at all flowrates except at 0.8 l/min and 1.0 l/min. Although no smooth trend is observed for the dependence on the mass of the matrix elements at 1.0 l/min for the low ionization potential matrices, the dependence of the matrix effect on the mass of the analyte elements is still clearly seen (see Figure 77).

F. Effect of a Matrix Element on Ion Signal-Nebulizer Flowrate Plot Profiles for Co and Pb

Changes in the parameter behavior plots with the introduction of a matrix element are shown for Co (light element) and Pb (heavy element) in Figures 78 and 79. Effects by the high ionization potential matrices are shown in Figure 78 and those for the low ionization potential matrix elements are shown in Figure 79. It can be seen from these plots that at low flowrates (<

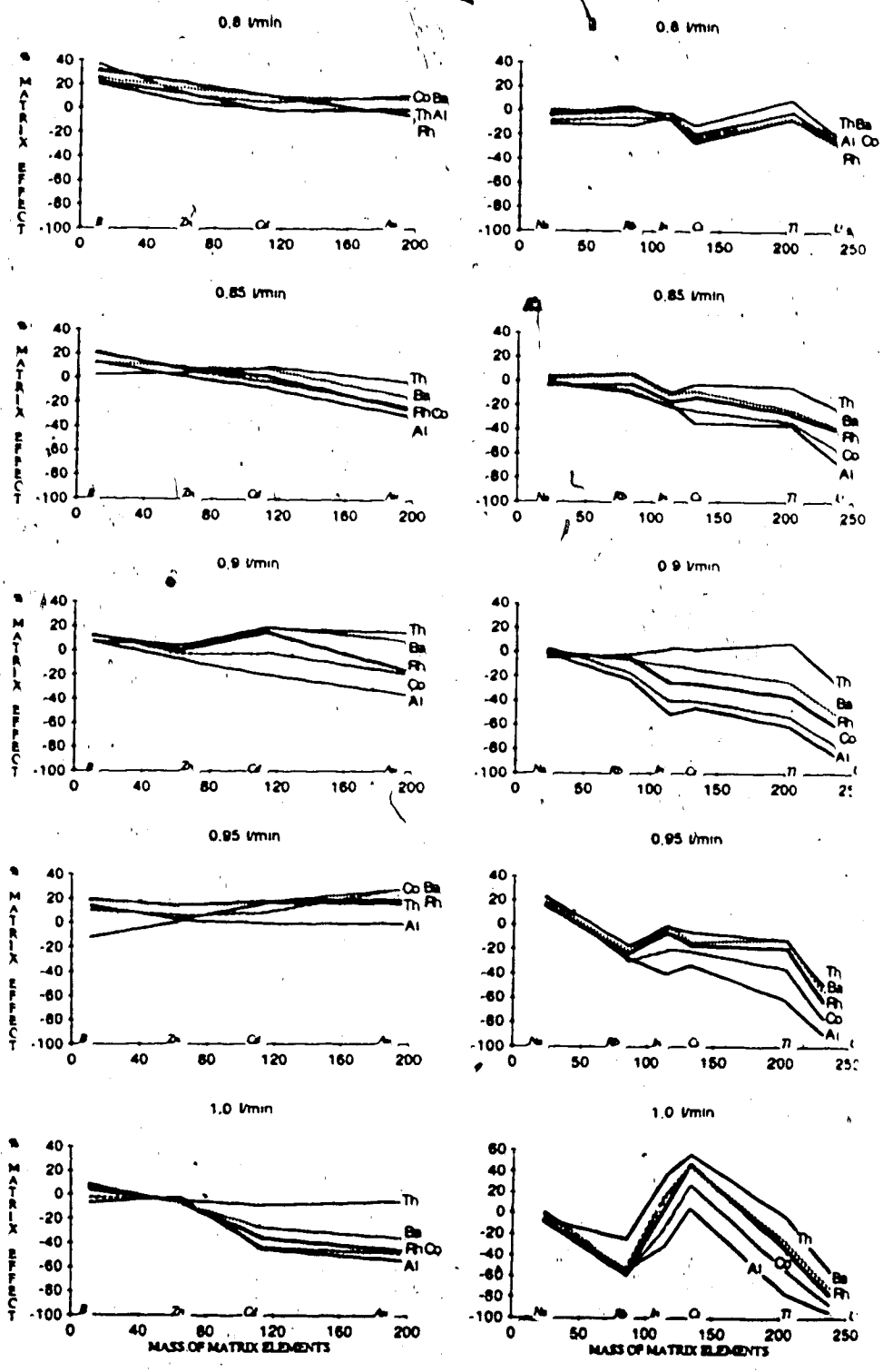


Figure 76. Matrix effect as a function of nebulizer flowrate and mass of matrix element for the high ionization potential matrices (first column) and for low ionization matrices (second column).

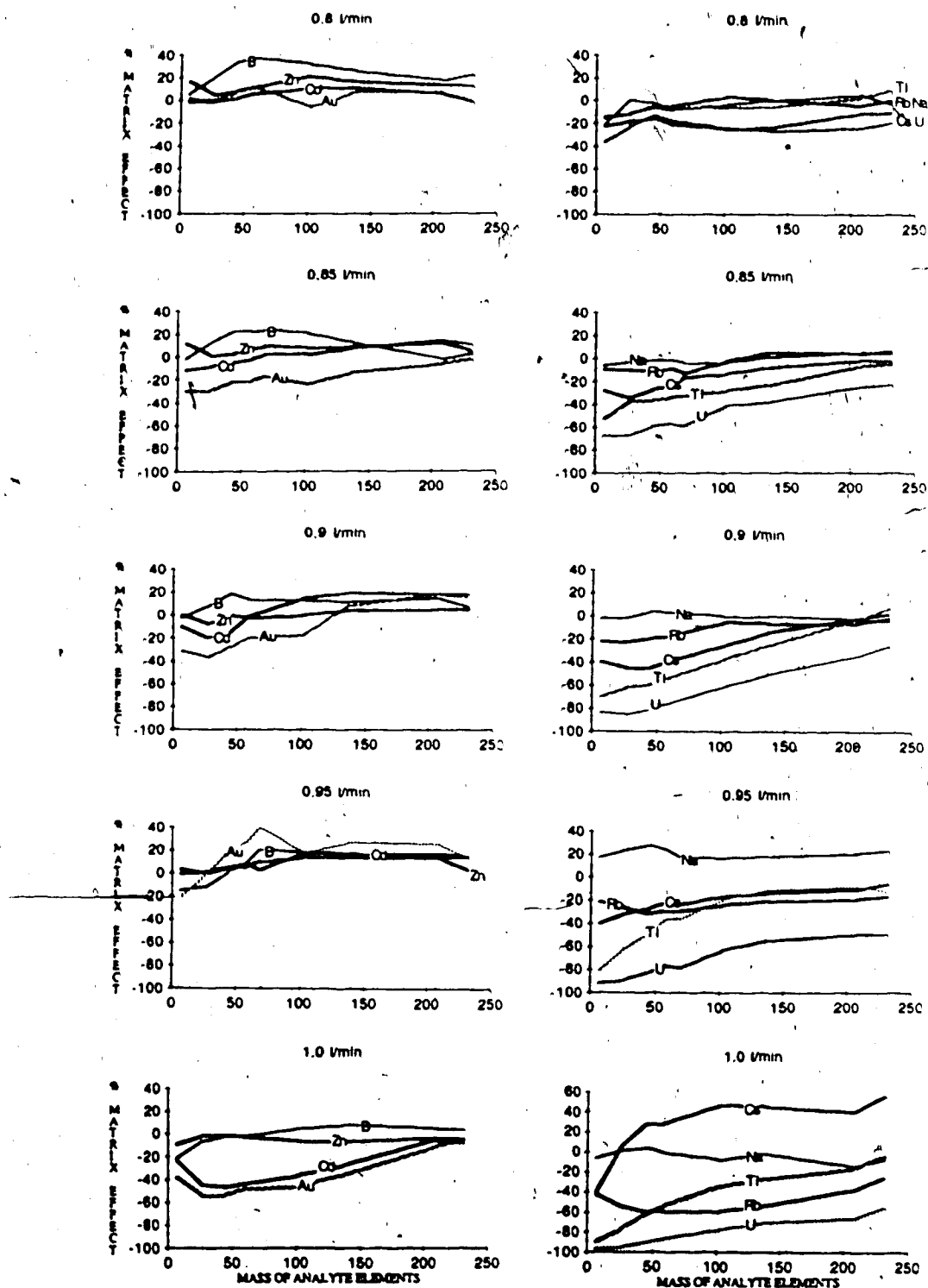


Figure 77. Matrix effect as a function of nebulizer flowrate and mass of analyte element for the high ionization potential matrices (first column) and for low ionization matrices (second column).



0.95 l/min), the slope of the parameter behavior plots is relatively flat. However, at higher nebulizer flowrates, there are some changes in the profile of the plots, especially for matrices containing heavy matrix elements. From Figure 78, it can be seen that in B and Zn matrices, the parameter plots are not changed significantly for Co and Pb. But in the Cd and Au matrices, the maxima of the plots are shifted to higher flowrates. This causes an enhancement of ion counts above a nebulizer flowrate of about 1.05 l/min. For the low ionization potential matrix elements in Figure 79, matrix effects are more severe and the change in the plot profile is not so obvious, although there seems to be also some shift in the maxima of these plots at high nebulizer flowrates.

From Figure 79, it can be seen that the jitter in the analyte signal-nebulizer flowrate parameter plots for Co with the K matrix and Pb with the Cs matrix gives rise to erratic matrix effect behavior. For the nebulizer flowrate of 1.0 l/min in Figure 75 the mass dependency plot swings from suppression to enhancement and back again to suppression. For nebulizer flowrates that maximize the analyte signal (1.0 l/min), slight shifts in the parameter plots can generate misleading matrix effect measurements when data are taken at only one nebulizer flowrate. This goes to show the difficulty that researchers have had in obtaining meaningful, reliable and transferable matrix effect data in ICP-MS.

These data show that at high nebulizer flowrates the plot profiles can be shifted. These shifts could be the result of changes occurring in the plasma discharge because of the presence of a matrix element, and also the result of changes occurring at the extraction interface. Since the maximum of the ion signal-nebulizer flowrate plot is critically dependent on the spatial distribution of the ions in the plasma as well as any physical changes at the

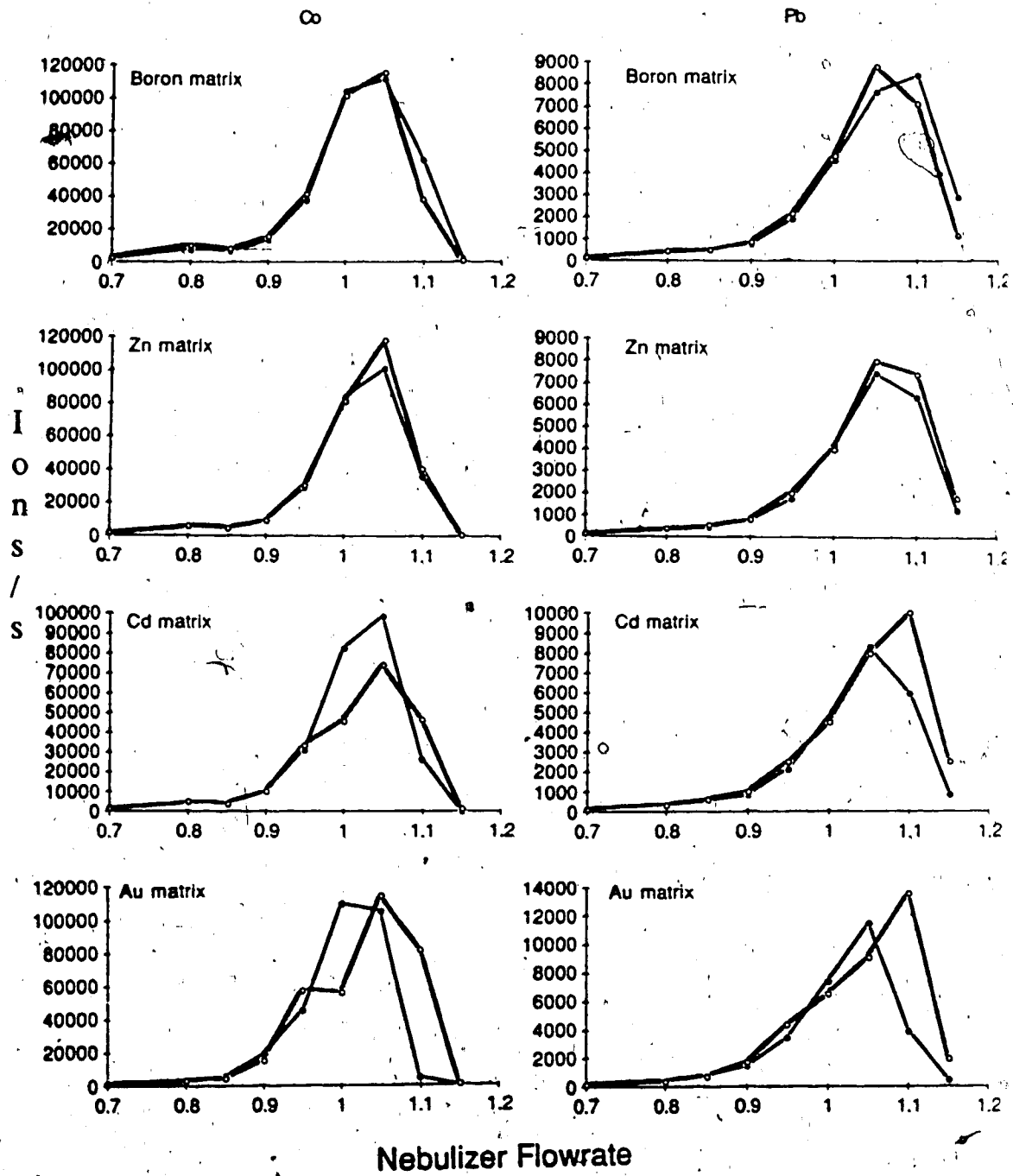


Figure 78. Effects of B, Zn, Cd and Au matrices on the ion signal-nebulizer flowrate plots for Co and Pb

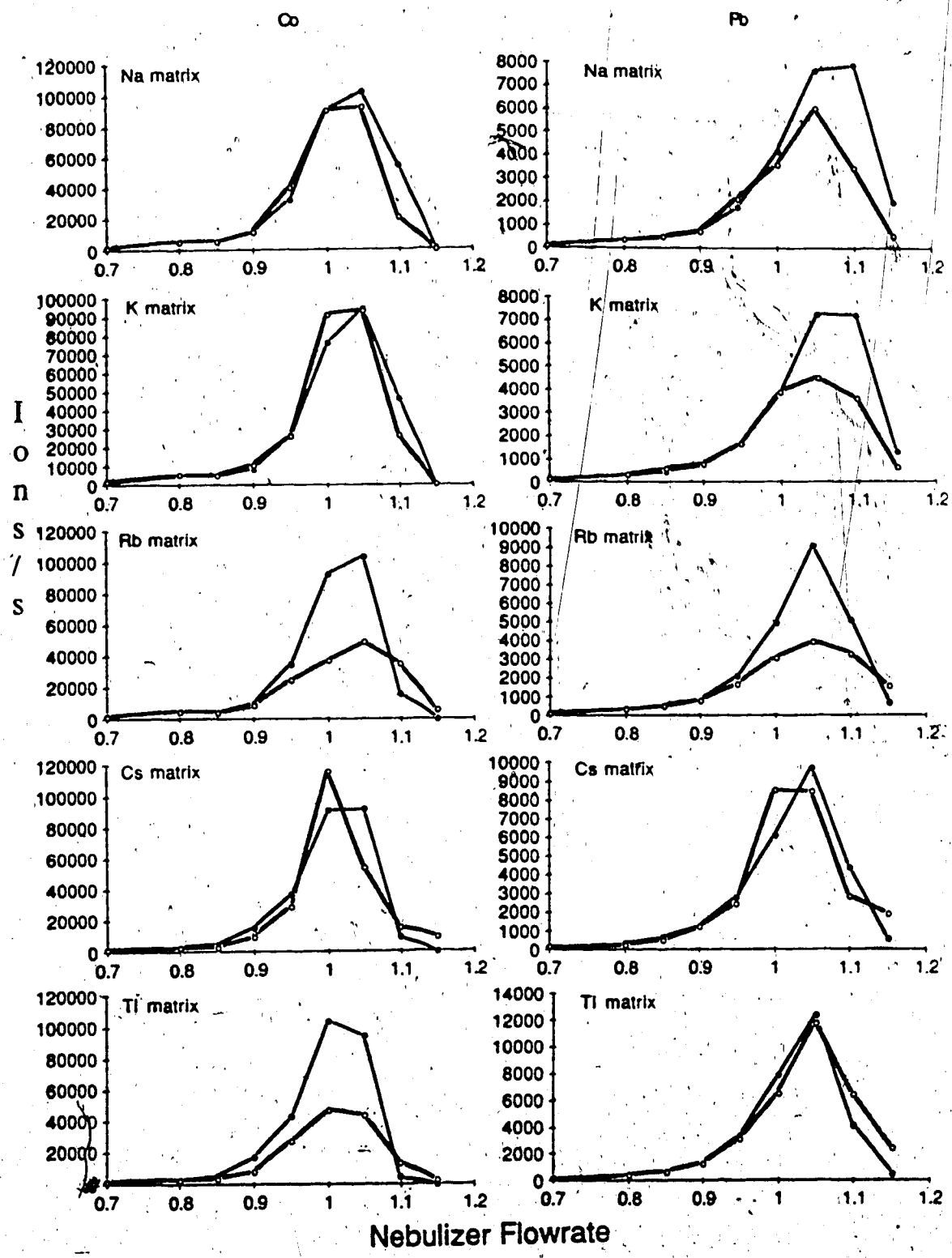


Figure 79. Effects of Na, K, Rb, Cs and Tl matrices on the ion signal-nebulizer flowrate plots for Co and Pb

extraction interface such as salt deposition in the sampling orifice, the data in this region is often noisy and variable. Furthermore, since the slope of the ion signal-nebulizer flowrate plot at high flowrates is steep, it is more susceptible to small differences in the nebulizer flowrate set by the mass flow controller. These factors therefore give rise to the poor reproducibility in the matrix effects observed at high nebulizer flowrates.

#### G. Matrix Effects in ICP-AES

Similar matrix effect experiments were carried out on an ARL 34000 ICP-AES in order to compare matrix effect behavior in ICP-MS to ICP-AES. Analyte elements studied were Li, Mg, Cr, Mn, Sr, Ba and Pb, and matrix elements were  $4.2 \times 10^{-3}$  M B, Zn, Cd, Au, Na, K, Rb, Cs and U. Matrix effects were measured at nebulizer flowrates of 0.9 l/min and 1.4 l/min. The plasma operating conditions were plasma power, 1.25 kW; plasma gas pressure, 40 psi; auxiliary gas pressure, 20 psi; and the observation height was 15-17 mm above the load coil. The integration time for each analyte spectral line was 20 s and 6 repetitive measurements were taken.

The data obtained at 0.9 l/min and 1.4 l/min are shown in Table 15. It is clearly seen that matrix effects in atomic emission spectroscopy are small and in general, less than 10 % for all types of matrices. The large apparent enhancement of the emission signals for Mg in U matrix and for Pb in Zn matrix are most probably the result of spectral overlap. A small increase in the enhancement of analyte emission is observed at 1.4 l/min in the low ionization potential matrices. These results clearly show that at the matrix concentration levels used in this experiment, matrix effects in ICP-AES are minimal and completely different to that observed in ICP-MS.

Table 15. Matrix effects in ICP-AES \*

Nebulizer Flowrate 0.9 l/min

| <u>Analytes</u> | <u>Li</u> | <u>Mg</u> | <u>Cr</u> | <u>Mn</u> | <u>Sr</u> | <u>Ba</u> | <u>Pb</u> |
|-----------------|-----------|-----------|-----------|-----------|-----------|-----------|-----------|
| B matrix        | 1.1       | -0.07     | 0.39      | 0.9       | 0.79      | 0.64      | 0.65      |
| Zn matrix       | -0.53     | 0.1       | 0.48      | -0.68     | -0.73     | -0.57     | 10.23     |
| Cd matrix       | 0.93      | -0.14     | 0.62      | 0.76      | 0.99      | 0.86      | 1.38      |
| Au matrix       | 2.06      | 2.48      | 2.5       | 3.14      | 2.33      | 2.35      | 3.55      |
| Na matrix       | 0.35      | 0.1       | 0.34      | 0.33      | 0.57      | 0.46      | 0.33      |
| K matrix        | -1.11     | 0.14      | -0.71     | -1.18     | -1.06     | -0.9      | -0.77     |
| Rb matrix       | 1.84      | 0.89      | 1.84      | 1.98      | 2.39      | 2.83      | 1.82      |
| Cs matrix       | 1.87      | -0.17     | 1.33      | 1.6       | 2.11      | 1.8       | 1.09      |
| U matrix        | 4.9       | 41.0      | 4.5       | 6.6       | 6.75      | 7.0       | 4.4       |

Nebulizer Flowrate 1.4 l/min

| <u>Analytes</u> | <u>Li</u> | <u>Mg</u> | <u>Cr</u> | <u>Mn</u> | <u>Sr</u> | <u>Ba</u> | <u>Pb</u> |
|-----------------|-----------|-----------|-----------|-----------|-----------|-----------|-----------|
| B matrix        | 4.98      | -0.07     | -0.36     | -0.21     | 0.26      | 0.17      | 1.47      |
| Zn matrix       | 2.03      | -0.7      | -0.61     | -0.61     | 0.68      | 0.53      | 13.58     |
| Cd matrix       | -4.95     | 0.7       | 1.77      | 2.8       | 0.76      | 1.72      | 0.14      |
| Au matrix       | 2.0       | 0.98      | 1.92      | 3.14      | 1.64      | 2.31      | 1.5       |
| Na matrix       | 15.85     | 1.54      | 1.14      | 3.71      | 2.68      | 2.78      | 8.52      |
| K matrix        | 19.3      | 2.1       | 1.55      | 3.63      | 2.63      | 4.84      | 7.94      |
| Rb matrix       | 15.08     | 1.9       | 1.55      | 3.63      | 2.63      | 4.84      | 7.94      |
| Cs matrix       | 20.83     | 0.84      | 0.49      | 2.95      | 3.11      | 3.96      | 9.32      |
| U matrix        | 6.8       | 71.0      | 3.7       | 5.1       | 4.5       | 6.9       | 8.1       |

\* Values are in percentage

## H. Summary on Matrix Effects in ICP-MS

Despite the complexities observed for matrix effects in ICP-MS, some clear trends emerge from the data in Chapter 5 and Chapter 6. First, a general type of matrix effect certainly exists. It is a serious effect and generally results in suppression of analyte signals in the presence of high concentrations of matrix elements. The degree of the matrix effect is strongly dependent on the nebulizer flowrate and tends to be less severe at low nebulizer flowrates than at high nebulizer flowrates. The minimization of the matrix effect by running at lower nebulizer flowrate normally means that one is running at conditions which are sub-optimal with respect to signal sensitivity by as much as an order of magnitude. While suppression effects seem most general, it is possible to observe enhancements, particularly at high nebulizer flowrates where the data also may exhibit considerable variability. In fact, data jitter and as a result misleading trends can be a serious problem in ICP-MS matrix effect studies for measurements carried out at one set of conditions. Overall, if data are evaluated for a range of nebulizer flowrates, matrix effects are not significantly altered by changes in plasma power and sampling depth.

It appears that matrix effects are also dependent on the absolute concentration of the matrix elements and not on the relative concentration of the matrix element to the analyte. Effects are observed at matrix element concentrations as low as 100 ppm (0.01 %) and are generally quite severe by the 1000 ppm (0.1 %) level.

Definite mass trends are observed for the matrix effect. Heavy matrix elements cause more severe matrix effects and light analytes are more seriously affected. The worst case scenario is to try to determine Li in a U matrix.

There is some indication that two classes of matrix elements exist.

More severe matrix effects occur in the presence of matrix elements that have low ionization potentials and a high degree (~ 100 %) of ionization in the ICP. For matrix elements that have relatively high ionization potentials and that have a degree of ionization substantially less than 100 % in the ICP, matrix effects are smaller.

While many others have observed these same trends it must be noted that exception can be found for almost all these trends in the data of others and even in our own data. In particular, we have not yet studied the effect of the geometry of the interface sub-system and the geometry and voltage settings of the input ion optics on matrix effects. Some workers have observed that changes in the value of the parameters associated with these sub-systems can have a substantial effect on matrix effects. This is an important area of work for it is likely within these sub-systems that causes for these matrix effects will be found.

#### I. Discussion and Conclusions

In delineating the possible causes and sources of these matrix effects in ICP-MS, one should start with some comparisons to ICP-AES. In general these observed matrix effects are significantly more serious than analogous effects in ICP-AES. Certainly, suppressions and enhancements are observed in ICP-AES but normally they are in the 10 to 20 % range and are not significant until the matrix concentration is in the range of 1 % (10,000 ppm). The data in section G show that matrix effects in ICP-AES are small, particularly at 0.9 l/min, where most changes are less than 3 %. The matrix effects are larger at the higher nebulizer flowrate, a trend that is common in

ICP-AES, but still nowhere near the level or direction of the effects seen for ICP-MS.

However, this comparison is not completely valid. The data in section G reflect the changes in emission in the analyte channel on the direct reader and as such indicate changes in the excited atomic or ionic populations. A more valid comparison to optical results requires that comparisons be made to changes in the ground state ion population in the ICP induced by a matrix element. In other words, comparison must be made to matrix effect studies on atomic and ionic fluorescence or on atomic and ionic absorption results in the ICP. Very few such measurements have been made. Gillson and Horlick [71] summarized the ICP-AFS and ICP-AAS studies that have been reported and also presented a reasonably complete set of data on the effect of Na on Ca ionic and atomic fluorescence signals. At a plasma power of 1.25 kW and 13 mm above the load coil a 100 fold molar excess of Na suppressed the Ca ionic fluorescence signal by about 30 % and at 19 mm above the load coil, by about 5 %; for a variety of other observation heights and powers, suppression of the ionic fluorescence signal was observed.

These data correlate somewhat better with the ICP-MS data. Thus, some of the suppressions observed in the ICP-MS may indeed be occurring in the ICP. Perhaps the fact that the low ionization potential elements exert a more serious matrix effect in the ICP-MS is due, in part, to the fact that they suppress ground state ion population in the ICP while the high ionization potential matrix elements do not. More ICP-AFS interference data are required in order to verify this idea, but it remains a distinct possibility. However, given the mass dependencies of the ICP-MS matrix effects, causes and explanations must clearly be sought in the mass spectrometer, including the interface, ion lenses, and quadrupole sub-system.



Some of the mass effects could originate at the sampling interface. The sampler and skimmer cones are similar to systems used in molecular beam sampling processes. Mass separation effects have been noted during molecular beam sampling when a gas mixture is expanded through a supersonic nozzle similar to that of the ICP-MS interface. The mass separation effects are such that heavier species are concentrated onto the axis of the molecular beam and inversely, lighter ones diffuse away from the center axis [80]. Two main phenomena involved are pressure diffusion and Mach number focussing. A steep pressure gradient develops around the jet expanding through a nozzle and lighter molecules diffuse in an off-axis direction faster than heavier ones. As a result, the fraction of heavier molecules to the lighter ones increases along the central axis. Sherman [81] has analyzed this process in detail. Mach number focusing has to do with relative velocities in the molecular beam. In a so called seeded beam, one containing a minor heavy species in a light beam, the axial velocity of the trace heavy species is accelerated by the majority of the lighter species. This tends to focus the heavy species towards the central axis [80].

It is difficult to quantitatively transfer these phenomena directly to the ICP-MS situation. Our beam is primarily Ar. Thus, the Mach-focusing effect should concentrate heavy elements towards the axis as will the pressure diffusion effect. One of the stronger matrix effect trends observed was the suppression of a light analyte's signal by the presence of a heavy matrix element (i.e. U matrix on Li analyte). One can speculate that the above focussing effects are forcing more U species to the central axis of the beam formed after the sampling cone at the expense of the lighter Li species. Thus, when this beam is sampled by the skimmer, less Li signal is on axis because of the presence of U, and hence the Li signal is suppressed. While it fits the

trend, it must be emphasized that this is a highly qualitative speculation, particularly considering the fact that the theories dealing with the above phenomena were developed for neutral beams. Phenomena associated with charged beams are likely to be quite different. Thus, the above effects might play a role in matrix effects but they may in fact be quite minor.

For example, the matrix effect data presented earlier for  $Ba^+$  and  $Ba^{2+}$  in Figure 74 indicates that it is clearly mass/charge ratio that is important. This means that perhaps it is the ion trajectory through the input ion optics and/or the quadrupole mass spectrometer that is being disturbed by the presence of the matrix element. Thus,  $Ba^{2+}$  and  $Co^+$  should experience similar matrix effects and that is what is observed.

What one might call a "circumstantial interpretation" of the data in Figure 68 (chapter 5) also points in this direction. Recall the data presented in this figure showed that the degree of the matrix effect was highly dependent on the absolute concentration of the matrix element rather than the relative concentration of the matrix element to analyte. A high matrix element concentration (~ 1000 ppm) suppression of analyte signal was observed, while at the 10 ppm level of matrix element only small effects were observed even though the molar ratio of analyte to matrix was 1:1000 in both cases. Perhaps at low concentration the ion beam trajectories through the system are  $Ar^+$  dominated, what could be called "normal", and as the concentration of the matrix ion increases the beam trajectories become dominated and are affected by the matrix ion rather than by argon ions. Thus, matrix-induced space charge effects in the beam through the ion optics and the mass spectrometer could be a major cause of matrix effects. It does seem that matrix effects are minimal when conditions are such as to maximize  $Ar^+$  signals relative to

matrix and/or analyte signals, that is, dilute samples being run at lower nebulizer flowrates.

Two areas now certainly need to be investigated in detail. One is the effect of the sampler-skimmer geometry on matrix effects, in particular the effect of sampler-skimmer separation distance and the relative size of sampler and skimmer orifices on matrix effects. This should clarify the role of pressure diffusion and Mach-number focusing in matrix effects. Secondly, a systematic study of the effect of the input ion lens voltages and geometry on matrix effects is required. Some limited reports have indicated that matrix effects can be minimized by adjustment and alteration of lens parameters [82, 83]. In our own experience we have made some attempts at studying the effect of input ion optic lens voltage settings on matrix effects but have not yet found convincing evidence that matrix effects can be significantly improved. More work, however, is warranted in this area.

## CHAPTER 7

### CONCLUSION

It is well known by now that the ICP-MS is indeed a very promising technique for trace elemental analysis. Its superior basic quantitative characteristics are confirmed by data presented in Chapter 4. Its sensitivity and detection limits for most elements surpass any other spectroscopic technique except perhaps Graphite Furnace Atomic Absorption Spectroscopy. It has an additional advantage of being a rapid, multi-elemental technique for most of the elements in the periodic table. However, as with any new analytical technique, much research is required in order to fully understand the method, especially at a fundamental level, so that its full potential can be realized.

It was found that plasma operating parameters, especially nebulizer flowrate and plasma power, are key variables in affecting the analyte ion signal in ICP-MS. These two parameters interact in a parallel manner to provide characteristic nebulizer flowrate-power parameter behavior plots. The ion signals are also dependent on auxiliary flowrate, sampling depth, and torch geometry. From this study, one can see that the analyte ion signals in the ICP-MS depend in a complex manner on many parameters. Although the effect of the operating parameters of the mass spectrometer on the analyte signal was not studied in this thesis, it is well known now that the analyte signal depends significantly on the input ion lens voltages. The study on the operating parameters in ICP-MS is important with respect to selecting optimum operating parameters for the instrument. It also helps to clarify confusing single parameter results.

When ICP-MS was first introduced, the method was said to be free from spectral overlaps because of the inherent simplicity of mass spectra.

Furthermore, matrix interference from concomitant salts was reported to be negligible. However these views were proved to be overly optimistic. This was shown by the data presented in Chapters 4 to 6. It was shown that matrix effects can be a serious problem in ICP-MS. Matrix effects can be divided into two main categories. In the first category, a matrix effect is caused by spectral overlap from the formation of polyatomic species in the ICP-MS. These polyatomic species include background molecular species of acid matrices such as  $\text{ClO}^+$ ,  $\text{SO}^+$  and  $\text{PO}^+$  from hydrochloric, sulfuric and phosphoric acids. These major species plus their isotopic combinations can give rise to serious spectral overlap problems. Another type of matrix induced spectral overlap problem arises from the formation of  $\text{ArX}^+$  species when a high concentration of any element X, is present. For example,  $\text{ArNa}^+$  is formed when a high concentration of Na is present and this particular species causes an overlap with  $^{63}\text{Cu}$ . The identification and documentation of these polyatomic species in various matrices are, therefore, very important in order to avoid possible spectral interference problems.

The second category of matrix effects is the matrix induced change in analyte signal. This class of matrix effect is more complex, however, some clear trends were found. This matrix effect occurred with all types of matrix elements and depended significantly on the absolute matrix concentration and nebulizer flowrate. Dilution of a sample solution containing a 1:1000 ratio of analyte to matrix element changed an overall suppression effect on the analyte signal to no matrix effect even though the analyte to matrix element ratio remained the same. Serious matrix effects were found at higher nebulizer flowrates and relatively small matrix effects were found at low nebulizer flowrates. Based on these two observations, it could be seen that the relative concentration of the matrix ion to argon ion in the ion beam is important, and the matrix effect

observed could be a result of a change in the space charge of the ion beam. A certain mass dependency in the matrix effect was also found. Light analyte elements are most effected by a heavy matrix element. For example, determining Li in the presence of excess U results in a severe matrix effect. This mass effect can be qualitatively explained by mass separation effects in the expanding supersonic beam. However, there is evidence that it is the mass-to-charge ratio that is important in giving rise to the mass trend in the matrix effects.

Some of the matrix effects observed may be attributed to processes occurring in the plasma and were found to correlate well with ICP-AFS and ICP-AAS data. However, most of the matrix effect phenomena observed are unique only to ICP-MS. The explanations put forward for the causes of the matrix effects observed in this thesis in most instances, are still highly speculative, much more research is required before they can be proven conclusively. It is now certain that attention has to be directed to the mass spectrometer (especially the input ion optics) and the sampling interface in order to obtain answers to the observed matrix effects.

This study on ICP-MS also brought out certain implications for the quantitative determination of trace elements in real samples. First, minimization of the matrix effects can be only brought about by dilution of the sample and/or by lowering the nebulizer flowrate. Both these steps result in a loss of analyte signal. Since the technique has excellent detection limits, it is possible to dilute the sample or lower the nebulizer flowrate and still make accurate and sensitive determinations. However, these steps will limit the capability when sub-ppb concentration levels in the sample are sought. In such cases, the standard addition method or the use of an internal standard may prove useful. However, an internal standard may not be effective because of the mass

dependency of the matrix effect. One can use multiple internal standards to correct for the mass dependency but this can become tedious. A problem can also arise when determining an analyte which has an overlap from a background species. In the presence of a high concentration of a matrix element, the background species is also suppressed or enhanced by the matrix element. Therefore, to measure the analyte in the presence of an overlapping background species and a matrix element, one requires a blank subtraction from an ultra-pure solution of the matrix element. This could pose a problem especially for determinations at the sub-ppb level because of the unavailability of ultra-pure standards.

## REFERENCES

1. V. A. Fassel and R. N. Kniseley, *Anal. Chem.* 46, 1110A (1974).
2. R. S. Houk, V. A. Fassel, G. D. Flesch, H. J. Svec, A. L. Gray and C. Taylor, *Anal. Chem.* 52, 2283 (1980).
3. A. R. Date and A. L. Gray, *Analyst* 106, 1255 (1981)
4. A. L. Gray and A. R. Date, *Analyst* 108, 1033 (1983).
5. D. J. Douglas, *Canadian Research* 16, 55 (1983).
6. R. S. Houk and J. J. Thompson, *Amer. Mineralogist* 67, 238 (1982).
7. A. R. Date and A. L. Gray, *Int. J. Mass Spectrom. and Ion Phys.* 48, 357 (1983).
8. R. S. Houk and J. J. Thompson, *Biomed. Mass Spectrom.* 10, 107 (1983).
9. V. A. Fassel and R. N. Kniseley, *Anal. Chem.* 46, 1155A (1974).
10. V. A. Fassel, *Anal. Chem.* 51, 1290A (1979).
11. J. P. Robin, *Prog. Analyt. Atom. Spectrosc.* 5, 79 (1982).
12. R. S. Houk, V. A. Fassel and H. J. Svec, *Dyn. Mass Spectrom.* 6, 234 (1981).
13. P. W. J. M. Boumans, *Theory of Spectrochemical Excitation*. Hilger & Watts, London (1966).
14. ~~B. L. Caughlin~~ and M. W. Blades, *Spectrochim. Acta* 40B, 1539 (1985).
15. R. S. Houk, *Anal. Chem.* 58, 97A (1986).
16. N. Furuta, *Spectrochim. Acta* 41B, 1115 (1986).
17. P. Kebarle and A. M. Hogg, *J. Chem. Phys.* 42, 668 (1965).
18. R. Campargue, *Rev. Sci. Instr.* 35, 111 (1964).
19. A. N. Hayhurst, F. R. G. Mitchell and N. R. Telford, *Int. J. Mass Spectrom. and Ion Phys.* 7, 177 (1971).



20. R. V. Serauskas, G. R. Brown and R. Pertel, *Int. J. Mass Spectrom. and Ion Phys.* 16, 69 (1975).
21. J. E. Fulford and D. J. Douglas, *Appl. Spectrosc.* 40, 971 (1986).
22. J. A. Olivares and R. S. Houk, *Anal. Chem.* 57, 2674 (1985).
23. A. Kantrowitz and J. Grey, *Rev. Sci. Instr.* 35, 111 (1964).
24. H. C. W. Beijerinck, R. J. F. Van Gerwen, E. R. T. Kerstel, J. F. M. Martens, E. J. M. Van Vliembergen, M. R. Th. Smits and G. H. Kaashoek, *Chem. Phys.* 96, 153 (1985).
25. J. B. Anderson and J. B. Fenn, *Phys. Fluids* 8, 780 (1965).
26. P. P. Wegener, *Molecular Beams and Low Density Gasdynamics*, Vol 4, Chapter 1, Marcel Dekker, New York (1974).
27. J. A. Olivares and R. S. Houk, *Appl. Spectrosc.* 39, 1070 (1985).
28. W. L. Fite, *Research Note No. 1* (1971).
29. J. B. Anderson, R. P. Andres and J. B. Fenn, *Adv. Chem. Phys.* 10, 300 (1966).
30. R. Kinglehofer and P. Lohse, *Phys. Fluids* 7, 379 (1964).
31. J. Fernandez le la Mora, *J. Chem. Phys.* 82, 3453 (1985).
32. L. Valyi, *Atom and Ion Sources*, John Wiley & Sons, London (1977).
33. G. Lawson and J. F. J. Todd, *Chem. Brit.* 373 (1971).
34. P. Dawson, *Quadrupole Mass Spectrometry and Its Applications*, Elsevier, Amsterdam (1976).
35. A. L. Gray, *Spectrochim. Acta* 40B, 1525 (1985).
36. D. J. Douglas and R. S. Houk, *Prog. Analyt. Atom. Spectrosc.* 8, 1 (1985).
37. D. J. Douglas, *ICP Inform. Newslet.* 16(3), 191 (1984).
38. G. Horlick, S. H. Tan, M. A. Vaughan and Y Shao, *Radiation Chemistry*, Chapter 10, edited by Montaser and Golightly, VCH Publishers Inc., 1986.

39. A. L. Gray, *Analyst* 100, 289 (1975).
40. A. L. Gray, *Anal. Chem.* 47, 600 (1975).
41. D. J. Douglas and J. B. French, *Anal. Chem.* 53, 37 (1981).
42. D. J. Douglas, E. S. K. Quan and R. G. Smith, *Spectrochim. Acta* 38B, 39 (1983).
43. D. J. Douglas and J. B. French, *Spectrochim. Acta* 41B, 197 (1986).
44. A. R. Date and A. L. Gray, *Analyst* 108, 159 (1983).
45. A. R. Date and A. L. Gray, *Spectrochim. Acta* 38B, 29 (1983).
46. A. L. Gray and A. R. Date, *Int. J. Mass Spectrom. and Ion Phys.* 46, 7 (1983).
47. A. R. Date and D. Hutchison, *Spectrochim. Acta* 41B, 175 (1986).
48. A. R. Date, Y. Y. Cheung and M. E. Stuart, *Spectrochim. Acta* (in press).
49. C. W. McLeod, A. R. Date and Y. Y. Cheung, *Spectrochim. Acta* 41B, 169 (1986).
50. J. W. McLaren, D. Beauchemin and S. S. Berman, *Anal. Chem.* (in press).
51. J. W. McLaren, A. P. Mykytiuk, S. N. Willie and S. S. Berman, *Anal. Chem.* 57, 2907 (1985).
52. R. G. Smith, E. J. Brooker, D. J. Douglas, E. S. K. Quan and G. Rosenblatt, *J. Geochem. Explor.* 21, 385 (1984).
53. D. W. Boomer and M. J. Powell, *Can. J. Spectrosc.* 31, 104 (1986).
54. J. W. McLaren, A. P. Mykytiuk, S. N. Willie and S. S. Berman, *Anal. Chem.* 57, 2907 (1985).
55. B. T. G. Ting and M. Janghorbani, *Anal. Chem.* 58, 1334 (1986).
56. R. S. Houk, V. A. Fassel and H. J. Svec, *Organ. Mass Spectrom.* 17, 240 (1982).

57. G. Horlick, S. H. Tan, M. A. Vaughan and C. A. Rose, *Spectrochim. Acta* 40B, 1555 (1985).
58. M. A. Vaughan and G. Horlick, *Appl. Spectrosc.* 40, 434 (1986).
59. S. H. Tan and G. Horlick, *Appl. Spectrosc.* 40, 445 (1986).
60. A. L. Gray, *Spectrochim. Acta* 41B, 151 (1986).
61. R. S. Houk, H. J. Svec and V. A. Fassel, *Appl. Spectrosc.* 35, 380 (1981).
62. R. S. Houk, A. Montaser and V. A. Fassel, *Appl. Spectrosc.* 37, 425 (1983).
63. J. A. Olivares and R. S. Houk, *Anal. Chem.* 58, 20 (1986).
64. R. M. Brown, S. E. Long and C. J. Pickford, paper presented at XXIV CSI, Garmisch-Partenkirchen, 1985.
65. A. L. Gray, *Analyst* 110, 551 (1985).
66. P. Arrowsmith, *Anal. Chem.* (in press).
67. S. J. Jiang and R. S. Houk, *Anal. Chem.* 58, 1739 (1986).
68. M. W. Blades and G. Horlick, *Spectrochim. Acta* 36B, 861 (1981).
69. N. Furuta and G. Horlick, *Spectrochim. Acta* 37B, 53 (1982).
70. G. Gillson and G. Horlick, *Spectrochim. Acta* (in press).
71. G. Gillson and G. Horlick, *Spectrochim. Acta* 41B, 619 (1986).
72. S. R. Koirtiyohann, J. S. Jones and D. A. Yates, *Anal. Chem.* 52, 1965 (1980).
73. G. Gillson, private communication.
74. R. M. Belchamber and G. Horlick, *Spectrochim. Acta* 37B, 71 (1982).
75. E. D. Salin and G. Horlick, *Anal. Chem.* 52, 1578 (1980).
76. C. T. J. Allemade, *Anal. Chem.* 38, 1252 (1966).
77. M. W. Blades and G. Horlick, *Spectrochim. Acta* 36B, 881 (1981).
78. G. R. Kornblum and L. De Galan, *Spectrochim. Acta* 32B, 455 (1977).
79. R. Avni and F. S. Klein, *Spectrochim. Acta*, 28B, 331 (1973).

80. S. Yamazaki, M. Taki and Y. Fujitani, *Jap. J. Appl. Phys.* **18**, 2191 (1979).
81. F. S. Sherman, *Phys. Fluids*, **8**, 773 (1965).
82. F. E. Lichte, 1987 Winter Conference on Plasma and Laser Spectrochemistry, Lyon, France. Paper No. C4.
83. D. Douglas, 1987 Winter Conference on Plasma and Laser Spectrochemistry, Lyon, France. Paper No. C55.